IMPACT-INITIATED COMBUSTION OF ALUMINUM

A Thesis Proposal
Presented to
The Academic Faculty

by

Jennifer L. Breidenich

In Partial Fulfillment
of the Requirements for the Degree
Doctor of Philosophy in the
School of Materials Science and Engineering

Georgia Institute of Technology
December 2015

IMPACT-INITIATED COMBUSTION OF ALUMINUM

Approved by:

Professor Naresh Thadhani, Advisor
School of Materials Science and Engineering
Georgia Institute of Technology

Professor Thomas H. Sanders, Jr.
School of Materials Science and Engineering
Georgia Institute of Technology

Professor Arun M. Gokhale
School of Materials Science and Engineering
Georgia Institute of Technology

Doctor Sunil Dwivedi
School of Materials Science and Engineering
Georgia Institute of Technology

Doctor Suhithi Peiris

Defense Threat Reduction Agency

Date Approved: 18 September 2015

To my wife and partner in life,

Burke Doherty,

for her love and support, for her patience, and for bringing out the best in me.

ACKNOWLEDGEMENTS

Many people have been instrumental in helping me to complete this work. First, I would like to thank my advisor, Professor Naresh Thadhani for his support, guidance, and encouragement throughout my time at Georgia Tech. Additionally, I would like to acknowledge my committee members, Dr. Dwivedi, Professor Gokhale, Dr. Peiris, and Professor Sanders, for their mentorship and insights over the past five years. I would also like to thank Susan Bowman, for keeping her door open, being available to answer any questions, big or small, and for being a listening ear when needed.

I am very grateful for the thoughtful discussions and support from current and past members of the High Strain Rate Lab at Georgia Tech, including Stefany Holguin, Sukanya Sharma, Alex Bryant, Rene Diaz, Manny Gonzales, Parveen Sood, Ricky Whelchel, Sean Kelley, Brady Aydelotte, and Tyler Jackson. Special thanks to Dr. Greg Kennedy for always being available to bounce ideas off of and for being able to solve almost any problem that arises in the lab, to Dr. Paul Specht for teaching me the basics of CTH and for passing on several very useful MATLAB codes, to Dr. Chris Wehrenberg for his helpful experimental advice and training, and to David Scripka for his help with all laser and spectrograph issues. Additional thanks to Dr. Zhitao Kang who made all of the CdTe quantum dots and aided in the analysis of the absorbance spectra for the mesoscale diagnostics project. I also appreciate the helpful discussions with Dr. Summers, one of the PI's for the mesoscale diagnostics project, and with our collaborators at UIUC, Profesor Dlott and Dr. Banishev.

Several undergraduate students were extremely helpful in collecting data for this work. Thanks to Julien Turner for all of his help with making samples, taking shots, collecting SEM images, and writing MATLAB scripts, to Sadie Roberts for her help with the making samples and preparing microstructure images, and to Sean McGaha and Jon Wroblewski

for their help with making samples and collecting SEM images. Additional thanks to Peter Marshall for all of his help with the SEM and to Dr. Igor Kovalenko and to Dr. Alexandre Magasinski for their help with the BET analysis.

I want to thank my wife, Burke Doherty, for getting me through the day to day and for always reminding me of the light at the end of the tunnel.

Last, this work could not have been completed without funding from DTRA under contract number HDTRA1-10-1-0038 and HDTRA1-12-1-0052.

Contents

List of Tables

List of Figures

SUMMARY

This work focuses on the understanding of impact-initiated combustion of aluminum powder compacts. Aluminum is typically one of the components of intermetallic-forming structural energetic materials, such as Al+Ni, Al+Ta, and Al +W. Intermetallic-forming structural energetic materials (SEMs) are highly desirable for several applications due to their rapid energy release characteristics and mechanical properties. The impact initiation of intermetallic reactions is dependent on the mixing ability of the two reactants, their varying elastic/plastic properties, and morphologies. Additionally, reaction occurrence has been observed to be sensitive to factors including the impact velocity and the density of the powder compacts, as well as the size, shape, and mechanical properties of the constituent particles. The characterization of these intermetallic reactions is further complicated by the ability of aluminum to combust due to its reaction with oxygen in the environment.

In order to better understand the process of reaction initiation in intermetallic-forming SEMs, this work focuses on the understanding of impact-initiated combustion of compacts of one of the intermetallic-forming SEM constituents, aluminum powders. Aluminum powders of various sizes and different levels of mechanical pre-activation are investigated to determine their reactivity under uniaxial stress rod-on-anvil impact conditions, using a 7.62 mm gas gun. The compacts reveal light emission due to combustion reaction upon impact at velocities greater than 170 m/s. Particle size and the level of mechanical pre-activation affect the compact behavior on the particle-level, influencing particle-particle interactions, pore collapse, and particle-scale deformation and mixing. Ultimately, these processes influence combustion initiation on the particle-level by controlling the localized friction, strain, and heating between particle surfaces, as well as on the continuum-scale, by controlling the

amount of energy required for compaction and deformation of the powder compact during uniaxial stress loading. Particle size and compact density affect the void space, surface area available for reaction, and interactions between the particles. Mechanical pre-activation, such as that achieved via high-energy ball milling (HEBM) or high strain machining, strain hardens the starting materials, affecting the particle and continuum-level ability for plastic deformation. In order to understand the relationship between these properties and reactivity, the starting materials are characterized according to their microstructure and mechanical properties. Compacts composed of larger diameter aluminum particles (approximately 70 μm) are shown to be more sensitive to impact initiated combustion than those composed of smaller particle diameters. Additionally, mechanical pre-activation by high energy ball milling (HEBM) of the aluminum powders increases the propensity for reaction initiation at low velocities.

The mechanistic processes leading to reaction initiation in the Al samples are investigated via high speed and IR imaging of light associated with the reaction. Images captured during compaction and deformation, revealing light emission and temperature rise, were correlated with meso-scale CTH simulations performed using real microstructures of aluminum powder compacts. Areas of localized strain and heating during deformation of the particles were observed, which were used to explain the processes leading to react initiation and the impact-initiated combustion sensitivity of Al powders as a function of powder characteristics.

The results of mesoscale CTH simulations reveal that initiation of combustion reactions in aluminum powder compacts is closely tied to mesoscale processes, such as particle-particle interactions, pore collapse, and particle-level deformation. Traditional pressure and velocity sensors are large in surface area and spatially average out the effects of these mesoscale processes, rendering them incapable of probing the heterogeneous processes taking place at this length scale. In order to address this issue, quantum dots (QDs) are investigated as possible meso-scale pressure sensors for probing the shock response of

heterogeneous materials directly. Impact experiments were conducted on a QD-polymer film using a laser driven flyer setup at the University of Illinois Urbana-Champaign (UIUC). *In situ* time-resolved spectroscopy is used to monitor the energy shift and intensity loss as a function of pressure over nanosecond time scales. Shock compression of a QD-PVA film results in an upward shift in energy (or a blueshift in the emission spectra) and a decrease in emission intensity. The magnitude of the shift in energy and the drop in intensity is a function of shock pressure; this relationship can be used to track the differences in the shock pressure at the voids and interfaces of granular materials, such as aluminum powders. Quantum dot-based mesoscale diagnostics pave the way for a better understanding of the mesoscale mechanisms involved in the high strain rate-initiation of intermetallic reactions.

Chapter I

INTRODUCTION

1.1 Motivation and Impact

Upon combustion, aluminum releases large amounts of energy due to its high heat of reaction (ΔH_R = -7422cal/g). This property makes aluminum an extremely effective component of various high explosive systems. Energy release from high explosives is generally initiated by mechanical means, through the propagation of a high pressure or shock wave through the material following high speed impact. Thermally-initiated combustion reaction mechanisms are fairly well understood in aluminum [1], but the mechanism of impact-initiated reactions occurring under high strain rate loading conditions, typically a result of the detonation of high explosives, are poorly understood, making these systems difficult to control safely.

The United Nations reported that from 2013 to 2014, civilian casualties increased by 22% in the conflict in Afghanistan [2]. This dramatic rise was attributed to the increase in ground engagement across Afghanistan, during which both sides increasingly used high explosives systems. Civilian casualties that occur as a result of high explosives devices are due to both the primary effect of the high pressure blast of the explosive and the secondary effect of the fragmentation produced by the explosive. Fragments, created by the shattering of the explosive casing during the high pressure blast, are dangerous at much greater distances from the explosive than the blast itself. Additionally, the zone of both the blast and fragmentation are indiscriminate in nature, often resulting in collateral damage in the form of civilian injury or death [3]. Of the 2014 civilian casualties in Afghanistan, resulting from explosives, 37% of the deaths were attributed to pro-government forces and could be considered collateral damage [2].

A better understanding of the relationship between the design, fragmentation, and reactivity of these explosives could allow for better control of the explosive blast zone, resulting in increased civilian safety. As an explosive initially detonates, it sends a high pressure shock wave (under conditions of uniaxial strain loading) through the casing material. Additionally, hot gases expand within the casing, resulting in enhanced stress, tensile failure, and finally fragmentation, ejecting shards of the casing through the air at high velocities. These fragments eventually strike a target and react, under impact conditions of uniaxial stress loading [4].

Traditionally, explosive casings have been composed of a metal, such as steel, which has ideal mechanical properties for penetration. Yet, these steel casings are heavy and non-reactive, leading to increased fragmentation and a higher likelihood of civilian death. Structural energetic materials (SEMs) are considered to be an ideal alternative explosive casing material. SEMs are a non-explosive, non-detonable material capable of releasing large amounts of anaerobic heat of reaction through impact or shock-induced combustion. This property makes them safe to handle under normal conditions. Additionally, their mechanical strength can be sufficient enough for them to act as a warhead and penetrate targets when needed. SEMs of a range of material types, including combinations of thermites, intermetallics, metal-polymer mixtures, matrix materials, and hydrides, have been developed and studied with respect to their reactivity and mechanical and blast enhancement properties [5].

Intermetallic-forming SEMs are of particular interest because of their combination of high strength and high heats of reaction. The initiation of intermetallic reactions, such as in the case of Al+2B (ΔH_R = -371cal/g), 2Al+Ti (ΔH_R = -314cal/g), Al+Ni (ΔH_R = -330cal/g), and 2Al+Zr (ΔH_R = -267cal/g) [6], is dependent on the mixing of the two reactants, the varying elastic/plastic properties of the reactants, and the reactant morphologies [7, 8]. Additionally, reaction occurrence has been observed to be sensitive to factors including the impact velocity, the density of the intermetallic-forming powder mixture

compact, and the size and shape of the particles [9, 10, 11]. The mechanical and thermal processes leading to reaction initiation of intermetallic-forming materials under high strain rate conditions are difficult to identify and characterize because so many variables affect the occurrence of reaction in these materials.

The characterization of these intermetallic reactions is further complicated by the ability of aluminum to combust, which is assumed to occur according to the well-known reaction [12],

$$Al + O_2 = AlO + O \tag{1}$$

During impact initiation of a reaction of an intermetallic-forming mixture under high strain rate loading, several scenarios are possible: (1) an aluminum combustion reaction may be the precursor for the initiation of the intermetallic forming reaction, (2) an intermetallic-forming reaction may promote the aluminum combustion reaction, or (3) both an intermetallic-forming reaction and an aluminum combustion reaction may coincide. The occurrence of an intermetallic-forming reaction cannot be differentiated from the combustion of aluminum without the use of time-resolved spectroscopic analysis to identify the constituents of the transient states present during reaction and to determine the reaction products.

In order to isolate the processes that dominate the initiation of aluminum combustion as opposed to the intermetallic-forming reaction under high strain rates, this study is focused on investigating the impact initiation of the combustion reaction of a single-component system, composed of only aluminum. In addition to being a component of various structural energetic material systems, aluminum can also be used as a casing or shape charge material by itself. Aluminum is lightweight, high strength, inexpensive, and combustible. Although these properties might result in reduced penetration, they also lead to enhanced blast generation and potentially lower collateral effects. Understanding how combustion initiates under impact loading of aluminum will allow for more efficient and safe use of high explosive systems.

The extremely fast rates of mechanically-initiated reactions, typically occurring in time

frames on the order of microseconds or less, and the role of the mechanics of deformation require high resolution spatial and temporal monitoring to understand the reaction processes. Very few instruments are capable of monitoring the time-resolved structural and chemical changes in reaction products within this time and spatial scale. As a result, understanding of the reaction processes and their kinetics has relied on post-reaction recovery experiments, which provide little information on how and when the reaction products were formed and the role of transition states. Such studies of heterogeneous materials undergoing transitions at high rates, highlight the need for non-existent *in situ* meso-scale diagnostics. An ideal meso-scale diagnostic is capable of the *in situ* probing of the material states and providing both spatial- and time-resolved information about the pressures and/or temperature history of the material during mechanically initiated processes. A better fundamental spatial and temporal understanding of mechanically-induced processes would promote the design and control of high explosives and other heterogeneous materials. Embedded particle level sensors, such as dyes and quantum dots, are promising potential meso-scale diagnostics due to their small size and fast response time. Yet, further development and characterization of these material systems is needed to mature them into a reliable tool for measuring high rate processes occurring at the meso-scale.

1.2 Research Objectives and Plan of Work

The focus of this work is to understand the impact-initiated combustion of aluminum. The relationship between starting material properties and reaction initiation conditions under high speed impact is poorly understood. The extremely high reaction rates, on the order of tens of microseconds, and the meso-scale interactions that take place prior to reaction initiation, complicate the identification of the processes dominating reaction initiation. In order to understand and potentially control the process of impact-initiated combustion in aluminum, the technical approach is focused on addressing the following fundamental issues:

a.) *Under what conditions, e.g. impact velocity, compact density, particle size, level of mechanical pre-activation, does the combustion reaction occur in aluminum powder compacts? Is it possible to finely control reaction initiation by altering these conditions?*

b.) *How does the aluminum combustion reaction initiate? What bulk or localized processes are most likely to lead to reaction initiation?*

c.) *Can new meso-scale diagnostics be developed to interrogate local particle-level interactions in heterogeneous systems, such as powder compacts?*

These issues guide the systematic study of the aluminum powder compact and prompt the investigation of a new method of probing meso-scale processes with high time-resolutions. In this thesis, the technical background for the work is presented in Chapter 2. The progress made in understanding thermally-initiated combustion and mechanically-initiated combustion in aluminum and aluminum-containing systems will provide a foundation for the study described here. Additionally, background on computational and experimental methods for observing mesoscale processes provide a starting point for developing advanced methods. Chapter 3 provides a description of the microstructure, mechanical, and compaction behavior of the aluminum powders being investigated as well as the experimental setup for the uniaxial stress rod-on-anvil impact testing. Next, the results of impact-initiated reactivity, established from experiments performed under uniaxial stress rod-on-anvil impact conditions, will be presented in Chapter 4. Chapter 4 will conclude with an overview of the experimentally obtained measurements of temperature rise during the impact process. In Chapter 5, the effects of density, impact velocity, particle size, mechanical properties, and compaction behavior on reactivity will be analyzed using a logistic regression analysis. The process of reaction initiation is investigated through connection of measured reaction initiation timing and temperature rise in the samples to computational analysis using real 2-D microstructures. In Chapter 6, the development of meso-scale diagnostics that can be

used to probe heterogeneous materials, similar to aluminum powder compacts, is discussed. Lastly, Chapter 7 will summarize the contributions of this work and outline possible future directions.

Chapter II

TECHNICAL BACKGROUND

2.1 Thermally-Initiated Aluminum Combustion

Thermal initiation of aluminum powder combustion occurs as aluminum is heated and rapidly oxidizes. Over the last several decades, studies have shown that thermal initiation of aluminum combustion is dependent on heating rate, particle size, and the environment. This section will briefly summarize the thermal initiation of aluminum combustion to help inform impact initiated studies of aluminum powder compacts.

2.1.1 Early Models of Thermally-Initiated Aluminum Combustion

Significant advancements in the understanding of thermally-initiated metal combustion began in the 1960's with Irvin Glassman's [13] observation that metal combustion can be compared to the hydrocarbon droplet combustion model. Based on this theory and their experimental results, Brzutowski and Glassman [14] drew the conclusion that metal particle combustion was dependent on the melting and boiling points of the metal and its oxide and that burning time is equal to D^2, where D is the particle diameter. Specifically, in the case of aluminum, an amorphous aluminum oxide shell (γ-Al_2O_3) covers the aluminum particle and dictates the metal's combustion mechanism. Glassman [13] noted that the ignition temperature of aluminum was similar to the melting point of its oxide (2045°C) and concluded that combustion will occur once oxygen is able to penetrate through the melted oxide layer by diffusion. Separately, Friedman and Macek [15] also reported findings agreeing with Glassman's theory that the ignition temperature of aluminum corresponds to the melting point of the aluminum oxide shell. Glassman's [13] original hydrocarbon droplet combustion model was the basis for the development of many subsequent models describing both the ignition and burning behavior of metal particles.

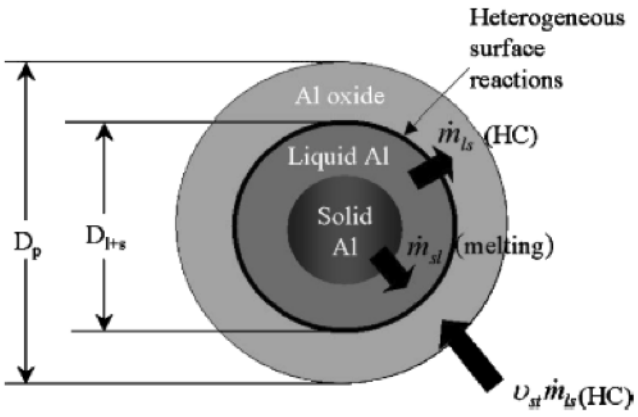

Figure 1: Possible mechanism for heterogeneous aluminum particle ignition. Note that the oxide layer thickness is exaggerated for clarity. (From [19])

Many of the early metal ignition and burning models augmented Glassman's initial model by adding in variables to account for oxide condensation, formation of oxide caps, assymetrical burning, and non-steady state burning [16, 1]. Yet, other early combustion models considered alternative ignition mechanisms that would take into account more complex oxidation kinetics [17] and heterogeneous surface reactions [18], not considered at all in Glassman's diffusion-based representation. Gremyachkin's model [18] made the assumption that the particle temperature does not reach the boiling temperature of the metal, and therefore, the gas phase reactions can be neglected. Instead, he postulated that the primary interaction between the liquid aluminum metal and the solid aluminum oxide is in the form of a heterogenous surface reaction as illustrated in Figure 1 [19].

2.1.2 Heating Rate Effects

The case for a non-diffusion based aluminum ignition mechanism was made stronger by experimental evidence. In 1977, Breiter [20] published a review of metal ignition research and cited aluminum ignition temperatures ranging from 467°C to approximately 2027°C. This data set, showing ignition of aluminum at temperatures less than 2045°C, could not be explained by diffusion of the oxidant through the melted aluminum oxide layer. Breiter

pointed out that although the distribution of temperatures was large, the ignition temperatures were centralized around two distinct temperatures, the melting point of aluminum (660°C) and the melting point of aluminum oxide (2045°C). This trend was due to two separate combustion mechanisms: (1) a kinetics controlled combustion mechanism near the melting point of aluminum and (2) a diffusion controlled mechanism near the melting point of aluminum oxide. Ignition in the kinetic regime occurs when the heat released by the chemical reaction between the metal and oxidizer exceeds the heat lost, allowing for autoignition. In that same year, Merzhanov, Grigorjev, and Gal'chenko's [21] aluminum wire ignition experiments, focused on the interaction between aluminum and its oxidants, also added to the case for a combustion mechanism that includes more complex kinetics, dissimilar from Breiter's proposed mechanism [20]. The results gave an ignition temperature slightly lower than the aluminum oxide melting point (1667 to 2045°C) for samples with strong oxidants and thin initial Al_2O_3 films. The authors [21] used thermal-kinetic theory, incorporating heterogeneous surface reactions, to model the observed behavior.

The presence of a kinetics controlled region of ignition well-below the melting point of Al_2O_3 was attributed to the existence of cracks in the Al_2O_3 shell, which allow increased interaction between aluminum and the oxidizer [22]. Lokenbakh *et. al.* [23] performed a more in depth study on the cracking of oxide shells at various heating rates and its effect on agglomeration and ignition. They noted that the difference in thermal expansion coefficients between aluminum and Al_2O_3 was most likely the cause of the particle cracking. At higher heating rates, the aluminum core expands rapidly enough to completely disrupt the oxide layer as shown in Figure 2. A very distinct combination of a high heating rate and a lower initial temperature dictates the threshold between agglomeration and ignition. Under the range of heating rates reportedly tested, from 1727°C/min up to 15,000°C/min, only agglomeration occurred as a result of aluminum's high oxygen affinity (ΔG° = -1583kJ/mol), which drives up oxidation rate and allows for rapid healing of the disrupted oxide layer.

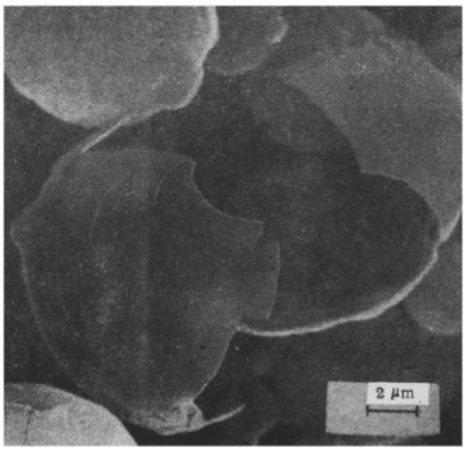

Figure 2: Cracking of the aluminum oxide shell observed at heating rates of 4700°C/min. (From [23])

To further explain the possibility of thermomechanically induced cracking of the oxide shell, Rozenband [24] developed a strength model to describe the behavior of metal particles during heterogeneous ignition. In order to formulate the model, he used the simplifications that (1) because the metal oxide is brittle, the plastic limit (σ_{pl}), flow stress limit (σ_f), and elastic limit (σ_e) converge to one point on the stress-strain curve, requiring that equivalent stress, σ_{eq}, is greater than the plastic limit, σ_{pl}, for oxide failure to occur and (2) adhesion force between the metal and oxide is greater than the deformation forces that the particle is subject to, therefore the oxide does not peel off the metal. The model concludes that the stress arising at the aluminum-aluminum oxide interface during a temperature rise of 533°C can overcome the σ_{pl} of 10 nm thick oxide layer (2.94 GPa), lead to oxide cracking, and lower aluminum combustion initiation temperatures [24].

2.1.3 Particle Size Effects

Closely tied to the dependence of aluminum ignition temperature on heating rates, aluminum ignition has also been shown to be dependent on initial aluminum particle size. Huang *et. al.* [25] summarized the dependence of aluminum ignition temperature as a function of particle diameter reported by several research groups as shown in Figure 3. At

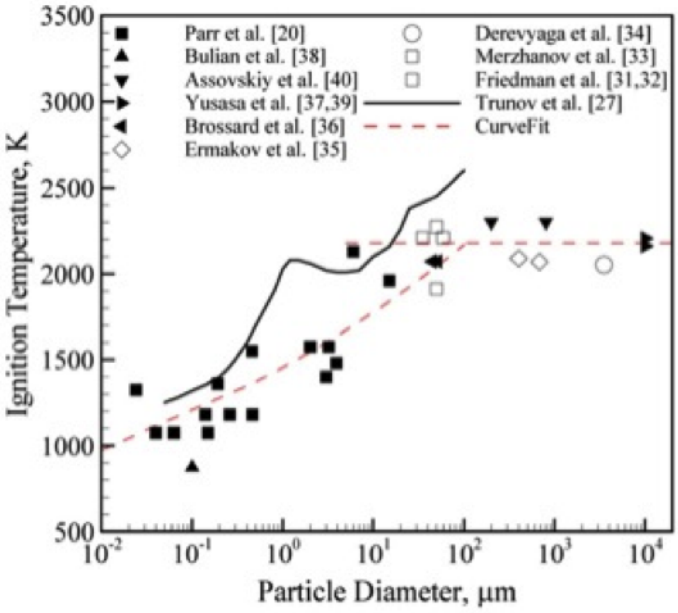

Figure 3: Ignition temperature of aluminum as a function of diameter in oxygen containing environments. (From [25])

particle diameters above 100μm, the ignition temperature remains above the aluminum oxide melting temperature and a diffusion mechanism is assumed. Yet, for smaller particles, the ignition temperature almost linearly decreases with a decrease in particle size. The difference in ignition behavior at lower temperatures is attributed to either aluminum oxidation and alumina polymorphic phase transitions described by Trunov *et. al.* [26] or to the cracking of the aluminum oxide shell due to thermal stresses as described above, and more recently by Levitas [27] and Rai [28]. Levitas [27] showed that the rapid volume change in aluminum, results in a pressure release of 0.1 to 4.0 GPa which causes spallation of the oxide layer. Rai [28] used heated stage microscopy and single particle mass spectrometry to demonstrate the rupture of the oxide layer as a result of rapid heating to the melting point of aluminum.

2.1.4 Shock Waves and Environmental Effects

Research on shock waves and environmental effects on the ignition and combustion of metals started to become more prevalent in the 1970's and 80's due to safety concerns of the ability of metal powders to self-ignite. Boiko *et. al.* [29] examined aluminum particle combustion in a reflected shock wave by depositing a layer of metal particles on the bottom of a shock tube and allowing them to be lifted by the gas suspension behind the shock wave front. They used a high speed camera to qualitatively observe light emission and a laser stroboscope that generated a series of light pulses to record the time scale. Under maximum pressures of 1-3 MPa, the 3-5 μm sized aluminum particles exhibited an ignition temperature lower than aluminum oxide melting temperature, at approximately 1550°C.

Although indicative of increased ignition sensitivity at increased pressures, the above study does not address the effects of high pressure behind the shock front on the physical properties of the particles and the resulting chemical effects on the aluminum combustion reaction. Zhang's [30] shock tube experiments on 100 nm and 2 μm Al particles indicated that detonation sensitivity was increased with higher pressures and smaller particle sizes. Based on these results they described the ignition mechanism as kinetics-limited as opposed to diffusion-limited and developed a qualitative expression to describe the aluminum reaction time with respect to particle size and initial pressure. Yoshinaka [31] conducted experiments on 31 μm diameter spherical and flake aluminum particles in an aluminum capsule subjected to separate shock pressures of 12.9 and 6.4 GPa. SEM images of the recovered samples showed signs of shear damage of the aluminum oxide shell in the case of the spheres and a shattering into finer particles in the case of the flakes. Both fragmentation mechanisms exposed the aluminum metal, potentially causing the increased detonation sensitivity of the aluminum particles.

Schlöffel [32] conducted a more in depth study on the behavior of 5 μm particles in a shock tube using time resolved spectroscopy to gain information on the chemical constituents of the reaction and to estimate temperatures during the reaction. For experiments

in argon, at pressures greater than 1 MPa and at temperatures between 500°C and 2550°C, the AlO spectrum was not observed at all. Yet, AlO was observed at shock pressures below the bond strength of Al_2O_3, but not at the high pressure that should cause the bond to break from direct shock stress. The authors concluded that the high-slip flow between the gas and the particles breaks the Al_2O_3 bonds by rapid heating. The authors also saw a stronger AlO spectra in the experiments conducted in argon compared to the weaker AlO spectra seen in experiments with air. This result could be due to the consumption of AlO by the molecular oxygen during the experiments in air, resulting in the following reaction:

$$AlO + O_2 = AlO_2 + O \tag{2}$$

Schlöffel's research [32] also illustrated that time resolved spectroscopy can be a useful tool in deciphering the chemical constituents and, consequently, the kinetics of a shock event.

Schlöffel's work [32] also showed that the presence of environmental oxygen obviously plays a large role in the oxidation kinetics and the resulting ignition conditions and burn time of the metal particle. Several other studies center around the effect of environmental oxygen on burn time as opposed to ignition. Gill *et. al.* [33] observed that above 21% oxygen level, the effect of oxygen concentration on combustion time of micron-sized Al particles is minimal. However, burning in oxygen concentration below 21% causes a substantial increase in combustion time.

2.1.5 Summary of Thermally Initiated Combustion of Aluminum

The thermal ignition behavior of aluminum is a factor of heating rate, particle size, and shock pressure. Aluminum particles were historically thought to combust at the aluminum oxide melting temperature of 2045°C [14]. Yet, more recent studies have shown that particles of less than 100 μm diameter combust at temperatures as low as 750°C due to rupture of the aluminum oxide shell. Faster heating rates can enhance the rupture of the oxide shell [25]. Additionally, increased pressures, as low as 1 MPa, have been shown to increase the

sensitivity of aluminum particles to thermal combustion [29]. Although these factors have been well studied experimentally, no model has been developed to capture the non-steady state burning behavior of this system as a function of all of these variables. Most recently, experimental studies have been designed to capture data that rigorously considers all of these variables in order to eventually approach a comprehensive model that accounts for all mechanisms that might occur during aluminum combustion [34, 35]. A knowledge of the effects of particle size, pressure, and heating rate on thermally-induced combustion of aluminum particles can inform studies on mechanically-induced combustion.

2.2 Mechanically Initiated Combustion of Aluminum

2.2.1 Overview of Mechanically Initiated Combustion of Aluminum

In addition to undergoing thermally-initiated combustion reactions, aluminum powders or their compacts can undergo combustion reaction due to high strain rate deformation, as a result of shock wave propagation due to explosive loading or impact. Reaction initiation under these conditions is highly dependent on the compaction and deformation behavior of the metal particles. During the compaction and deformation processes, the heating associated with mechanical work, rapid void closure, particle-particle impacts, and the generation of dislocations can all aid in the impact initiation of reaction.

2.2.1.1 Summary of Loading Scenarios

As illustrated in Figure 4, metal powder compacts can be loaded dynamically under conditions of uniaxial strain (a) and uniaxial stress (b). Uniaxial strain loading is typically achieved in a parallel plate impact configuration as shown in the schematic in Figure 4 (a). In this configuration, the powder compact is inertially constrained in the direction perpendicular to the impact plane and therefore, experiences only one dimensional strain [36]. Impact by a flyer plate sends a one dimensional compressive shock wave through the sample. The magnitude and duration of the shock wave can be controlled by the flyer plate material, thickness, and impact velocity. During impact, the input stress, propagated stress,

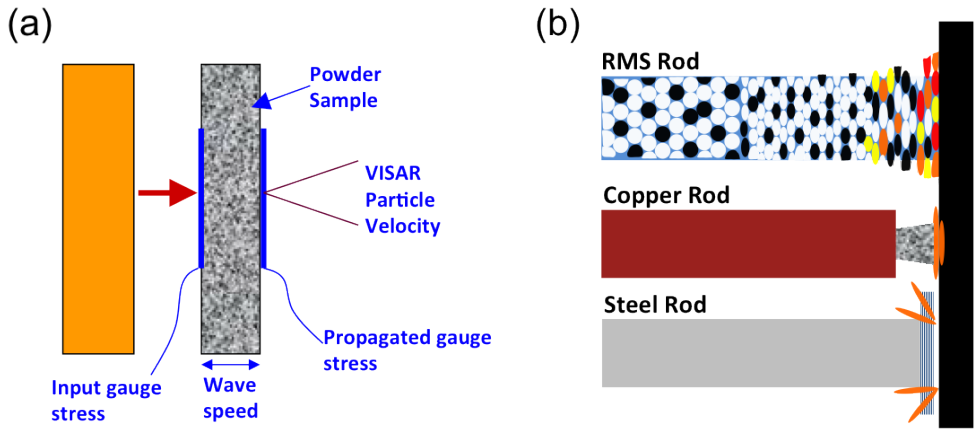

Figure 4: Examples of possible loading scenarios and their energy calculation: (a) uniaxial strain and (b) uniaxial stress.

and particle velocity can be measured by stress gauges placed on the front and back of the sample [36]. Uniaxial stress loading is achieved by impacting a rod-shaped sample against a rigid anvil as illustrated in the schematic in Figure 4 (b) [36]. If the lateral dimension or diameter is small enough, then the sample experiences stress only in one dimension, that is in the direction parallel to impact. This type of loading allows the sample to undergo large strain not only in the axial, but also along the lateral dimensions.

2.2.1.2 Role of Compaction and Deformation

Loading conditions, whether by uniaxial stress or by uniaxial strain, have varying effects on a powder compact and ultimately determine the compact response. Yet, the basic principles governing the particle-level micromechanical response during compaction are similar regardless of the loading scenarios. During compaction, a variety of processes can occur, including void collapse, impact of particle interfaces, formation of defects, and heating. The occurrence and extent of these processes effect the amount of energy available for reaction initiation and the mechanism of reaction initiation.

The relationships between the various modes of energy dissipation during compaction

in metal powders is not well-established. Often different processes overlap and interact with one another, rendering the underlying cause of the resulting phenomenon, such as reaction initiation, difficult to determine. Meyers, Benson, and Olesky [37] provided a thorough review of the microstructural processes possible during shock compaction as illustrated in the schematic in Figure 5. They identified the following eight energy dissipation mechanisms: plastic deformation, microkinetic energy, melting at interparticle surfaces, defect energy, friction energy, fracture energy, gas compression, and chemical reaction. Using these mechanisms, they developed an analytical expression that takes into account strength, size, porosity, and temperature to describe the energy requirement of compaction. The expression was applied to a model experiment illustrated in Figure 6 that investigated the impact of a flat plate of aluminum against a semi-cylinder of copper. The region of the microstructure that corresponded to a normal impact, shown in Figure 6 (a), did not result in any bonding, but the region of the microstructure that corresponded to an inclined impact, shown in Figure 6 (b), led to severe interfacial deformation and bonding. Based on these observations, Meyers, Benson, and Olesky [37] concluded that energy dissipation associated with only plastic deformation energy, microkinetic energy, and frictional energy are dominant during the consolidation of metal powders. These processes themselves can lead to melting at the particle interfaces, generation of defects, fractured particles, and energy release due to reaction [37].

Frictional energy is the energy associated with particle-particle contact during rearrangement at the shock front [37]. As the shock wave moves through the material, particles slide around one another to deform, causing friction, which can dissipate energy in the form of heat and in the formation of defects. The amount of frictional energy in a sample is closely related to the porosity and particle size. A higher porosity increases the void volume and allows more particle rearrangement. Whereas, a larger particle size decreases the surface area available for such interactions, as it increases the corresponding interaction stress as the force is applied over a smaller area.

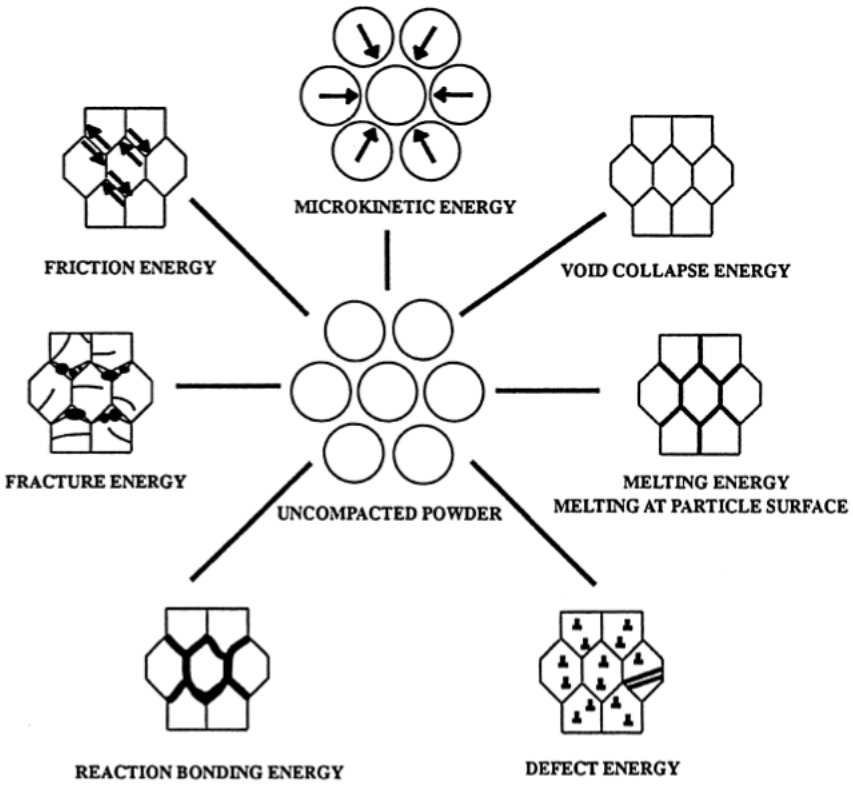

Figure 5: Mechanisms of energy dissipation during compaction. (From [37])

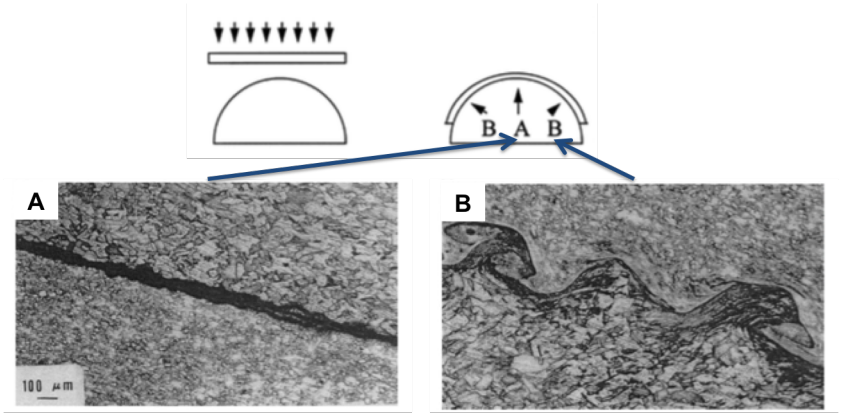

Figure 6: Experiment used to identify dominant energy dissipation mechanisms. Micrograph A shows the portion of the microstructure that corresponds to normal impact. Micrograph B shows the portion of the microstructure that corresponds to inclined impact. (From [37])

Plastic deformation energy is associated with the energy required for void collapse [37]. As particles move into open void space, they must flow around one another and plastic yielding must occur. During this process, the contact area increases and the effective pressure causing yielding falls until the yield strength is reached [38]. The void collapse energy is a function of the particle geometry, particle contact areas, and mechanical properties of the individual and/or adjacent dissimilar particles [37].

Microkinetic energy is associated with continued plastic flow following void collapse [39, 37]. The intense flow resulting from dynamic compaction often dissipates in the form of localized melting and jet and vortex formation. As material strength decreases, microkinetic energy increases, due to increased turbulent flow [39].

In addition to the micro-scale deformation that occurs during compaction, as voids collapse and particles continue to flow around each other, bulk deformation on the continuum scale of the sample is also occurring, especially in the case of materials subjected to uniaxial stress loading. The conversion of the energy from bulk plastic deformation into latent energy in the form of heat or the generation of defects is well known [40, 41]. Under dynamic conditions, plastic deformation occurs at increased rates, enhancing the conversion of plastic work into heat [42].

2.2.2 Reaction Initiation Under Uniaxial Strain Loading

Uniaxial strain conditions allow for the controlled and reliable monitoring of a material under shock loading. With the material experiencing strain in only one dimension, the hydrostatic component of stress increases rapidly until it surpasses the dynamic flow stress. As long as the velocity of the pulse increases with increasing pressure, a shock wave will form. The shock wave is assumed to have no apparent thickness, and the conditions behind the shock front can be related to the original state using the Rankine Hugoniot equations of state [36]. The ease of applying mathematical relationships to the material condition and response during shock has led to many systematic studies of the shock compaction process

and shock-induced reaction of porous reactive materials.

2.2.2.1 Shock Compaction of Porous Materials

Porous materials or powder compacts were originally studied under shock conditions to push the thermodynamic limits of solid materials [43]. Upon shock compression, a material exhibits a pressure (P) - volume (V) compressability relationship specific to that material. This relationship is termed the Hugoniot and is schematically illustrated in Figure 7 for a solid and porous material. The conservation of energy equation,

$$E - E_0 = \frac{1}{2}(P + P_0)(V - V_0) \tag{3}$$

establishes the P-V state immediately behind the shock front and can be used to determine the energy, *E*, at a specific state. For highly porous materials, the initial state, V_{00}, is shifted to the right as a result of an expansion in volume due to the presence of interparticle void space. As the powder is shock compacted, void collapse and densification occurs rapidly, resulting in a large net reduction in volume. Compaction of a porous material leads to a significantly higher internal energy when compared with the solid counterpart of the material as signified by the shaded areas under the curve in Figure 7. The Mie-Grüniesian equation of state,

$$P - P_0 = \frac{\gamma}{V}(E - E_0) \tag{4}$$

where γ is the Grüniesen parameter, can be used to approximate the Hugoniot for the powder [44] by performing a shift from the solid material Hugoniot at constant volume. This method of determining the porous Hugoniot state is known as the isochoric approach. An alternate approach, the isobaric approach, involves performing a constant pressure adjustment on the solid Hugoniot to determine the porous Hugoniot [45].

In 1969, Herrmann [46] incorporated the Mie-Grüniesian equation of state (Equation 4) into the development of the P-α model, to describe pore collapse that is required for densification. This constitutive model considers the compaction behavior separately in each of the elastic and plastic regimes in order to describe the behavior of a powder compact upon

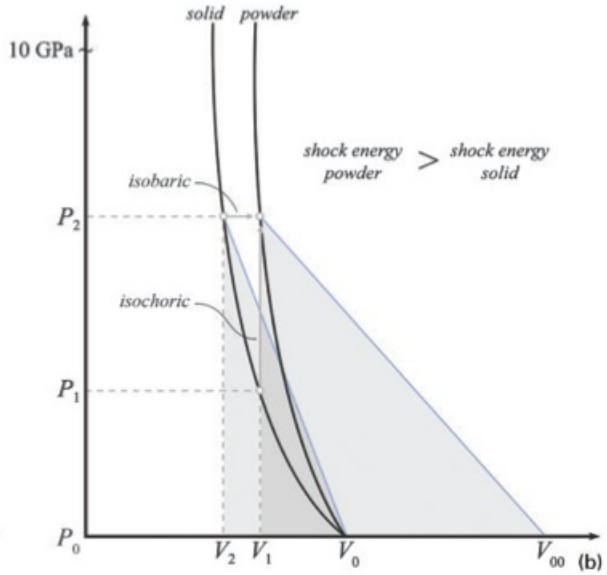

Figure 7: Pressure-Volume relationship of a solid material versus a powder illustrating the energy difference between the solid and powder material. (From [43]).

impact. In the early 1970's, Carroll and Holt [47] built on Herrmann's P-α pore collapse model to account for rate effects during shock compaction of a porous material. The model was subsequently modified to account for deviatoric stresses and material viscosity and applied to the shock wave compaction of porous aluminum by Butcher *et. al.* [48]. The steady state rise time predicted by Butcher's model [48] matched experimental data well. In 1998, Bonnan *et. al* [49] studied the quasi static and shock behavior of aluminum using time-resolved diagnostics and correlated the results to Carroll and Holt's [47] pore collapse model. Bonnan *et. al.* [49] compared the behavior of porous aluminum under quasi-static loading and under shock loading. The use of different loading rates helped them to further understand and describe the physical mechanisms of void collapse and plasticity that contribute to shock compression of 91% dense and 83% dense aluminum compacts and correlate the behavior to models. Although these models and experiments led to a better understanding of the bulk compaction behavior of aluminum powders, they did not go so far as to probe the particle level interactions and resulting mechanochemical processes or the possible reactions in these systems.

2.2.2.2 *Observation of Shock-Induced Reactions and the Effects of Powder Morphology*

The rapid increase of internal energy that occurs during shock compaction of highly reactive powder mixtures can result in a reaction that can be divided into two kinetics-based categories, shock-assisted or shock-induced [50]. Shock-assisted reactions are a slower, atomic-diffusion driven, class of reactions that follow the unloading front of the peak pressure state. They result from shock-activation and elevated temperatures, and occur in time scales on the order of thermal equilibrium, from tens of microseconds to milliseconds. Shock-induced reactions occur during the time scale of the high pressure state, within the first tens of nanoseconds of the shock impact, with the crush-up process dominating the response. Monitoring of shock-induced reactions occurring in the time scale of pressure equilibration require time-resolved diagnostics to identify the factors promoting such rapid reaction initiation [43]. Although studies conducted over the past twenty years have been able to detect reaction occurrence, due to limitations in the spatial resolution of time-resolved diagnostics, these studies have not been able to narrow down the precise mechanisms that initiate shock-induced reactions.

Evidence of shock-induced reactions between aluminum and lithium perchlorate was seen in the early 1980's, by Kovalenko *et. al.* [51]. The group used post-shock microstructural and thermal analysis to establish the occurrence of a reaction. Although informative, post-reaction analysis alone makes it impossible to deduce the kinetic behavior. Later, Batsanov *et. al.* [52] were the first to use time-resolved measurements to observe shock induced reactions in the equiatomic Sn + S system. The experimentally determined P-V relationship displayed an abrupt shift in the slope when compared to the calculated Hugoniot for the porous mixture. This shift in the Hugoniot indicates a change in internal energy of the system, suggestive of a reaction taking place within the timescale of the shock state.

Nanosecond scale time resolved diagnostics were first employed by Graham *et. al.*

[53] who used PVDF (poly-vinyl-di-fluoride) stress wave gauges. The nanosecond resolution provided by the use of PVDF gauges allowed for a more detailed analysis of the volume displacement from the calculated mixture Hugoniot. Eakins and Thadhani [8] used PVDF gauges to investigate the shock compression behavior of mixtures of flake nickel and spherical aluminum powders. As shown in the plot of shock velocity versus the input stress in Figure 8 (a), a shock velocity greater than the predicted shock velocity at stress levels above 3.5 GPa [8] was observed. Figure 8 (b) shows the results plotted in pressure volume space, exhibiting a volume expansion at high pressures, following the crush-up to full density. The volume expansion, indicative of the reaction of a heterogeneous materials or a "ballotechnic reaction", is attributed to the exothermic energy released from reaction. Experiments investigating the shock compression behavior of a mixture of $\sim$40 μm spherical nickel and spherical aluminum powders, did not show similar shock velocity increase or volume expansion indicating no reaction in this mixture at pressures up to 6GPa. The reactivity of mixtures of flake Ni and spherical Al at stress levels above 3.5 GPa and the absence of reaction in mixtures of spherical Ni and Al up to stress levels of 6 GPa indicates the role of morphology and micromechanical effects on shock induced reaction initiation.

2.2.2.3 Shock-Induced Reaction Mechanisms

As discussed above, compaction and deformation during high strain rate loading lead to enhanced strain and heating on the particle and bulk level, resulting in impact-initiated (or shock-induced) reactions. The mechanisms leading to such shock-induced reactions in compacts of intermetallic-forming and powder mixtures vary as a function of several factors, including, the elastic and plastic properties of the reactant materials, their morphology and size, the packing density, the uniformity of the mixing of the materials, and the imposed loading conditions. Shock-induced reaction initiation is believed to occur in the same timescale as the crush-up process [43]. Therefore, it is assumed that the mechanisms responsible for initiation of shock induced reactions are related to those that influence the

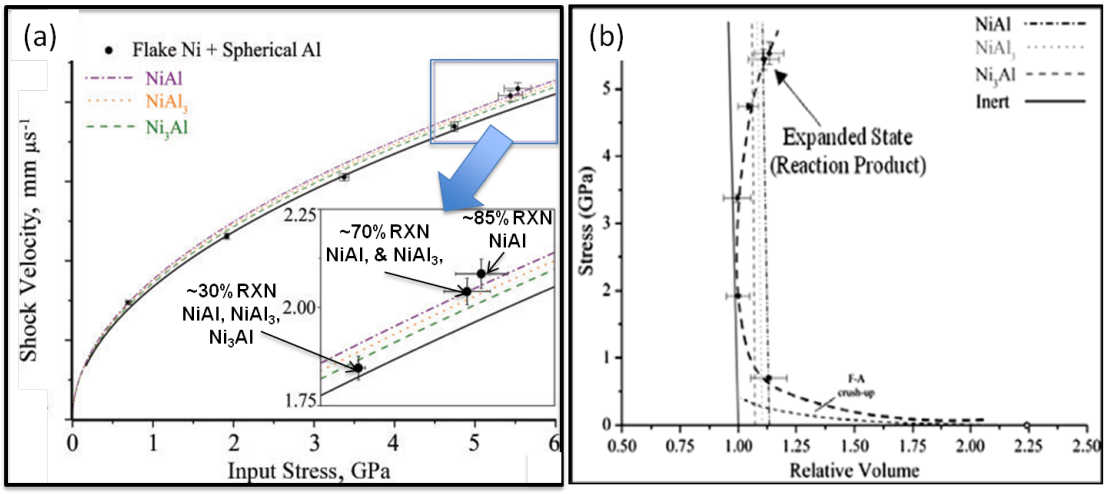

Figure 8: (a) Shock velocity vs. input stress of Ni + Al mixtures (b) Measured input stress vs. calculated relative volume plot for 45% TMD flake Ni and equiaxed Al mixture. The expanded state at stresses exceeding the crush strength of the Ni+Al, giving rise to a ballotechnic curve, is indicative of a shock-induced reaction. (From [8])

crush-up process of powders during densification [43]. The possible mechanisms that have been conjectured include mechanochemical or thermochemical mechanisms. The thermochemical mechanism focuses on the conversion of the mechanical work of densification and deformation of the powder mixture compact to thermal energy, which initiates the combustion reaction. The mechanochemical model considers particle-particle interactions and resulting mixing of constituents from plastic deformation as the cause of increased reactivity [54].

The thermochemical model is based on the reaction occurring in the time scale of thermodynamic equilibrium. Boslough [55] developed the concept of a thermochemical model for the reactivity of Al+Fe_2O_3 thermite mixtures, originating from the similarity between "heat" detonations occurring upon shock loading and explosive detonations. The model used a constant volume assumption, basic shock theory, and thermal equilibrium to predict the conditions necessary for reaction initiation based on temperature increase from shock compression. Although the model was able to accurately predict an increase in temperature due to the reaction of the thermite, Al+Fe_2O_3, the model neglects the reaction mechanism

[55] and does not account for the effects of particle morphology on the threshold for reaction initiation [54].

Mechanochemical processes are those that involve enhanced plastic flow and mixing between particles at the microscale levels. The mechanochemical mechanism views interparticle contact points as playing a role in controlling the local stresses that can eventually lead to enhanced plastic deformation. Plastic deformation increases particle flow into and around voids, intensifying the solid state reactivity of the material [50]. Both morphology and size of the powders influence the number of interparticle contacts and have an effect on the magnitude of the local stresses and the extent of plastic flow at the particle level. Studies of shock-induced reaction synthesis [56, 57] have concluded that reaction initiation of intermetallic-forming mixtures is dependent on morphology and size of reactants in addition to their elastic and plastic properties which clearly points to the influence of mechanochemical processes on reaction initiation.

Although post-mortem microstructure evaluation of shock-compressed materials at conditions just below the reaction threshold can point to the dominance of one reaction mechanism over another, *in situ* direct observation of these mechanisms remains a challenge. Jetté *et. al.* [58] used a wide array of diagnostics, including thermocouples, photomultiplier tubes (PMT's), and pyrometers to examine the onset of bulk exothermicity in reactive powders that were shock compressed by the detonation of a high explosive in close proximity to the sample. Thermocouples allowed the authors to observe different temperature profiles on the interior and exterior rim of an arrested reactive mixture of $4Al + Fe_2O_3$. This result combined with the observation that burning speed was independent of pressure furthered their argument that bulk reaction onset was most dependent on the prevalence of shock-induced localized reaction initiation centers. Reaction initiation was assumed to begin locally, in small zones, and then spread out by diffusive or convective burning, a theory that may be attributed to the dominance of the mechanochemical mechanism.

Direct observation of impact-initiated reaction by the mechanochemical mechanism

relies on probing of the material state at the mesoscale level during shock compression. Current time-resolved analytical techniques cannot observe an impact-initiated reaction at both the high time-scale and small length scale required. Therefore, most studies that attempt to decipher a reaction initiation mechanism and the effect of interparticle contacts have relied on computational simulations and post-mortem microstructure analysis.

2.2.3 Reaction Initiation under Uniaxial Stress Loading

Uniaxial stress loading conditions initially expose the material to one dimensional stress with straining allowed in all three dimensions. In porous samples, once compaction occurs, the high levels of strain in three dimensions lead to enhanced deformation, intense shear, and ultimately reaction initiation. Uniaxial stress loading experiments typically involve a long, small diameter cylinder impacted against a rigid anvil at high velocities. If the impact results in stress exceeding the elastic limit of the cylindrical, rod-shaped sample, then the impacted front undergoes plastic deformation until the energy is fully dissipated. The work of plastic deformation can be converted to heat which can result in thermochemical reaction initiation in the case of a reactive material. With compacts of reactive powder mixtures, plastic deformation can also lead to enhanced flow, impact, and mixing at the particle level, resulting in localized strain and heating, and eventually mechanochemical reaction initiation.

2.2.3.1 Uniaxial Stress Loading Techniques

In 1948, Taylor outlined a method to determine the dynamic mechanical response of a material subjected to uniaxial stress [59]. In the so-called rod-on-anvil impact (Taylor test), as stress at the impact end of the rod surpasses the elastic limit, plastic deformation occurs in three dimensions, usually at strain rates from 0 to $10^5\ s^{-1}$. The shape (dimensional) change of the rod can be analyzed to determine the material's dynamic yield strength. Rod-on-anvil impact tests have also been used to investigate impact-initiated reactions in structural energetic materials, [7, 60]. The occurrence of reaction has been observed to be a

function of density of the powder compact, morphology of the reactant powders, and their mechanical properties.

Ames [60] studied the energy release upon impact of a cylinder composed of various metal powders mixed with a fluoropolymer binder against a rigid anvil and found that the temperature and pressures produced during such rod-on-anvil impact tests were not enough to drive a reaction. For example, an Al-PTFE cylinder upon impact first experienced high levels of shear, brittle fracture, and then only sometimes progressed to reaction initiation. The high levels of shear, necessary for reaction to take place, dissipated energy to fracture prior to reaction initiation. In order to obtain more information about the reaction energy being released, Ames and others [60] at the Naval Surface Warfare Center, Dahlgren developed a vented calorimetry chamber or the so-called "pig test". In the pig test, a rod or spherically-shaped sample initially impacts the thin outer "skin" material (approximately 1/16th inch thick) of the chamber. Upon impact, there is an initial, short-lived impact-induced reaction on the microsecond time scale and the remaining sample fractures into multiple fragment that continue to travel into the chamber and impact a rigid anvil, where the fragments undergo an aerobic, sustained reaction in the millisecond time scale. The chamber is equipped with pressure sensors that can provide a measure of the amount of energy that can be extracted from a energetic material. Densmore [61] also used the pig test to study the behavior of Ni-Al and Al-PTFE, but added a two color pyrometer to obtain temperature measurements of the initial reaction and afterburn.

Du and Thadhani [62] developed a simpler method, in which, small samples of energetic materials are mounted onto a copper rod and impacted against a rigid anvil. They observed that reactions, evidenced by light emission captured using high speed imaging, occurred following densification and severe lateral plastic deformation in various aluminum-based intermetallic forming mixtures. Impact initiated reactions in Ta+Al mixture compacts occurred at the lowest threshold velocities in contrast to compacts of powder mixtures

of W+Al and Ni+Al, in both ambient and vacuum (<50 mTorr) conditions. The Ta+Al mixtures showed a reaction threshold below that of pure aluminum powder compacts in air (implying intermetallic reaction) while W-Al and Ni+Al mixtures showed reaction thresholds above that for combustion of pure aluminum.

Alternate loading methods, including both drop weight testing [63, 64] and combined compression/shear testing [65, 66, 67, 68] have also been used to investigate the reactivity of structural energetic materials. During a drop weight test, a weight of known mass is dropped from a certain height onto a small amount of the energetic material. The impact velocity and strain rate are much lower than that achieved during a rod-on-anvil impact test, approximately 5 m/s and $10^2\ s^{-1}$, respectively. Yet, similar to a rod-on-anvil impact test, reactions in these experiments are presumed to be initiated by the extreme plastic deformation in the sample upon impact [64]. The combined compression/shear test was developed by Asay [65] and consists of a steel fixture equipped with a sapphire viewing window that holds the sample of interest. A plunger with a rounded end is placed in contact with the sample, and a brass projectile, fired from a gas gun, impacts the plunger at varying velocities. This configuration sends a reproducible strain field into the material of interest [65].

2.2.4 Porosity and Particle Size Effects on Reaction Initiation

During uniaxial stress loading of a powder compact, porosity and particle size affect the void structure, void volume, and particle-particle interactions. Consequently, these properties have a prominent effect on the micromechanical behavior of the system, influencing the frictional energy between particles, the plastic deformation energy as particles flow into void spaces, and the microkinetic energy of deformation and reactant mixing beyond void collapse. Gourdin [69] conducted dynamic compaction experiments to study the role of voids in his investigation of the shock compaction behavior of monosized spherical copper powders. Post-mortem microscopy showed a distinct microstructure. On the upstream side

of the shock propagation direction, particles had a smooth, convex shape, and the downstream side exhibited sharp peaks. The resultant structure indicated that voids are filled faster than particle deformation can occur at the particle interfaces due to the increased speed of shock wave release at the free surface of a particle versus the slower shock wave speeds at the particle-particle contact points. The effect is averaged out in broader particle size distributions which are more efficiently able to fill voids [69]. Gourdin's studies illustrate the added complexity and range of shock conditions that heterogeneous porous materials experience during high strain rate loading.

Chiu [70] and Olney [71] studied porous, granular Al-W composites under dynamic conditions and found that a decrease in porosity of the composites correlated to higher compressive strength [70]. Simulation results showed that composites that were not bonded at the particle interfaces were able to rearrange and avoid shear localization while the bonded samples were forced through certain deformation paths which resulted in localized shear and shear band formation [71]. In a different study, using the drop weight impact test, Hunt and Patoya [64] investigated reaction initiation of intermetallic-forming mixtures of Al and Ti, Ni, Zn, Hf, and W. They found that increasing the density of samples increased the sensitivity to impact initiated reactions. Porosity in both cases effects the material response, by controlling the availability of deformation paths of the sample undergoing uniaxial stress. Lower porosity leads to decreased availability of deformation paths and increased plastic strain, which can contribute to reaction initiation.

With respect to particle size, Chiu *et. al.* [70] studied the strength of Al-W composites as a function of W particle size. They found that the dynamic strength of composites with fine W particles was much larger than the strength of composites with coarse W particles. They postulated that this was due to the "force-chains" created by smaller particles being more effective than those created by larger particles due to increased contact area in the smaller particles. In studying this same system, Olney [71] observed that larger tungsten particles created more kinks in the shear band path as aluminum underwent localized high

strain flow to move around the tungsten. In the earlier mentioned study of the reaction initiation of intermetallic-forming mixtures impacted by a drop weight, Hunt and Pantoya [64] found that reducing Al particle size improved sensitivity to reaction in some Al + metals. They hypothesized that the smaller particles had a higher surface area that would allow for enhanced diffusion of reactants. A direct comparison between Chiu [70] and Olney's [71] studies and the study by Hunt and Pantoya [64] cannot be made because they were performed using different strain rates and diagnostics. Yet, together, the two studies highlight the importance of the correlation between particle size and dynamic strength and their effect on reaction initiation. Dynamic strength of reactant constituents influence the energy required for compaction. From a macroscale perspective, as dynamic strength increases, more energy is used during the compaction process, leaving less available for reaction initiation. From a microscale perspective, the influence of particle size becomes more complicated as particle size directly influences particle-particle interactions. Cheng *et. al*. [9] investigated Al-Fe_2O_3 nanostructured thermites prepared by self-assembly and solid-state mixing. They observed increased reactivity upon thermal initiation in the self-assembled nano-thermite mixtures. Yet, the mixed micron-sized thermites were most sensitive to mechanical initiation of reaction. These results were attributed to the fact that mixing using self-assembly promotes contact between Al and iron oxide, which influences thermochemical reaction initiation. During impact, larger particles result in higher localized strains due to the few interparticle contacts compared to more evenly distributed strain achieved during impact initiation of nano-sized particles.

2.2.5 Mechanical Property Effects on Reaction Initiation

The effect of the mechanical properties of reactants on reaction initiation have primarily been investigated with respect to two-component mixtures and the varying elastic and plastic properties of the components [7, 71, 72]. Olney [71] studied porous, granular Al-W

composites and the shear localization resulting from the interactions between hard tungsten and softer aluminum particles. Their work showed that the harder tungsten particles had a tremendous effect on the formation of shear bands. The presence of the tungsten particles in dynamically compressed material caused kinks in the shear band that deviated the path of the band, possibly leading to localized hot spots. Wei *et. al.* [72] did an in-depth investigation of the failure mechanisms of explosively compacted aluminum powder combined with either Nb, Ni, Mo, W, or Ta through rod-on-anvil impact testing and simulations. They found that damage in Ta+Al and Ni+Al compacts was a result of shear localization in the continuous Ta phase and tensile separation at the Ta-Al particle-matrix interface. The strength of the entire compact was primarily determined by the continuous Ta-matrix phase, and samples with an Al-matrix phase had a much lower strength and lower rate sensitivity.

Work by Aydelotte and Thadhani [7] went further and investigated the impact initiated reactivity of Ni + Al, Ta + Al, and W + Al mixtures that had been prepared by explosive compaction. SEM images of the respective mixtures shown in Figure 9 (a) reveal the difference in the microstructure. Both mesoscale simulations and experiments using the rod-on-anvil impact setup were performed to understand the mechanisms contributing to reaction in these mixtures. Ta+Al required the lowest kinetic energy for reaction initiation due to increased topological connectivity in the reinforcement matrix phase, ductility in both constituents, reduced tendency of the reinforcement phase to work harden, high average density, good interface adhesion, and minimum spatial separation between reactants [7]. As shown in Figure 9 (b), simulations reveal that Ta + Al exhibited the highest plastic strain in the Ta-matrix when compared with W + Al and Ni + Al, which show plastic strain predominantly in the aluminum-matrix phase. Energy dissipated in plastic work is dissipated as heat, and therefore, the Ta has a higher deformation induced temperature increase. The Ta + Al configuration was additionally aided by the connectivity of the Ta phase. Al was able to flow into pore spaces of Ta, as opposed to the case of Ni + Al and W + Al,

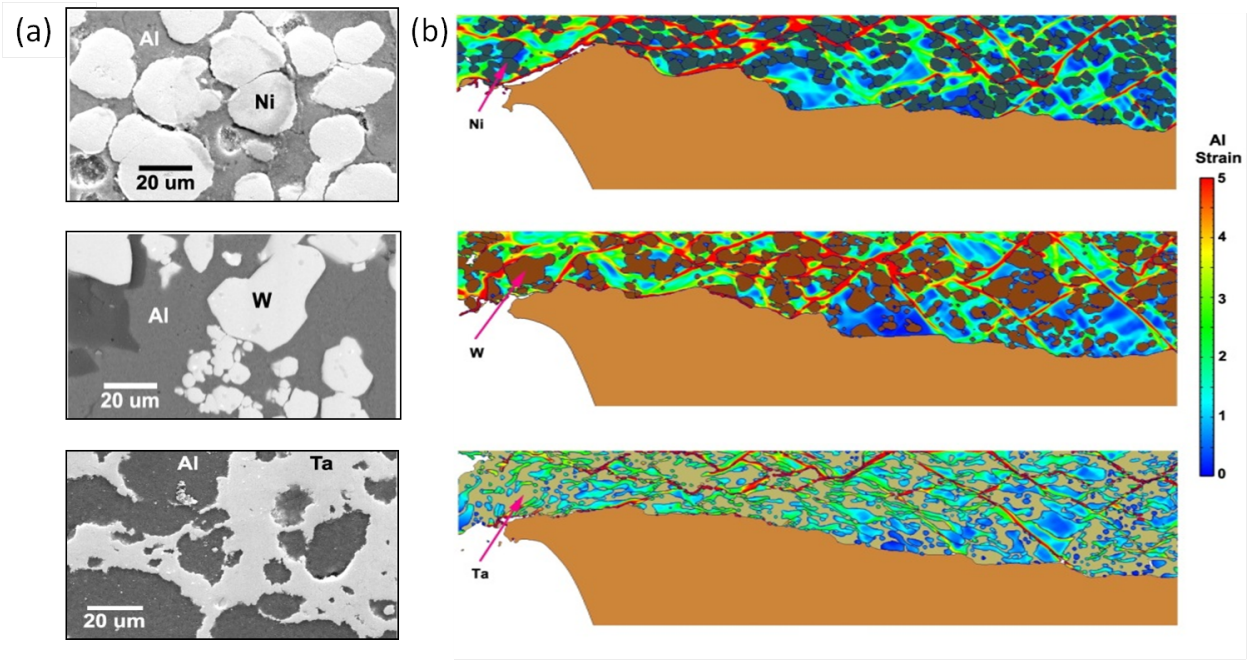

Figure 9: (a) SEM images and (b) CTH simulations following compaction and deformation of Ni+Al, W+Al, and Ta+Al. (From [7]).

where the spherical Ni and W powders were surrounded by a matrix of aluminum which underwent most of the deformation, resulting in limited mixing and therefore no reaction.

Information about the dynamic behavior of aluminum alone can be obtained from Olney *et. al.*'s [71] study of the dynamic behavior of Al + W composites. They examined the effects of the constitutive properties of aluminum in their study and observed that a reduction of the aluminum yield stress increased the bulk damage and plastic strain in the sample in addition to altering the shear band path. They also investigated the removal of thermal softening parameter from the constitutive equation and saw that it did not have an impact on the strain fields, pointing to the importance of softening from plastic deformation of aluminum around tungsten. Lastly, with respect to only aluminum systems, Chiu [70] showed that porous aluminum had significant strain hardening during dynamic compression testing. Therefore, strain hardening of aluminum prior to exposing it to impact conditions can effect its response.

2.2.6 Mechanical Pre-activation Effects on Uniaxial Stress Initiation

The previously described experiments illustrate that mechanical properties strongly effect material response to dynamic compression and, thus, the occurrence of impact initiated reactions. One method of investigating mechanically induced reaction initiation further is to strain the starting materials prior to subjecting them to high strain rate loading. Pre-strained samples can be prepared by high energy ball milling (HEBM), plane strain machining, and shock compression. These techniques can be employed to both increase mixing (in cases when a second material is used) and to strain harden the samples before use. As a material is cold-worked, such as through the process of high energy ball milling or high strain machining, most of the mechanical energy put into the material is dissipated as heat, but a fraction of the energy is stored and raises the internal energy [73].

2.2.6.1 Effect of High Energy Ball Milling on Reactivity.

Reeves *et. al.* [68] instigated the thermal and mechanical initiation of several types of Ni+Al powders using DTA-TGA and Asay's combined compression/shear test apparatus [65]. The DTA-TGA trace illustrating the thermal reaction initiation behavior is shown in Figure 10 (a). For thermal reaction initiation, they noted that HEBM'd mixtures of Ni+Al, pictured in Figure 10 (b), began exothermic heat release indicative of reaction at much lower temperatures than even nanoscale mixtures of Ni+Al. The ignition temperatures for both cases were well below the reaction temperature for micron sized, unmilled samples. Not only was the exothermic heat release onset temperature different, but also, the temperature profiles of each were markedly different. Heat release for HEBM was gradual through the solid state reactions, while heat released from nano-sized powder was quickly released. Mechanical initiation was then studied by Asay's [65] combined compression/shear test. Alternately, mechanical initiation results showed that HEBM materials were unable to be activated at 400m/s, most likely due to the lack of mixing during impact. Yet nanopowders mixtures were easily ignitable at velocities as low as 257m/s. In short, particle size

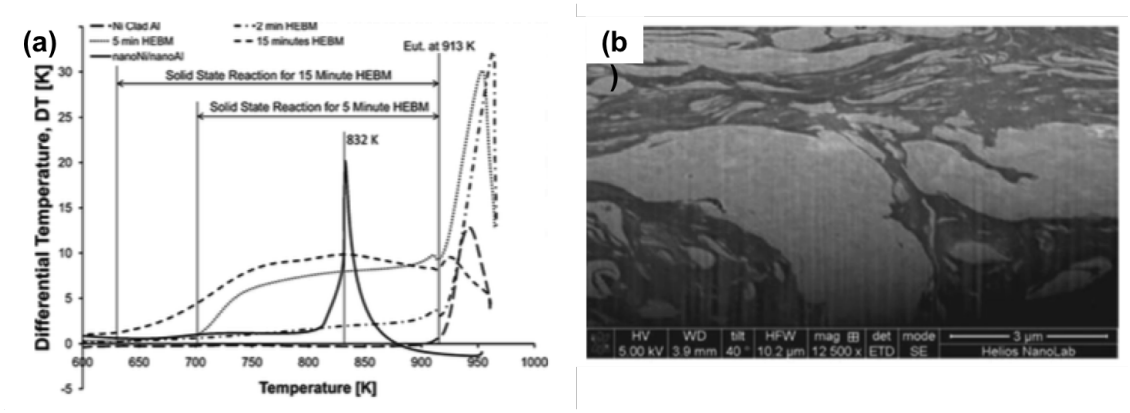

Figure 10: Results from Reeves' study [68]: (a) DTA-TGA traces of Ni + Al mixtures. (b) SEM micrograph of Ni + Al HEBM sample. (From [68])

reduction has a different effect on thermal and mechanical reaction initiation than HEBM. HEBM produces greater sensitivity to thermal reaction initiation, while reducing particle size has a greater effect on mechanical initiation of reaction [74]. Manukyan *et. al.* [67] built on this study and designed nanolaminate Ni + Al particles using dry HEBM and wet grinding. The small particles containing a high fraction of the nanolaminated Ni + Al were the most sensitive to both thermal and mechanical reaction initiation.

Mason [66] also investigated mechanically-activated micron scale Ni/Al powder in the Asay compression/shear impact setup [65] and found that changing the milling time had a significant impact on the ignition threshold and combustion behavior. As milling time increased, the Ni and Al powders fracture and mix to form a coarse Ni and Al structure with micron scale features. Eventually, with even greater milling times, a nanolaminate structure, with less than 30 nm thick Ni and Al nanolayers, was formed. As milling time increased, the ignition threshold decreased, and the nanolaminate structures showed the most sensitivity to impact initiation. Ignition began at the impact face of the sample, the portion in contact with the plunger, and at the edges of the sample. Once these localized reaction initiation hotspots reached the thermal ignition threshold, the initiation spread through the sample. The authors [66] postulated that increased HEBM time led to the formation of microdeformations, amorphous Al, and nanolaminates in the Ni/Al composites, which

increased the sensitivity of the HEBM samples to impact initiation.

Arrested reactive milling (ARM) involves high energy ball milling a sample of powder mixtures with intermittently halting the process before the self-sustaining reactions begin. Herbold *et. al.* [11] studied the conditions necessary for impact-initiated reaction occurrence in ARM Ni + Al using the rod-on-anvil impact set-up. Figure 11 (a) shows SEM micrographs of the two HEBM'd Ni + Al mixtures studied, 50 μm Al + 10 μm Ni ((a) and (c)) and 2 μm Al + 100 μm Ni ((b) and (d)), milled for 35% of the time to react ((a) and (b)) and 65% of the time to react ((c) and (d)). The authors examined the kinetic energy needed to initiate reaction as a function of milling time and the powder compact density. The plot of impact energy versus milling time shown in Figure 11 (b) illustrates that initially, the necessary kinetic energy for reaction decreases as the fresh surfaces of the constituents are in close contact with minimal strain hardening. Yet, following 4000 seconds of milling time, the required kinetic energy for reaction increases due to strain hardening of the powder grains. They also observed, as shown in the plot of impact energy versus compact density in Figure 11 (b), that the energy required for reaction initiation decreases with an increase in compact density. The results of these studies illustrate that HEBM experiments provide valuable information regarding mechanisms involved in impact-initiated reactions.

2.2.6.2 Effect of High Strain Machining on Reactivity.

In addition to HEBM, pre-strained materials can also be prepared by high strain machining. Shankar *et. al.* [75, 76] employed plane-strain machining to create chips of ultra-fine grain (UFG) aluminum 6061. In accordance with the Hall-Petch relationship, UFG and nanocrystalline materials are stronger and harder than their coarse-grained counterparts due to the increased number of grain boundaries. In Shankar's work [75, 76], the strengthening of Al 6061 can be solely attributed to grain refinement because solution treated Al 6061 does not contain any precipitates in the matrix that might contribute to strengthening. Optical microscopy of the Al 6061 indicated that the bulk material was made up of large

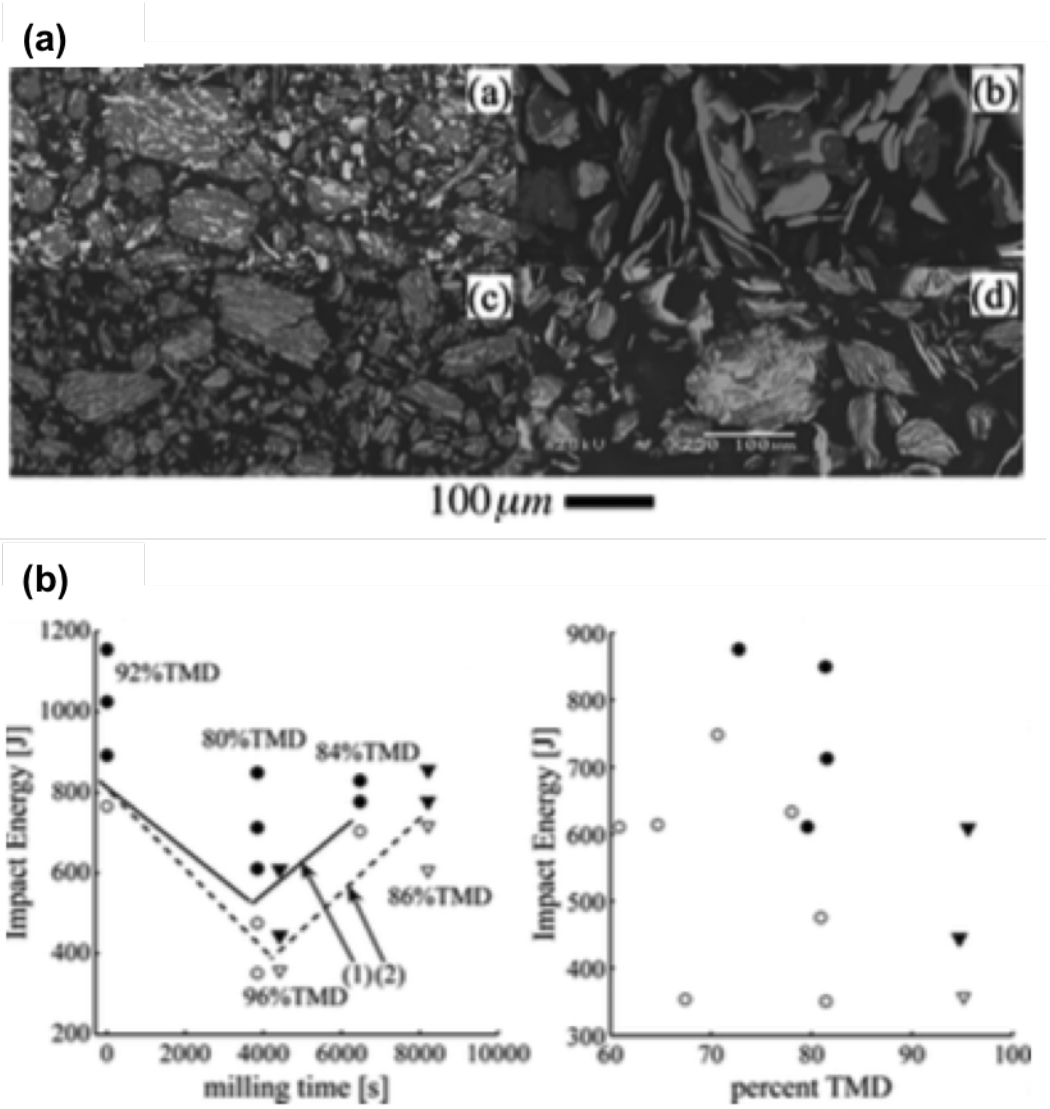

Figure 11: Results from Herbold's Ni + Al HEBM study [11]. (a) SEM micrographs of HEBM Ni + Al powders. (b) Effect of milling time on the kinetic energy necessary for reaction. Each point indicates a different experiment. The circles are 50 μm Al + 10 μm Ni mixtures, and the squares are 2 μm Al + 100 μm Ni. Filled in shapes indicate reaction occurrence and open shapes indicate no reaction occurrence. (From [11])

equiaxed grains containing ultra-fine grains as a "flow-line" type microstructure often seen in materials deformed by large plastic strains. The average equiaxed grain size of the bulk Al 6061-T6 was $\sim$75 μm, and its Vickers hardness was 110HV. UFG Al 6061 of a range of grain sizes and Vickers hardness values could be prepared by changing the rake angle of the tool employed during machining. A +5°rake angle tool gave a shear strain of $\sim$3.2, a grain size of 82$\pm$30 nm, and a hardness value of 150$\pm$33 HV. While a -20° rake angle tool gave a higher shear strain of $\sim$5.2, a grain size of 75$\pm$20 nm, and a hardness value of 159$\pm$3 HV. TEM confirmed that the chips had a very fine microstructure and a diffraction pattern characteristic of randomly oriented subgrains.

2.2.6.3 Effect of Shock Loading on Reactivity.

Shock loading can also pre-strain a material, similar to the processes of HEBM and high strain machining. Shock compression causes extensive plastic deformation, fluid-like turbulent flow, heating, particle size reduction, and mixing of constituents with fresh, cleansed surfaces. These processes change the mechanical, physical, and chemical properties of the powders. Shock waves can also generate defects and cause grain size reduction, which increases mass transport rates through defects and along grain boundaries. The overall result of shock compression is enhanced solid state chemical reactivity.

Enhanced solid state chemical reactivity due to shock-assisted effects was first recorded in Ni-Al mixtures by Hammetter *et. al.*[77]. Differential thermal analysis (DTA) showed that while unshocked, mechanically mixed Ni-Al powders only gave an exotherm at 650°C, corresponding to melting (eutectic) of aluminum; the mechanically mixed Ni-Al powder mixture, gave two exotherms, at 550°C and at 650°C . The pre-initiation exotherm at 550°C corresponds to a solid-state reaction resulting for shock compression of the powders. A similar study by Dunbar *et. al.* [78] not only demonstrated the enhanced solid state reactivity in shock-modified Ni-Al powder mixtures, but the study also illustrated the effects of morphology on the magnitude of the two exotherms. Coarse/rounded morphology of the

powders reacted mostly in the liquid state, while the fine and flake morphology powders reacted mostly in the solid state. Fine morphology allows for greater surface area contact between the Ni and Al, enhancing solid state diffusion and reactivity. The flake powders allow for extensive deformation and flow of both Ni and Al, which enhances mixing and diffusion. These studies show that shock-loading can increase the solid state reactivity through the generation of defects, shorter diffusion distances, and more intimate contacts at higher packing densities.

Although enhanced reactivity due to mechanical activation is well documented in binary systems, the effects on a single component system, such as aluminum, remain to be investigated. The compressive behavior of aluminum powders has also been well characterized throughout the years, but aluminum powder reactivity under high strain rate conditions has not been investigated.

2.3 Constitutive Modeling of Meso-Scale Effects

Computational simulations can be used to determine the constituent material properties that have the largest influence on reaction initiation. During uniaxial stress loading, the sample can undergo compaction and deformation upon impact against a hardened anvil. Combustion initiation can occur during either compaction or subsequent deformation and is a function of the compact density, microstructure, and the mechanical properties of the reactant material. Constitutive relationships describing powder compaction and metal deformation under shock loading generally define the bulk response of the material. However, the effects of pressure (or stress), temperature, and strain at the meso-scale can best be determined by incorporating real or simulated microstructures with meso-scale features into computational simulations and applying the constitutive relations for each feature individually. Such meso-scale computational approaches have been used and extended to determine the processes contributing to shock compaction of powders and impact-initiated combustion reactions in powder mixtures.

2.3.1 Powder Compaction Models

During powder compaction, particle deformation and flow occurs during the process of void elimination. As voids collapse, heat is generated from the particle level plastic flow, impact of particle interfaces against one another, and the rapid volume change. The starting void volume, particle size, particle strength, and particle surface area all have an effect on the particle level processes and, in turn, on the amount of localized heat and strain created. The Fischmeiser-Artz [79] and the p-alpha [46] compaction models are commonly used to describe the bulk powder compaction process.

2.3.1.1 Fischmeister Artz Compaction Model

In the late 1970's, Fischmeister and Artz published a study on the compaction of bronze powders [80] aimed at experimentally investigating microstructures at various stages of the compaction process. They observed that both the contact area and the coordination number continuously increase during compaction. In 1982, they extended these observations to develop a model based on the geometry of the surface of the particles [79]. The model was centered around the following three stages of deformation:

1.) *Particle rearrangement*. This stage is often ignored as particle rearrangement occurs quickly, at the very beginning of the compaction process under minimal load application and does not contribute significantly to the compaction behavior.

2.) *Unconstrained deformation*. During this stage, the powders resist densification as a function of the number and size of the contact areas between the particles. Geometry, plasticity, and force transmission are all taken into account in this stage.

3.) *Constrained deformation*. During constrained deformation, the neighboring particles start to impinge on one another and impede particle flow. As compaction continues, there is a continuous increase in contact impingement that correlates to a continuous increase in the volume fraction of the powder compact that is harder to compress.

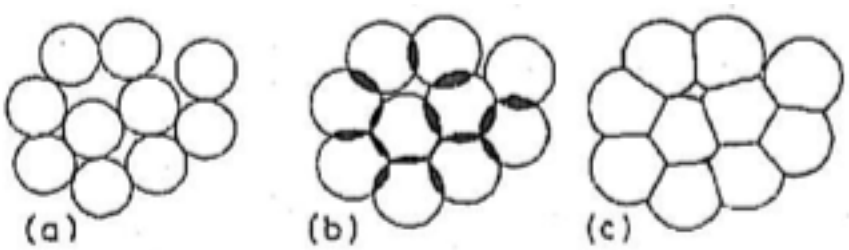

Figure 12: Schematic of Fischmeister-Artz model. (a) Particles grow around fixed centers until a certain packing density is reached. (b) Material that overlaps is deposited on the free surface of particles. (c) The overlapping material is truncated, giving the new radius of the deformed spheres. (From [79])

The analytical model depicted schematically in Figure 12 takes into account the growth of contact areas, the creation and growth of additional contact points, strain hardening, and increasingly constrained deformation. During stage two, the particles deform independently, without constraint from their neighbors. The pressure needed to compact the particles during this stage is given by,

$$p(D) = \frac{3}{4\pi}\frac{a(D)Z(D)}{R^2}D\sigma_f(D) \tag{5}$$

where *D* is the relative density, *a* is the average contact area, *Z* is the average coordination number and σ_f is the flow stress of the powder material. Once the sample reaches approximately 92% TMD, the unconstrained deformation model cannot account for the increased resistance to deformation as contact area is increased and triple points start to form. At this point, the third stage of constrained deformation begins to take over, and the pressure needed to compact the particles is given by,

$$p(D) = k\sigma_f ln\frac{a(1)Z(1)}{a(1)Z(1) - a(D)Z(D)} \tag{6}$$

Again, the contact area (a) and coordination number (Z) at the initial density and at full density serve as the basis for the expression. The constant, *k*, in equation (6) is a geometrical constant and is usually set to 2 to give the best agreement between simulations and experiments. Both of the deformation stages are combined by a linear rule of mixtures,

which takes the form of

$$p = f_h p_h + f_s p_s \tag{7}$$

where f is the volume fraction of the "harder" (indicated by the subscript, h) more densely packed, constrained portion and the "softer" (indicated by the subscript,s) less dense portion of the compact, and p is the respective yield criteria for the constrained and unconstrained deformation. The volume fraction of the harder component can be found in in terms of the length of the interfaces, L_v, and is given by the expression,

$$f_h(D) = \frac{L_v(D)}{L_v(1)} \tag{8}$$

Given these variables, the compaction process can be modeled using the equation,

$$p(D) = \sigma_Y(D) \left[\frac{3}{4\pi} \frac{a(D)Z(D)}{R^2} D[1 - f_h(D)] + 2 f_h(d) \ln \frac{a(1)Z(1)}{a(1)Z(1) - a(D)Z(D)} \right] \tag{9}$$

According to this equation, as the volume fraction of the sample undergoing unconstrained deformation decreases, the volume fraction for the portion of the sample undergoing constrained deformation increases and eventually takes over, which allows the expression to take into account the contributions from both densification mechanisms. Particle size distribution will effect the relative density (D) and the average coordination number (Z), therefore the model is most accurate for mono-sized particles. Additionally, spherical particles correlate most closely to the model prediction, but the particle shape effect decreases as stress increases.

Meyers [81] modified this Fischmeister-Artz compaction model into a form that can be used to determine, an alternate variable, the crush-up pressure, P_Y of the powder. The crush-up pressure provides information about the resistance to compaction of a powder. The modified version of the Fischmeister-Artz equation developed by Meyers [81] assumes that (a) particles are spherical and that (b) plastic yielding occurs at stresses greater than 2.97 times the yield strength, σ_Y, of the powder. Under these assumptions, the crush-up pressure needed to reach a given density of powder, P_y, is given by

$$P_y = P_0 + 2.97\rho^2 \left(\frac{\rho - \rho_0}{1 - \rho_0} \right) \sigma_Y \tag{10}$$

where P_0 is the initial stress required for rearrangement, ρ_0 is the initial packing density, σ_Y is the powder yield strength.

2.3.1.2 P-alpha Compaction Model

The p-alpha model, was devised by Herrmann [46] in 1969 and describes the compaction of porous materials under shock loading. Earlier models assumed that the compaction of porous materials to solid densities under shock conditions occurred under negligible stress and ignored the powder compaction process. The p-alpha model incorporates the parameter, α, which allows the model to account for both the compaction behavior under low stresses and the thermodynamic behavior of the material under high stresses. The parameter, α, describes the distention of the material and is given as,

$$\alpha = \frac{\nu}{\nu_s} \tag{11}$$

where ν is the specific volume of the porous material and ν_s is the specific volume of the the corresponding solid material. Once the material has densified to its fully dense (solid) state, α will be equal to unity, and the expression collapses into the Hugoniot equation of state for the material which includes the pressure, specific volume, and internal energy. The equation of state (EOS) of the solid is given by $p = f(\nu_s, E)$, and the EOS of the porous material is given by $p = f(\frac{\nu}{\alpha}, E)$. In order to describe the porous material along the Hugoniot, α, must be described as a function of its thermodynamic state,

$$\alpha = g(p) \tag{12}$$

where variation with internal energy, *E*, is implicit. Specific internal energies for porous and dense materials are assumed to be under identical temperature and pressure. Additionally, shear strength is neglected in this model.

The p-alpha model is phenomenological and describes the elastic and plastic behavior of the material as shown in Figure 13. Initially, compression is elastic. Next, at relatively low pressure, plastic deformation begins and permanent volume change takes over. For

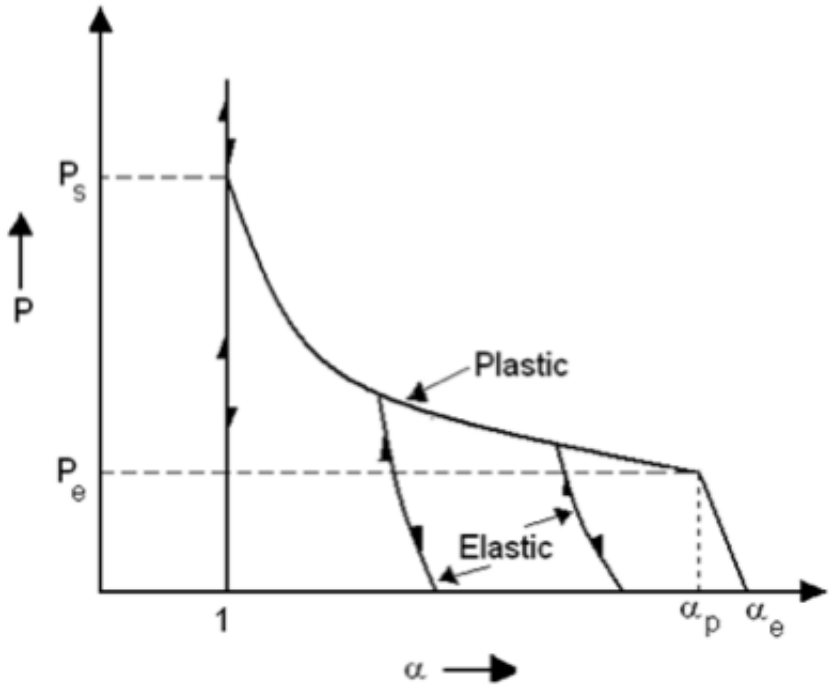

Figure 13: Schematic of the compaction behavior of a ductile porous material. (From [46])

porous materials close to solid density, the material is more likely to be constrained by the surrounding material, and elastic deformation will take the form of volume compression with little change in α. As a result, similar to the Fischmeister-Artz theory [79], plastic deformation is expected to require much higher pressures under these conditions.

The plastic regime, $\alpha = g_p(p)$ can simply be expressed in the form of a polynomial, as,

$$\alpha = \alpha_0 + \alpha_1 p + \alpha_2 p^2 + \alpha_3 p^3 + ... \tag{13}$$

Butcher and Karnes[82] applied a quadratic equation for porous iron, by setting α_3 equal to zero, finding the appropriate values for α_0, α_1, and α_2, according to the plastic behavior of the material, and setting

$$\alpha_p' = (-2)\frac{\alpha_p - 1}{p_s - p_e} \tag{14}$$

In this case the simple form of the equation is,

$$\frac{\alpha - 1}{\alpha_p - 1} = \left[\frac{p_s - p}{p_s - p_e}\right]^2 \tag{15}$$

Hermann [46] went on to show that this simple expression for the compaction relationship combined with the solid EOS fits the experimental Hugoniot data for porous iron and aluminum. One of the greatest benefits of this model is that it can easily be incorporated into computational simulations to describe compaction under shock conditions. One of its drawbacks is that it neglects phase changes such as melting.

Carroll and Holt [47] refined Herrmann's p-alpha model [46] by taking into account rate dependent behavior. They used a nonlinear second order differential equation that relies on the yield strength and a material constant to describe the three phases of dynamic pore collapse. In their expression, the changes in porosity of the first two phases is small, allowing these phases to be modeled by a simplified approximation until a critical pressure, P_{crit}, is reached to initiate the third phase of pore collapse. In 1974, Butcher [48] experimentally validated the p-alpha relationship using Herrmann's equations and updated the Carroll and Holt model to include deviatoric stresses, a material viscosity term, and a hydrostatic pressure term.

2.3.2 Meso-scale Computational Investigations

The Fischmeister-Artz [79] and P-Alpha compaction models [46] correlate well to experimental observations and provide a good foundation for understanding the overall compaction behavior of powders. These continuum level, "bulk" models rely on porosity and pressure to describe compaction but do not capture the meso-scale associated with particle and void morphology. Enhanced strain localization and heating at the particle-particle interfaces have been shown to contribute to increased reactivity in powders or powder mixtures [7]. Therefore, when evaluating the reactivity of powders, it is necessary to understand compaction and subsequent deformation behavior at the particle level. Two dimensional particle-level models can be idealized or constructed from real microstructures and used to investigate particle level effects to provide information regarding the magnitude and extent of deformation and heating on the local scale.

One of the first particle level descriptions of compaction was developed by Gourdin [83], who observed that the magnitude and extent of local temperature changes have a profound effect on the consolidation process and need to be taken into account during dynamic consolidation. To set up the model, Gourdin [83] assumed that some fraction, *f*, of the energy, *E*, from a shock wave entering an uncompressed powder is deposited into the particle interfaces as they slide over each other during densification. The model also assumes that the net shock energy that is deposited at the particle interface is a uniform, constant flux, F_0, which is described as,

$$F_0 = \frac{fE}{A\tau} \tag{16}$$

where *A* is the measured surface area per unit mass of the powder and τ is the rise time of the shock wave. Additionally, the flux is assumed to be applied only for a time, τ, and the particles are assumed to be spherical, with an area diameter, *D*. These assumptions, illustrated schematically in Figure 14 allow the thermal transport equation,

$$\frac{dT}{dt} = \alpha \nabla^2 T \tag{17}$$

which provides a temperature profile for a powder particle, to be solved. One key feature of the model is the incorporation of the energy flux, which allows a large energy contribution, *E*, to be balanced with a larger rise time and surface area per unit mass, τA. Therefore, even if the energy input is large, a highly porous powder compact composed of small diameter or irregularly shaped (high surface area) particles will have a low energy flux, leading to low surface temperatures and no interparticle melting. The largest thermal effects are assumed to be seen in spherical powders with moderate packing density, and surface temperature should increase even more with increased particle size. This energy flux model is able to provide a general sense of the magnitude of temperature change and its effect on the microstructure but lacks the ability to provide detailed information on microscopic processes, such as plastic flow and void collapse, that occur during consolidation.

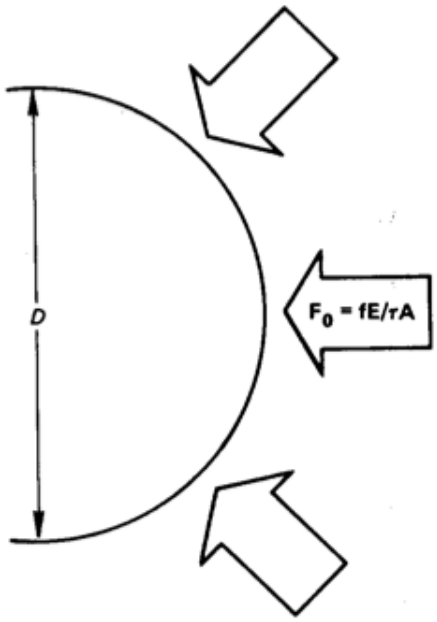

Figure 14: Schematic of single particle energy deposition model. (From [83])

Williamson [84] used the principles of Gourdin's energy deposition model [83] and was one of the first to incorporate 2D spatially-resolved particle level models into the study of the consolidation of metal powders. He investigated the following three powders systems: a mono-sized distribution of particles, a bimodal distribution of particles, and hollow particles [84]. Use of a 2D computational simulation provided further insight into the relationship between metal powder compact properties, such as particle size distribution and void fraction, and heating and deformation at the particle interfaces. To set up the computational simulation, the powder compact, approximated by infinitely long stainless steel cylinders with an 80 μm diameter in two spatial directions, was compressed by the impact of a copper flyer against the copper cover plate that sandwiched the compact. A 2D Eulerian finite difference code was used to simulate material consolidation and deformation over time. In the computational simulation, friction and heat conduction were neglected because the short time scale of the consolidation and the particle size don't allow significant energy transfer by conduction.

Figure 15 illustrates simulations showing the increases in localized deformation and

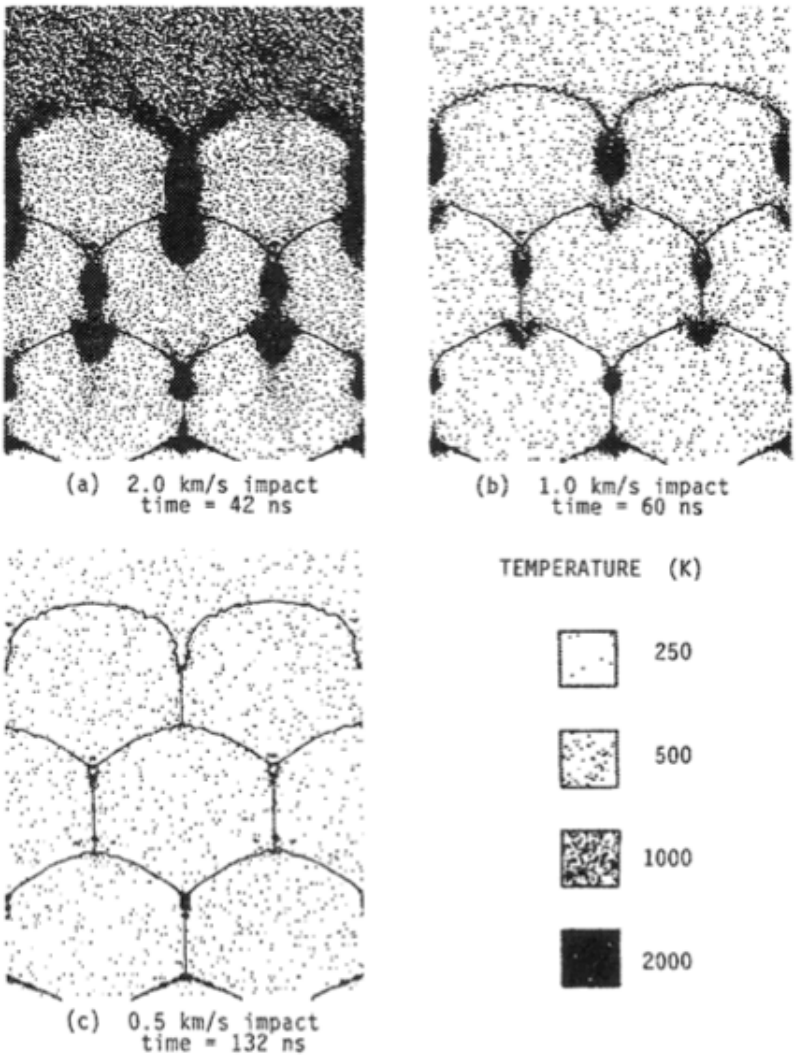

Figure 15: Compaction of mono-sized particles at various velocities. Darker areas indicate higher temperatures. (From [84])

temperature with increasing velocity during the shock compression of mono-sized powder particles. Williamson [84] postulated that the rapid particle deformation that occurs to fill interstitial voids during compaction results in large energy deposition at the particle surface, resulting in high temperatures. Figure 16 plots the differences in temperature at the interstitial sites between a bimodal and a mono size distribution of powders. In the case of the bimodal particle size distribution, the filling of particles results in a lower peak temperature in interstitial sites. Experimental evidence of this was observed by Wright *et. al.* [85] in their study of explosively compacted stainless steel powders of varying sizes. They demonstrated that larger particles, which inherently have a larger interstitial size, showed higher surface temperature and were more likely to bond to one another than smaller particles. The last set of powders in Williamson's study [84], the hollow particles, showed more extensive high temperature regions due to increased void volume. Additionally, Williamson [84] examined the effect of interstitial gas on localized energy deposition and saw an increase in surface temperature and more extensive particle melting due to compression of the gas. Yet, the effects of the interstitial gas on energy deposition are less dominant than particle size effects. Experiments showed that the gas has sufficient time to vacate the voids prior to particle deformation.

The largest shortcoming to Williamson's work [84] was that he used a small computational domain that included only one unit cell to investigate these powders. Benson [86, 87] built on this work and investigated a larger computational domain when studying the compaction of a random particle size distribution of a moderate number of cylindrical and rectangular morphologies of copper. The computational results showed an increase in temperature at the surface of the particles, similar to the temperature profile predicted by Gourdin [83]. Further, increased turbulent flow was observed in the cylindrical particles when compared to the rectangular particles, where flow was limited to the vertical particle boundaries.

Nieh *et. al.* [88] investigated the compaction of nano-aluminum through 2D planar

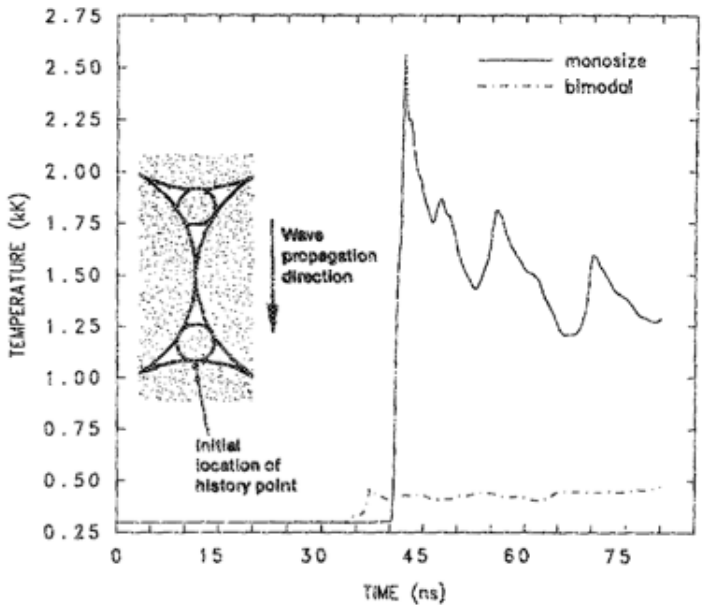

Figure 16: Comparison of temperatures observed in bimodal and mono-sized particle distributions at the tracer point indicated in the inset. (From [84])

simulations and experiments. They modeled the material response with a Gruneisen equation of state and a Steinberg-Guinan plasticity model, ignoring the alumina shell. Shock compression of a 54% dense compact of aluminum powders, ranging in size from 150nm to 250nm, at 2GPa, resulted in a sample that contained 5nm pores. Yet, a computational study of the same system under the same shock compression conditions predicted a fully dense sample. The authors [88] cited the following two reasons for the discrepancy between the computational and experimental results: (1) The computations did not incorporate an aluminum shell and (2) The energy per unit volume required to collapse a spherical void is observed to be 13% greater than the predicted energy required to collapse a cylindrical void of a perfectly plastic material based on computations. Austin *et. al.* [89] applied similar techniques to study spatially resolved aluminum-iron oxide thermite powder mixtures in a polymer binder. Their computational study provided spatial temperature and pressure profiles that gave insight into the local thermomechanical behavior of the system under shock loading. Additionally, the authors were able to correlate the averaged pressure profiles from

the simulation with experimental results and obtain Hugoniot data.

Baer [90, 91] applied 2D numerical simulations to a 3D structure to investigate the initiation of reactive HMX particles. An idealized 65% TMD sample of an arbitrary size distribution of closely packed particles was created using Monte Carlo and molecular dynamics methods. Upon impact at 1.0 km/s, the simulation showed a high pressure wave entering the sample and causing rapid deformation and spikes in the temperature and pressure at the material contact points as illustrated in Figure 17. Reaction initiation in this system is controlled by the competition between the hot spot generation from plastic deformation and hot spot degradation resulting from thermal conduction. Samples with a high degree of plastic deformation and less thermal conduction were more likely to generate hot-spots that sustain a reaction. Additionally, Baer [90] investigated the effect of particle morphology by impacting an ordered array of mono-sized cubes and mono-sized spheres. The resonance effect of the ordered spherical particles resulted in higher pressures in that system than the system with cubic particles which has a more disordered particle orientation. Baer [90] extended his analysis to examine reaction initiation and employed the two state history variable reactive burn model developed by Kerley [90]. This approach assumes that the reaction is triggered at a certain pressure threshold. The simulations showed that larger-sized particles initiated at lower pressure threshold. Overall, this work suggested that heterogeneous materials experience fluctuating stress states and localization of energy due to plastic deformation.

The previously mentioned meso-scale computational studies have all been on idealized structures, which ignore highly irregular configurations. Eakins and Thadhani [92] performed meso-scale computations using more representative experimental conditions by incorporating real microstructures acquired from SEM images into the simulation. To import the experimentally acquired microstructure, manual thresholding was used to separate each phase in the binary image. Next, a vectorized image of each phase was constructed, and the resulting vectorized description was converted to the DIATOM compatible code [92].

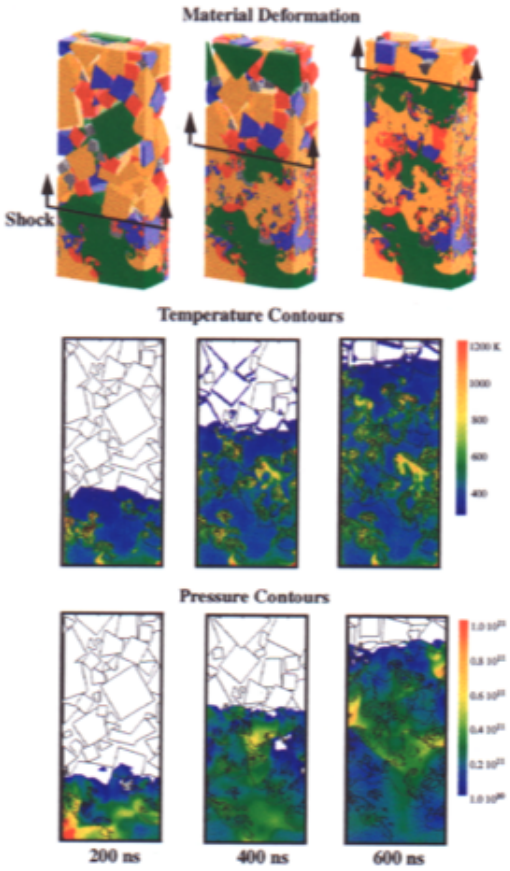

Figure 17: Impact of 3D porous mixture of HMX particles at 1km/s. The upper row gives a 3D rendering of the materials over the first 600ns of impact. The middle and lower rows show a midplane cross-section of temperatures and pressures, respectively, over time. (From [90])

By simulating the shock compression of Ni + Al mixtures at porosities ranging from 45% TMD to 80%TMD and impact velocities ranging from 0.5km/s to 1.0km/s, they were able to identify the following three dominant mechanisms of plastic deformation and energy dissipation: focused flow ("jetting"), particulation, and vortex formation. These deformation mechanisms cause local fluctuations in temperature and pressure which can be observed in the highly irregular shock fronts and high pressure states in granular materials.

2.4 Experimental Methods for Observing Meso-Scale Effects

Pre- and post-mortem material characterization and mesoscale simulations can provide information about the particle-level processes that take place during the compaction and deformation of a heterogeneous material system under high strain rate loading. Yet, these techniques do not provide *in situ* information about the particle-level mechanical, chemical, or thermodynamic transition states associated with shock compression. The resulting mechanistic descriptions of material behavior under high strain rate loading are thus often based on assumptions. The complex particle scale processes, including pore collapse, particle deformation, and localized heating, that take place during shock loading of heterogeneous materials necessitate that *in situ*, mesoscale sensors be developed to study and understand the material behavior under such high strain rate loading conditions. *In situ* methods, using embedded and non-embedded sensors, provide direct, nanosecond time-resolved information about the shock compression conditions and the material response to those conditions. Interferometry, imaging, and stress gauges have become standard techniques for time-resolved analysis of shock events. More recently, advances have been made to employ dyes and quantum dots as mesoscale probes that can capture information about particle level processes during shock compression.

2.4.1 Diagnostics Based on Non-Embedded Sensors

Diagnostics employing non-embedded sensors can capture time-resolved information about the thermodynamic states without being in contact with the sample. One advantage of these

sensors is that because they are not in contact with the sample, they do not have any effect on the material-shock wave interaction. The resulting data can be assumed to capture the shock states in the material in its purest form. Additionally, the stand-off distance from the shock event gives these probes a longer lifetime, as they are not destroyed by the shock wave as quickly as embedded sensors might be. The longer lifetime allows the sensor to provide a greater amount of time-resolved information.

One of the drawbacks of non-embedded sensors is that they are only able to capture information at the surface of the material. Interferometry and high-speed imaging are the most commonly used techniques for acquiring information about a shock event at a distance. Interferometry provides information about the particle velocity at the back surface of the material. Imaging can be done at any material surface, but still only captures the material response in two dimensions.

2.4.1.1 Interferometry

Displacement interferometry was first used to investigate the mechanical properties of materials under high rate loading in 1965 by Barker and Hollenbach [93]. Interferometer operation relies on the interference patterns that form when two highly coherent, monochromatic beams are offset. The beams are reflected off of a mirror or other surface and monitored by a photomultiplier tube or streak camera. Interference that disrupts the original pattern can occur in two ways, by (1) displacement or (2) velocity [36]. Displacement interferometry is based on the Michelson interferometer principle. As the mirror (or material of interest behind the mirror) moves, the reflected beam is displaced. When the displaced sample beam is overlayed onto the constant reference beam, it creates an interference fringe pattern. Alternately, velocity interferometry is based on the principle of Doppler-shifted frequency. As the mirror moves, the frequency of the reflected beam changes with respect to the reference beam and an interference fringe is formed.

One of the most commonly used systems for monitoring free surface velocity during

shock loading is the VISAR (Velocity Interferometry System for Any Reflector) developed by Barker and Hollenbach in 1972 [94]. The other two velocity interferometry systems primarily in use are the Fabry-Perot system and the Heterodyne photo doppler velocimetry (PDV) system [95]. An additional system, an ORVIS, is composed of similar optics as the VISAR, but the PMT detector is replaced with a streak camera [95]. Compared to a Fabry-Perto system, a VISAR system is more flexible, sensitive, and better time-resolved, but the data analysis is much more complicated than the Fabry-Perot system. All of these systems are able to provide highly accurate velocity information and nanosecond time resolution at a spot size of 50 to 200μm [95].

The VISAR has been used by several researchers to investigate heterogeneous materials under shock conditions. Baer *et. al.* [96] used four VISAR probes to monitor PBX9501 under isentropic loading conditions. When compared with numerical simulations of the same system and loading conditions, the measured VISAR profiles showed an additional dispersive region at the beginning of each signal that increased with increasing thickness, which was not observed in the simulation. This dispersive region was attributed to mesoscale effects from the binder interacting with crystallites. In 2014, Borg *et. al.* [97] investigated the shock compression behavior of PVDF-filled aluminum foam using VISAR and found that the experimental response correlated well with the average response from the simulations, but the experiments did not capture the distribution of states present in the simulations of the heterogeneous system.

VISAR and other velocity interferometry systems only provide free surface velocity at a single point. A line imaging interferometer system has been developed to capture two dimensional, spatially resolved information about the heterogeneous response of a granular system [98]. Instead of tracking the shock compression response of a material at only a single point, the line ORVIS illuminates the target along a line segment of the material of interest using multiple fringes. The fringes are monitored over the duration of the shock by a streak camera, and the free surface velocity along the illuminated line segment of the

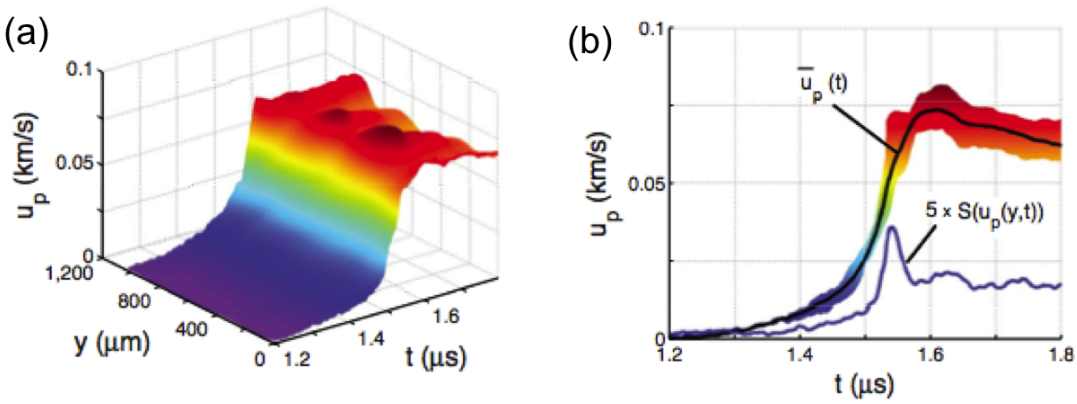

Figure 18: Example of line VISAR data. (a) Line VISAR trace of tungsten carbide filled epoxy, showing a spatial change in velocity across the sample over time. (b) Average velocity response of the tungsten carbide filled epoxy with the standard deviation given in blue. (From [100])

sample can be obtained with up to 10μm spatial resolution [99].

Vogler *et. al.* [100] used both point VISAR and line-VISAR to study the shock compression of tungsten carbide and alumina filled epoxy composites. The line-VISAR trace plotted in Figure 18 (a), captured two peaks in velocity at two distinct locations, indicative of a variation in local response. The standard deviation of the average velocity along the different positions was found to vary significantly across the sample at any given time. Figure 18 (b) plots the average velocity over time and the standard deviation of velocity. It can be seen that the greatest spatial difference in velocity is observed during the ramp, when the velocity increases rapidly. This measurement highlights the difference between the particle level response and the average response of a heterogeneous material under high strain rate loading conditions [100]. Other researchers have used line-imaging VISAR to study mesoscale processes such as pore collapse [101], the response of a welded joint [101], phase transformations in iron [102], and shock wave structure [102].

2.4.1.2 Imaging

Advances in fiber optics, electronics, memory storage, and sensors have paved the way for the development of high speed imaging and IR cameras. High speed cameras collect

images at several million frames per second and allow for direct observation of events, such as fracture, deformation, and reaction initiation, that occur under high strain rate loading conditions. Direct observation by a camera provides a temporally and spatially resolved view of the material response to high strain rate loading and enables a better understanding of the mechanisms responsible for failure and reaction initiation under these conditions.

High speed imaging can be used to make a variety of quantitative and qualitative observations about the behavior of a system under high strain rate conditions. Quantitatively, using the dimension of each pixel and the time between each frame, both the impact velocity and the radial strain rate can be calculated. The impact velocity can be tabulated by measuring the gap in sequential photographs [36]. Additionally, the rate of change of the radius between frames can be used to determine the radial strain rate. Qualitatively, high speed imaging can be used to observe the state of a flyer in a laser-accelerated flyer system [103], the ablation of particles [104, 105], and the presence of reaction initiation [11, 68], among other phenomena.

The development of high speed color imaging and IR sensors has recently made it possible to obtain spatial, time-resolved images of temperature changes in systems under high strain rate loading. Thermal imaging is made possible through the use of blackbody emission theory. Blackbody intensity is a function of temperature, and when that relationship is well characterized, it can be leveraged to determine the temperature of an object based on its intensity at a given wavelength [106]. Reeves *et. al.* [68] used a high speed IR camera to investigate the correlation between reaction initiation and heating in Ni/Al heterogeneous systems under a combination of compressive and shear loading. The left side of Figure 19 (a) shows that samples containing nano-sized Ni and Al, reacted, and heat that was generated initially continued to propagate for several milliseconds as the reaction continued. Alternately, samples of Ni and Al that had been high energy ball milled did not react, and although the temperature increased initially, the temperature began to drop within two milliseconds [68] as illustrated on the right hand side of Figure 19 (a). High

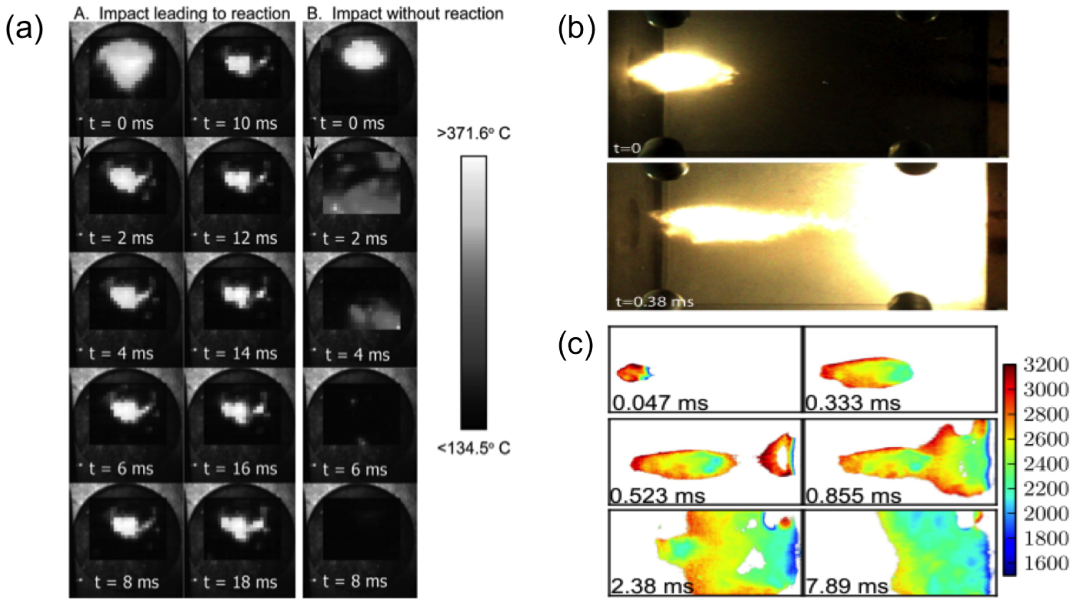

Figure 19: Thermal imaging of reactive materials. (a) Compression/shear loading of Ni/Al, showing temperatures of a nano-size Ni/Al that reacted and HEBM Ni/Al that didn't react (From [68]). (b) High speed images of NiAl impacting a front plate and rear anvil and (c) thermal images of NiAl in the same configuration (From [61]).

speed IR cameras are generally limited to inter-frame times of hundreds of microseconds. In order to overcome this time-resolution limitation, Densmore *et. al.* [61] constructed a two-camera imaging pyrometer. Highly time-resolved spatial images of the temperature were captured by directing light from the experiment into a beamsplitter which sent the light to two high speed color cameras, each equipped with a 700nm and 900nm bandpass filter, respectively. The ratio of the two camera signals is a function of temperature, and the temperature at each pixel can be numerically tabulated using the two intensity values [61]. With this setup, Densmore *et. al.* [61] were able to observe the heating of several reactive materials (RM), including Ni/Al, which is illustrated in Figure 19 (b) and (c), impacting a front plate and rear anvil at 1700m/s. Thermal imaging captured the immediate cooling of the Ni/Al RM following impact against the anvil at a temperature of 3600K.

Although high speed imaging and thermal imaging can provide a much clearer picture

of the mechanisms at play during high strain rate events, there are still limitations to overcome. Imaging at this high of speed requires very low exposure times, which leads to low amounts of light and therefore, difficulties in obtaining a clear image. Additionally, the memory limitations of many cameras require a tradeoff between high time resolution and high spatial resolution. Images that are highly time-resolved are often pixelated and blurry.

2.4.2 Diagnostics Using Embedded Sensors

Diagnostics employing embedded sensors provide a way to probe material response to shock loading directly. They range in size from the molecular scale, for example dyes, to several millimeters, for example piezoelectric and piezoresistive stress gauges. Larger gauges are sufficient to capture the bulk response of a material, but the heterogeneous responses of a granular material are averaged out over the larger surface area of the gauge. Over the last 15 years, new embedded sensors have been developed that have the ability to probe the mesoscale response of a material during a shock loading event.

2.4.2.1 Stress Gauges

Stress gauges have been in use for over 100 years. There are two main classes of stress gauges, piezoresistive and piezoelectric gauges. Piezoresistive stress gauges, typically comprised of manganin, carbon, or ytterbium, monitor changes in resistivity with pressure [36]. Alternately, piezoelectric stress gauges, typically comprised of quartz, lithium niobate and some polymers, generate electricity when stressed. One of the greatest distinctions between the two types of stress gauges is that while piezoresistive gauges require an external power source to function, piezoelectric gauges do not require an external power as the current is provided by the piezoelectric gauge directly.

Piezoresistive gauges were first used in 1911 by Bridgeman [36], who used manganin coils immersed in pressurized fluids to monitor resistivity changes with pressure. Manganin gauges require inputs for a pulsed power supply and outputs to a voltmeter as shown in Figure 20 (a), and are able to monitor stress up to 30GPa and have a time-resolution of 50 to

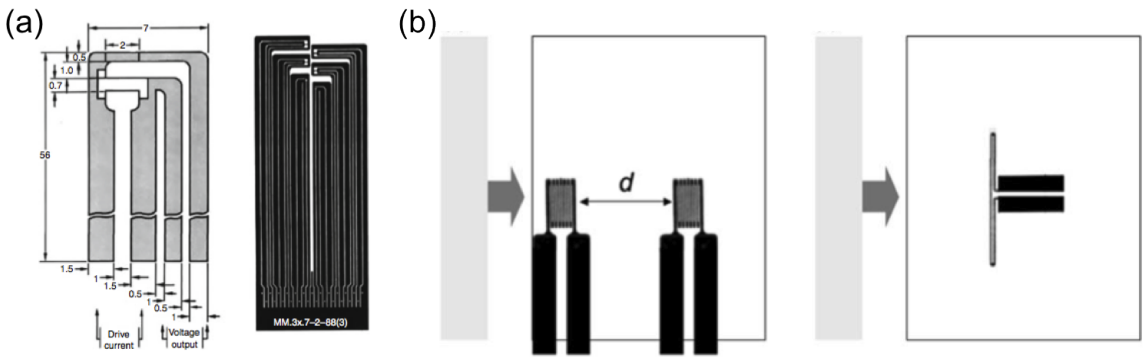

Figure 20: Examples of manganin gauges. (a) Close up images of single and multiple four lead manganin gauges (From [95]). (b) Two configurations used to monitor pressure wave, longitudinally placed grid gauges and T-gauges. (From [107]).

100ns. They are protected by insulating materials, can range in size from a few millimeters to meters, and can take on any desired shape. Their versatile geometry and accuracy allows them to still be relevant to investigate material response to shock impact. Bourne *et. al.* [107] used two types of embedded manganin gauges, a T-shape and a grid, to monitor the shock response of semicrystalline metals. In one experimental setup, two grid gauges, embedded at a longitudinal distance, *d*, between each other, as shown in Figure 20 (b), were used to track the longitudinal stress pulse passing through the gauge, the development of the pulse, and the time of travel between each location, to get a shock velocity and the Hugoniot elastic limit for the material. In another experimental setup, a T-shaped gauge was mounted a known distance from the impact face, as shown in Figure 20 (b), and used to measure the lateral stress component. The combination of direct measurement of the longitudinal and lateral stress and post-mortem analysis of the recovered samples allowed Bourne *et. al.* [107] to link the direct continuum scale measurements to microstructural evolution during shock compression. For instance, BCC metals, due to their low density of mobile dislocations, exhibited the slowest rise times, while FCC materials show a rapid rise in plastic wave because their Peierls stress is low [107] .

Piezoelectric gauges were first used in 1921 by Keys [36]. As a pressure gradient is applied between two electrodes, piezoelectricity is generated and can be monitored as a

function of pressure. Quartz has been shown to have piezeoelectric properties, and it functions well as a shock stress gauge [108]. Additionally, PVDF functions as a piezoelectric gauge and has the added benefit of being as thin as 25μm [36]. Eakins *et. al.* [8] used PVDF gauges to monitor both the input and propagated stress wave at the front and back end of a Ni/Al powder mixture. They measured shock velocity and input stress, plotted them as shown previously in Figure 8, and observed an increase in velocity above an input stress of 5 GPa for a 45% TMD flake Ni and equiaxed Al mixture, indicative of a shock-induced reaction. Jordan *et. al.* [109] used VISAR and both manganin and PVDF stress gauges to investigate the shock equation of state (EOS) of an Al-MnO_2-epoxy composite. The combination of these diagnostics allowed them to observe regions of nonlinearity in the EOS that were indicative of heterogeneous phenomena, such as compaction, viscoelastic effects, and the formation of multiple phases.

The large surface area of both piezoelectric and piezoresistive gauges makes these sensors inadequate for measuring mesoscale effects. Although these stress gauges can provide some information about microstructural behavior by illustrating trends in the continuum behavior of different types of materials, they do not provide a direct measure of mesoscale events. A smaller surface area sensor that is able to provide a highly time-resolved response is needed to probe the mesoscale processes that occur in heterogeneous materials.

2.4.2.2 Fluorescent Dyes

Fluorescent dyes hold much promise as a potential mesoscale optical pressure sensors. Their small size and ultrafast response time, only limited by the optical electronic transition time, which is on the order of picoseconds, makes fluorescent dyes an ideal candidate for meso-scale sensors. Shen and Gupta [110] were the first to use dyes to monitor the shock response of a material. In their study, rhodamine 6G was used to probe the behavior of liquid ethanol under shock pressures of up to 1.87 GPa. The rhodamine demonstrated a redshift in the fluorescence emission that was somewhat larger than the shift observed under

static high pressure loading conditions. The effects of temperature increase were found to be minimal and the difference in the shift was attributed to a shock-induced reorientation of the dye molecules . The redshift emission from the dyes during shock compression was observed to increase linearly with input pressure increase from 0.2 to 2.0 GPa. Lee *et. al.* [111] built on the work done by Gupta, and developed an "optical nanogauge" composed of a rhodamine 640-doped PMMA film. This nanogauge showed an absorbance redshift when exposed to shock pressures of 2.0GPa that correlated well with the response from static compression at that pressure range.

The work, using fluorescent dyes as optical nanogauges, has been refined by the Dlott group over the past five years [112, 113, 114, 115]. They conducted all of their studies on the laser-driven flyer plate set-up at the University of Illinois Urbana-Champaign (UIUC), depicted schematically in Figure 21 (a), and described in detail elsewhere [116, 114]. Briefly, a Nd:YAG laser sends a several nanosecond pulse through a beam shaping device that converts the Gaussian shaped pulse to a flat-top shape to provide planarity. The pulse is focused with a lens down to the desired diameter onto an aluminum flyer that is adhered to a glass substrate. Upon interaction with the adhesive, the expansion from the plasma accelerates the 700 μm diameter flyer to impact the dye-doped polymer backed by a PVA cushion followed by a glass plate, as illustrated in the schematic in Figure 21 (b). The impact velocity is controlled by the input energy of the Nd:YAG laser. A dichroic beam splitter is placed at the back end of the sample to allow analysis of particle velocity by PDV and to monitor the dye emission using a spectrograph/streak camera.

In one of their first studies, Brown *et. al.* [112] observed the time-resolved emission of rhodamine 640 embedded in PMMA, as it was shocked at 5.2 GPa. The time-resolved spectra shown in Figure 22 (a) illustrates a loss of intensity and red shift at nanosecond time intervals as a function of shock compression. Again, the emission redshifts as a function of pressure correlated well (but not exactly) as a function of pressure, with quasi-static measurements taken on a diamond anvil cell. They hypothesized that this difference was

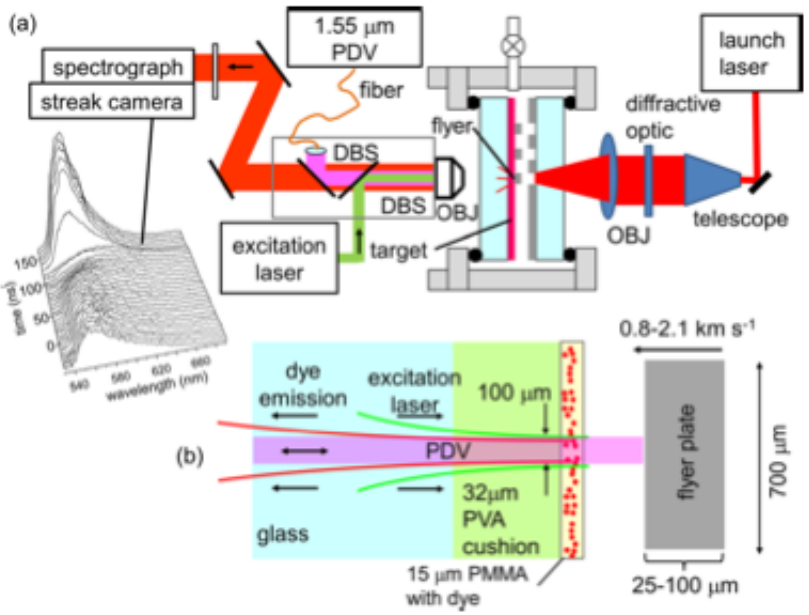

Figure 21: Laser driven flyer setup used to investigate fluorescence response of dye doped polymers under shock impact. (From [114])

due to the longitudinal stresses and higher temperatures that are associated with shock compression. The authors also noted that PMMA is inhomogenous on the length scale of its polymer chains due to the possible chain conformation transitions and therefore the local and global responses of PMMA will be different.

Brown [113] developed a way to more quantitatively describe the changes in rhodamine dye intensity, red shift, and peak half width as a function of shock pressure using the method of moments. Given that $I(\lambda, t)$ is the wavelength (λ)-resolved spectrum at time *t*, the zeroth moment, which is equal to the instantaneous wavelength-integrated area or intensity, is,

$$M^{(0)}(t) = \int_0^\infty I(\lambda, t) d\lambda \tag{18}$$

The first moment, which is equal to the instantaneous average wavelength, and gives the redshift magnitude is,

$$M^{(1)}(t) = \frac{1}{M^{(0)}(t)} \int_0^\infty \lambda I(\lambda, t) d\lambda \tag{19}$$

These functions are easy to automate and make calculating the intensity and redshift much simpler. Using this method, Brown [113] showed that the redshift, pictured in Figure 22

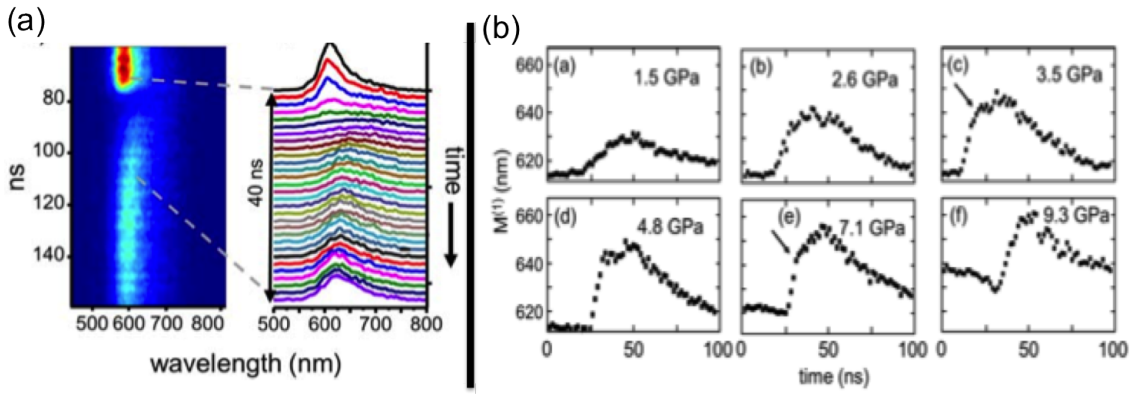

Figure 22: Spectral response of rhodamine 640 in PMMA to shock impact. (a) Time resolved spectra of rhodamine 6G emission as PMMA is shocked at 5.2 GPa. The spectra shows a loss in intensity and a red shift as the shock is applied (from [112]). (b) Shock induced redshift in rhodamine. *a-f* give the red shift at increasing pressures (From [113]).

(b) stopped increasing with pressure above 6 GPa, pointing to an entropy-dependent barrier crossing process under shock conditions as opposed to an enthalpy-dependent process. The activation entropy (ΔS) represents the ratio of the number of states in the transition state to the number of states in the initial state, and the activation enthalpy (ΔH) represents the amount of energy needed to reach a transition state. If the activation entropy is low in the transition state, then the rate will not increase regardless of the amount of energy (ΔH) put into the system, as observed in the rhodamine-PMMA system. Additionally, there was a smaller redshift in the shocked system than in the statically compressed system [113]. This less apparent red-shift made constructing a reliable calibration curve, correlating the redshift to the dynamic pressure, unfeasible.

Another dye, rhodamine 6G, gave a greater emission intensity and was insensitive to temperature changes. Therefore, rhodamine 6G became the basis for further testing for the shock induced response of dyes. Banishev and Dlott [115] found that the emission intensity of rhodamine 6G decreased linearly with an increase in dynamic pressure as shown in Figure 23. They found that the optical response under these conditions is based on the mechanism of intersystem crossing. Increases in pressure divert the population of the

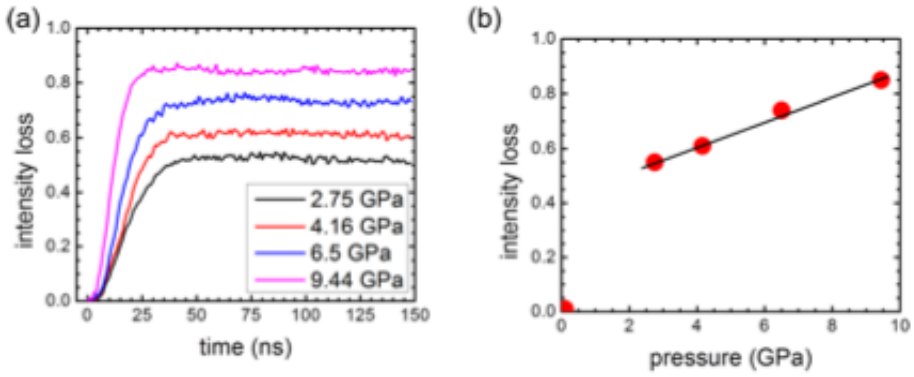

Figure 23: (a) Loss of rhodamine 6G intensity over time at shock pressures ranging from 2.75 GPa to 9.44 GPa. (b) Linear increase in loss of intensity with shock pressure (From [115]).

emissive S1 state to the dark T1 state, which results in a pressure-induced loss of emission intensity [115]. This explanation was confirmed by theoretical calculations. They also found that the presence of oxygen effected the emission response of the dye. Dye emission was further used to investigate the localized shock behavior of PMMA [114].

2.4.2.3 Quantum Dots

Semiconductor quantum dots represent another material that has the potential for use as a mesoscale pressure sensor. In semiconductors, the electronic energy level spacing is greater than the temperature, and optical excitation across the gap becomes dependent on the particle size [117]. Therefore, spatial confinement of a semiconductor in all three dimensions, making it a "0D" material or a quantum dot, leads to unique optical and electrical properties. As the size of the semi conductor is decreased, the band gap spacing is increased, leading to higher energy transitions, and resulting in blueshift in the fluorescence emission, as shown in Figure 24 (a) and (b) [117, 118]. This intrinsic change in optical properties as a function of size in semiconductor quantum dots has been leveraged by several researchers to monitor localized pressure and temperature changes [119, 120, 121, 122].

In 1988, Alivisatos *et. al.* [119] was one of the first to investigate the behavior of semiconductor quantum dots as a function of pressure, when they used a diamond anvil

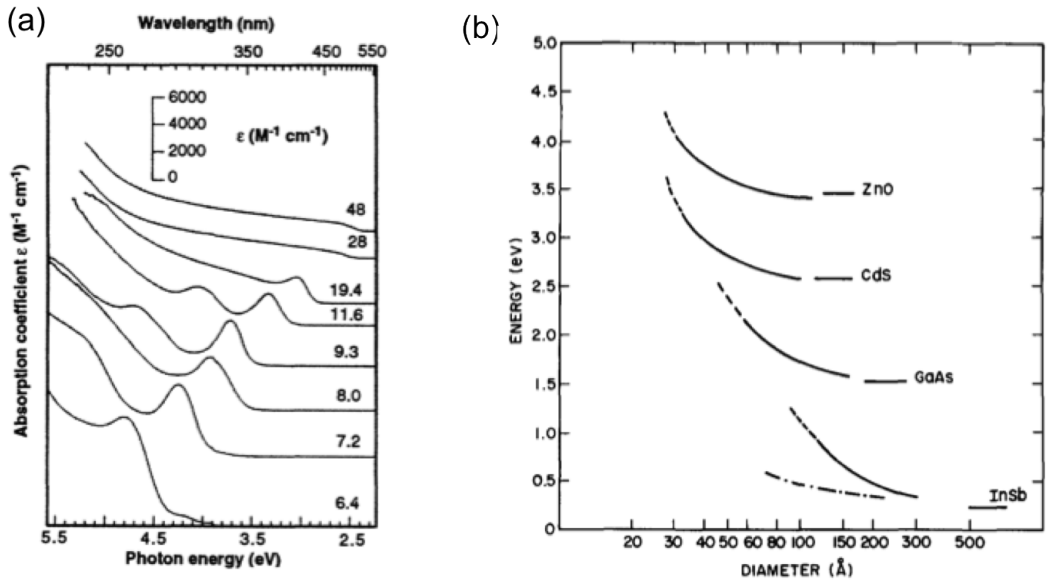

Figure 24: Optical properties of QD. (a) Change in band gap energy as a function of diameter (From [117]) (b) in multiple semiconductor systems (From [118]).

cell (DAC) to investigate 4.5 nm CdSe microclusters in methanol solution at pressures up to 3.5 GPa. When compared with bulk CdSe, the microclusters had a deformation potential that corresponded well to bulk samples indicating that the lattice properties, which are dominated by local, nearest neighbor forces remain the same in samples composed of microclusters as in the bulk samples. Yet, the optical electronic behavior of the CdSe microclusters showed an increasing blue shift with an increase in pressure, and it differed considerably from the bulk behavior, indicating that the optical behavior was mostly dependent on quantum confinement [119]. Zhuravlev *et. al.* [120] studied the NIR emission of 3, 5, and 7 nm PbSe in a DAC and found that the bulk deformation potential dominated the nanocrystal optical response under pressures up to 5 GPa. As pressure increased, the band gap energy decreased. Therefore, instead of a blueshift, Zhuravlev *et. al.* [120] observed a redshift in emission as a function of increasing pressure in the near IR. An observed increase in band gap energy with a decrease in nanocrystal size was attributed to the increasing optical effects of quantum confinement as size is decreased. Further modeling work by Kamisaka [123] showed that this discrepancy in the direction of the wavelength

shift between PbSe and CdSe was valid and could be explained by optical response theory that takes into account the electronic states and the electron-phonon coupling.

Another study of the pressure dependent optical behavior of 5.5 nm CdZnSe and 3.5 nm CdSe in a DAC [121] agreed with Alivisatos' results [119], showing a linear band gap energy increase with increasing pressure. Additionally, at pressures above the critical pressure of 5.9 GPa, the pressure at which the wurtzite to rock salt polymorphic phase transition occurs, the energy gap increase does not continue to increase linearly. The critical pressure drops to 5.4 GPa in the alloyed, CdZnSe quantum dots, indicating that the pressure dependent optical behavior can be finely controlled. Wittenberg [124] took this work one step further and investigated this phase transition under dynamic conditions in a setup similar to the one used by Dlott [114]. A 250nm layer of polyvinyl (butyral-co-vinyl alcohol-co-vinyl acetate) (PVB) containing 5% CdSe nanocrystals (4nm diameter) was sandwiched between a glass-aluminum-PVB layer and an epoxy backer and shocked at pressures ranging from 2.3 to 3.75 GPa. At pressures of 2.3 GPa, a blue shift and a decrease in intensity is observed. Several minutes after the shock wave has passed, the sample does not continue to exhibit a blue shift indicating that the response is due to the elastic compression of the wurtzite lattice, which causes an increase in the band gap energy and the blue shift [124]. Additionally, Wittenberg *et. al.* [124] observed that the critical pressure for the phase transition from wurtzite to rock salt decreases to 3.2GPa under dynamic conditions, indicating that multiple nucleation events per particle exist [124] under these dynamic conditions.

The topology of the nanocrystal also has an effect on the optical response as a function of pressure. Choi *et. al.* [122] investigated CdSe core-CdS arm nanocrystals in spherical, linear, and branched topologies in a DAC under both hydrostatic and non-hydrostatic conditions at pressures of up to 6.0 GPa and observed variations in response between the different topologies. As reported previously [119, 121], all nanocrystals exhibited an increasing blueshift under increasing pressures as shown in Figure 25. Yet, under hydrostatic

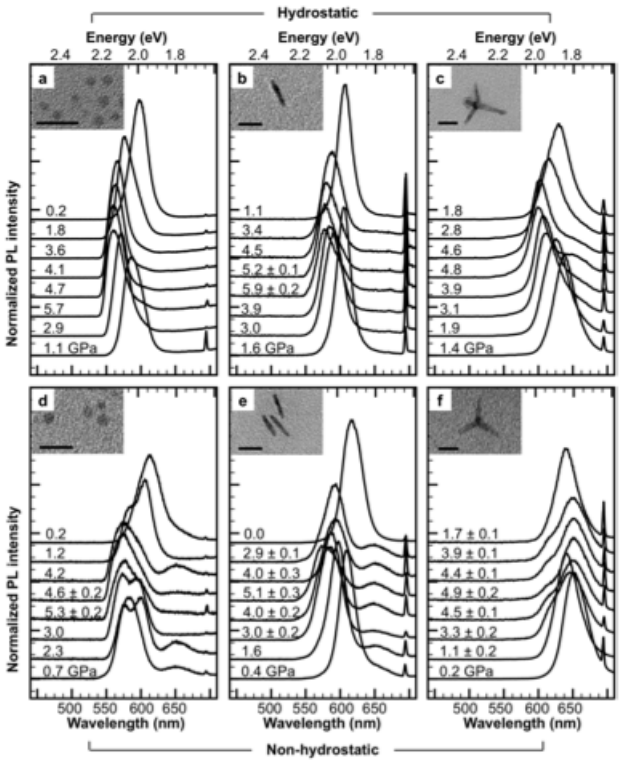

Figure 25: The optical response of quantum dots (a,d), rods (b,e) and tetrapods (c,f) under increasing hydrostatic (a-c) and non-hydrostatic (d-f) pressures (From [122]).

pressure, the blue shift in the tetrapod topology was more significant, because the multiple arms make them more sensitive to stress. The tetrapod arms bend and stretch at the same time, depending on its orientation to the stress axis, exposing the CdSe core to large shear stresses that amplify the band gap energy increase. The response in the tetrapod was leveraged to construct a luminescent nanocrystal stress gauge that could be incorporated into various micromechanical systems to provide spatially resolved information about local stresses [125].

Other researchers have taken advantage of semiconductor nanocrystals and developed nanocomposite sensors that change intensity as a function of pressure [126]. Although these studies provide a solid foundation of information about the behavior of semiconductor nanocrystals under pressure, only Wittenberg's work [124], investigated nanocrystal behavior under dynamic loading. More shock compression studies are needed to be able to

develop a reliable quantum dot-based mesoscale pressure sensors.

Chapter III

MATERIALS SYSTEMS AND EXPERIMENTAL SETUP

This work is focused on studying the initiation of combustion reaction in aluminum powder compacts under uniaxial stress rod-on-anvil impact conditions. As depicted schematically in Figure 26, the aluminum powder compact mounted on a copper rod is impacted against a hardened steel anvil. Upon impact, the compaction and deformation of the powder and the compact at extremely high strain rates can result in the initiation of a combustion reaction of aluminum with the available oxygen in the environment. The influence of the microstructural and mechanical properties differentiating the various types of aluminum powder samples as they undergo compaction and deformation was used to understand the following issues:

a.) *Under what conditions, e.g. impact velocity and powder compact density does the combustion reaction occur in compacts of various types of aluminum powder? How can the initiation of combustion of aluminum be controlled by altering the impact conditions and compact characteristics?*

b.) *Can initiation of the combustion of aluminum powder compacts be attributed to the effects of bulk or localized deformation? What are the bulk or localized deformation processes that control the threshold for the onset of the combustion reaction?*

3.1 Overview of Material Systems

Various factors, including powder compact density, microstructure, mechanical properties, and impact velocity, affect the dynamic densification and deformation of aluminum powder compacts during uniaxial stress loading. In order to isolate the factors and processes that control the threshold conditions for initiation of the combustion reaction, the following two

Figure 26: Schematic of uniaxial stress rod-on-anvil impact experiment.

starting material types were investigated: aluminum powder of a range of particle sizes and aluminum powders prepared by mechanical pre-activation.

3.1.1 Aluminum Powders of a Range of Particle Sizes

The role of particle size was investigated through experiments performed on commercially available spherical aluminum powders of various sizes. Aluminum particles, ranging in diameter from hundreds of nanometers to over one hundred microns were purchased through the company Valimet [127]. The Valimet powders are prepared by the process of inert gas atomization to obtain smooth, spherical particles. As a result of their processing conditions, the aluminum powders contain a maximum of 0.1% by weight volatiles, 0.2% by weight oil and grease, and 0.2% by weight iron [127]. Figure 27 (a)-(d) displays SEM micrographs of 3.5 μm diameter powder (Valimet H-2), 8 μm diameter powder (Valimet H-5), 20 μm diameter powder (Valimet H-15), and 70 μm diameter powder (Valimet H-60), respectively. It can be seen from the SEM micrographs that all Al powders are near spherical and have a smooth surface.

3.1.2 Mechanically Pre-activated Aluminum Powders

The effect of mechanical pre-activation on the impact-initiation of a combustion reaction of aluminum powder compacts was studied by examining the powders that had been mechanically pre-activated by either high energy ball-milling (HEBM) or by high strain machining.

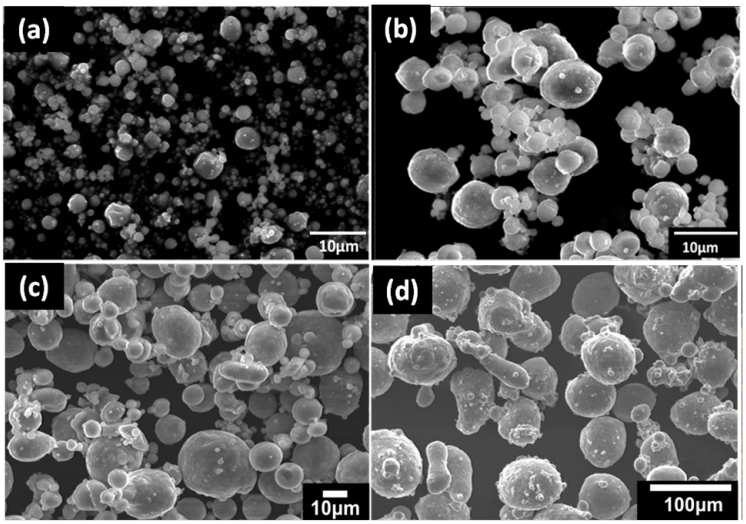

Figure 27: SEM images of Valimet H-series aluminum powders: (a) H-2, (b) H-5, (c) H-15, and (d) H-60 aluminum.

The HEBM powders were prepared by loading 5 g of Valimet H-60 aluminum powder along with five, 6.3 mm diameter alumina balls in an alumina vial. The powders were loaded into the vials in a glove box purged with argon to ensure that the sample was not exposed to atmospheric moisture or oxygen. Contact with moisture or oxygen can result in the initiation of a self propagating reaction during the ball milling process. The alumina seals on the vial were reinforced with electric tape prior to removal from the glove box. The samples were transferred to a SPEX mill and ball milled for 10 minutes, 30 minutes, and 60 minutes. Milling causes the spherical aluminum powders to go through the processes of fracture, plastic deformation, and cold welding as observed in the SEM micrographs shown in Figure 28 (a) - (c). It can be seen that as ball milling time increases, the resulting particles become more flattened or flake-like.

The other mechanically pre-activated powder type, highly strained aluminum 6061 chips, was prepared using a plane-strain machining method developed by Shankar *et. al.* [75, 76] . As described in Section 2.2.6, plane strain machining is performed by a cutting tool that moves perpendicular to its cutting edge across a bulk material and removes a specific depth of the bulk material. The angle of the tool introduces large uniform shear strains

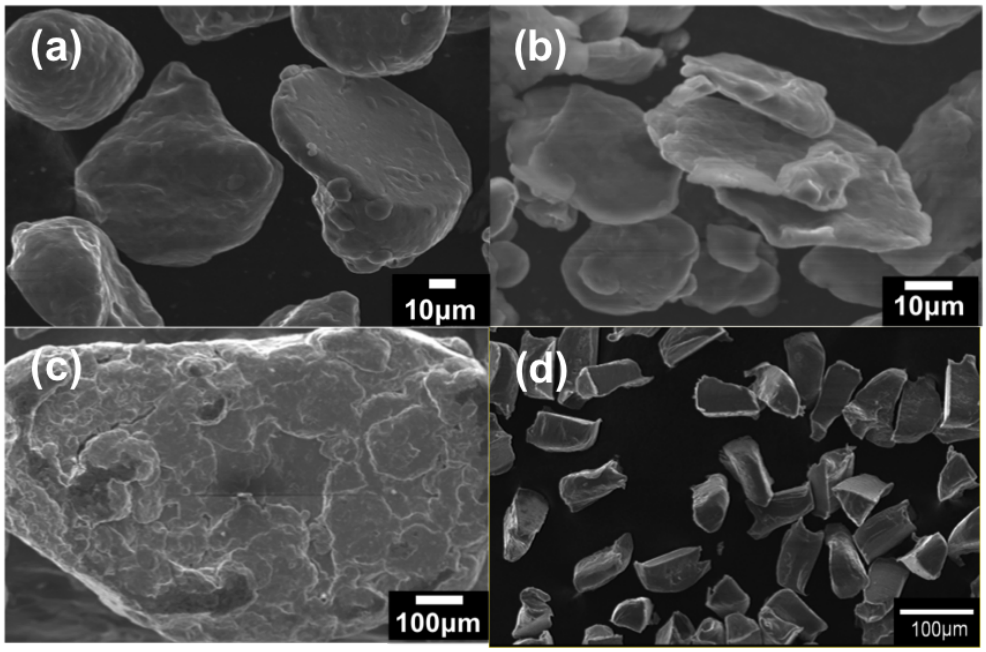

Figure 28: SEM images of mechanically pre-activated aluminum. Valimet H-60 following 10 minutes (a), 30 minutes (b), and 60 minutes (c) of ball milling. Ultra fine grain aluminum platelets prepared by high strain machining (d).

($>>1$) to a very narrow deformation zone in the bulk material and results in the formation of chips of ultra-fine grain (UFG) size. UFG chips can be prepared by using only one pass of the tool at a sufficiently slow velocity (10 mm/s), which serves to control the temperature during chip formation. The resulting highly strained aluminum chips shown in the SEM micrograph in Figure 28 (d) contain ultrafine grains that strengthen the Al6061 and are approximately 80 μm x 80 μm x 30 μm in size, giving them a platelet shape.

3.2 Microstructural Characteristics of Starting Powders

A measure of the powder size alone does not thoroughly characterize the microstructure of any given powder type. Therefore, detailed analysis of the microstructural characteristics, including particle size distribution, surface area to volume ratio, and specific surface area was performed for each system to clearly delineate the differences between the two types of starting materials.

3.2.1 Particle Size Distribution

An accurate measure of the particle size distribution for all samples was gained using either the Saltykov analysis [128] or sieve analysis [129]. In order to obtain the particle size distribution by the Saltykov Analysis, the starting powders were mounted in epoxy and sectioned through the thickness. The cross-section was ground, polished, and imaged using the light microscope. The largest, heaviest particles typically have a tendency to settle at the bottom of the epoxy puck, while the smaller, lighter particles remain suspended towards the mid-section of the epoxy. Imaging the cross-section captured all of these particles, as shown in Figure 29 (a) - (d). Images of greater than 100 particles were converted into a binary image, imported into Matlab as shown in Figure 29 (e) - (h), and analyzed using the Schwartz-Saltykov method [130].

Particle size measurements made using the Schwartz-Saltykov method were based on the measured diameters of spherical particles in the 2D cross-section [128]. Once the particle diameters were measured, the particle sizes were divided into k groups of particles, each group spanning a size interval of Δ. The number of groups of particles, k, indicates the number of bars on the histogram. Using the relationship between k and Δ, the diameter for the largest particles can be given as,

$$D_{max} = k\Delta \tag{20}$$

allowing the smallest group's diameter to be defined as Δ, and the second group to be defined as 2Δ. In order to define the number of particles per unit area, N_A, in a group j (the group number for the section on that plane of polish), Saltykov [128] noted that a group is made up of contributions of particles with diameters from higher groups in addition to that group alone. Next, the number of particles per unit area N_A are related to the number of particles per unit volume N_V, by Saltykov's basic equation [128],

$$N_A(i,j) = N_V(j)\Delta(\sqrt{(j^2-(i-1)^2)} - \sqrt{(j^2-i^2)}) \tag{21}$$

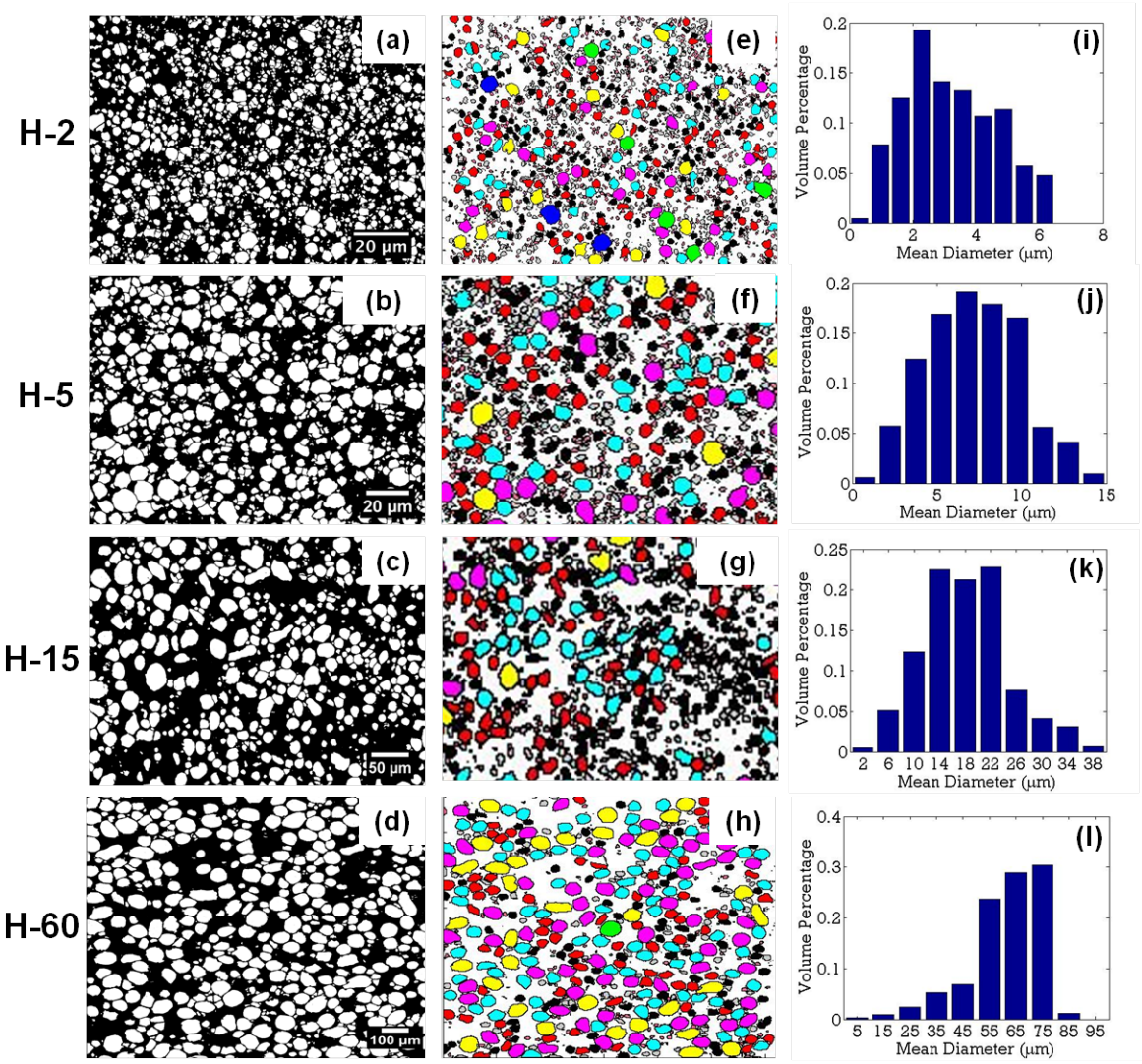

Figure 29: Obtaining particle size distribution by the Saltykov method in Matlab. Micrographs were converted to binary images (a-d). The images were processed using the Salktykov analysis in Matlab and a particle map (e-h) and histogram (i-l) were generated for each as-received particle type.

where *i* refers to the size groups of a section. This general relationship can be used for any number of groups and can be extended to obtain the particle size distribution for ellipsoids.

Figure 29 (e) - (h) shows the particle map produced by the Saltykov analysis performed on all H-series Valimet aluminum particles, H-2 (e), H-5 (f), H-15 (g), and H-60 (h). The particle size distribution was divided into k=10 groups for each powder type. The histogram for each powder type plotted in Figure 29 (i) - (l), shows a normal particle size distribution for each of the Valimet H-series powders. The particle size distribution was replotted with respect to the largest particle, H-60, as shown in Figure 30 (a). Of the H-2, H-5, H-15, the H-60 samples examined, H-60, which contained the largest particles, was characterized by the widest particle size distribution with particle sizes ranging from 31 μm to 82 μm and centered at approximately 67 μm. The H-2, H-5, and H-15 aluminum powders contained particles less than 35 μm in diameter and were characterized by a narrower particle size distribution. The average particle diameters centered around distinctly different values, 4 μm, 13 μm, and 18 μm, respectively, for the H-2, H-5, and H-15 aluminum powders.

High energy ball milling resulted in powders that were irregularly shaped and could not by analyzed by the Schartz-Saltykov method. Therefore, particle sieving was used to obtain an accurate particle size distribution [129]. The sieves (3" diameter) were arranged in ascending order ending with the largest on top, and the aluminum powder (5.0 g) was loaded into the uppermost sieve. The assembly was placed in the sieve shaker and shaken for fifteen minutes. Powders were removed from each sieve and weighed individually to obtain a mass fraction for each sieve.

Figure 30 (b) illustrates that the observed particle size distribution of H-60 changed as ball milling time increased, following trends consistent with processing by ball milling, which causes fracture and cold-welding. When analyzed by sieving, the as-received H-60 particle diameter ranged in size from less than 45 μm to less than 90 μm, consistent with the Saltykov analysis of H-60. Upon ball milling for ten minutes, the particles fractured and plastically deformed, to produce 4.5% by mass additional particles with a diameter of

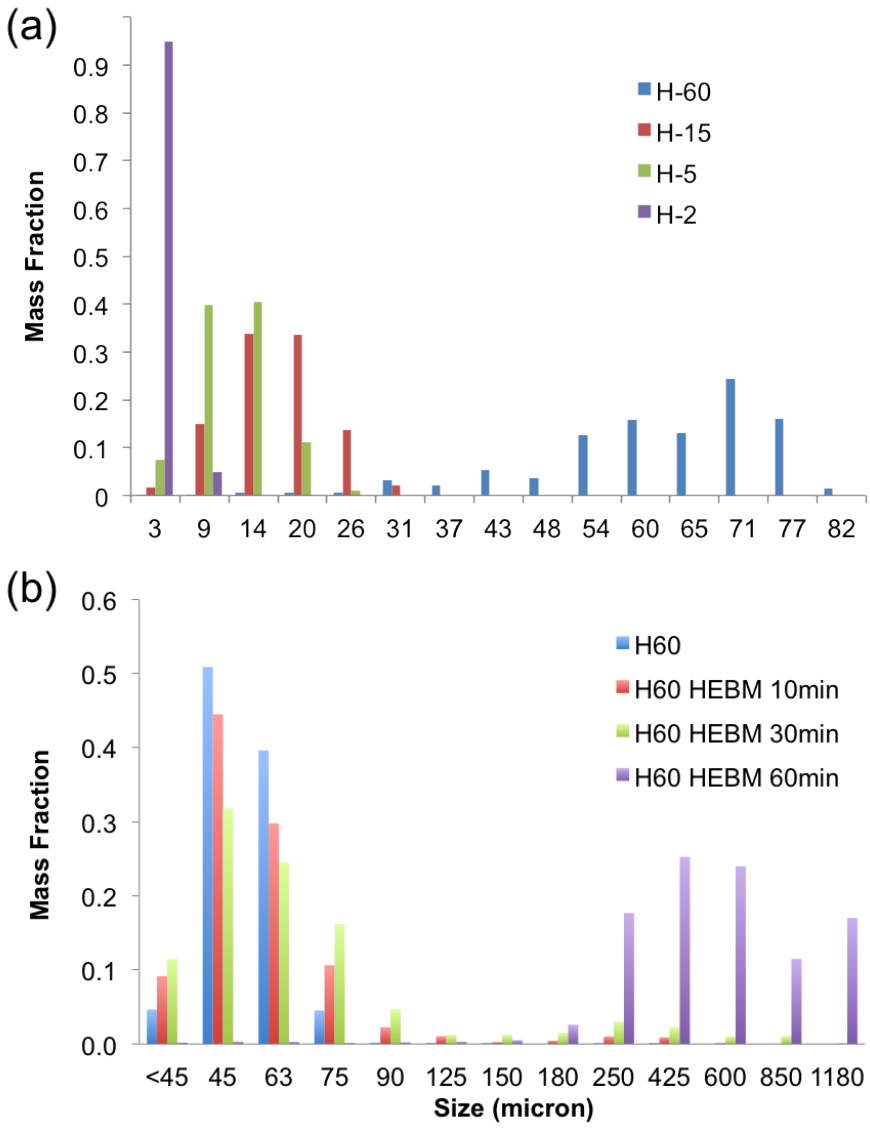

Figure 30: Particle size distribution for Valimet particles of different sizes(a) and for H-60 high energy ball milled samples (b).

less than 45 μm. Additionally, after ten minutes of ball milling, a small fraction of the H-60 particles were observed to cold weld, resulting in 3.7% by mass of particles ranging from 90 μm to 425 μm in size. As ball milling was continued for 30 minutes total, particles continued to fracture, deform, and cold weld together, creating a broader, almost bimodal distribution of particle sizes with 10.3% by mass of the particles centered at a diameter of 250 μm and the remaining 90% of the particles centered at a diameter of approximately 60 μm. Finally, with a ball milling time of 60 minutes, the particles cold weld together, to create a particle size distribution ranging from 180 μm to greater than 1mm and centered at approximately 500 μm.

3.2.2 Surface Area of Powders

The surface area per unit volume (S_v) of each powder type was measured using an intersection counting method [128]. Powder compacts of approximately 90% TMD were prepared for each powder type, mounted in epoxy, and sectioned vertically. The cross-section was polished and etched in Keller's reagent for approximately 20 seconds. A montaged image of each sample was captured on the Leica DM IRM microscope, and a set of 48 cycloid-shaped test lines were superimposed on each image, with the minor axis of the cycloid parallel to the vertical axis. The average number of intersections between the cycloid and the microstructural boundaries per unit of the cycloid length, P_L, were counted for each sample. The P_L value is related to the S_v through the equation [128],

$$S_v = 2\overline{P_L} \tag{22}$$

Only one sectioning plane was necessary to reliably measure the system because the compacts were axially pressed and the vertical axis is also the axis of symmetry. The use of a cycloid-shaped line allowed for features at all orientation angles from the vertical plane to be probed [131].

Table 1 shows that as expected the smallest diameter particles, H-2, have the highest

Table 1: Surface area per unit volume values for aluminum compacts and specific surface area values for aluminum powders.

Powder Type	$S_v(\frac{1}{mm})$	Specific Surface Area ($\frac{m^2}{g}$)
H-2	1885.7 ± 3.08	2.63
H-5	824.3 ± 11.15	2.58
H-15	441.9 ± 0.42	0.35
H-60	105.7 ± 0.29	0.10
H-60 HEBM 10 minutes	108.3 ± 0.10	0.38
H-60 HEBM 30 minutes	166.9 ± 0.15	0.40
H-60 HEBM 60 minutes	237.5 ± 0.39	0.28
Highly strained aluminum	196.2 ± 0.19	NA

S_v, while the largest particles have the lowest S_v. However, as the H-60 particles are ball-milled, their S_v increases with ball milling time, consistent with increased fracture and deformation due to ball milling undergone by the as-received H-60 particles over time. The highly strained aluminum platelets had an S_v of 196.2 mm^{-1}, which is a higher S_v than the H-60 and H-60 HEBM 10 minute and 30 minutes samples, but a lower S_v than the H-60 samples that had been ball milled for 60 minutes.

Specific surface area (SSA) measurements were made using the Brunauer-Emmett-Teller (BET) method. The BET method is an extension of Langmuir theory and is based on gas adsorption onto a solid surface [132]. By analyzing the amount of gas adsorbed onto a surface, the amount of surface area per unit mass or the specific surface area (SSA) of a material can be found. The SSA provides an additional way of analyzing the amount of surfaces available for reaction in each sample.

In order to collect BET data, approximately 2.0 grams of starting powder was loaded into a glass cell, degassed under nitrogen, and heated to 300°C overnight. Once the sample was degassed, the cell was loaded into a Micromeritics Tristar II BET to undergo the absorption and desorption process in the presence of nitrogen. Each sample was measured two times.

As shown in Table 1, the smallest particles, H-2 and H-5, have the highest SSA. As the

particle size increases, SSA decreases. Fracture and deformation during ball milling for 10 minutes and 30 minutes result in an increase in SSA from the original H-60. After 60 minutes of ball milling, cold-welding of the particles results in a decrease in SSA. There was not enough sample available to conduct BET analysis of the highly strained aluminum platelet samples.

3.3 Mechanical Properties of Starting Powders

The mechanical properties of the starting powders effect the compaction and deformation response of the samples during uniaxial stress loading, which in turn determines their subsequent reactivity. Materials of higher strength can require more energy input for the compaction and deformation processes, leaving less energy available for reaction initiation. In order to further understand the mechanisms controlling reactivity, the mechanical properties of the various starting powders and their compacts were determined, as influenced by their inherent strength, lattice strain, and compaction behavior.

The strength or flow stress at which the various aluminum powder particles undergo plastic deformation in the process of compaction was approximated based on the hardness of the aluminum particles, using Tabor's Rule [133]. According to Tabor's approximation, the Vicker's hardness can be related to the yield strength by the relationship, HV=3*σ_Y [133]. Hence, the Vickers Hardness value (HV) was obtained for the as-received H-60 aluminum powders, high energy ball milled powders, and the highly strained aluminum platelets, which were mounted in epoxy, ground, and polished prior to hardness testing. At least ten individual aluminum particles of each powder type were indented using a Leco MHT Series 200 hardness tester with a Vickers tip at a load of 10 gmf to calculate the microhardness value provided in Table 2. Less than 50% of the entire particle was indented to ensure that the indenter did not pass completely through the particle. The H-60 aluminum powders became more strain-hardened and their hardness values increased, as ball milling time increased. The highly strained aluminum platelets had the highest hardness value of

128.3HV as a result of their ultra fine grain structure.

The diameter of the Valimet H-2, H-5, and H-15 aluminum particles is smaller than the indenter tip; hence, their hardness value could not be determined. Instead, the Hall-Petch relationship [134, 135], given in Equation 23, was used to approximate the yield strength for these powders, which were prepared by the same method as the Valimet H-60. The Hall-Petch relationship is based on the assumption that as particle size or grain size decreases, dislocations become more difficult to propagate through the grain and will pile up at the grain boundaries, requiring higher stresses to pass through the grain boundary, thereby increasing the strength of the material. The strength approximated using the Hall-Petch relationship, is given by:

$$\sigma_Y = \sigma_0 + \frac{k_y}{\sqrt{d}} \tag{23}$$

where σ_0 is the material constant for the inherent yield strength of the material without considering grain size strengthening effects, k_y is the Hall-Petch strengthening coefficient, and *d* is the average grain diameter. For aluminum, the strengthening coefficient was assumed to be 0.04 MPa*m$^{-0.5}$ [136]. The value for σ_0 was calculated from the measurements of H-60. The HV for H-60 was 42.3 kg/mm^2, giving a σ_Y of 14.1 MPa for H-60 by Tabor's Rule. The average diameter of the H-60 particles from the Saltykov Analysis was 67 μm. As a result, the Hall-Petch relationship gave a σ_0 = 9.21 MPa for as-received H-60 aluminum particles, which is commensurate with reported literature values for pure aluminum [136]. Using this value, the Hall-Petch relationship was used to roughly approximate the yield strength for the H-2, H-5, H-15 particles, which were found to be 29.2 MPa, 20.3 MPa, and 18.6 MPa, respectively.

X-ray diffraction (XRD) line broadening analysis was also performed on all mechanically pre-activated aluminum powders to deduce the degree of retained elastic strain and thereby infer the extent of strain hardening due to dislocation density increase. Mechanical pre-activation may lead to retained microstrain as well as reduction in crystallite size. These effects can be quantified by performing the Williamson-Hall analysis [137] on XRD

Table 2: Vickers hardness values and yield strength of all aluminum powder particles.

Powder Type	Vicker's Hardness Value (kg/mm^2)	Yield Strength (MPa)
H-2	n/a	29.2
H-5	n/a	20.3
H-15	n/a	18.6
H-60	42.3 ± 2.6	14.1
H-60 HEBM 10 minutes	39.5 ± 6.1	13.2
H-60 HEBM 30 minutes	47.2 ± 5.4	15.7
H-60 HEBM 60 minutes	64.0 ± 4.7	21.3
Highly Strained Platelets	128.3 ± 14.0	42.7

traces obtained from various samples.

XRD line broadening can also result from a combination of both specimen imperfections and experimental imprecision. Negligible instrumental peak broadening was measured, requiring no corrections. Hence, broadening due to the sample (B_m) was assumed to be equal to the overall broadening (B_o), quantified by the full width half max (FWHM) of the XRD peaks. Broadening due to crystallite size, B_c, was determined using the equation,

$$B_c = \frac{k\lambda}{(L\cos\theta)} \tag{24}$$

where, L is crystallite size, θ is the diffraction angle, and λ is the wavelength of the incident x-rays. The parameter, k, is a constant, dependent on particle shape and peak broadening measurement method. Broadening due to lattice strain (B_s) was determined using,

$$B_s = \eta\tan\theta \tag{25}$$

where, η is the lattice strain. The overall broadening, B_m, was assumed to be the sum of broadening due to crystallite size, B_c, and the broadening due to lattice strain, B_s. Hence,

$$B_m = B_c + B_s \tag{26}$$

or,

$$B_m = \frac{k\lambda}{L\cos\theta} + \eta\tan\theta \tag{27}$$

Table 3: Lattice strain values for mechanically pre-activated aluminum powders.

Powder Type	Lattice Strain (η)
H-60	n/a
H-60 HEBM 10 minutes	0.0013
H-60 HEBM 30 minutes	0.0006
H-60 HEBM 60 minutes	0.0005
Highly Strained Platelets	0.0049

or,

$$B_m \cos\theta = \frac{k\lambda}{L} + \eta \sin\theta \tag{28}$$

A Williamson-Hall plot of $B_m\cos\theta$ versus $\sin\theta$, exhibits the linear relationship, with the slope related to the lattice strain and intercept to the crystallite size.

XRD analysis was performed on aluminum powders placed into a backloading sample holder and pressed with a glass slide until flat. The Panalytical X'Pert PRO Alpha-1 XRD machine with Cu-Kα_1 radiation and a solid state X'Celerator detector was used to obtain X-ray patterns. All H-series Valimet powder samples were analyzed by XRD and almost identical signatures were observed. Figure 31 (a) shows an example of a typical XRD trace obtained for the aluminum powder.

Line broadening was observed in the XRD peaks for the high energy ball milled H-60 aluminum and for the highly strained aluminum platelets as shown by the typical trace in Figure 31 (b). The full width half max value was calculated using the XRD processing software Jade 9, and the Williamson-Hall analysis was performed using H-60 as a baseline to account for instrumental broadening. As shown in Figure 32, the Williamson-Hall analysis for the HEBM samples gave a shallow slope and, hence, negligible lattice strain, while the slope for the highly strained Al platelets was higher. Actual lattice strain values are listed in Table 3. The lattice strain obtained from the Williamson-Hall plot for the highly strained aluminum platelets is 0.0049 which is markedly higher than that for the high energy ball milled samples.

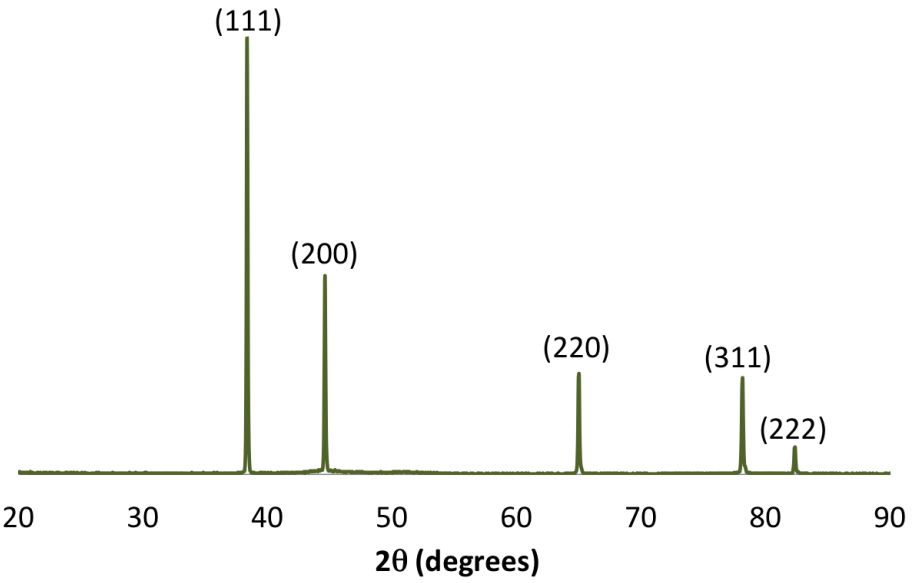

Figure 31: X-ray trace typical of Valimet H-series aluminum powder samples.

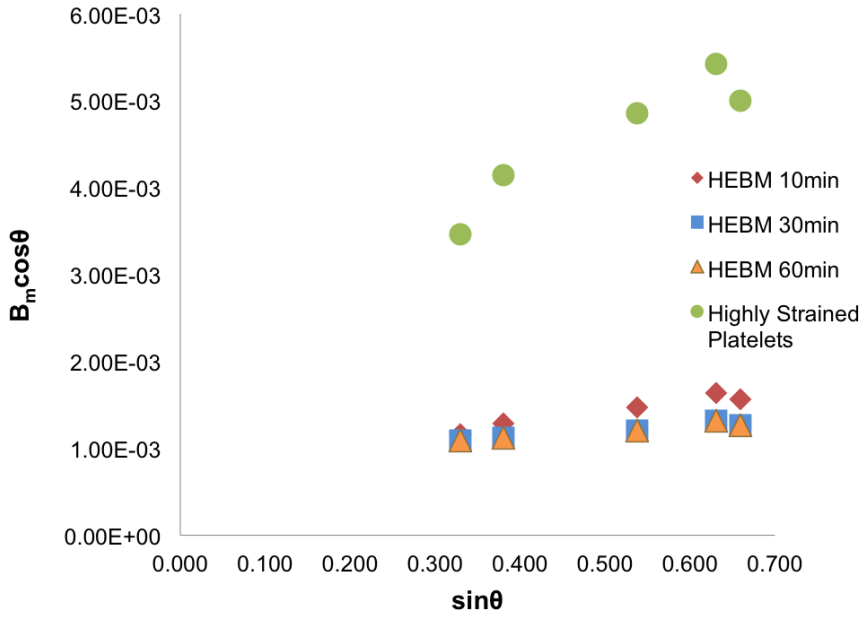

Figure 32: Williamson-Hall plot of HEBM and highly strained platelet samples.

3.4 Compaction Behavior of Aluminum Powders

The work of Fischmeister and Artz [79], summarized in *Section 2.3.1*, illustrates that the compaction behavior of a powder is a function of the initial compact density, the powder particle morphology, and the mechanical properties of the components. Compaction curves were obtained experimentally by loading approximately 1.2 g of each powder type into a 12.7 mm diameter cylindrical die and quasi-statically compressing the powder, using an MTI Instrument as shown in Figure 33. As the force was sequentially increased to loads up to a maximum of 700 MPa, the displacement was measured *in situ* via an Accupro Gold depth gauge, with a sensitivity of .025 mm. An error of $\pm$.0063 mm was assumed to account for human error in reading the gauge and variations at each pressure.

The compaction curve as a plot of the applied force versus %TMD for each of the different aluminum powder types is shown in Figures 34-35, . The compact density of all powder particles increases as applied force is increased. Figure 34 shows that the smallest, H-2 particles, require the highest applied force throughout the compaction process, while the largest, H-60, particles require less applied force to achieve the same densities as H-2 particles. As the particle size increases, an abrupt change in the slope at $\sim$86% TMD becomes apparent in the compaction curve as less pathways become available for voids to be filled. The compaction curve for the HEBM powders, given in Figure 35, shows that all HEBM powders required greater applied force than that needed to compact the as-received H-60 powder, up to a compact density of $\sim$93%. After this point, HEBM 30 minute and HEBM 60 minute powders become less difficult to compact to 100% TMD. Again, an abrupt change in slope is observed at $\sim$86% TMD.

Each powder compaction curve was fitted to a quartic function with a R^2 fit of greater than 0.99. Figure 36 shows how the quartic function was extrapolated to 100% TMD to obtain the effective yield stress of each powder. Additionally, the quartic function was integrated from 92% to 100% TMD, the region where constrained deformation occurs, to obtain the energy of compaction in that region. Table 4 provides the calculated effective

Figure 33: Photograph of the setup used to collect compaction data. Powder were pressed in the die at increasing loads and the punch displacement was measured by the depth gauge.

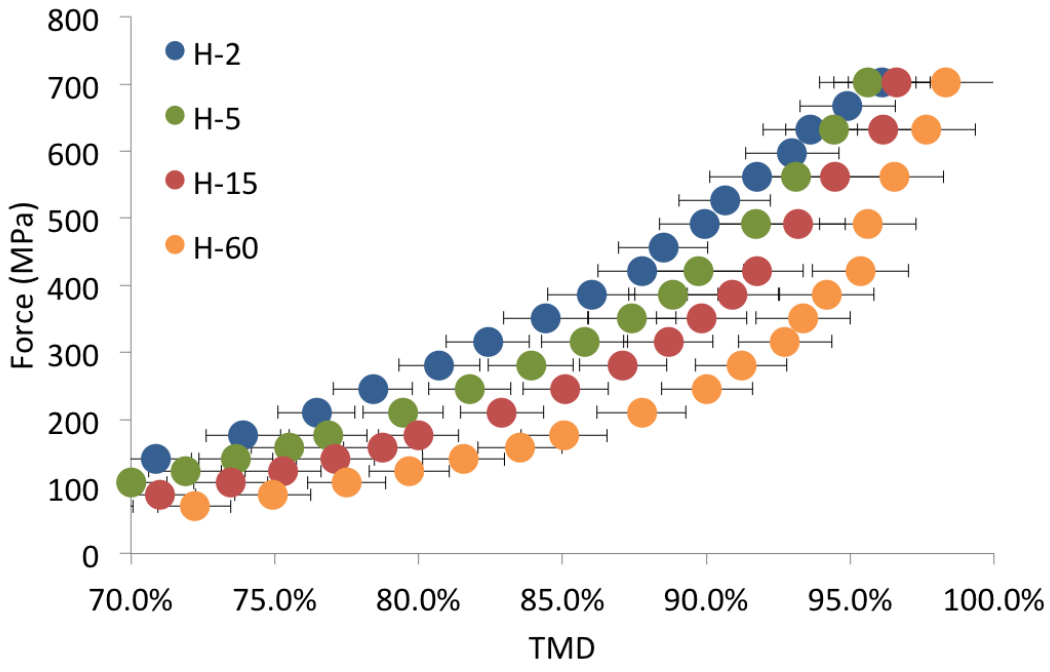

Figure 34: Quasi-static compaction curves for H-2, H-5, H-15, and H-60

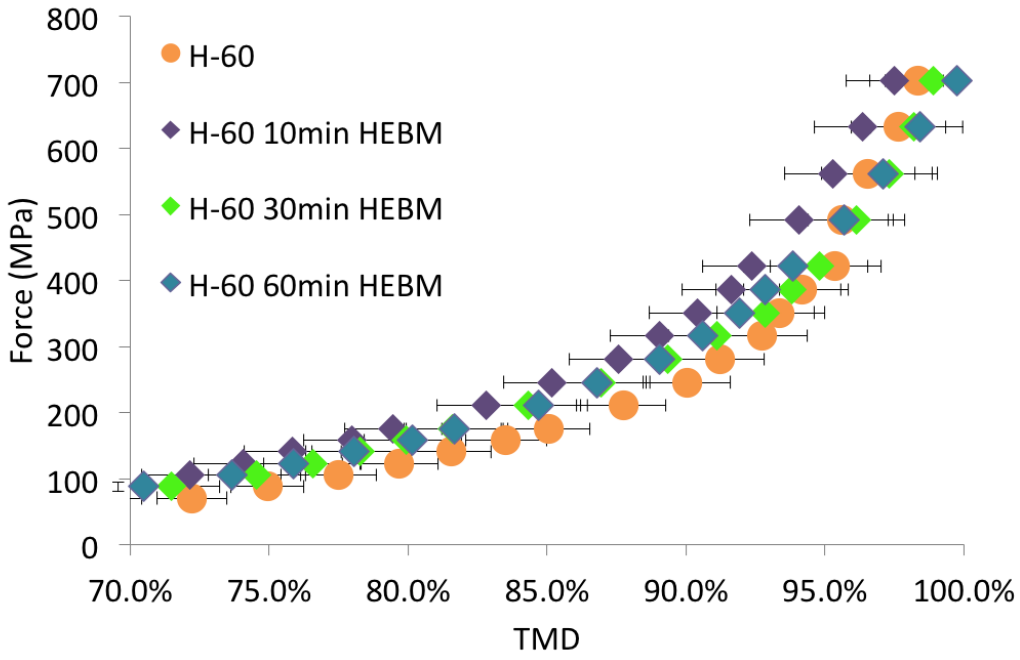

Figure 35: Quasi-static compaction curves for H-60, H-60 10min HEBM, H-60 30min HEBM, and H-60 60min HEBM aluminum.

yield stress and the compaction energy for each powder type. The H-5 powders required the highest pressure for compaction, 1044 MPa, and the highest compaction energy, 26.1 J. Not including the H-2 samples, the compaction pressure and energy required to achieve 100% TMD decreased as powder size increased. The HEBM 10 minute sample required higher compaction pressures and energies than the H-60 powders. However, as the ball milling time was increased to 30 and then to 60 minutes, the energy and pressure required for compaction of samples decreased.

The Meyers approximation [81], described in detail in Section 2.3.1.1, was used to obtain the instantaneous flow stress, σ_Y, or contact pressure at each particle contact point for each data point in the compaction curve. The values of the instantaneous flow stress for each particle type at each point during the compaction process are plotted as a function of density in Figure 37. The instantaneous flow stress provides a measure of how resistant each particle is to compaction. It can be seen that the smallest, H-2, particles are the most

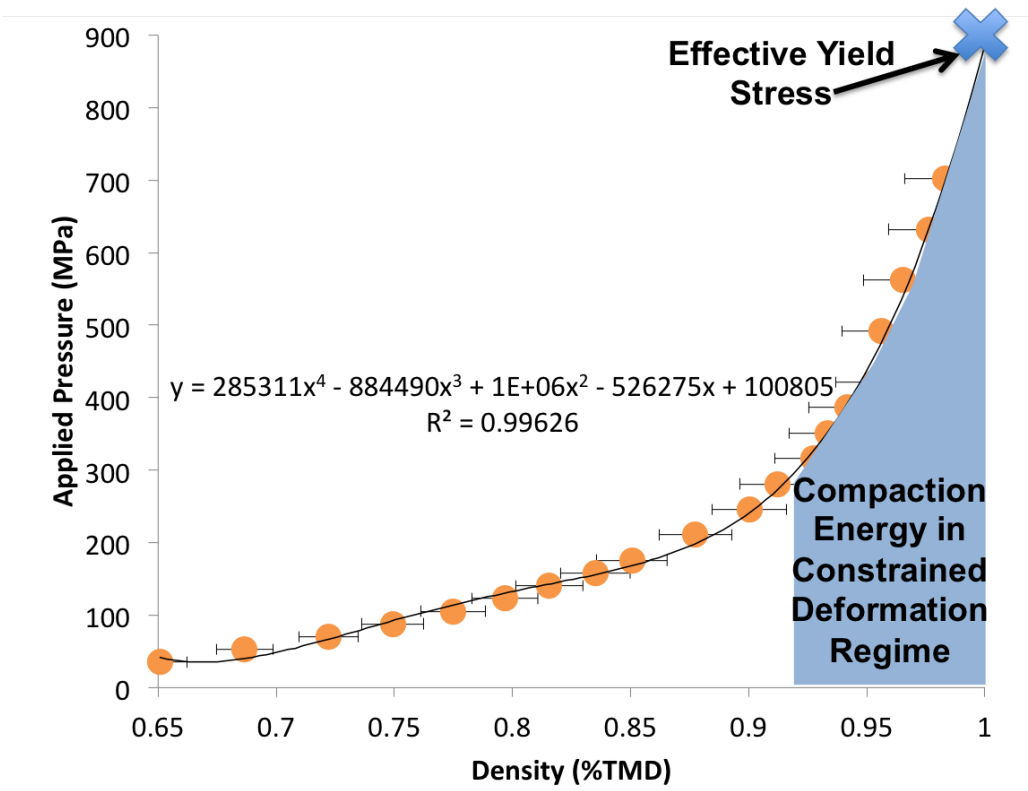

Figure 36: The compaction curve for the H-60 powder fit to a quartic function. The "x" indicates the value for the effective yield strength of each powder, and the area under the curve gives the energy of compaction.

Table 4: Mechanical properties calculated from the compaction curve.

Powder Type	Effective Yield Stress (MPa)	Compaction Energy (J)
H-2	884.1	25.4
H-5	1044	26.1
H-15	981	23.7
H-60	891	19.1
H-60 HEBM 10 minutes	916	22.2
H-60 HEBM 30 minutes	776	18.2
H-60 HEBM 60 minutes	724	18.6

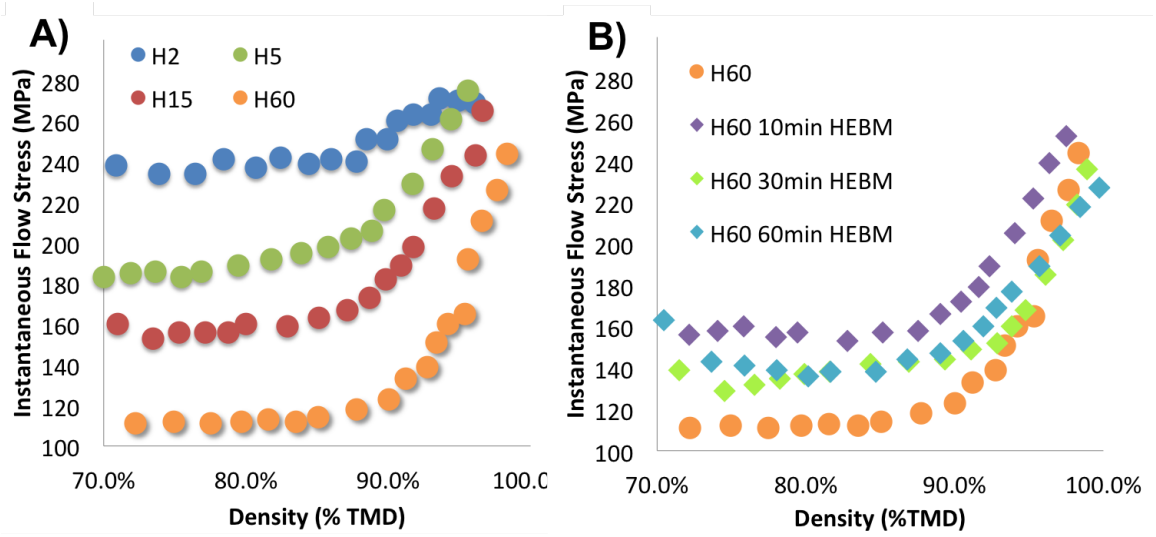

Figure 37: The instantaneous flow stress at each point during compaction for each particle. (a) Instantaneous flow stress values for particles of different sizes. (b) Instantaneous flow stress values for particles that had been mechanically pre-activated.

resistant to compaction, having the highest instantaneous flow stress values. As particle size increases, the instantaneous flow stress decreases, allowing the largest particles, H-60 to be compacted the most easily. Mechanical activation of H-60 aluminum powder by HEBM resulted in higher instantaneous flow stress.

3.5 Experimental Setup

3.5.1 Powder Compact Preparation

Rod-on-anvil impact experiments require that the aluminum starting powder take the form of a quasi-statically compressed cylindrical compact as illustrated in Figure 38 (a). The powders were placed in a 3.19 mm die and pressed at 2400 lb in an automated Carver press to yield powder compacts that were 3.19 $\pm$ 0.2 mm diameter by 2.0 $\pm$ 0.2 mm high and ranging in density from 80% to 99.8% TMD. In some cases, when lower densities (80% to 90%) were desired, a set of several washers was placed on top of the die and around the punch as the sample was undergoing the pressing process to stop the punch at the desired

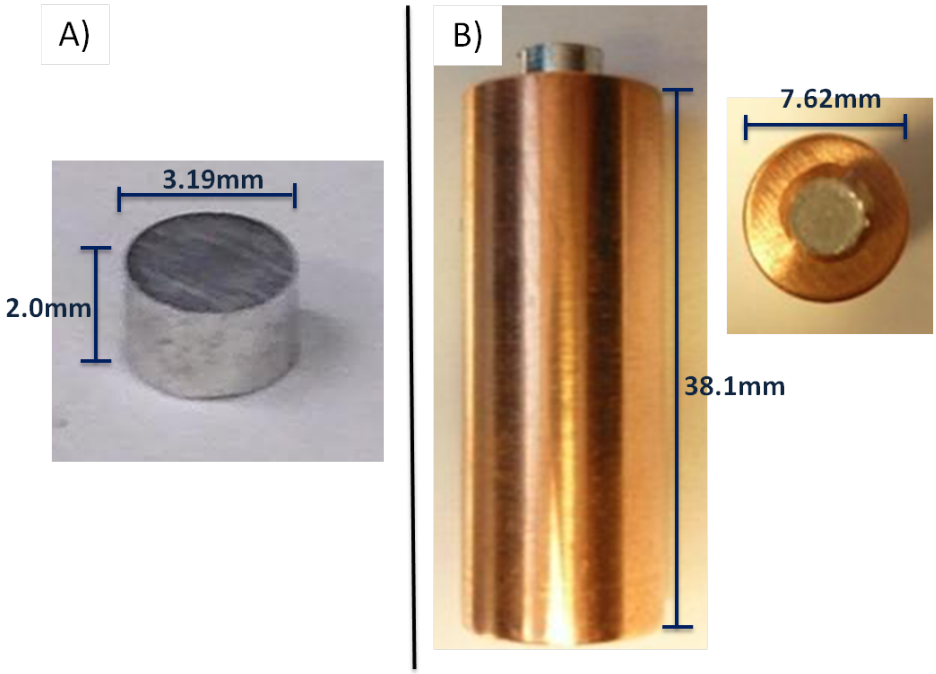

Figure 38: Images of H-2 powder compact (A) and powder compact mounted on a copper projectile (B).

height of approximately 2.0 mm. Once pressed, measured, and weighed, the powder compacts were adhered to a copper projectile (7.62 mm diameter by 38.1 mm high) with a 24 hour thin film epoxy. Figure 38 (b) illustrates a photograph of the aluminum compacted material on the copper projectile. Prior to adhesion, all copper projectiles were lapped and thoroughly cleaned by sonication with the following series of solvents: methanol, soapy water, methanol, and acetone. The compact-copper assembly was placed under a weight for 24 hours to ensure good bonding and planarity. The final samples were weighed and stored in small ziplock bags prior to performing the impact experiments.

3.5.2 Uniaxial Stress Rod-on-Anvil Impact Experiments

The aluminum powder compacts mounted on the copper rods were impacted against a hardened steel anvil (588.9±6.6 HV) using the 7.62 mm gas gun at Georgia Tech pictured in Figure 39. The rod-on-anvil impact subjects the samples to uniaxial stress loading conditions. Experiments were performed in air over a range of velocities, from 150 m/s to 480

Figure 39: Experiment chamber on 7.62 mm caliber gas gun and high speed framing camera used for visualization of events.

m/s, in order to determine the "threshold" impact velocity, defined as the minimum velocity necessary for reaction initiation. The velocity was adjusted by changing the pressure of helium gas that was allowed to build up in the valve-controlled chamber behind the projectile. The velocity was measured by laser beam interruption using two 635 nm lasers, each a well-defined distance from one another and perpendicularly aligned with the path of the projectile inside the chamber as illustrated schematically in Figure 40. The time needed for the projectile to cross the path between the first and second laser was measured using an up-down counter. The velocity measurement lasers were also used to trigger the IMACON 200 camera and other diagnostics to begin capturing images as the projectile impacts the anvil. The error in the distance measurements between the lasers and anvil results in an uncertainty of approximately 1 μs.

The IMACON 200 high-speed framing camera can capture 16 frames at 200 million frames per second and 50 ns inter-frame times. It was outfitted with a 135 mm Nikon lens to capture the densification and deformation process upon impact of the compacts against the anvil. The IMACON 200 camera also captured the emission of light. The observation of the captured light in more than one consecutive frame was used as an indicator of the occurrence of an impact-initiated combustion reaction of aluminum. Lighting present either during compaction of the powder, during deformation of the compacted powder as the sabot impacted the anvil, or several microseconds following complete deformation was

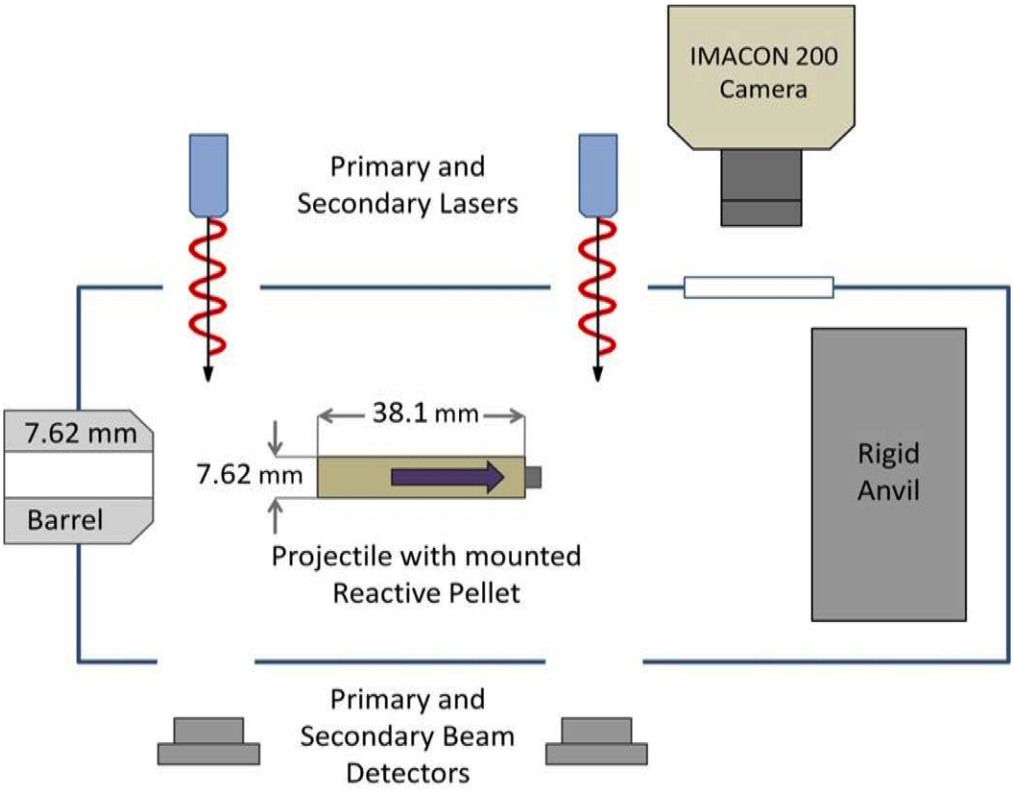

Figure 40: Schematic of uniaxial-stress rod-on-anvil experiments

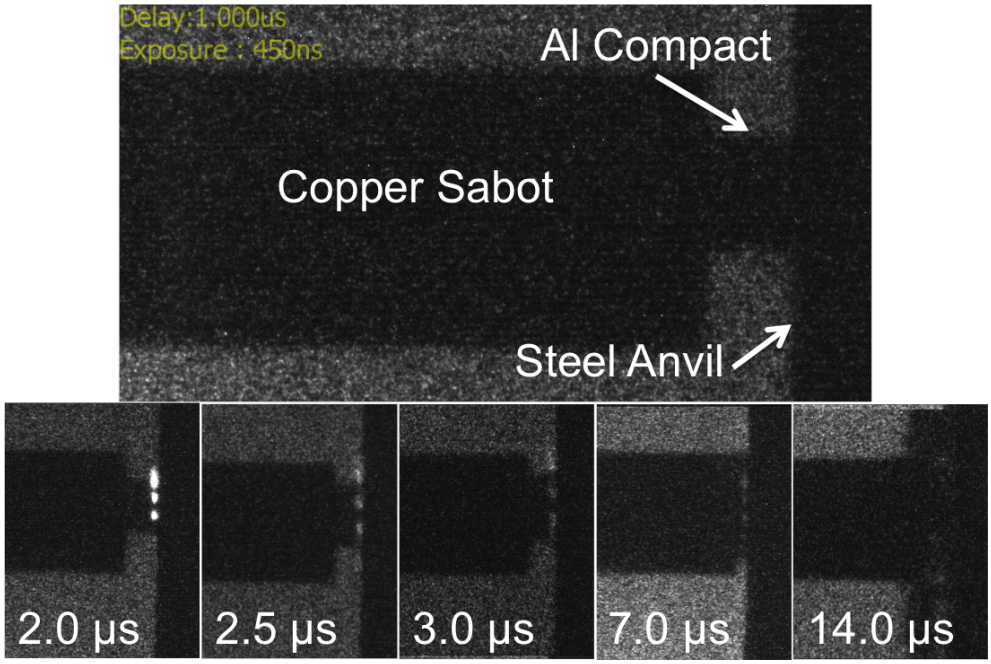

Figure 41: High-speed images of a highly strained platelet aluminum powder compact affixed to a copper projectile impacting a hardened steel anvil at 222 m/s. The first image shows the fixture at the initial moment of impact. The image at 2.0 μs shows the compact emitting light during compaction. The images at 2.5 and 3.0 μs show emission during deformation. The image at 7.0 μs shows light emission during the sabot-anvil impact. The image at 14.0 μs shows light emission after complete deformation of the compact.

considered to be indicative of the reaction. Figure 41 shows an example of light emission captured by the IMACON camera as a highly strained aluminum platelet powder compact impacts the anvil at 222 m/s in air.

The camera software, hardware, timing, and flash settings were standardized for all impact experiments when the occurrence of reaction was being evaluated. In order to maximize the detection limit of the camera, the gain was set to 10 (out of 11), and the f-stop on the software and the lens was set to 1.8 (out of 32). The flash level was set as low as possible, so as not to drown out any signal coming from the aluminum combustion reaction. The timing program was also standardized as outlined in Table 5 to collect signals for the longest exposure times possible and to capture all portions of the densification, deformation, and post-deformation processes.

Table 5: Timing schedule set on the Imacon camera to capture light emission from combustion

Frame Number	1	2	3	4	5	6	7	8
Start Time (μs)	0.5	1.0	1.5	2.0	2.5	3.0	3.5	4.0
Exposure Time (ns)	250	250	250	250	250	250	250	250
Frame Number	9	10	11	12	13	14	15	16
Start Time (μs)	5	6	7	8	10	12	15	18
Exposure Time (ns)	250	250	450	450	450	450	450	450

The impact velocity of the projectile provided the kinetic energy available for a possible reaction. The mass of each copper projectile and aluminum pellet sample did not vary much from one experiment to another. Therefore, the impact velocity (instead of the impact energies) can also be used as an indicator of the threshold conditions for reaction initiation.

The profile view of the impact of the projectile against the hardened steel anvil does not provide clear information about the reaction process. In order to examine the reaction initiation process spatially within the pellet, a transparent sapphire anvil was used in place of the hardened steel anvil [138]. As shown in the schematic of the sapphire anvil assembly, in Figure 42, a 1.00" diameter by 2.00" long sapphire rod (Meller Optics) was inserted into a UHMWPE sleeve. The sleeve and sapphire were pressed into a 4340 steel collar and attached to a 4340 steel support plate containing a UHMWPE ring with a 0.8" inner diameter. The steel collar and plate assemblies are attached to a large steel base containing a silver coated elliptical mirror placed at a 45 degree angle behind the sapphire anvil.

The mirror allows the front face of the sample to be reflected into the camera as shown in Figure 43 (a). Therefore, as a metal powder compact impacts the sapphire anvil, images of light emission at the front face of the metal powder compact can be captured to provide spatial information about the process of reaction initiation. Figure 43 (b) shows an example of the images captured. The incorporation of a sapphire viewing window into the PMMA window of the gun chamber also allowed IR images to be captured from the front face of the metal powder compact during compaction and deformation.

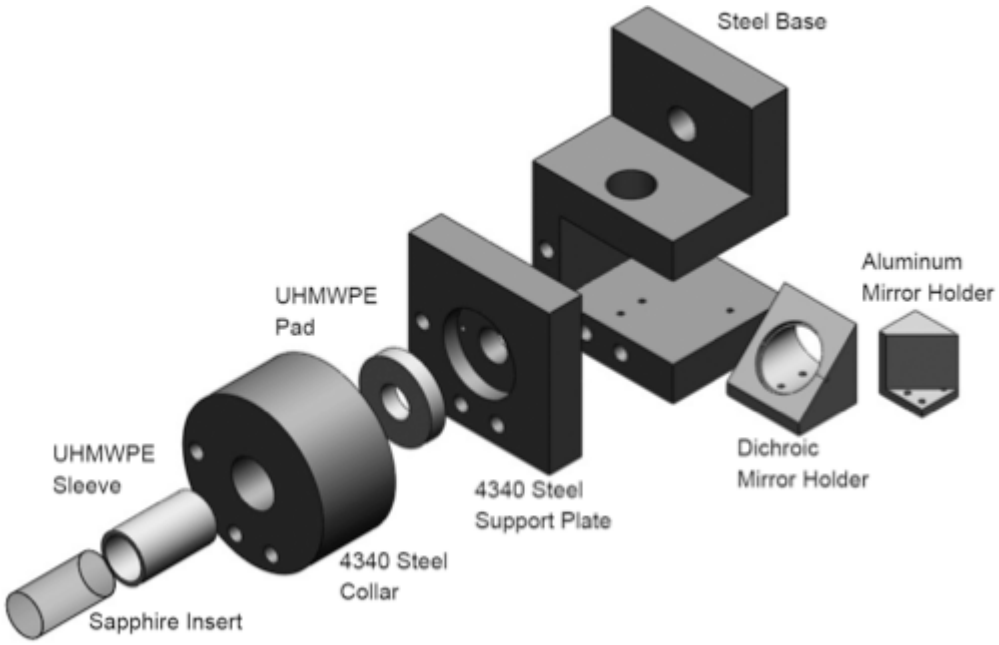

Figure 42: Schematic of the sapphire anvil assembly (from sapphire).

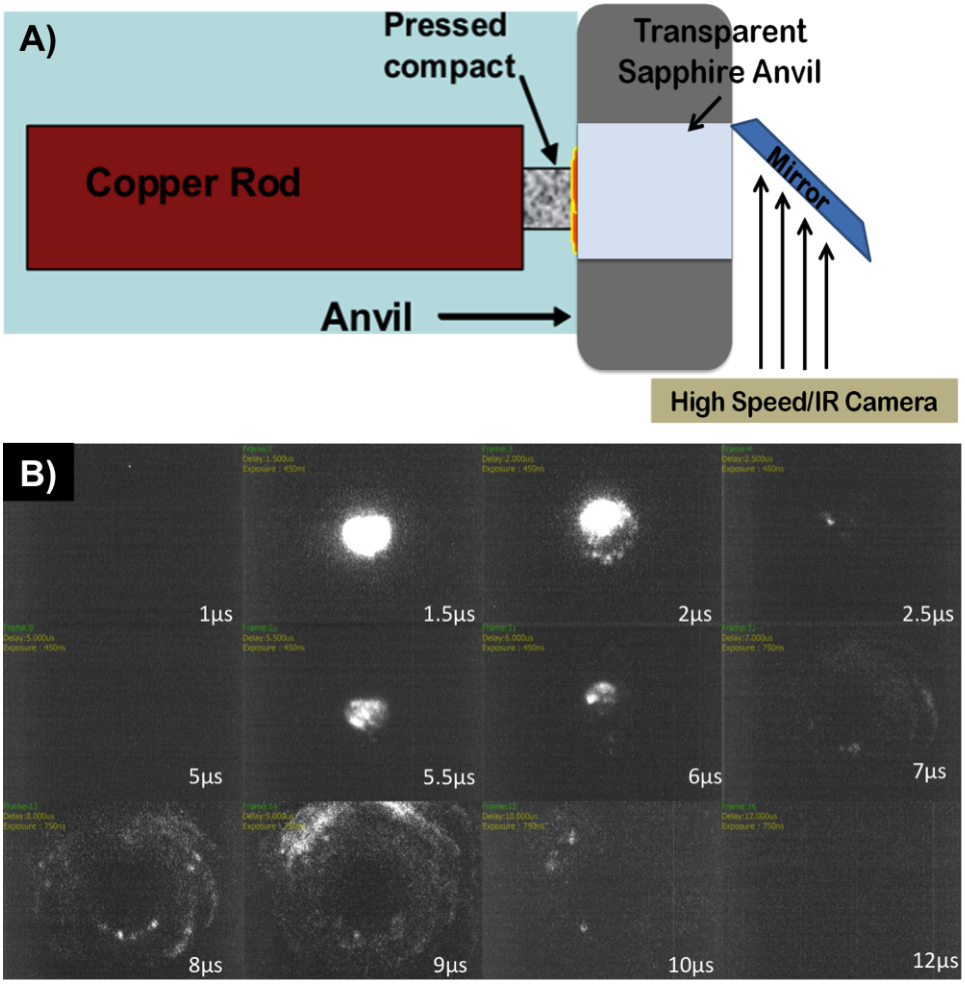

Figure 43: (a) Schematic of an impact experiment using the sapphire anvil. (b) Images collected from back face of anvil using the Imacon camera

Chapter IV

EXPERIMENTAL RESULTS OF IMPACT-INITIATED REACTIONS

In this chapter the results of the experiments performed to investigate the impact-initiated combustion of different types of aluminum powder compacts will be presented. One of the primary goals of this work is to determine the effects of starting aluminum powder characteristics on the initiation of reaction under uniaxial stress rod-on-anvil impact conditions. An in-depth understanding of the effects of starting powder characteristics on the reaction initiation threshold can potentially allow for fine control of the reaction sensitivity of aluminum powders. As described in the previous chapter, the starting powder size and the level of mechanical pre-activation of the starting powders were varied, along with the density of the powder compacts. The compacts of varying powder characteristics were impacted against a hardened steel anvil under uniaxial stress loading in air. Evidence of reaction was determined by the observation of light emission during the time-scale when the powder compact undergoes compaction and deformation between the copper projectile and steel anvil. In this chapter the characteristics of light emission associated with the combustion reaction of aluminum during uniaxial stress rod-on-anvil impact experiments will be described. Additionally, spatial information regarding the temperature rise during compaction and deformation, as recorded by an IR camera, will also be presented.

4.1 Evaluating Impact-Induced Reactivity Based on Observed Light Emission

In this study, the processes occurring following impact of the aluminum powder compact against the steel anvil are observed by a high-speed framing camera. The emission of light captured in more than one frame of the camera is considered to be indicative of reaction

occurrence. Light emission can occur at any point during compaction, deformation, or following the compaction and deformation processes. Additionally, light emission related to jetting at the instant of impact is not associated with aluminum combustion, but differentiating between these is not straightforward. Chemical analysis methods, such as *in situ* spectroscopy, have the potential to provide the most reliable information regarding the occurrence of a combustion reaction and resulting light emission; yet, these experiments require much more light than is generated with the 3.2 mm x 2.0 mm aluminum powder compact to repeatably measure the aluminum combustion spectrum.

4.1.1 Spectroscopic Evidence of Aluminum Combustion

In situ, time-resolved spectroscopic measurements were performed during the uniaxial-stress rod-on-anvil impact experiments in order to confirm that the light emission observed by the framing camera was indeed due to aluminum combustion. Spectroscopy is one of the few microsecond, time-resolved analytical techniques that can provide transient chemical reaction information associated with impact-induced reactions [14, 12, 139]. The combustion of aluminum is assumed to proceed by the oxidation of aluminum as shown in Equation 1 in Section 1.1. The reaction products, ionized aluminum and aluminum monoxide, are known to give distinct emission wavelengths centered at 395nm and 485nm, respectively.

Low levels of light emission and the unpredictable spatial variation in light emission during the reaction make light collection from the setup used in the present work very challenging. In order to optimize the setup, the fiber optics, lenses, spectrograph, and the orientation of the fiber with respect to the impact face were varied. The best microsecond time-resolved spectroscopic information was collected using an Andor Shamrock 303mm Czerny-Turner type spectrograph coupled to a Newton electron multiplier CCD camera (EMCCD). A 25 μm core fiber optic equipped with a Romack collimater (B-OD .25 X LG .75 inch Cd-28NA NIR SMA no AR) was mounted inside the gun chamber, pointed at the area of impact light emission, and used to deliver light to the spectrograph following

impact. Once at the spectrograph, the light was focused onto the top row of the EMCCD camera, and the light intensity was saved, one row at a time, every 6 μs. Each row of pixels in the CCD provides spectra for a different time point in the experiment, allowing for the capture of microsecond duration time-resolved spectra.

Figure 44 illustrates an example of light emitted as an H-2 aluminum powder compact impacts the anvil at approximately 480m/s. The light was captured with the Andor spectrograph and EMCCD camera. The time-resolved spectra for this experiment, shown in Figure 45, very clearly illustrated the stages associated with the kinetics of the aluminum combustion reaction. Initially, AlO emission, corresponding to the $B^2\Sigma^+ \rightarrow X^2\Sigma^+ \Delta v$= 0, 1, 2, 3 bands is observed from 400 to 500 nm [12]. As time continues, the AlO Δv= 0 and 1 bands at 490 nm and 470 nm begin to decrease in intensity and the aluminum lines, at 394.4 nm and 396.1 nm become more intense. A spectra was collected every 6 μs, but, for clarity, Figure 45 shows only the spectra collected every 30 μs. The starting time of the spectral data generated is arbitrary, as the trigger timing of the spectrograph was not synced exactly with the impact event. Instead the spectrograph trigger time was offset several microseconds prior to impact, to account for any error in the timing of the impact event. Additionally, the apparently long lifetime of the aluminum reaction may be due to the over-saturation of light causing one row of the CCD to bleed over to the next, causing the reaction to appear longer.

Ideally, the kinetics of the aluminum combustion reaction under impact conditions could be explored in-depth using the above-mentioned setup, but this experiment could not be repeated due to low levels of light around the entire impact area. At lower velocities, the light emitted during impact is not intense enough to be captured by the spectrograph. However, the spectra captured in Figure 45 provides clear evidence of the link between light emission upon impact of an aluminum powder compact against a steel anvil and the occurrence of an aluminum combustion reaction as confirmed via time-resolved spectroscopy. In this work, unless otherwise noted, the observation of light emission indicates that a reaction

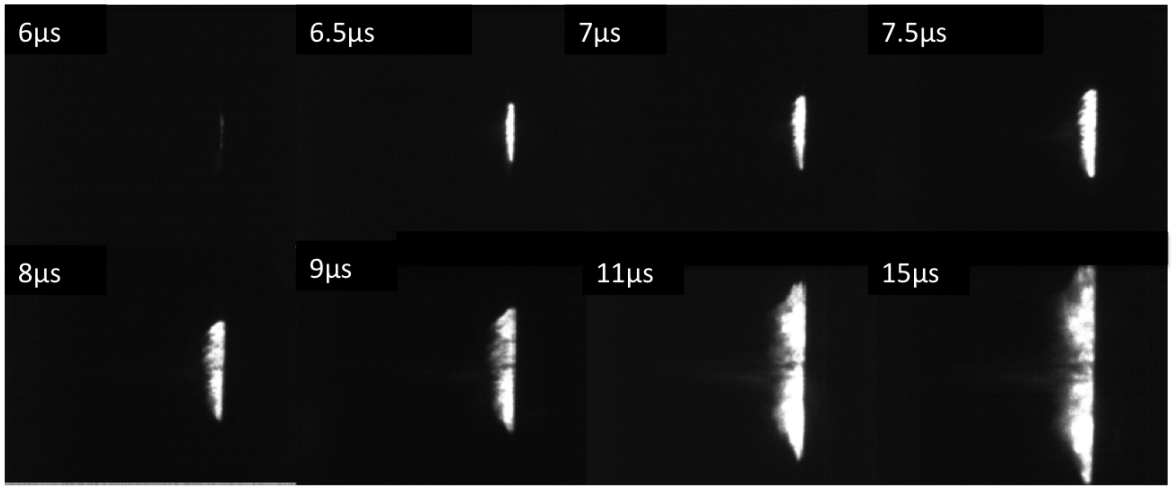

Figure 44: Framing camera images of a H-2 aluminum powder compact impacting the hardened steel anvil at approximately 480m/s. This experiment provided enough light to obtain spectral data.

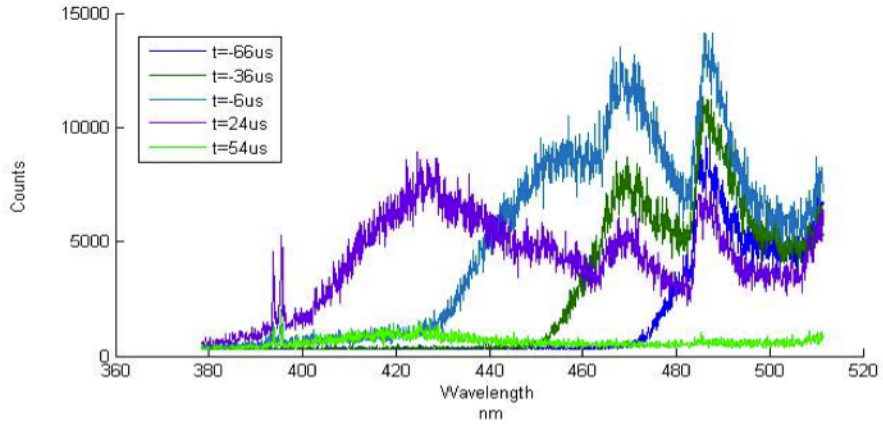

Figure 45: Time-resolved spectroscopic measurements of the combustion of a porous aluminum compact by impact initiation. Note: the timings listed are off due to misalignment of the anvil and a software problem. The sequence is correct, and the spectra pictured are meant to provide information on the dramatic change in the chemical constituents over time.

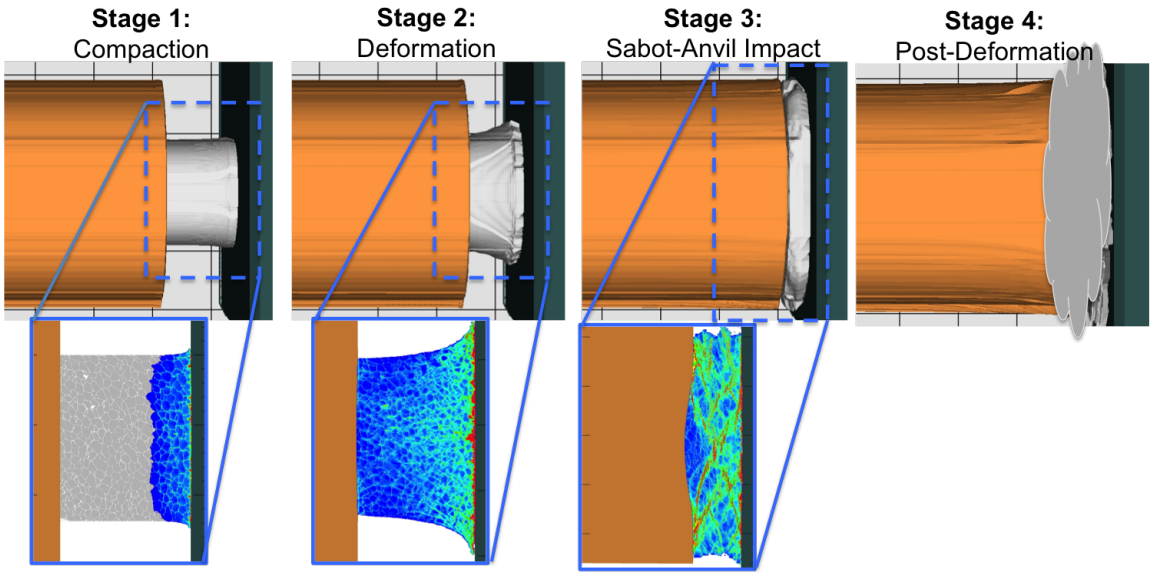

Figure 46: Schematic of the four stages of the impact process: (1) compaction (2) deformation (3) sabot-anvil impact (4) post-deformation. The magnified portion of stages 1 through 3 indicates the levels of strain that the powder compact is undergoing during each stage.

has occurred.

4.1.2 Light Emission Timing

The IMACON framing camera is capable of collecting ten million frames per second and can capture light emission during several frames of each stage of the impact process, compaction, deformation, the sabot-anvil impact, and post-deformation. Figure 46 illustrates these respective process stages as obtained via 3-D and 2-D computations. Light emission observed during the aluminum powder compaction and deformation process is considered as corresponding to the impact-induced aluminum combustion reaction initiation. Once initiated, the reaction can either be sustained until all the reactants are depleted; or, without enough continued kinetic energy, micro-mechanical energy, or heating, the reaction can be quenched within several hundred nanoseconds of its initiation. In the present work, the focus was only on reaction initiation, in terms of the effects of the characteristics of aluminum powders on the threshold conditions for initiation.

The first stage of the impact process, compaction, occurs upon impact, between 0 and

2 μs after the powder compact first touches the anvil. At the particle level, the impact-induced pressure waves move into the compact and layer after layer of aluminum particles rearrange, locally flow, and plastically deform around one another until all of the voids have collapsed [43, 57, 140], as shown in the magnified image of the simulated compaction stage shown in Figure 46. Light emission corresponding to reaction can occur during any stage of the compaction process. Figure 47 (a) illustrates an example of the observed light emission once the sample first impacts the anvil and compaction begins in the 0.5 - 1.0 μs timescale for impact at 200 m/s. Light emission spreads across the front/impact face of the compact which can be quenched or can continue until the powder is fully compacted and even after the copper projectile starts to deform against the steel anvil. Reaction initiation during the compaction stage can thus be due to rapid void closure and subsequent heating or the energy release from friction and particle level plastic deformation as the powder undergoes compaction.

Once the compaction process is complete, stage two, or the deformation stage, begins approximately after 2 μs and typically lasts for up to 6 μs. During this deformation stage, the powder compact continues to undergo plastic deformation at extremely high strain rates ($\sim 10^5$ s^{-1}) across the front face of the steel anvil as shown in the magnified image of the deformation stage in Figure 46. The latent energy available in the form of heat or the generation of defects from the mechanical work of plastic deformation can be enough to support reaction initiation, or sustained reactivity, during this deformation stage. In such a case, light emission across the impact face of the compact, the area undergoing the highest amount of plastic deformation, can be observed as shown in Figure 47 (b).

Following complete deformation of the aluminum powder compact, the third stage occurs as the copper sabot itself continues to deform against the aluminum and steel anvil, generating even higher pressures than that generated through the remaining material. This occurs after 8 μs and by this time a large portion of the aluminum may even have squeezed outwards, beyond the circumference of the copper projectile. The aluminum remaining

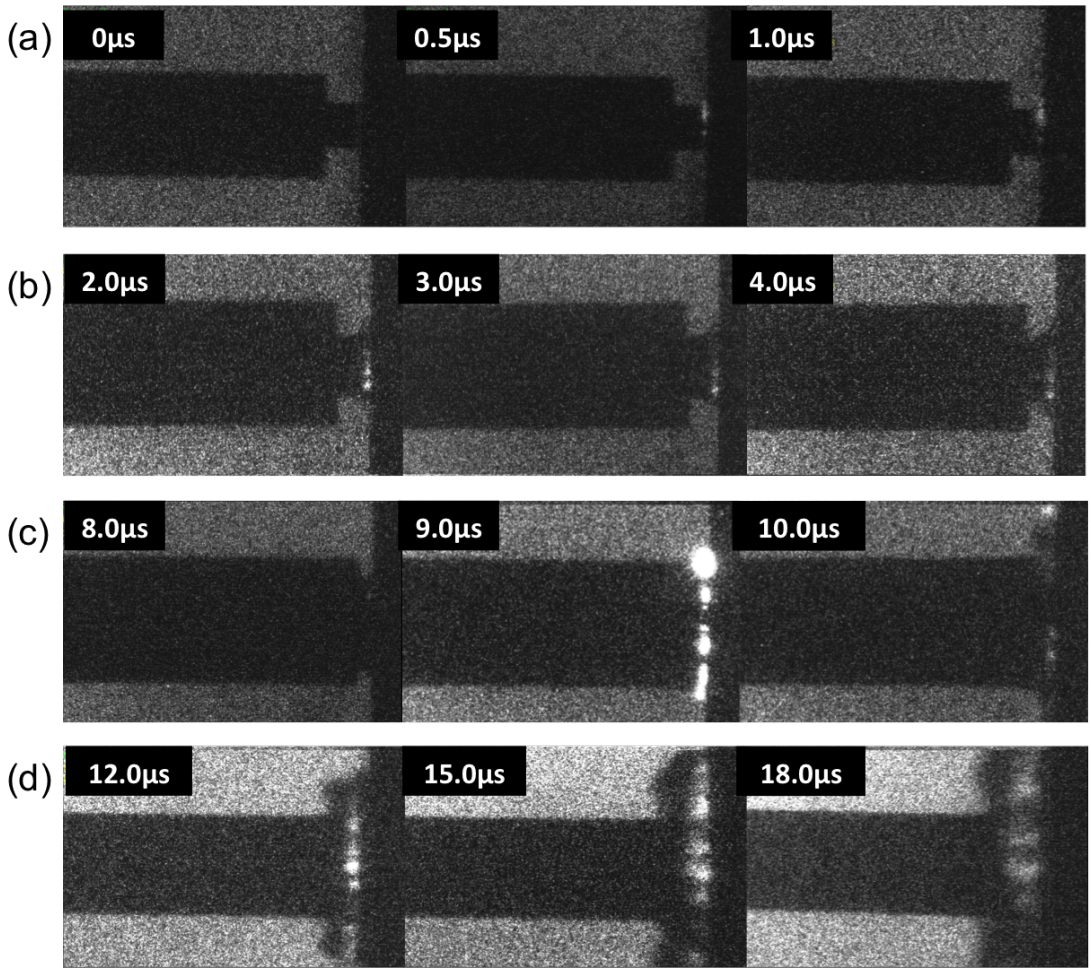

Figure 47: Images of light emission during (a) compaction of 91.4% H-5 at 255 m/s, (b) deformation of 97.4% H-5 at 290m/s, and the (c) sabot-anvil impact of 91.6% H-60 at 257m/s, and (d) following compaction and deformation of a 92.3% H-2 at 249 m/s. The exposure time of each image is 250 ns.

between the copper projectile and steel anvil undergoes extremely high shear strain as the copper and aluminum shear together as illustrated in the magnified image of the third stage in Figure 46. The combination of high pressure and high shear can lead to sustained and/or additional reaction and light emission as illustrated in Figure 47 (c). In several samples, this reaction was observed to be sustained for several microseconds following the start of the deformation of the copper projectile and aluminum against the steel anvil. The fourth and last stage of the impact process, post-deformation, begins approximately 12 μs after initial impact of the powder compact against the anvil. During the post-deformation stage, the highly strained aluminum powder compact can fragment, forming a particulate cloud which can also react and result in light emission as observed in Figure 47 (d).

Light emission corresponding to reaction initiation can thus be observed at several stages following the impact of the aluminum powder compact against the steel anvil. Correlating the timing of reaction initiation during the impact process and the sample type is necessary to provide an understanding of the processes leading to reaction initiation. In the present work, light emission timing was distinguished as occurring due to reaction either during compaction, during deformation, during the sabot deformation against the competed aluminum and anvil, or following complete compaction and fragmentation of the aluminum and recorded for all impact experiments.

4.1.3 Impact Flash and Jetting

Light emission due to jetting or ionization of air can also be observed during rod-on-anvil impact experiments. Jetting is an intense flash that is typically observed during a hypervelocity impact at velocities greater than 2 km/s [141, 142, 143, 144]. It is generally attributed to the emission of a stream of hot or molten material from two colliding bodies [145]. Light emission as a result of ionization can also be observed as an intense flash, but is attributed to the ionization of atoms of air near the impact site [146].

As both ionization and jetting result in an intense flash of light, the two phenomena

can often be difficult to distinguish without high speed *in situ* spectroscopy. Light emission due to jetting and ionization have been shown to be dependent on the mass, velocity, and makeup of the impacted particles [146, 143]. Additionally, porous materials [147] and those impacting at an angle of greater than 15° [148] have been shown to be more sensitive to the impact flash generation. Impact velocities of at least 1 km/s are required to produce the impact flash. Yet, Becker [141] has noted that impact flash was an even greater function of the experimental setup and did not remain consistent with material types as the experimental setup changed.

Other researchers, including Thornhill *et. al.* [144], have observed similar impact flash that was prompt and lasted for a sub-microsecond duration in their two stage gas gun setup. In the presented work, a flash of light observed for less than a microsecond (less than two frames) was considered to be attributed to impact flash and not indicative of an aluminum combustion reaction. Additionally, any experiment exhibiting light emission as a result of an angled impact, for example, as pictured in Figure 48 was considered to be due to jetting, and not accounted for being indicative of reaction. Experiments that produced an intense, jet-like flash upon impact, during which the emission persisted for several frames and the projectile gave no indication of an angled impact, were counted as a indicative of reaction. An example of such an experiment is shown in Figure 49. The high intensity emissions observed in the experiments performed in the present work were most likely not a result of ionization as these were performed at impact velocities (150 to 300 m/s) much lower than the sound speed of air (345 m/s), where air ionization is much less likely to occur.

4.2 Reactivity as a Function of Aluminum Powder Characteristics

Uniaxial stress rod-on-anvil impact experiments were conducted on compacts of aluminum powders of various sizes, as well as on aluminum powders that had been mechanically pre-activated by high energy ball milling, as well as highly strained aluminum platelets obtained from machining. Additionally, the density of the compacts and the impact velocity

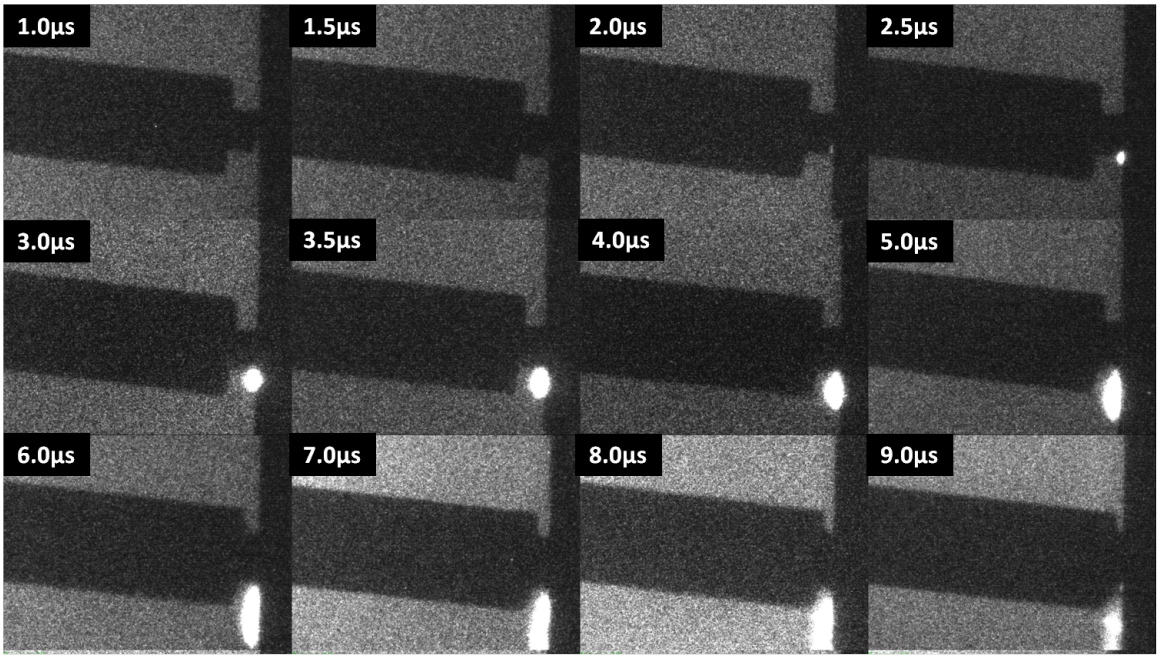

Figure 48: Image of a H-60 HEBM'd for 10 minutes impacting the anvil at 175m/s and causing jet formation. Due to the angled impact, this data point would be thrown out.

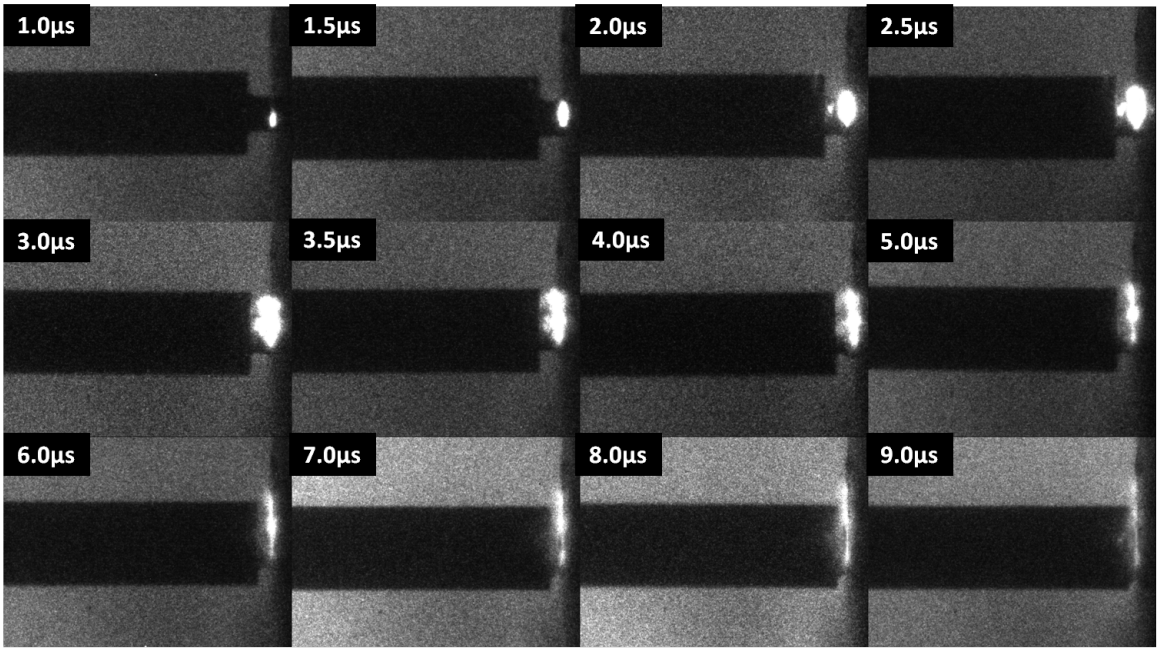

Figure 49: Image of a H-60 HEBM'd for 30 minutes impacting the anvil at 185m/s and causing jet formation. The image and recovered sample provided no evidence of an angled impact, therefore this experiment was counted as a reaction.

were varied. Figures 50 - 57 show plots of velocity as a function of % TMD (theoretical maximum density) illustrating the reactivity of each sample type as evidenced by light emission. Each point on the plot is indicative of one experiment, with observation of light emission during compaction (blue plus sign), deformation (orange circle), the sabot-anvil impact (green triangle), or following complete deformation (red square) being indicative of reaction. Open blue squares are indicative of experiments where no light emission and therefore no reaction was evident.

For each type of aluminum powder, the reaction threshold can be identified as the lowest velocity at which reaction initiation evident by light emission is observed. Each plot illustrates how sensitive the corresponding mixture is to undergoing impact initiated reactions. The threshold velocity was determined by taking an average of the lowest three velocities at which light emission was observed as evidence of reaction initiation. The standard deviation of the three lowest reaction velocities is also provided.

The compact density versus impact velocity plot in Figure 50 reveals the lowest impact velocity (reaction threshold) for H-2 (4 μm) aluminum powder compacts. The reactivity threshold for the smallest, H-2, aluminum powders, is 244$\pm$5 m/s. It can be seen in Figure 50 that all of the H-2 powder compacts show variability in reaction initiation in terms of the stage at which the reaction (or light emission) is first observed. The various stages correspond to the compaction, deformation, sabot-anvil impact, or even post deformation. In the case of four of the eight samples that reacted, a sustained reaction was observed through all four stages of the impact process.

Compacts composed of H-5 (13 μm diameter) aluminum powders had a reactivity threshold of 251$\pm$7 m/s. As shown in Figure 51, typically, light emission from the H-5 compact began during the compaction stage, immediately following initial impact, except in the case of one experiment where light was only observed following complete deformation. In general, the light emission was observed immediately upon impact, across the

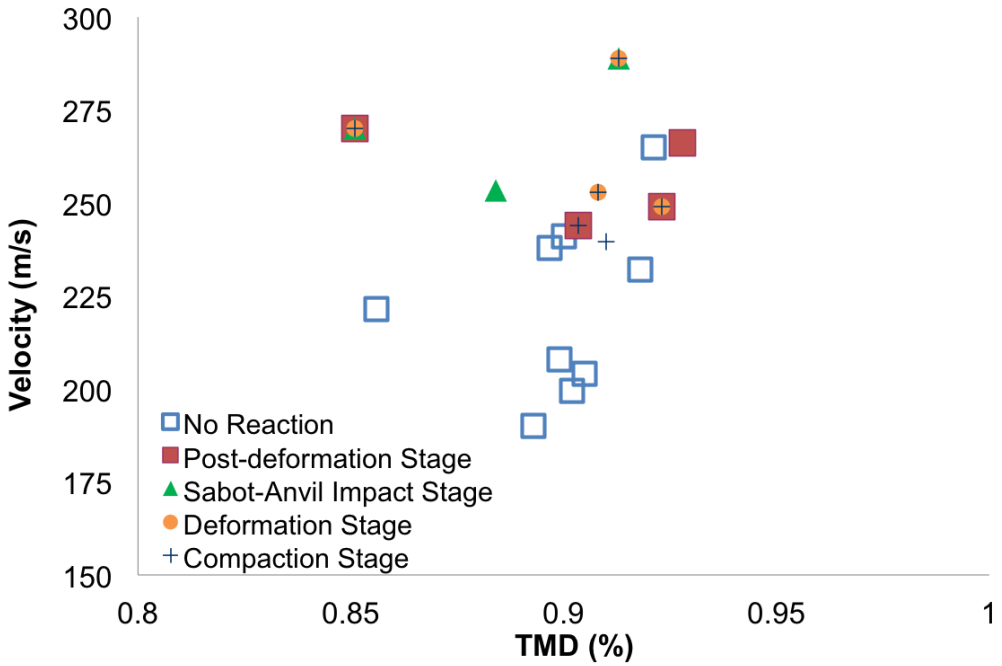

Figure 50: Reactivity of H-2 of varying %TMD with respect to velocity.

impact face and was sustained throughout all four stages of the impact process. In a couple of experiments, the reaction and light emission was only sustained until the sabot-anvil impact.

The plot of impact velocity versus compact density for H-15 (18μm diameter) powder compacts shown in Figure 52 indicates a reaction threshold of 229$\pm$8 m/s. The different symbols corresponding to various stages of observed light emission show much more scatter than for compacts of the finer H-2 or H-5 aluminum particles. Light emission was first observed during either the compaction, deformation, sabot-anvil impact, or post-deformation stage in the various experiments. In most of the experiments in which reaction occurred, light emission was not sustained past complete deformation. Additionally, several experiments at high velocities (above 275 m/s) did not show light emission.

The reactivity threshold for compacts of H-60 (67μm diameter) aluminum powder was 196$\pm$5 m/s. As shown in the velocity versus density plot in Figure 53, light emission was observed during the compaction, sabot-anvil impact, or following complete deformation

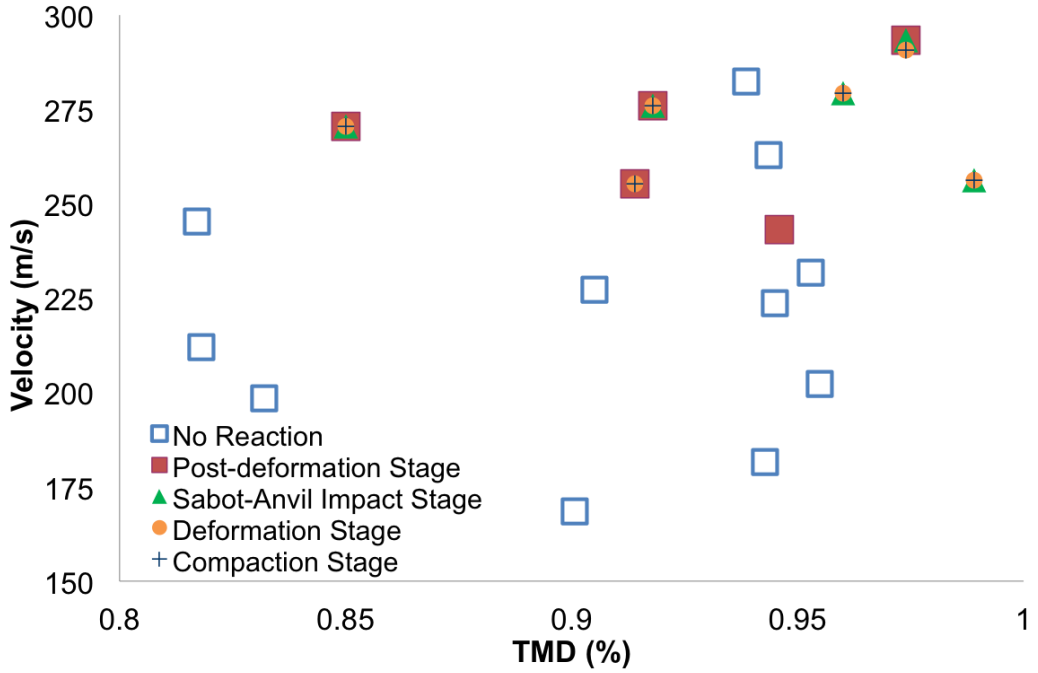

Figure 51: Reactivity of H-5 of varying %TMD with respect to velocity.

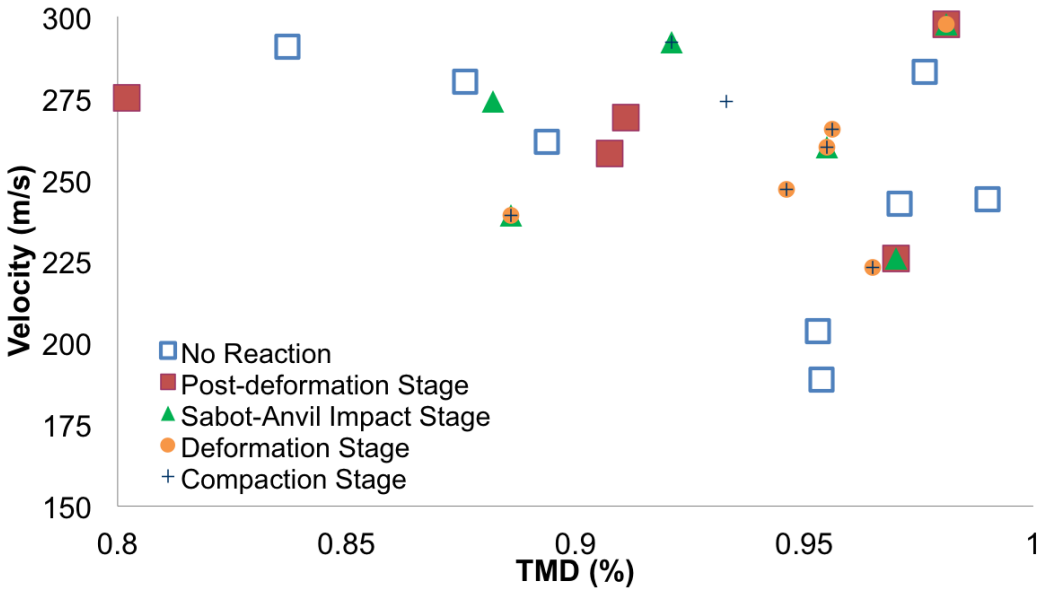

Figure 52: Reactivity of H-15 of varying %TMD with respect to velocity.

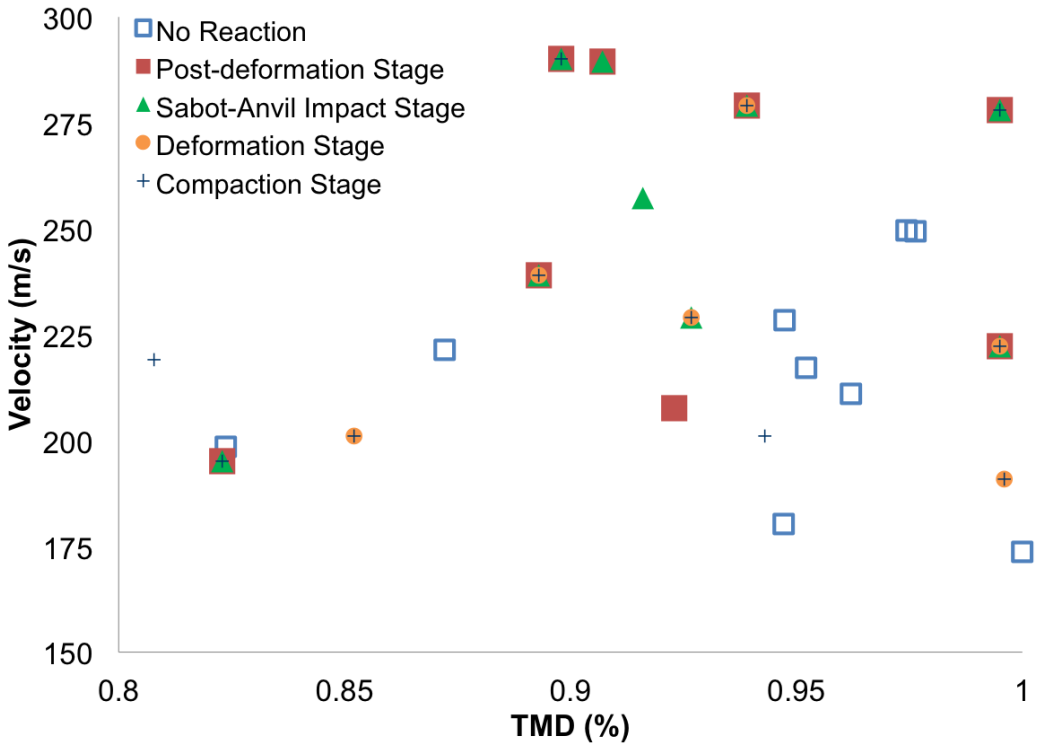

Figure 53: Reactivity of H-60 of varying %TMD with respect to velocity.

in the various experiments. In most of the experiments for H-60 aluminum powders, the reaction first initiated during the compaction stage and was observed to be sustained until the stage following deformation.

The reactivity threshold for compacts of 10 minute HEBM H-60 aluminum powders was found to be 208±13 m/s as illustrated in Figure 54. For the impact experiments performed on this aluminum powder type, light emission due to reaction was observed during the initial compaction stage following impact and was sustained through the sabot-anvil impact stage. Only in half of these cases did the reaction light emission continue past the sabot-anvil impact and into the post-deformation stage. Compacts composed of 30 minute HEBM H-60 aluminum powder had the lowest reactivity threshold, with reaction initiation and corresponding light emission observed at velocities as low as 189±8 m/s. As shown in Figure 55, reaction light emission began during the compaction stage and continued through at least the deformation stage. Samples of H-60 that underwent high energy ball

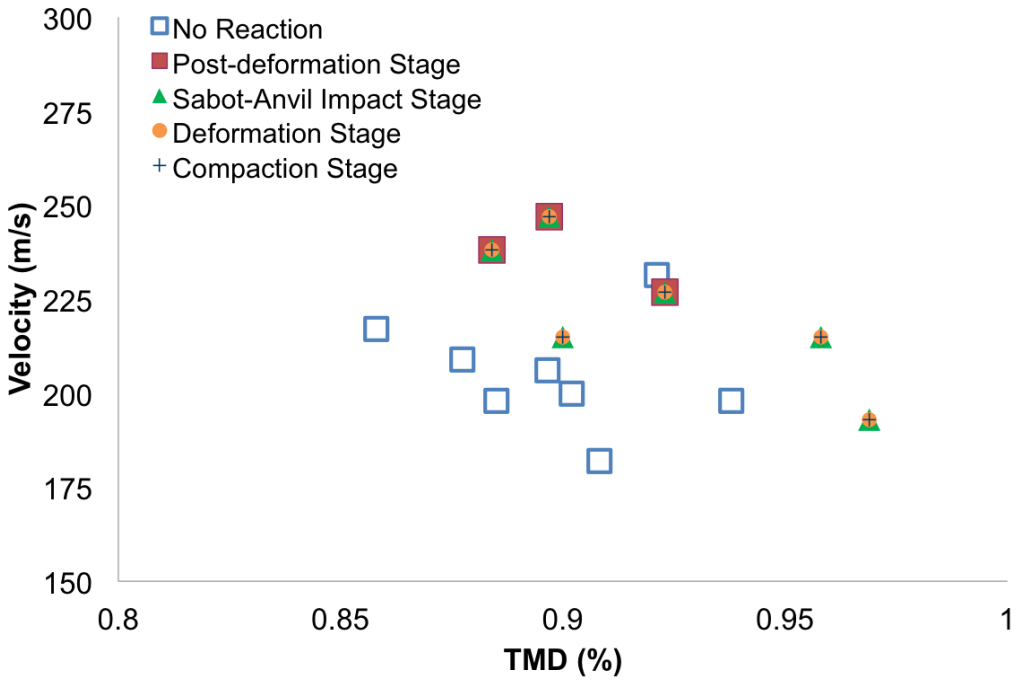

Figure 54: Reactivity of H-60 HEBM'd for 10 minutes of varying %TMD with respect to velocity.

milling for 60 minutes had a reactivity threshold of 210±4 m/s, with intense light emission observed consistently during the compaction stage in all experiments as illustrated in Figure 56.

Compacts of the highly strained aluminum platelets show a reaction threshold velocity of 201±6 m/s. As shown in Figure 57, light emission from platelet compacts indicating reactions was observed during the compaction stage and is typically continued to be observed throughout the entire impact process and all the way through the post-deformation stage.

Figure 58 (a) and (b) displays a summary of the results of experiments revealing the reaction threshold for all aluminum powder types investigated under rod-on-anvil impact conditions. The reaction occurrence for powder compacts of all H-series Valimet powders of various sizes is shown in Figure 58 (a). The plot shows powders with increasing size

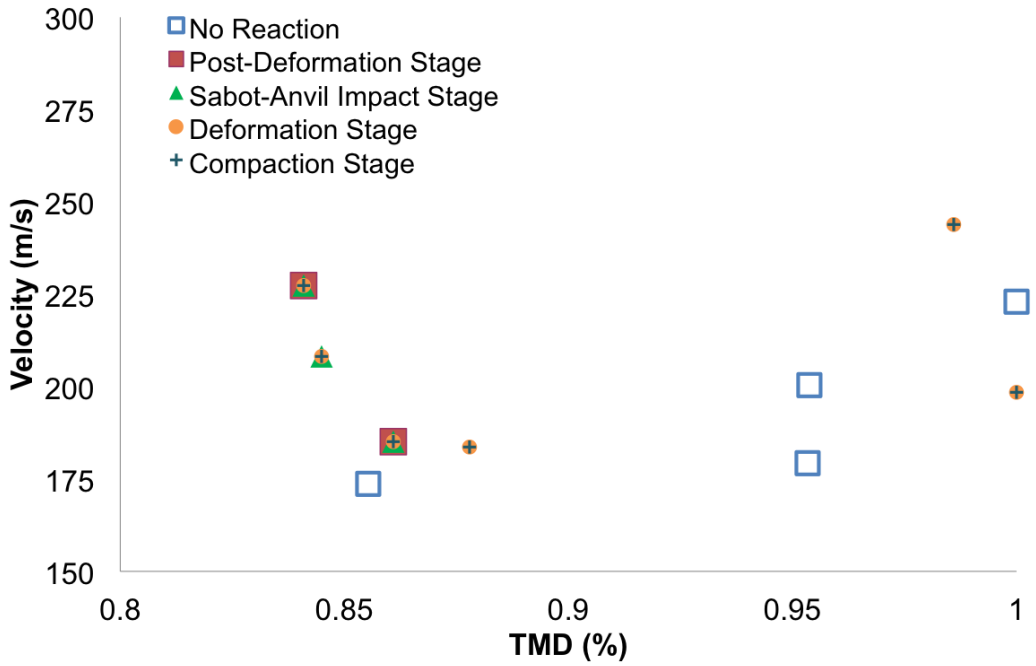

Figure 55: Reactivity of H-60 HEBM'd for 30 minutes of varying %TMD with respect to velocity.

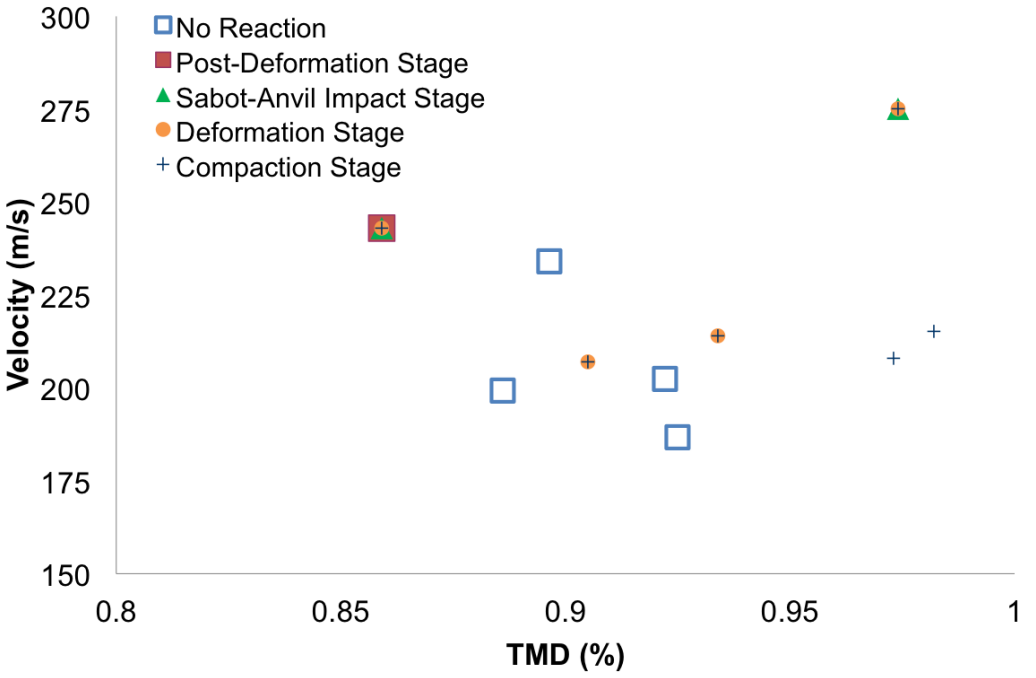

Figure 56: Reactivity of H-60 HEBM'd for 60 minutes of varying %TMD with respect to velocity.

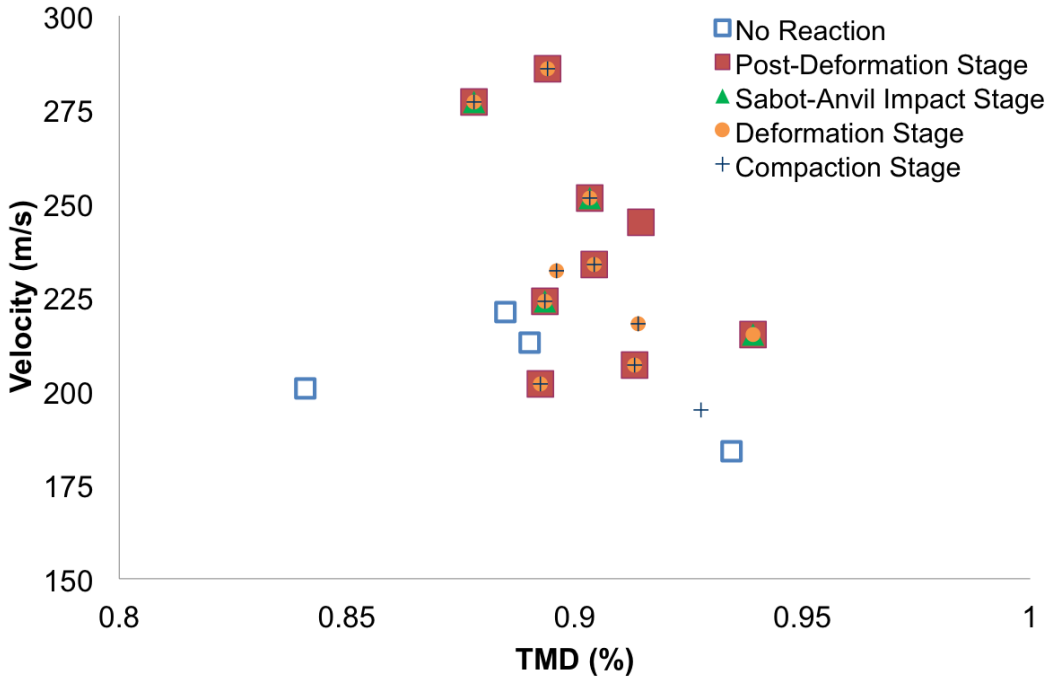

Figure 57: Reactivity of highly strained aluminum platelets of varying %TMD with respect to velocity.

along the x-axis, revealing that as the aluminum powder size increases, the velocity threshold for reaction initiation decreases. Figure 58 (b) illustrates the reaction threshold trend for powder compacts of mechanically pre-activated powders. The plot shows powders of increasing mechanical pre-activation along the x-axis, with the reaction threshold initially increasing, followed by a decrease for further HEBM powders. A longer, 60 minute, ball milling time and exposure to high strain machining results in a higher reaction threshold.

Figure 58 (a) and (b) account for compact density by separating the reaction occurrence of each powder type into two bins, one for 80% to 90% TMD compacts and another for 90% to 100% TMD compacts. The plots show that the higher compact density samples (90% to 100% TMD) have a slightly lower reaction threshold than the lower compact density samples (80% to 90% TMD) for all powder types except for 30 minute HEBM powders.

Figure 59 shows a summary of the reaction threshold for all of the various aluminum powder types investigated. It can be seen that the reactivity threshold decreases from

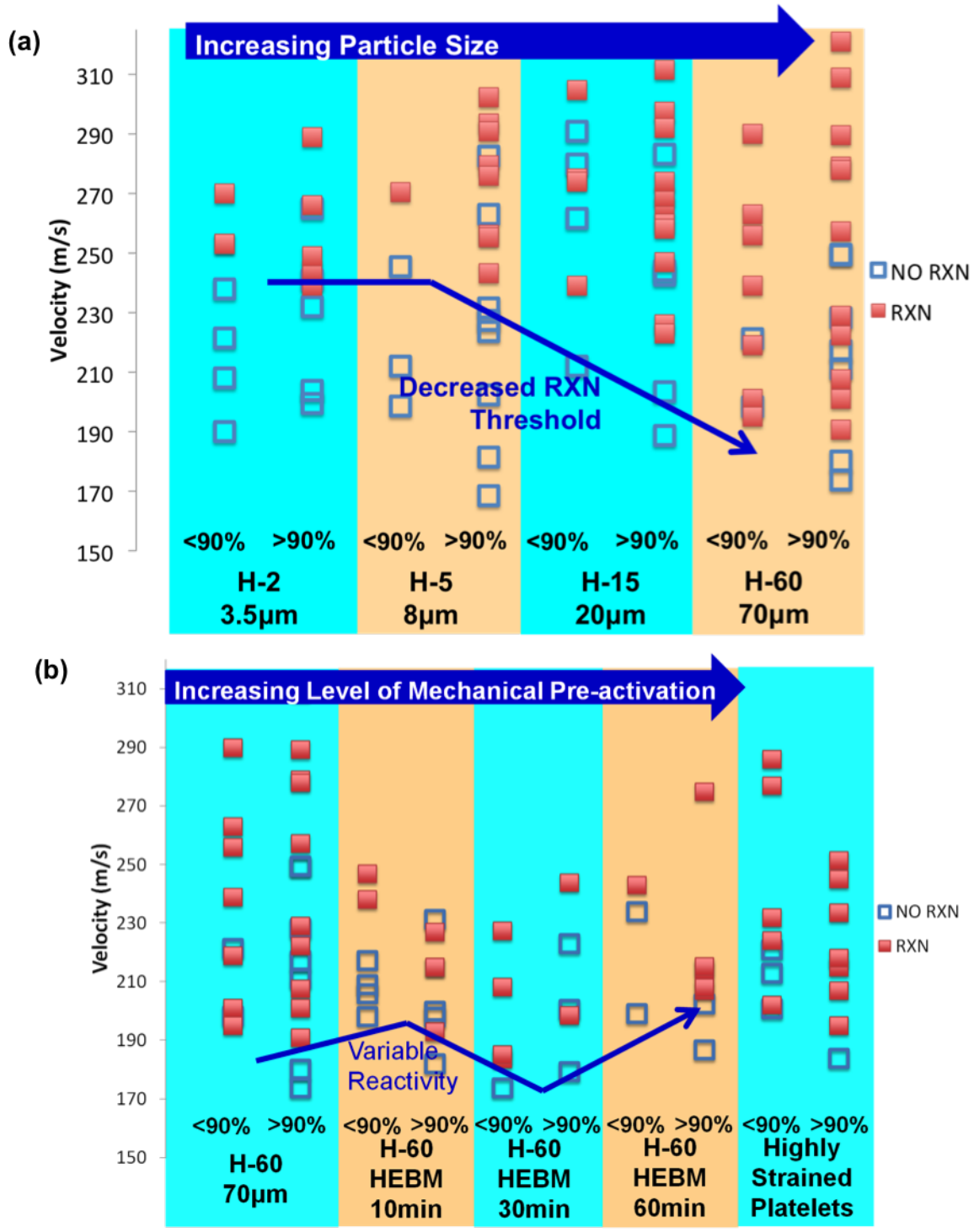

Figure 58: A summary of reaction occurrence in all samples tested. (a) Reaction occurrence in Valimet H-series powder compacts. (b) Reaction occurrence in mechanically pre-activated powder compacts.

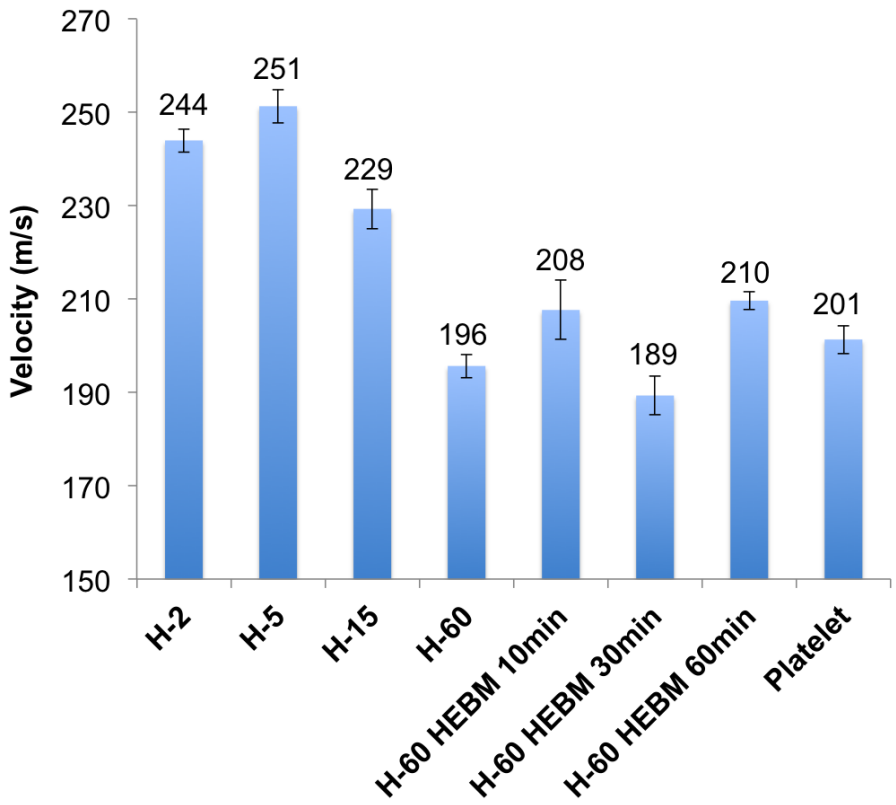

Figure 59: The calculated velocity threshold for reaction of each powder type.

244±5 m/s to 196±5 m/s as the powder diameter increases from 4 μm (H-2) to 67 μm (H-60). Mechanical pre-activation of H-60 powders via high energy ball milling slightly increases the reaction threshold to 208±13m/s after 10 minutes of ball milling, but then the reaction threshold decreases to 189±8 m/s after 30 minutes of ball milling, and lastly, it increases to 210±4 m/s after 60 minutes of ball milling. The highly strained platelets have reaction threshold 201±6 m/s which is higher than that for the H-60 and H-60 HEBM 30 minute samples but is lower than that for the H-60 HEBM 10 minute and 60 minute samples.

Trends in light emission timing are difficult to pinpoint as light emission timing varied with particle type, velocity, and compact density. For the H-2, H-5, H-15, and H-60 samples, plotted in Figures 50 to 53, no patterns were apparent as light emission was generally observed during any of the stages of compaction, deformation, sabot-anvil impact,

or post-deformation during the impact process. For the mechanically pre-activated aluminum powders, plotted in Figures 54 to 57, light emission was typically observed during the compaction process only.

4.3 Temperature Measurements Using IR Camera Imaging

The IRC906 Infrared camera system was used to obtain spatial information about the temperature of the aluminum powder compact during the stages of compaction, deformation, sabot-anvil impact, and following complete deformation. As the aluminum compact mounted on the copper projectile impacts the anvil, localized heating at the aluminum particle interfaces and bulk heating resulting from extensive overall deformation can occur. The IR camera provides a snapshot in the temperature reached at different locations of the impacted sample over a certain period of time. These temperatures can be compared to the predictions from computational simulations and theoretical calculations to better understand the influence of heating on the impact-initiated combustion of aluminum powder compacts.

4.3.1 Calibration of the IR Images

Prior to collecting temperature data during impact, the IR camera was calibrated to get an accurate measure of the temperature. The IR camera provides an intensity value in A/D counts, which increase as either the temperature or the exposure time increases. A calibration curve was created by plotting the known temperature of a blackbody plate versus the A/D counts at a constant exposure time. In order to collect calibration images, the IR camera was first focused into the chamber of the 7.62 mm single stage gas gun at the position where the temperature measurement of the rod-on-anvil impact would take place, both as a profile view to the impact or at the front impact face of the sapphire anvil through a 45 degree mirror. An Omega BB-2A blackbody plate was placed inside the chamber at the rod-on-anvil impact position and set to the desired temperature. The temperature of

the blackbody plate was confirmed using an Omega HH-12 thermocouple. Once the temperature stabilized, three images of the blackbody plate were captured by the IR Camera. The average value of the A/D counts within a circular region (170 pixels in diameter) at the center of the image was tabulated and recorded as the A/D intensity at that temperature point. Images were captured at exposure times ranging from 1 to 50 μs and at temperatures ranging from 100 to 325°C. Figure 60 shows a graph of A/D counts as a function of temperature at an exposure time of 2 μs. These data points were fit to the cubic equation,

$$y = 161.11 + 2.24x + .0127(x - 218.6)^2 + 3.42E - 05(x - 218.6)^3 \qquad (29)$$

which was used to quantify the temperatures achieved during the compaction and deformation processes associated with the rod-on-anvil impact experiments. The standard deviation of the average A/D count measured combined with the error of the best fit line resulted in a maximum of 6% error in the temperature measurements.

An emissivity correction of the aluminum powder compact was performed to obtain accurate experimental temperatures. The emissivity of the aluminum powder compact was calculated by heating a half inch diameter aluminum pellet to 80°C in the furnace and collecting images of the heated aluminum pellet using the IR camera. The average A/D counts of the heated aluminum pellet were compared to the expected A/D counts for a black body at 80°C, from which the emissivity correction of 0.85 was obtained for the aluminum powder compacts.

4.3.2 Measurement of Bulk Profile Temperature During Rod-on-Anvil Impact Experiments

Once the calibration curve was established, *in situ* 2D images of the heating that takes place during compaction and deformation of the aluminum powder compact were captured using the IR camera. The IR camera can collect an image of the temperature at a maximum rate of 125 Hz; the 7.9 ms interframe time allows only one image to be collected during either compaction, deformation, sabot-anvil impact, or following complete deformation

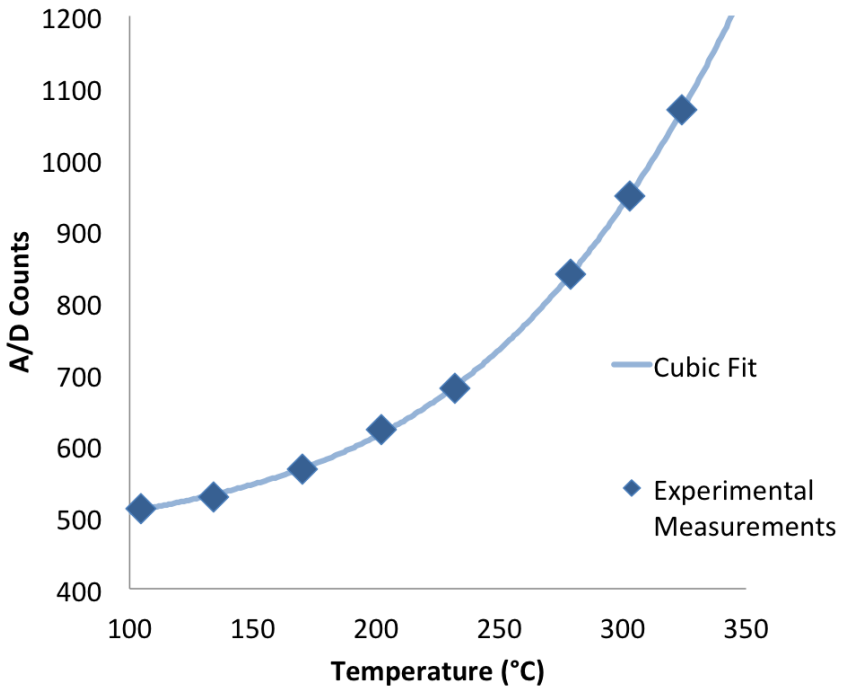

Figure 60: Calibration curve for the IR camera at 2 μs exposure times. Each point represents the A/D value obtained at each temperature and the line is the best fit of the data.

per experiment. Although the collection speed is limited, both the exposure time and the triggering of the IR camera can be precisely controlled. The exposure time can be set to a minimum of 1 μs using the IRC software, allowing for thermal observation of a very discrete segment of the deformation event. The triggering of the IR camera is controlled by the Up-Down Counter (UDC), which sends separate TTL pulses to the IR camera and the Imacon high speed framing camera and enables the collection of synchronized high speed and IR images with an uncertainty of less than 0.5 μs. Capture of images from both the IMACON high speed framing camera and the IR Camera at the same time provides information about the radial strain state and the possible occurrence of reaction (based on light emission) within the powder compact throughout the time that the temperature measurement is collected.

Figure 61 shows an example of the data collected during an IR imaging shot. The high speed framing camera image (A), the IR image (B), and an overlay of the IR and

framing camera images (C), are all captured during a single experiment, as an H-2 powder compact impacts the anvil at 245m/s. Images from the high speed camera are shown in Figure 61A and allow for observation of both the radial strain, approximately 60%, as the compact impacts the anvil and the reaction that occurs during the IR image capture over the 2 μs exposure time of the IR image. The IR image shown in Figure 61 (B) provides information about the average heating and the maximum temperature rise observed over the exposure time of the IR image capture, between 2 and 4 μs after initial impact against the anvil. Temperature increase is observed in the form of a vertical line at the impact face of aluminum powder compact where compaction and deformation initially occur. The average temperature observed during impact was calculated by taking the average A/D count for all regions of the image that were above the background temperature and were not oversaturated by light emission from reaction. The aluminum powder compact shown in Figure 61 (B) produces an average temperature of 201 ± 11°C upon impact. The highest temperatures, reaching a maximum of 254 ± 11°C, were observed on the outer edges of the compact, where the most deformation occurred. Figure 61 (C) shows both the IR image and the framing camera image, overlaid on top of one another, to indicate spatially where heating takes place.

IR images were captured during compaction and deformation for aluminum powder compacts of H-2, H-5, H-60, HEBM 10 minute, HEBM 60 minute, and platelet samples at time frame between approximately 2 and 4 μs after initial impact against the anvil, when the radial strain was approximately 60% in each powder compact. The average temperatures observed during impact are plotted in Figure 62 as a function of velocity. As shown in the figure, compacts composed of powders of varying sizes (A) and compacts of mechanically pre-activated powders (B) behaved similarly with respect to the average bulk temperatures observed. As velocity increases, temperature tends to increase. The maximum temperature reached was 210°C in the platelet samples.

The temperatures generated in powder compacts composed of H-2, H-5, H-60, and 10

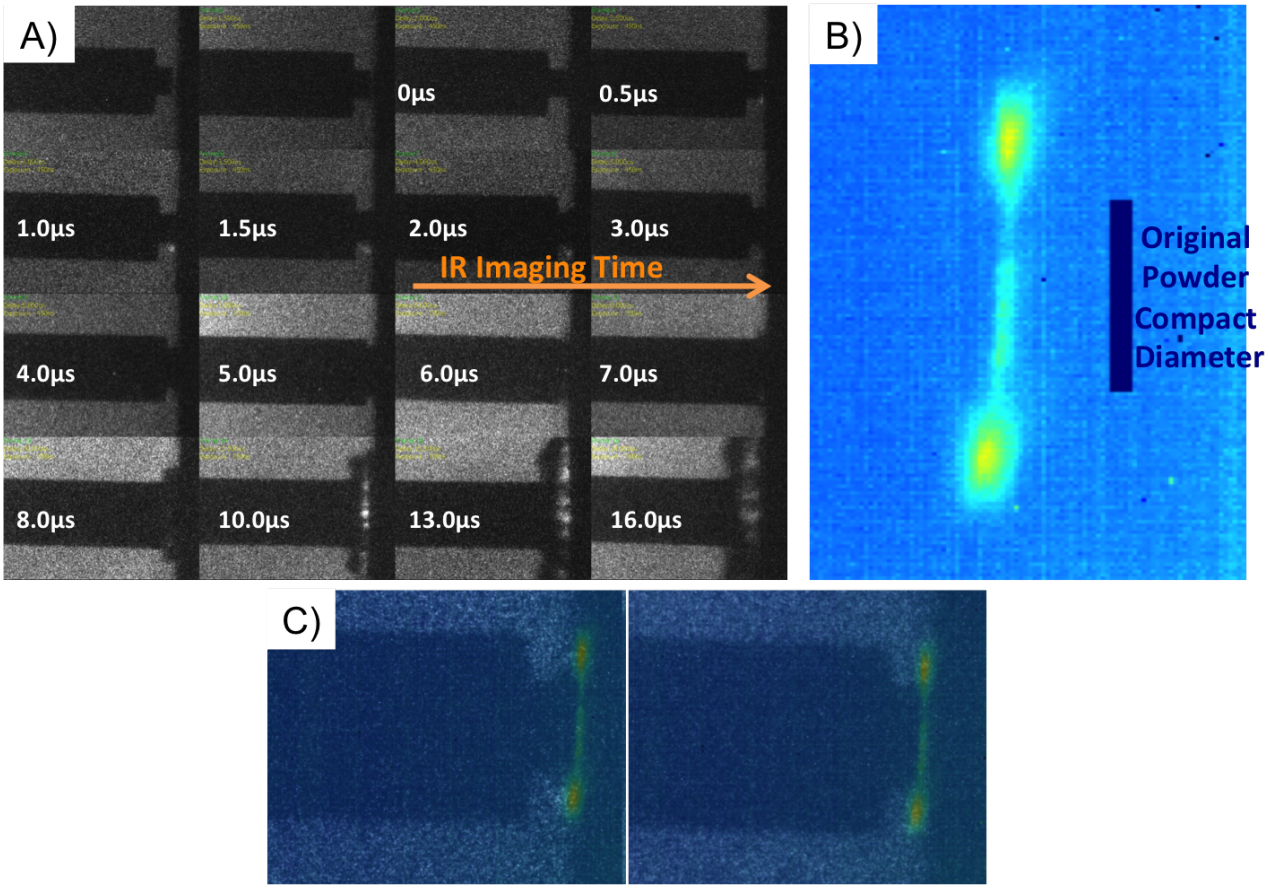

Figure 61: An example of the data collected during an IR imaging shot of an H-2 powder compact impacting the anvil at 245m/s: the high speed framing camera image (A), the IR image (B), and an overlay of the IR and framing camera images (C)

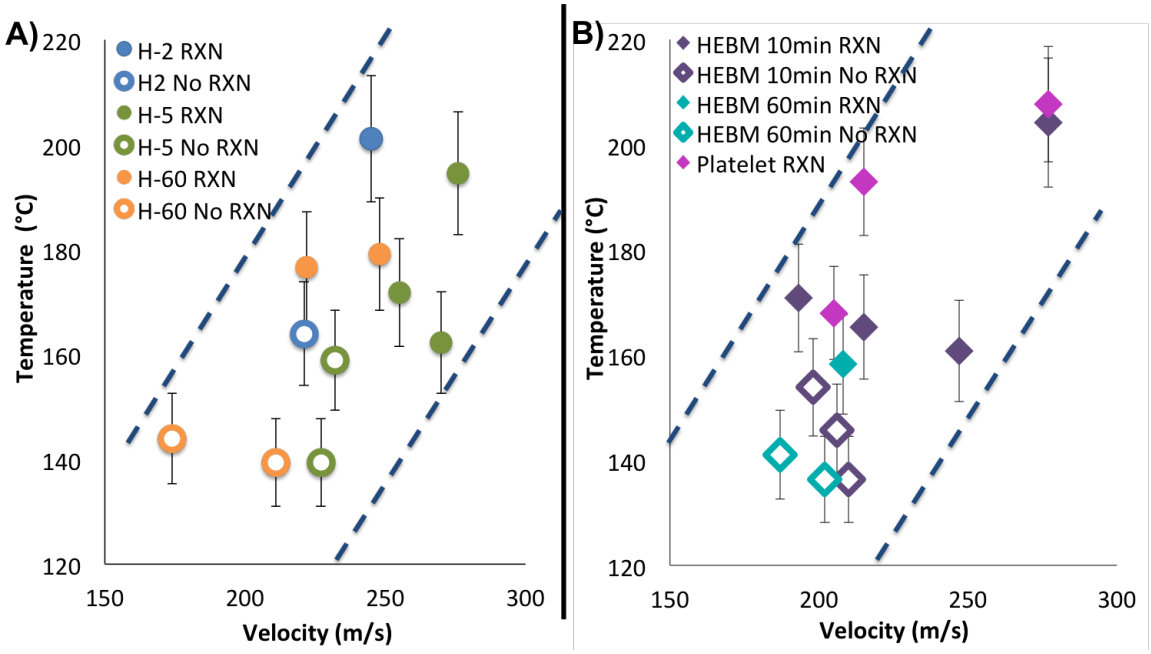

Figure 62: Temperatures observed in the deformed portion of aluminum powder compacts of various sizes and varying degrees of mechanical pre-activation as a function of velocity.

minute HEBM aluminum powders were investigated at later times following impact, between 4 and 6 μs after initial impact. At these later times, the powder compacts experience increased plastic deformation and higher levels of strain, approximately 100% radial strain, during impact. Figure 63 provides high speed images of the deformation process typically observed in a powder compact at 100% radial strain, immediately before the copper projectile impacts the steel anvil. IR images collected at this point in the deformation process are presented in Figure 64 for H-2 (A), H-5 (B), H-60 (C), and 10 minute HEBM (D) samples. The average temperature observed for H-2, H-5, H-60, and 10 minute HEBM was 145°C, 147°C, 172°C, and 201°C, respectively. Generally, at higher levels of strain, the level of heating should be greater, due to the conversion of larger amounts of mechanical work to thermal energy, but these samples exhibit a temperature rise similar to that observed at 60% radial strain.

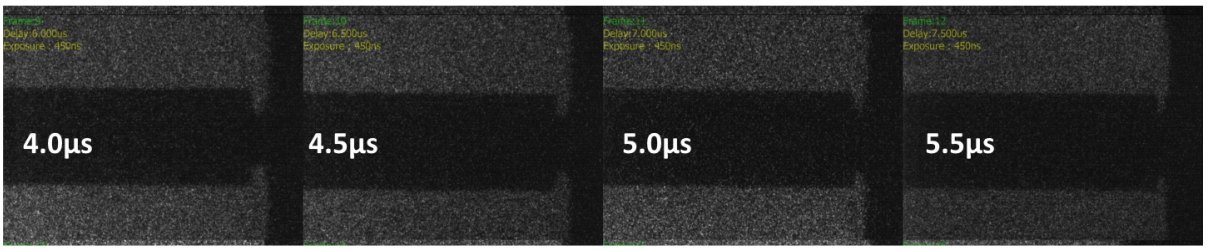

Figure 63: Imacon image of aluminum powder compact strain at a velocity of 275m/s and a strain of approximately 100%. Each IR image was collected over an exposure time of 2 μs, between 4 and 6 μs after initial impact as shown here.

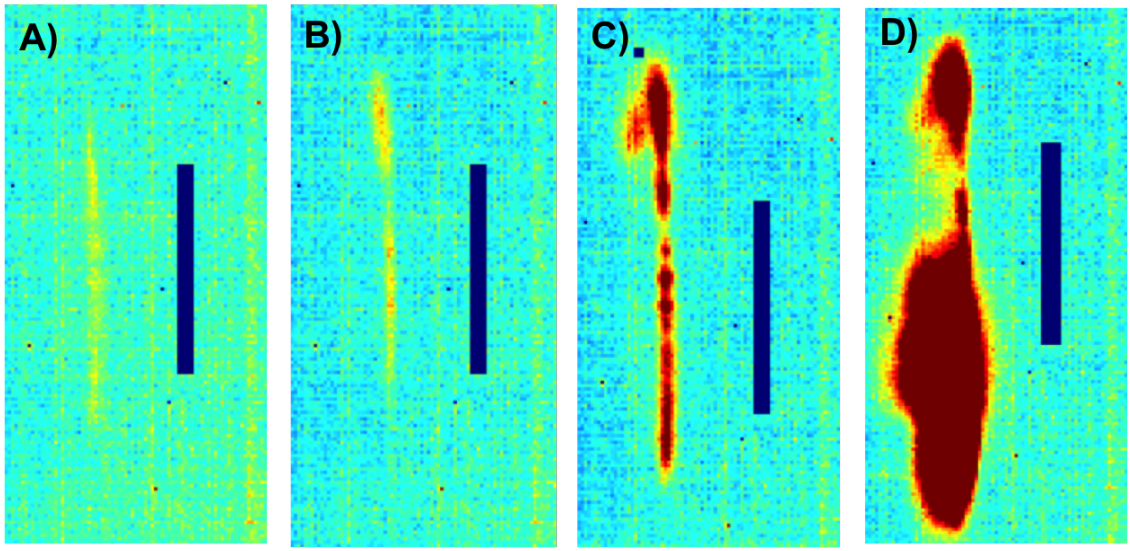

Figure 64: IR images of H-2 (A), H-5 (B), H-60 (C), and 10min HEBM H-60 at a velocity of 275m/s and a strain of approximately 100%. The vertical blue bar represents the initial diameter of the aluminum powder compact.

4.3.3 Measurement of Temperature at the Impact Face

The IR images captured as profile views at the time of impact can only provide information about the temperature of the aluminum compact along the outer edges where bulk deformation occurs. IR images collected at the impact face of the sample provide spatial temperature information about the interior temperature states of the compact during impact. IR images were captured at the impact face of the anvil through the use of the sapphire anvil setup shown in Figure 43 (in Chapter 3). As with previous IR experiments, high speed images were also captured during the impact face IR imaging experiments to better understand the relationship between heating at the impact face and the processes of sample compaction, deformation, and reaction. Figures 65 and 66 provide the high speed images captured over the exposure time of the IR image for each experiment. All IR images were captured for an exposure time of either 3 or 4 μs.

The experiments presented in Figure 65 were conducted on powder compacts composed of H-60 particles impacting the anvil at approximately 210 m/s. Figure 65 (a), (b), and (c) represent three different experiments performed under the same conditions, where images were captured at progressively later times during the impact process. Figure 65 (a) provides the IR image captured during the first stage of the impact process, compaction, from 0 to 2 μs following impact of the powder compact against the anvil. The dark red spots within the image of the powder compact represent areas where the sample temperature reaches 404°C, and areas in yellow represent areas where the temperature is 308°C. The 100°C variation in temperature within the pellet indicates that localized heating occurs during the compaction process. Figure 65 (b) shows the IR image captured during the deformation stage, from 3 to 7μs following initial impact of the powder compact against the anvil. Temperatures captured during deformation were much lower than those captured during compaction and following the copper rod-anvil impact. Typically during deformation, the highest amounts of heating occurred on the outer edges of the powder compacts, where most of the bulk and particle-level deformation occurred. In the IR image given in Figure 65 (b), the outer rim

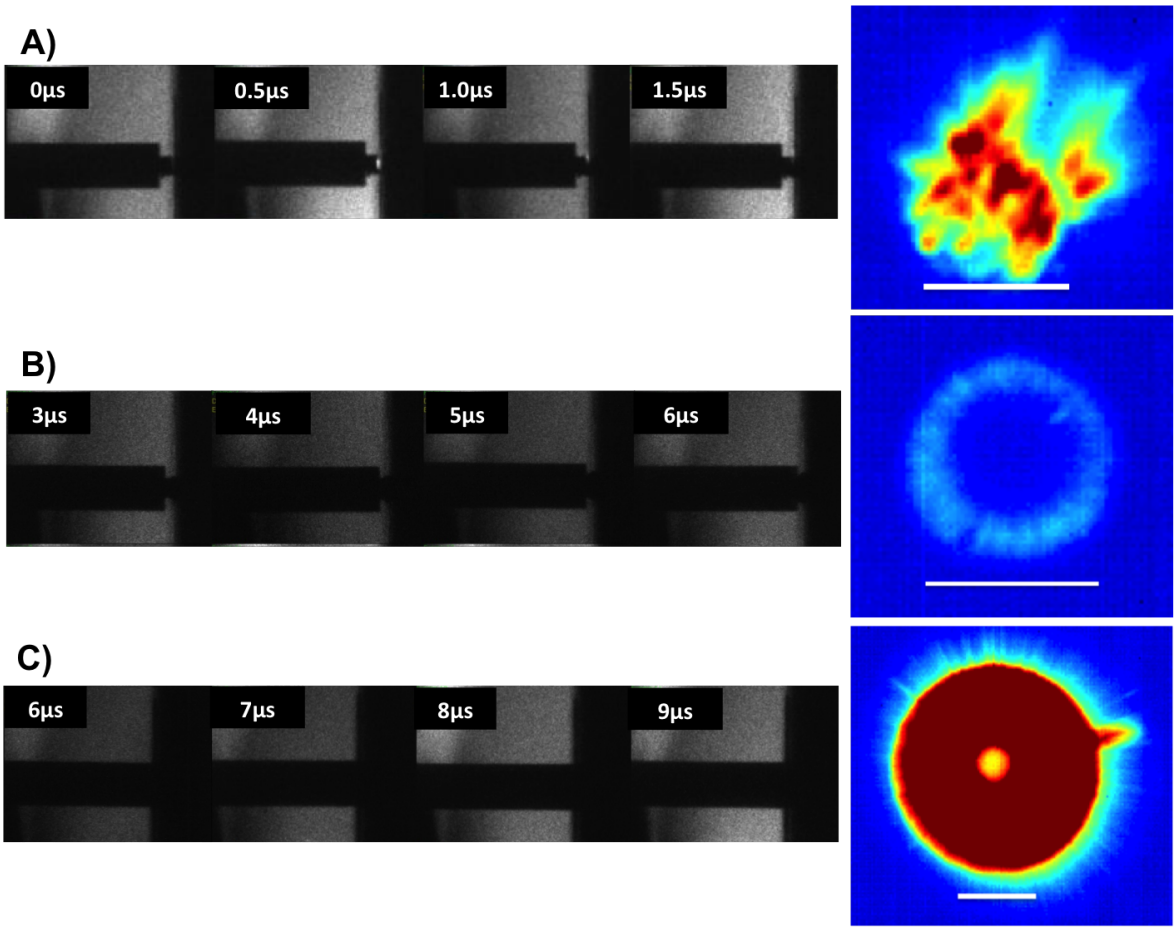

Figure 65: IMACON images captured from the profile of the impact and IR images captured from the impact face of the experiment during the same time frame as an H-60 powder compact impacts the anvil at approximately 210m/s. The white line represents the starting compact diameter, approximately 3.2mm. (A) Imacon and IR images captured during the crush-up phase, from 0 to 2 μs following impact. (B) Images captured during the deformation phase, from 3 to 7 μs following impact. (C) Images captured following complete deformation, from 6 to 10 μs following impact.

of the powder compact, shown in light blue, reached an average temperature of 195±12°C with temperatures ranging from 177 to 206°C, while the inner diameter of the compact remained at relatively low temperatures, 112±12°C. Figure 65 (c) provides the IR image captured during stage three of the impact process, during the sabot-anvil impact. Temperatures observed at this time point were much higher, reaching a maximum of 409±25°C. Again, the inner diameter of the powder compact remained at a low temperature, approximately 274°C, relative to the rest of the sample. Hot spots formed along the outer diameter of the pellet and typically reached temperatures of 393±24°C.

Figure 66 shows IMACON high speed framing camera and IR images of H-60 (A) and H-60 HEBM 30minute (B) powder compacts during deformation, from 3 to 6 μs after impacting the anvil at a velocity of 275 m/s. Both IR images, captured at an exposure time of 3 μs, show a low temperature inner diameter surrounded by a high temperature outer diameter, similar to the IR image presented in Figure 65 (B). The temperature of the H-60 sample varied from 136±7°C, at the center of the pellet, to 370±20°C at the center of one of the hot spots, while the average temperature within the diameter of the original pellet (given by the white bar) was approximately 253±15°C. Hot spots within the outer diameter of the pellet ranged in temperature from 238 to 364°C. The 30 minute HEBM sample shown in Figure 66 (B) had an average temperature of 269±16°C within the initial diameter of the pellet, but temperatures ranged from 153±7°C at the center of the pellet, to 336±14°C within some of the hot spots along the outer diameter of the pellet. In summary, similar temperatures and localized hots spots were observed in the H-60 and 30 minute HEBM samples during deformation at a velocity of 275m/s.

4.4 Summary of Results

Uniaxial stress rod-on-anvil impact experiments were performed on aluminum powder compacts of H-series Valimet powders with a range of particle diameters and of powders exposed to varying levels of mechanical pre-activation. Light emission, indicative

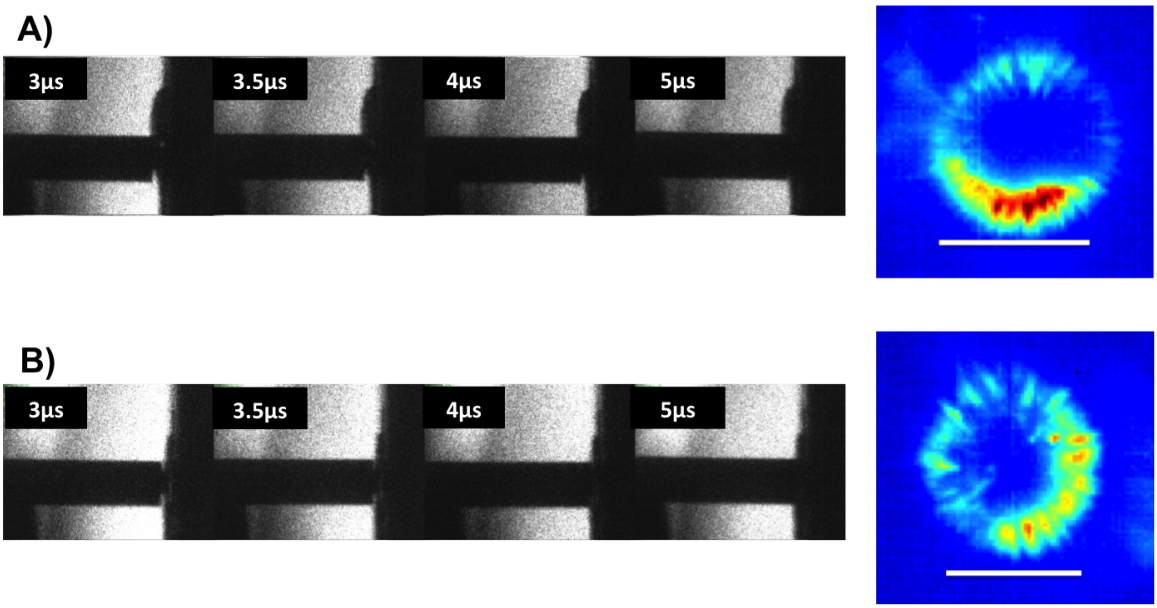

Figure 66: lMACON images captured from the profile of the impact and IR images captured from the impact face of the experiment during the same time frame as a powder compact impacted the anvil at approximately 275m/s. (A) Imacon and IR images captured during the deformation phase, from 3 to 6 μs following impact. (B) Images of H-60 HEBM 30minute captured during the deformation phase, from 3 to 6 μs following impact.

of reaction, was observed upon impact of the powder compact against the hardened steel anvil. Rod-on-anvil impact experiments were conducted at varying velocities and powder compact densities to determine the reaction threshold velocity for each powder type. The impact velocity, the powder compact density, and the light emission timing were plotted for each powder type investigated. These plots indicated the following results:

- As the particle diameter of the powders within the compacts increases, the reaction threshold velocity decreases.
- As the level of mechanical pre-activation of the powders within the compacts increases, the reaction threshold velocity varies in response. Initially, following 10 minutes of ball milling, the reaction threshold increases. Upon 30 minutes of ball milling, the reaction threshold velocity decreases. Last, upon 60 minutes of ball milling, the reaction threshold velocity increases.

- As powder compact density increases (or porosity decreases), the reaction threshold velocity shows a slight decrease for most aluminum powder types tested.

- Light emission timing varies with impact velocity and compact density for all H-series Valimet particles. Yet, the mechanically pre-activated particles typically initiated reaction (or first exhibited light emission) during the first stage of powder compaction.

Spatial images of temperature rise during impact were captured using the IR camera. The following trends and features of interest were observed:

- Images of the bulk profile temperatures indicate that samples typically reached temperatures ranging from 140°C to 210°C during deformation (at radial strain of $\sim$60%). Increased plastic deformation, to a radial strain of $\sim$100%, resulted in similar temperatures, ranging from 140°C to 201°C.

- In situ images of H-60 powder compact temperature rise at the impact face show that initially, during compaction, temperatures may reach 400°C. Yet, following compaction, during deformation, the outer diameter of the powder compact (the portion experiencing the highest levels of strain) exhibits the greatest temperature rise, up to only 200°C. During stage 3 of impact, as the aluminum compact is squeezed and highly strained between the sabot and anvil, aluminum temperatures reached 409°C.

- Impact face images of H-60 and 30 minute HEBM during the deformation stage at an impact velocity of 275 m/s show similar temperature rise to 350°C at the outer diameter of the straining aluminum powder compact.

Chapter V

IMPACT INITIATED REACTIONS: PROPERTY AND PROCESS EFFECTS

The processes influencing impact-initiated reaction and the effects of material properties on the initiation of the combustion reaction as evidenced by light emission in the various types of aluminum powders were investigated through logistic regression analysis of the kinetic energy threshold for reaction, and through a comparison of the light emission timing and the observed temperature rise with predictions from microstructure-based simulations. As discussed in the preceding chapter and as shown in Figure 59, the kinetic energy threshold for the impact-initiated combustion of aluminum is influenced by the type and size of the aluminum powder, as well as the level of mechanical pre-activation. In this chapter, a logistic regression analysis of reactivity is used to understand the influence of the powder characteristics, based on the properties of the aluminum powders measured in Chapter 3. Light emission timing is analyzed to understand the process and properties that contribute to reaction initiation. Additionally, images of temperature rise, captured by the IR camera during the compaction and deformation stages showing heating prior to the onset of combustion, are compared with predictions from 2-D microstructure-based simulations. The simulations reveal areas of localized strain and heating of the particles that vary in degree and magnitude as a function of powder properties and various stages of compaction and deformation. Correlations between experimental observations of temperature increase, with those predicted via computations are used to understand the processes leading to reaction initiation and the influence of various powder characteristics.

5.1 Logistic Regression Analysis of Reactivity Trends

In this section, logistic regression analysis is conducted to determine the influence of impact velocity and compact density on the occurrence of impact-initiated combustion reactions in aluminum. The likelihood of reaction initiation of combustion was observed to increase with increased velocity (due to increased kinetic energy input), allowing for the definition of a reaction threshold based on the minimum velocity required for reaction initiation. Additionally, the reaction threshold was observed to only be slightly decreased with an increased compact density. Last, increasing the particle size and mechanical pre-activation in the form of 30 minutes of high energy ball milling also decreased the reaction threshold. In order to analyze the effects of these multiple variables, the influence of impact velocity and compact density was separately studied through logistic regression analysis prior to determining the effects of starting particle size and level of mechanical pre-activation on impact-induced combustion reaction initiation of aluminum powder compacts.

Logistic regression is a modeling approach that can be used to describe the relationship between multiple independent variables and one dependent, binary response variable [149]. In the case of the rod-on-anvil impact-induced reaction initiation experiments, the dichotomous response variable would be the presence or absence of light emission indicative of a reaction. The independent variables are impact velocity, compact density, starting powder size, and level of mechanical pre-activation. The logistic regression analysis takes the following form,

$$\pi(x) = \frac{e^{\beta_0+\beta_1 x}}{1+e^{\beta_0+\beta_1 x}} \tag{30}$$

where β_0 is the intercept and β_1 is the parameter describing the behavior of independent variable *x*. As the number of independent variables increases, the expression in the exponential becomes $\beta_0 + \beta_1 x_1 + \beta_2 x_2 + ... + \beta_k x_k$. If there is no reaction, then $\pi(x) = 0$, and if a reaction is observed, then $\pi(x) = 1$. The impact velocity and reaction initiation relationship is shown graphically in Figure 67. In order to obtain a more meaningful, easier to use expression about the effect of the independent variable, *x*, the response, $\pi(x)$ is

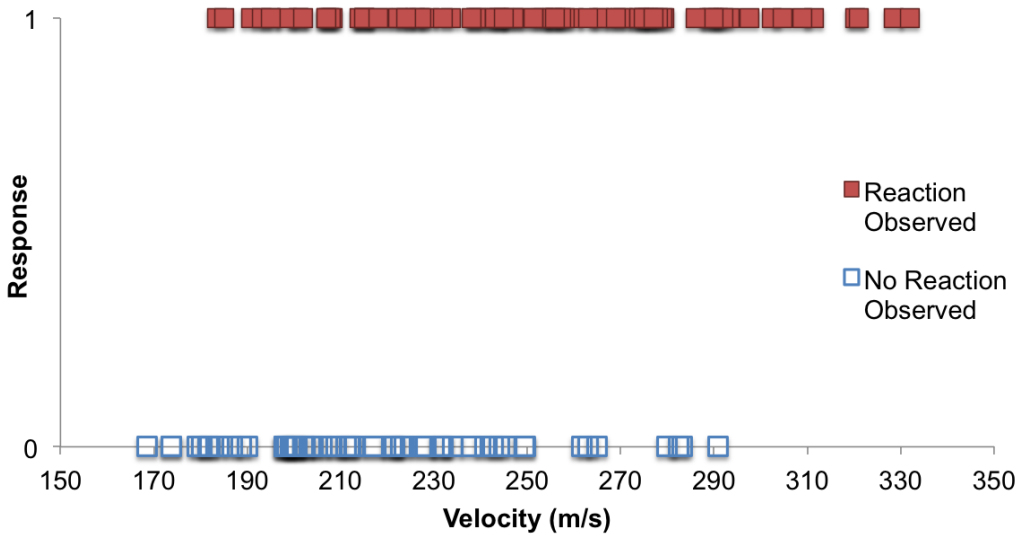

Figure 67: The reactivity and velocity relationship of all samples tested.

transformed using the following logit transformation, expressed as:

$$g(x) = ln\frac{\pi(x)}{1-\pi(x)} \tag{31}$$

$$g(x) = \beta_0 + \beta_1 x. \tag{32}$$

The logit transformation allows the logistic relationship to take on the properties of a linear regression, to be described as continuous, and to range from $-\infty$ to $+\infty$. Lastly, the error in a logistic regression centers on one of two values, either 0 or 1, and is expressed as a binomial distribution as opposed to a typical normal distribution.

In order to fit the logistic regression, the values for β_0 and β_1 must be obtained. The method of least squares, which is typically used to fit a linear regression, cannot be applied to a logistic model because of its dichotomous outcome. Instead, the method used to estimate unknown parameters for a logistic regression is based on the principles of the *maximum likelihood method* used for a linear regression. In short, the *maximum likelihood method* provides parameter estimates that maximize the probability of achieving the observed results [150]. First, a function, termed the *likelihood function*, is constructed. The *likelihood function* gives the probability of the observed results as a function of the

unknown parameters [150], in the form of,

$$l(\beta) = \prod_{i=1}^{n} \pi(x_i)^{y_i}[1 - \pi(x_i)]^{1-y_i} \tag{33}$$

This equation is achieved by assuming that $\pi(x) = 1$ represents the probability that the response is 1 (or a reaction is present) given x, and that $1 - \pi(x) = 0$ represents the probability that the response is 0 (or a reaction is not present). Therefore, for a pair, (x_i, y_i), the contribution to the *likelihood function* is $\pi(x_i)$ for $y_i = 1$ and $1 - \pi(x_i)$ for $y_i = 0$. This makes the contribution to the *likelihood function* for (x_i, y_i), $\pi(x_i)^{y_i}[1 - \pi(x_i)]^{1-y_i}$. By assuming that the observations are independent, the *likelihood function* given in equation 33 can be simplified. Next, in order to follow the method of maximum likelihood, the value of β that maximizes the *likelihood function*, $l(\beta)$, must be found. The log of $l(\beta)$, is a simpler form to work with. Therefore the equation above is converted to,

$$L(\beta) = \ln[l(\beta)] = \sum_{i=1}^{n} (y_i \ln[\pi(x_i)] + (1 - y_i) \ln[1 - \pi(x_i)]) \tag{34}$$

which gives us the *log-likelihood*. The β that maximizes the *log likelihood expression*, $L(\beta)$, is found by differentiating $L(\beta)$ with respect to β_0 and β_1 and setting the result to zero. The resulting likelihood equations,

$$\sum_{i=1}^{n} [y_i - \pi(x_i)] = 0 \tag{35}$$

$$\sum_{i=1}^{n} [x_i[y_i - \pi(x_i)]] = 0 \tag{36}$$

are nonlinear and require iterative methods that are typically completed by a statistical software program to find a solution and obtain the maximum likelihood estimate, $\hat{\beta}$, for each parameter [150]. In the case of the impact velocity and reactivity relationship, the statistical software, **JMP**, was used to calculate the intercept parameter, $\hat{\beta}_0$, to be 5.63$\pm$1.4, and the $\hat{\beta}_1$ parameter describing impact velocity to be -0.024$\pm$0.006, to give the logistic regression,

$$\pi(x) = \frac{e^{5.63 - .024 * \text{velocity}}}{1 + e^{5.63 - .024 * \text{velocity}}} \tag{37}$$

The negative log likelihood of the relationship was found to be 80.25.

Once the model has been fit using the *maximum likelihood method*, the significance of the model needs to be determined. The general approach to establishing whether or not a variable is significant is to compare the outcome of two models, one with and one without the variable in question, and then assess if the model without the variable in question provides as much information about the response as the model with that variable. For a linear regression, *analysis of variance* is typically used to determine the significance of a coefficient, but for a logistic regression, the comparison is based on the *log likelihood function*. Using the expression,

$$D = -2\ln\left[\frac{\text{likelihood of fitted model}}{\text{likelihood of saturated model}}\right] \tag{38}$$

one can compare the difference between the observed and predicted values. In this equation, *D* is the deviance and the expression within the brackets is termed the likelihood ratio. A saturated model contains the same number of parameters as data points. Therefore, for a logistic model, where the response is either 0 or 1, the likelihood of the saturated model is always 1, and *D* is simplified to,

$$D = -2\ln[\text{likelihood of fitted model}] \tag{39}$$

Now, the significance of the independent variable in question can be found by,

$$G = D(\text{model with variable}) - D(\text{model without the variable}) \tag{40}$$

or taking two times the difference between the negative log likelihood of the model with the variable and the model without the variable. Each variable or set of variables can be assessed by this method. When the impact velocity and reactivity relationship was assessed, the reduced model, which did not contain the parameter impact velocity, had a negative log likelihood of 90.09. Two times the difference between the negative log likelihood of the full (80.25) and the reduced model gives a G (or χ^2) value of 19.69.

In this study, the statistical software package **JMP**, was used to determine the effects of the impact velocity, powder compact density, particle size, and level of mechanical pre-activation on the reaction initiation response of aluminum powder compacts. For each independent variable tested, **JMP** calculates the maximum likelihood parameter estimate ($\hat{\beta}_0, \hat{\beta}_1, \hat{\beta}_2, ...$), the standard deviation of the estimate, the χ^2 of the estimate, and the P-Value. Additionally, **JMP** determines the significance of the *whole model*, by performing a *whole model test* and comparing the model containing all of the variables in question with a reduced model that contains no variables, only the intercepts. As described above, the difference between the *negative log likelihood* of the full and reduced models is found, and twice that value is used to determine the χ^2 for the *full model test*. Lastly, **JMP** provides a $Prob > \chi^2$ value, which gives the probability of obtaining a greater χ^2 value by chance alone, as opposed to if the full model fits no better than the reduced model [151]. This is similar to a p-value for the observed significance of a one tailed T-test. Small p-values indicate that there is a significant difference between the full and reduced model, and leads to the conclusion that the entire model or variables in question are significant. Whereas, large p-values indicate that a variable is not significant. Similarly, the **JMP** software can perform an *effect likelihood ratio test*, that assesses the significance of one variable by comparing the *negative log likelihoods* of the full model and a model without the variable in question. A resulting p-value of greater than 0.05 for a variable indicates that the variable is not significant to the model and can be ignored.

The logistic regression analysis can be a powerful tool to analyze the effects of different variables on the impact-initiated reactivity of aluminum but not all relationships can be understood by this analysis alone. The data set for each aluminum powder type (H-2, H-5, H-15, H-60, H-60 HEBM 10min, H-60 HEBM 30min, H-60 HEBM 60min, and highly strained platelets) contains different numbers of experimental observations that were made at various impact velocities and powder compact densities. Therefore, the logistic regression analysis can be used to investigate the effects of certain variables on one set

Table 6: Logistic analysis of impact velocity effects on reactivity. P-values indicating that a relationship is significant are given in bold.

	Number of Observations	(-)Log Likelihood	Chi Square	Effect Likelihood Ratio P-value
All samples	142	12.8	25.6	**<.0001**
H-2	17	5.17	10.34	**.0013**
H-5	21	7.16	14.32	**.0002**
H-15	24	0.35	2.94	.0858
H-60	29	3.11	6.22	**.0127**
H-60 HEBM 10 min	14	1.8	3.6	.0581
H-60 HEBM 30 min	11	0.22	0.44	.506
H-60 HEBM 60 min	10	0.28	.506	.128
Highly strained Al	16	2.1	4.2	**.0405**

of observations but cannot be used to quantitatively compare differences between sets of observations.

5.1.1 Reactivity as a function of impact velocity

Throughout Section 4.2 and in previous studies [7, 10, 11], reaction initiation has been observed to be a function of impact velocity. Hence, the reaction initiation of each sample type was examined as a function of the independent variable of velocity using a logistic regression analysis. The results of the logistic regression analysis are shown in Table 6. P-values of less than 0.05 (indicated in bold) from the *effect likelihood ratio test* reveal that velocity is significant for powder compacts of all aluminum types and, separately, compacts of H-2, H-5, H-60, and highly strained platelet aluminum powders.

Velocity was shown to not be as significant for H-15, H-60 HEBM 10 minute, H-60 HEBM 30 minute, and H-60 HEBM 60 minute aluminum powder. In the case of the HEBM samples, this discrepancy may partially be due to the small number of experiments performed for each of these sets of tests. Additionally, in these samples, only a small range of impact velocities, near the reaction threshold, were tested. In the absence of data points at much higher and much lower impact velocities than the threshold velocity, the dependence of reaction initiation on impact velocity is not observable by the logistic

regression analysis.

In the case of compacts composed of H-15 powder, 24 experiments were performed in order to determine the threshold impact velocity for reaction initiation. Yet, the logistic regression analysis indicates that impact velocity is not significantly related to reaction initiation response in these samples of this type of aluminum powder. Velocity may not be significant in this set of samples due to the possible heterogeneous nature of reaction initiation. Should reaction initiate in localized areas throughout the compact and not in the bulk, minor differences in microstructure and pore size and distribution from one compact to the next may play a slightly larger role in initiating reaction than impact velocity. Additionally, occurrence of reaction initiation was evidenced based on images captured by the high speed camera, only capable of probing two dimensions, in profile, of the reaction initiation event. It is possible that reactions that took place in a plane outside of view of the camera are undetected.

5.1.2 Reactivity as a function of powder compact density

The reaction initiation results presented in Figure 58 indicate that powder compact density in the range of 80% to 99% dense has a slight effect on the impact initiation of a combustion reactions in aluminum powders. Samples with a compact density of 80% to 90% TMD had a higher reaction threshold than samples with a higher compact density of 90% to 100% TMD. To further analyze this effect, the reaction initiation results for each sample type were examined as a function of the independent variables of impact velocity, compact density, and impact velocity*compact density by a logistic regression. As shown in Table 7, the p-values from the effect likelihood test again reveal that velocity is significant for powder compacts composed of all aluminum types and, separately, for aluminum powder compacts composed of H-2, H-5, H-60, H-60 HEBM 10min, and highly strained platelet powders. The variables of density and density*velocity do not play a significant role in increasing the likelihood of reaction initiation within the range of densities investigated. Only highly

Table 7: Logistic analysis of velocity and density effects on reactivity. P-values indicating that a relationship is significant are given in bold.

	Whole Model Test			Effect Likelihood Test		
	(-) Log-Likelihood	Chi Square	P-Value	Velocity P-Value	% Density P-Value	Velocity*%Density P-Value
All Samples	12.85	25.704	**<0.001**	**<0.001**	.9786	.7482
H-2	6.31	12.62	**0.0055**	**0.007**	.4476	.1337
H-5	7.62	15.24	**0.0016**	**0.006**	0.4119	0.4608
H-15	1.64	3.28	0.35	0.0754	0.5649	0.9421
H-60	4.5	9	**0.0293**	**0.0109**	0.0998	0.3936
H-60 HEBM 10min	5.13	10.26	**0.0165**	**0.015**	0.0861	0.1674
H-60 HEBM 30min	1.72	3.44	0.3285	0.1209	0.1017	0.4117
H-60 HEBM 60min	2.53	5.06	0.168	0.0847	0.16	0.6097
Platelets	5.78	11.56	**0.009**	**0.00019**	**0.0137**	0.0726

strained platelets showed compact density to be significant, but they did not show compact density*impact velocity to be significant to reaction initiation. Therefore, throughout the rest of this work, the compact density is not considered as a dependent variable for reaction initiation; only impact velocity is included in the logistic regression analysis.

The logistic regression analysis indicates that varying the compact density within the range of 80% to 100% TMD does not statistically have an effect on the reaction initiation threshold. A more targeted study of one powder type with a greater range of compact densities, such as 60% to 100% TMD, which was studied by Herbold *et. al.* [11] and observed to have an effect on the reaction threshold, may show that compact density is significant over a larger range of compact densities. As discussed in Section 2.2.4, several researchers [69, 64, 71] have noted that lower compact density leads to increased void space, which increases the availability of deformation paths and its extent. Because particles are able to more easily move through the open pore space, less strain and heating occur on the particle level within the sample, decreasing the likelihood of reaction initiation.

Table 8: P-values resulting from the logistic analysis of velocity and size, S_v, or SSA effects on reactivity. P-values indicating that a relationship is significant are given in bold.

	H-2, H-5, H-15, H-60			All Samples		All Samples, Except Platelets		
	x = Size	x = S_v	x = SSA	x = Size	x = S_v	x =Size	x = Sv	x = SSA
Sample Size		91			142		126	
x	0.066	0.397	.156	0.132	**0.0076**	0.1583	**0.025**	**0.0072**
Velocity	**<.001**	**<.001**	**<.001**	**<.001**	**<.001**	**<.001**	**<.001**	**<.001**
x*Velocity	0.207	**0.0108**	**0.014**	0.356	**0.021**	0.486	**0.015**	**0.011**

5.2 Effects of aluminum powder characteristics

5.2.1 Reactivity as a function of aluminum powder surface area

The dependence of the reaction initiation threshold was analyzed with respect to the average powder size, the surface area per unit volume ratio of the powder compacts (S_v), and the specific surface area of the powders (*SSA*). The following three sample populations were investigated: the H-Series Valimet aluminum powders, all samples, and all samples except for platelets. Table 8 provides the effect likelihood test p-values for the independent variables of size, S_v, *SSA*, and velocity, and velocity*size, velocity*S_v, and velocity**SSA*. As demonstrated previously, in Table 6, velocity is significant for all sample populations and variables tested. Average particle size and average particle size*velocity were not significant for all populations tested. For a sample population composed of only H-series Valimet aluminum powder samples of various sizes, neither S_v nor *SSA* are significant on their own. Yet, velocity*S_v and velocity**SSA* are significant. For a sample set composed of all samples tested, S_v alone was not significant, but velocity*S_v was significant. For a sample set composed of all samples except platelets, S_v and velocity*S_v and *SSA* and velocity**SSA* were significant.

The analysis shows that reaction occurrence is not directly dependent on particle size, which reveals that average particle size alone does not capture the effects of microstructural characteristics on reaction occurrence. Instead, S_v and *SSA* provide a better description of the microstructural characteristics of each powder, because they are a better measure of the

surfaces available for reaction. In general, an increase in the S_v of the powder compact and an increase in the *SSA* of the particles that make up the powder compact will increase the surface area of the inter-particle contact points. A higher surface area of contact points can either increase or decrease the likelihood of reaction. If reaction initiation is driven primarily by the availability of reactant at the interface, as observed by Hunt and Pantoya [64], or is similar to thermally-induced combustion initiation, as described in Section 2.1, which occurs at decreasing temperatures as particle size decreases [25, 26, 27, 28], then an increase in the surface area (or a decrease in the particle size) of aluminum would increase the likelihood of a reaction. Yet, if increased strain and heating at the interface are required to drive the combustion reaction, then samples composed of smaller particles are less likely to react due to the more uniform distribution and averaging of strain resulting in the greater number of lower stress inter-particle contacts. As described in Section 2.2.4, Chiu *et. al.* [70] observed that Al + W composites composed of fine W particles had a much higher dynamic strength than composites made with coarse particles, due to the strong "force-chains" that were created by the fine particles that came in contact with one another over a larger surface area than the coarse particles. Additionally, Olney [71] observed that coarser W particles resulted in more kinks in the shear band path of the Al, as it was forced to undergo localized high strain flow as it moved around the coarse W particles. Compacts composed of larger aluminum particles, with less surface area, take on higher localized stress due to the fewer contacts and lower surface area of interfaces, thereby resulting in higher temperature and strain at those interfaces.

The plot in Figure 68 (a) directly compares the reaction threshold for compacts composed of Valimet H-series aluminum particles as a function of increasing size/decreasing surface area per unit volume. It can be seen that the velocity threshold for reaction decreases as particle size increases (and correspondingly the particle surface area decreases). The dependence of reaction initiation directly on surface area alone points to a micro-mechanically dominated reaction initiation mechanism, where stress built up during the

impact process is intensely localized, in the form of strain and heat due to the fewer particle surfaces available in compacts composed of larger particles.

Figure 68 (b) shows the light emission timing and the reaction threshold of compacts composed of mechanically pre-activated aluminum particles. As HEBM time increases, S_v increases, but the reaction threshold varies with HEBM time and, thus, S_v. As the S_v increases to 167mm^{-1} with 30 minutes of ball milling, the reaction threshold reaches the lowest velocity observed for any sample. Yet, similar to the H-series Valimet particles, as the S_v continues to increase in highly strained platelets and H-60 60 minute HEBM samples, the reaction threshold velocity increases. Such a correlation between the reaction threshold and the S_v points to either a minimum S_v of 167mm^{-1} required for reaction initiation or to an enhancement of reactivity due to the strain-hardening and deformation imposed on the powders during the mechanical pre-activation process.

5.2.2 Reactivity as a function of mechanical properties

The influence of mechanical pre-activation on the likelihood of impact-initiated combustion of aluminum powders was further evaluated by comparing the velocity threshold for reaction initiation with the yield strength of the mechanically pre-activated aluminum powders. Sample populations composed of all powders and all powders except for platelets were investigated. Table 9 provides the p-values for the effect likelihood ratio test. As shown previously, impact velocity has significant effect on reaction occurrence for all sample populations. The p-values for yield strength and yield strength*velocity for all sample populations were above .05, indicating that yield strength alone does not correlate directly to the likelihood of reaction initiation.

The plot in Figure 69 compares the impact velocity threshold for reaction initiation in compacts of powder particles of increasing mechanical yield strength via pre-activation. It can be seen that the velocity threshold for reaction occurrence initially decreases with mechanical pre-activation, up to 30 minutes of high energy ball milling, and then increases

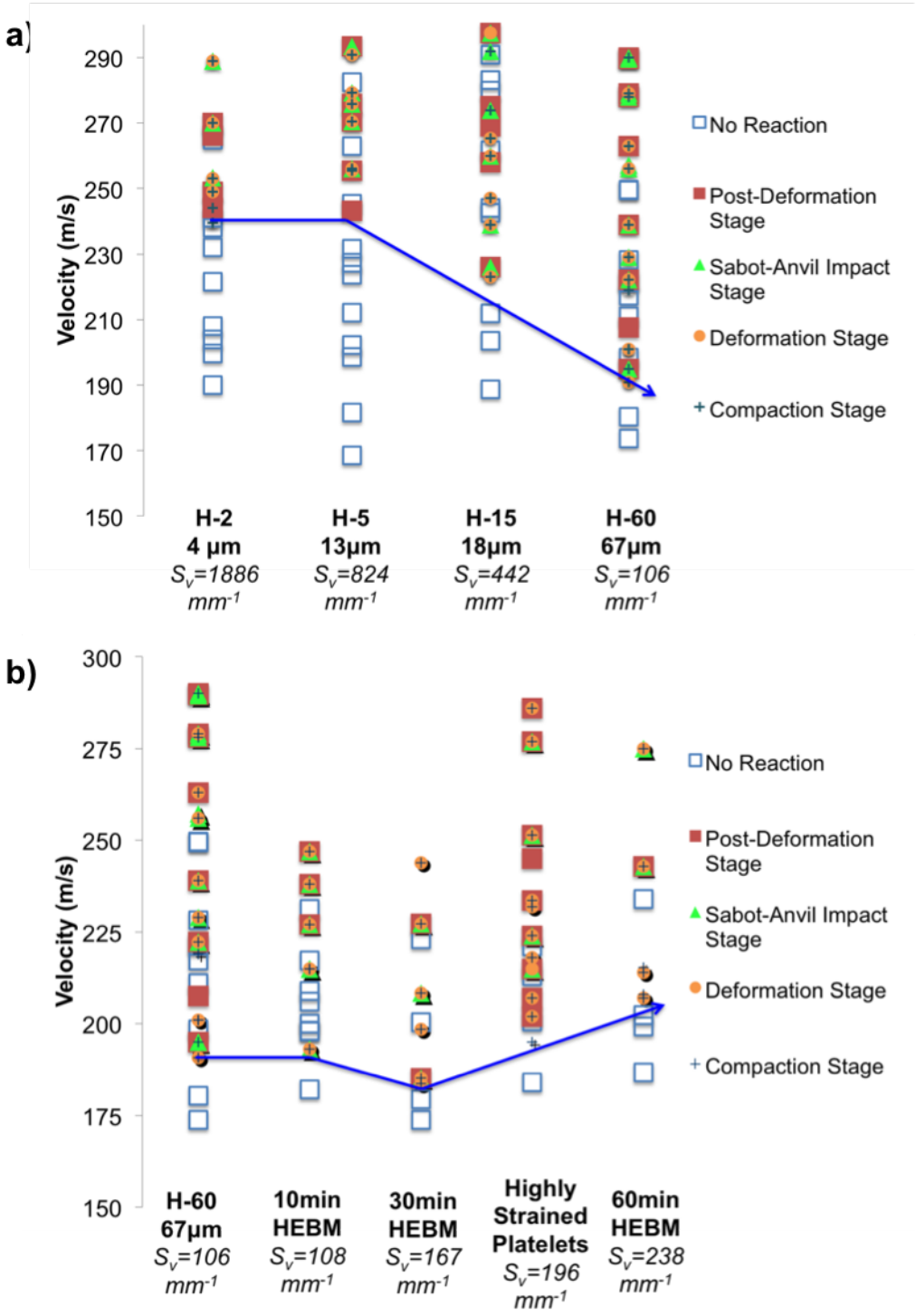

Figure 68: A comparison of the reactivity of powder compacts as S_v changes. (a) Reactivity of Valimet H-series powders. (b) Reactivity of mechanically pre-activated powders.

Table 9: Logistic analysis of velocity and yield strength effects on reactivity. P-values indicating that a relationship is significant are given in bold.

	All Samples	All Samples, Except Platelets
Yield Strength P-Value	0.305	0.118
Velocity P-Value	**<0.001**	**<0.001**
Yield Strength * Velocity P-Value	0.425	0.144

with continued mechanical pre-activation. As described in Section 2.2.6, Herbold *et. al.* [11] observed a similar trend in powder mixtures of Ni+Al that had been mechanically pre-activated by HEBM. Initially, after HEBM for a short time duration, the Ni+Al powder mixtures exhibited a lower velocity threshold for reaction, and with continued milling, the threshold velocity increased with milling time. Herbold suggested that HEBM leads to the exposure of fresh reactive surfaces and begins to individually deform the particles. The enhanced particle deformation during HEBM brings the constituents (or particles) in close contact with clean (nascent) surfaces. The increased availability of fresh reactive surfaces results in a decrease in the impact velocity threshold for reaction initiation. Longer periods of HEBM cause strain hardening in the particles, increasing the particle yield strength and making them more resistant to plastic deformation. As plastic deformation becomes more difficult, a greater amount of impact (kinetic) energy is required to achieve the amount of plastic strain needed to trigger the combustion reaction. Hence, with increasing strength of powders more energy is dissipated during the compaction and deformation process, leaving less impact (kinetic) energy available for reaction initiation.

The trends in reaction occurrence as a function of increasing aluminum powder particle strength, illustrated in Figure 69, demonstrates that as particle yield strength increases, powder compaction and deformation requires larger amounts of energy dissipation, which raises the kinetic (impact) energy threshold for reaction initiation. The increase in the velocity threshold for reaction with an increase in particle strength illustrates the combined influence of energy consumption (due to plastic deformation) and energy availability (from

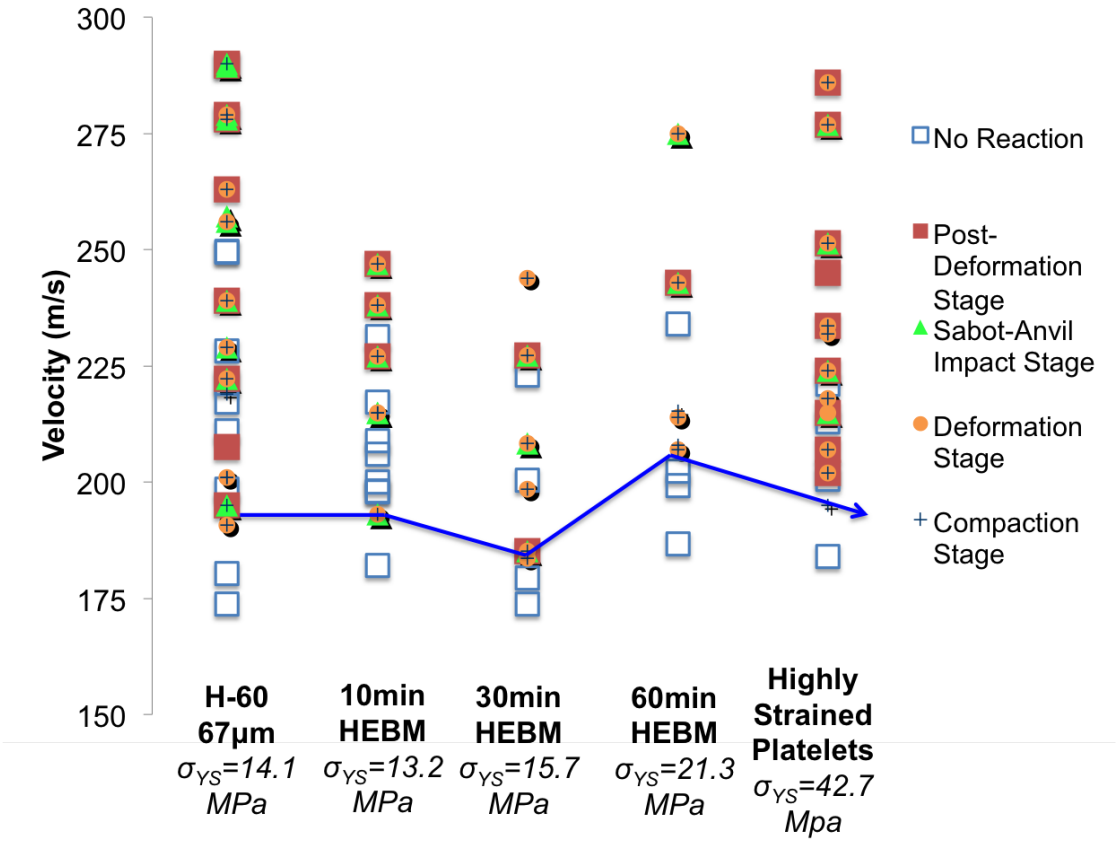

Figure 69: A comparison of the reactivity of powder compacts as mechanical pre-activation increases.

Table 10: Logistic analysis of velocity and compaction property effects on reactivity in all samples except for platelets. P-values indicating that a relationship is significant are given in bold.

	x = Effective Yield Strength	x = Compaction Energy
x P-Value	**.015**	**0.002**
Velocity P-Value	**<0.001**	**<0.001**
x * Velocity P-Value	0.528	0.122

the kinetic energy at various velocities) for the aluminum powder compact systems.

5.2.3 Reactivity as a function of compaction behavior

The compaction behavior of a powders is a function of the initial density of the powder compact, the powder particle morphology, and yield strength of the components [79]. These properties in turn influence the pressure versus density compaction curves, effective yield stress (corresponding to pressure needed to reach full density) and the compaction energy, or the work of densification of the powders. Similar to particle yield strength, the compaction energy and effective yield stress provide a measure of the resistance to powder compaction a sample is likely to exhibit. The compaction energy and effective yield strength also take into account the morphology of the particle, in terms of the surface area, the number of interparticle contact points (and area), and the density of the powder compact. The effect likelihood ratio test p-value for indicating the dependence of reaction occurrence on the effective yield strength, compaction energy, and impact velocity of a sample are provided in Table 10. The logistic regression analysis in fact indicates that the likelihood of reaction initiation is dependent on the compaction energy and effective yield strength.

5.2.4 Reactivity as a function of particle size distribution

Particle size distribution could not be directly analyzed by the logistic regression analysis, but variations in particle size distribution can play a role in micromechanical processes

and the energy needed for the compaction and deformation stage. All H-series aluminum particles exhibited a normal particle size distribution; whereas, HEBM powders revealed an increasingly bimodal particle size distribution as ball milling time increased. As discussed in Section 2.3.3 and illustrated in Figure 16, Williamson's [84] computational study of the compaction of cylindrical rods showed that particle size distribution directly effects the generation of the the peak temperature at the interstitial sites. The narrow, normal particle size distribution of the H-Series aluminum powders makes particle packing difficult, resulting in particle-particle contacts over minimal surface areas and well-dispersed void volume. During compaction, these powders, of normal particle size distribution, deform rapidly to fill in the void space, depositing energy and resulting in high temperature generation at the particle surface. A wide or a bimodal particle size distribution allows the small particles to settle and fill the interstitial space in between the large particles, thereby increasing the surface area of contact between particles and decreasing the void volume between the extremes in particle sizes; consequently, resulting in lower peak temperatures as shown by Williamson's computational study [84] and less likelihood of reaction initiation.

In order to investigate the effect of particle size distribution on reaction initiation, bimodal mixtures of aluminum powders were prepared. Mixtures with a bimodal size distribution were created by combining H-60 and H-2 powders in a 1:3 and a 3:1 ratio and mixing in a V-blender for 24 hours. Figure 70 shows micrographs of compacts composed of the 1:3 (a) and 3:1 (c) H-60:H-2 powder mixtures. Schematic representations of these mixtures are also illustrated in Figure 70 (b) and (d). Figure 71 plots the reaction occurrence for these mixtures as a function of the impact velocity. The left two columns in the figure show that as smaller, higher S_v, H-2 particles are added to H-60 particles, the reaction threshold increases as the S_v of the mixture increases. The right two columns show that as larger, lower S_v particles are added to H-2 particles, the S_v of the mixture decreases and the reaction threshold decreases. This behavior is expected based on the earlier observation, in Section 5.2.1, that the reactivity threshold decreases with a decrease in the S_v (or

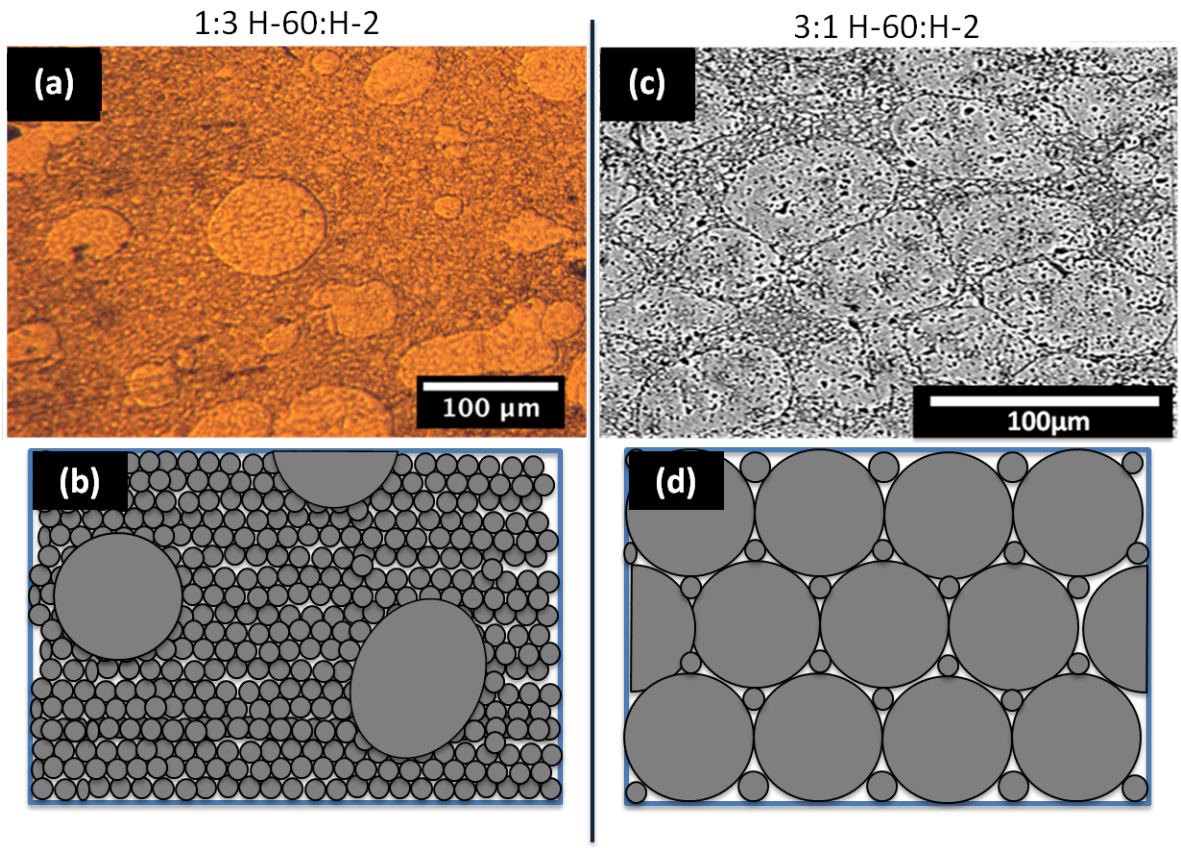

Figure 70: Optical micrographs of compacted (a) 1 to 3 and (c) 3 to 1 by volume mixture of H-60 to H-2. Schematic representations of compacted (b) 1 to 3 (d) 3 to 1 by volume mixture of H-60 to H-2

increase in size) of the Valimet H-series aluminum particles.

A comparison between the reaction threshold of the two types of bimodal powder compacts reveals that there is very little difference between the minimum velocity threshold required for reaction initiation in the mixtures. Yet, powder compacts composed of 1:3 H-60:H-2, the mixture with a higher S_v, were much more likely to initiate and sustain the reaction through complete deformation at velocities above the threshold velocity. The increased reactivity in the higher S_v, 1:3 H-60:H-2, powder mixture over the lower S_v, 3:1 H-60:H-2 powder mixture may, be due to the effects of particle size distribution. As shown in the micrograph and schematic in Figure 70 (c) and (d), a powder compact composed of

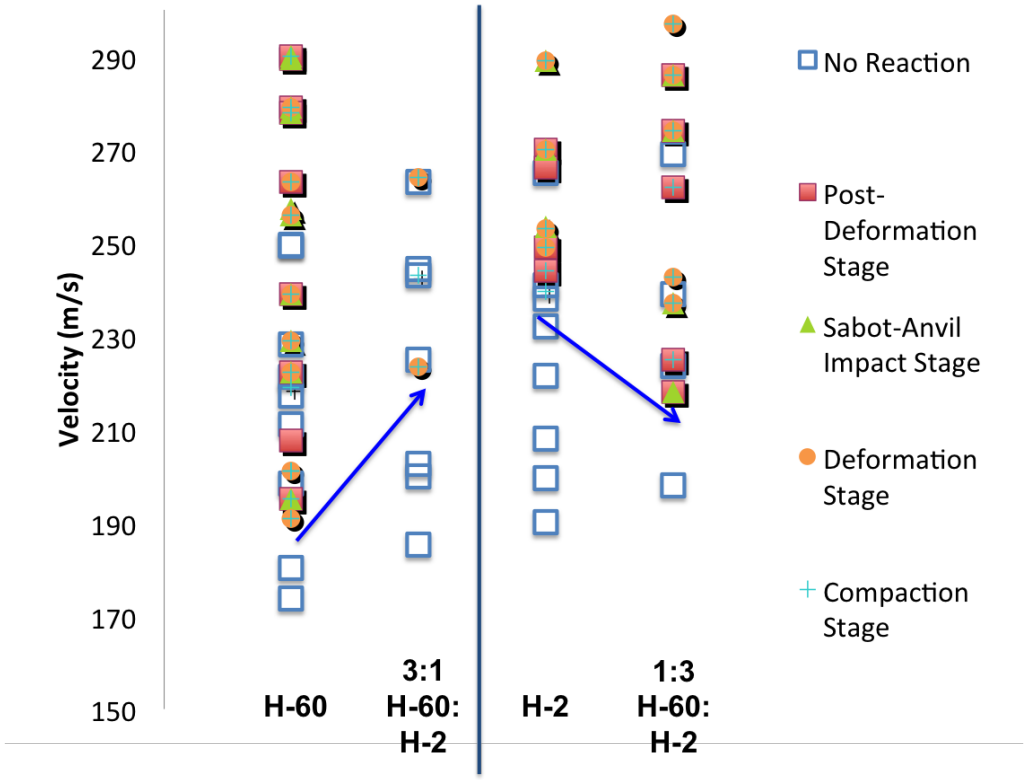

Figure 71: A comparison of the reactivity of powder compacts composed of a bimodal particle size distribution.

3:1 H-60:H-2 allows the smaller H-2 particles to settle into the interstitial space surrounding the larger H-60 particles. Whereas, the micrograph and schematic in Figure 70 (a) and (b) illustrate that a compact composed of the 1:3 H-60:H-2 powder mixture more closely resembles the H-2 microstructure with the addition of a few larger H-60 particles scattered throughout the H-2 particles. According to the study by Williamson [84], impact of a bimodal mixture similar to the 3:1 H-60:H-2 powder compact should result in lower peak temperatures at the particle interfaces and, thus, a decrease in the likelihood of that powder mixture to initiate reaction, consistent with the results observed in the present study.

5.2.5 Reactivity as a function of other effects

Other effects, such as the presence of an oxide layer on aluminum powders can also play a role in influencing the impact initiation of reactions in aluminum powder compacts. There can be competing effects as a result of the aluminum oxide layer. In particles of just a few microns in diameter or less, the temperature required for the ignition of combustion decreases due to a combination of aluminum oxidation kinetics, alumina shell phase transitions, and higher likelihood of cracking of the alumina shell [25, 26, 27, 28]. Alternately, as particle size decreases, the surface area per unit volume increases, resulting in an increase in the volume percent of the oxide layer relative to the aluminum reactant, which in turn can decrease the likelihood of reaction initiation. Assuming a 4 nm thick alumina shell [152], the volume percent of aluminum oxide for an H-60 aluminum powder compact is $\sim$0.04%, while the volume percent of oxide in compacts composed of the smaller H-2 particles is $\sim$0.75%. Results of the effects of particle size indicate enhanced likelihood of reaction initiation with larger particle size, but these do not appear to illustrate any obvious effects of the oxide layer on reactants.

5.3 Investigation of Post-Impact Processes Leading to Reaction

Direct information about the processes contributing to reaction, whether localized or bulk in nature, can be gained by (a) analyzing the light emission timing, (b) collecting temperature measurements during the impact event, and (c) comparing these observation with microstructure-based simulations. Analysis of the differences in the reaction light timing between each of the aluminum powder types may provide insight into the impact stage (compaction, deformation, sabot-anvil impact, or post deformation) that plays the most dominant role in reaction initiation. *In situ* temperature measurements provide information about the maximum temperatures achieved during the compaction and deformation process. In the absence of diagnostics available to probe temperature and pressure in the interior of the compacts, microstructure-based simulations provide information about the localized behavior of compacts and the particle-particle interactions, which can be correlated to measurements of temperature and light emission timing.

5.3.1 Summary of Results Based on Light Emission Timing

As described in Section 4.1.2, during rod-on-anvil impact experiments, light emission indicative of reaction can occur during initial compaction, deformation, sabot-anvil impact, or following complete deformation. Figures 50 to 57 in Chapter 4 display the light emission timing for each aluminum powder type as a function of compact density and impact velocity. Trends in reaction light timing may reveal information about the processes underlying the initiation of light emission.

Figure 72 illustrates the light emission timing as a map plotting the impact velocity and compact density (%TMD) for all H-series Valimet and mechanically pre-activated powders tested. Each filled data point indicates the stage corresponding to which light emission as indication of reaction was observed, while the open squares correspond to indication of no reaction. When all powders are considered together, it is difficult to detect any obvious trends in the light emission timing. At impact velocities of less than 200 m/s, light emission,

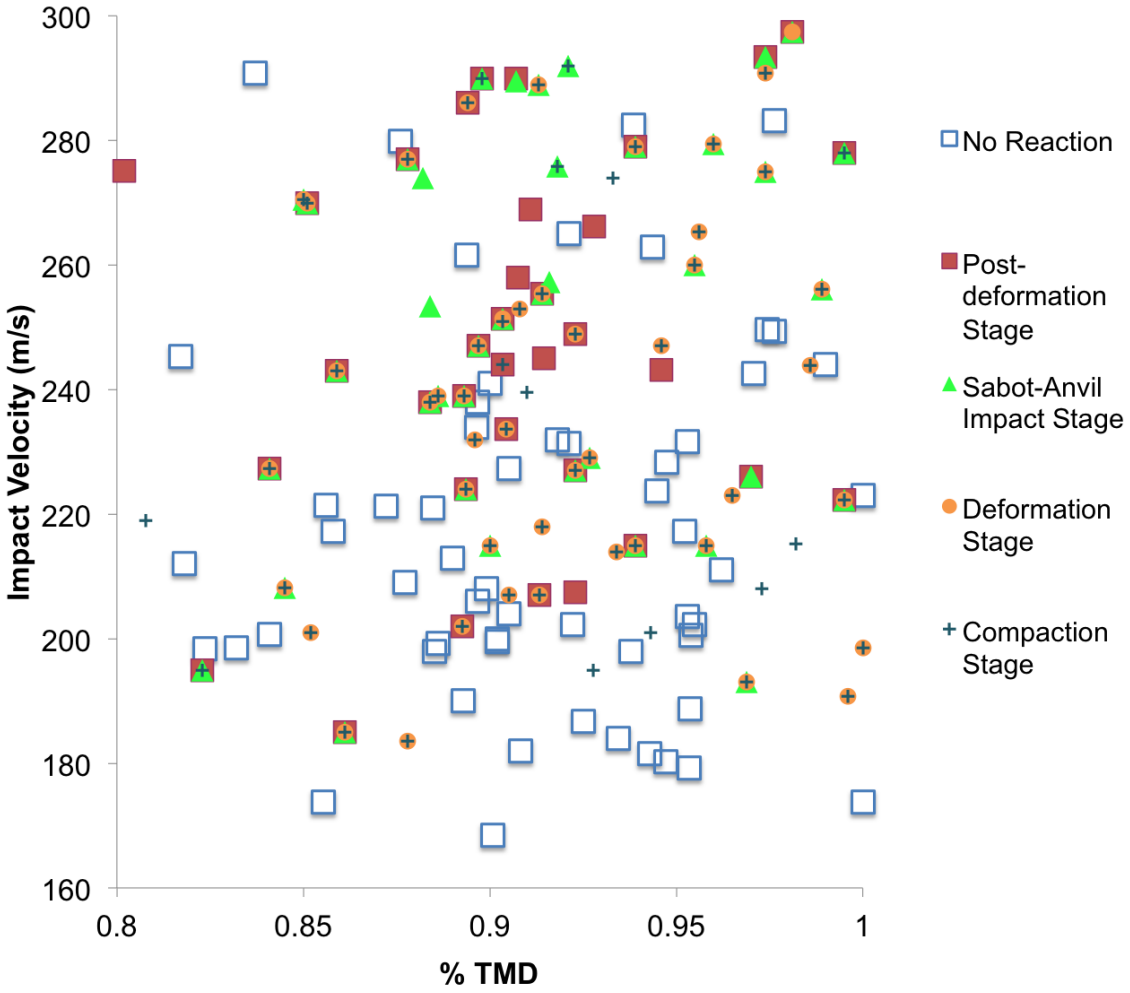

Figure 72: Light emission timing of all powders tested.

if any, is observed to begin almost immediately after the aluminum sample impacts the anvil, that is, during the compaction stage. Additionally, the lower right hand quadrant of the plot reveals conditions (impact velocity of less than 210m/s and %TMD of greater than 93%) under which reactions initiate during the crush up stage but are not sustained past the stage of sabot-anvil impact.

Figure 73 (a) plots the light emission timing of the H-series Valimet powders and (b) all of the mechanically pre-activated aluminum powders, both HEBM and platelets, as separate maps. In the map for the H-series Valimet powders, no obvious trend emerges.

It can be seen that light emission begins and ends at different stages of impact within the impact velocities and compact densities tested. Yet, in the mechanically pre-activated powders plotted in Figure 73 (b), two trends are noted. First, above compact densities of 95% TMD, reaction always initiates during the crush-up stage and is not sustained past the sabot-anvil impact. Second, light emission began during crush-up in almost all samples that reacted (28 of 30).

Map corresponding to the light emission timing of the fine H-series Valimet powders (H-2, H-5, and H-15) are plotted in Figure 74 in order to narrow in on any possible trends in the emission timing of the H-series Valimet particles. The plot in Figure 74 (a) shows the light emission timing of compacts of Valimet H-2, H-5, and H-15 powders, and the plot in Figure 74 (b) shows the light emission timing of compacts of Valimet H-2 and H-5 powders. Although the sample population was narrowed to the finest H-series Valimet aluminum powders, light emission timing trends are still not evident in either sample population.

The map corresponding to the light emission timing of only the HEBM samples, without the highly strained platelets is plotted in Figure 75. The plot of only HEBM light emission timing reveals that light emission from all HEBM samples began during the crush up stage. Again, as shown in Figure 73 (b), light emission and therefore the combustion reaction is not sustained past the sabot-anvil impact in any HEBM samples with a compact density of greater than $\sim$93%. These trends can be used to better understand the processes leading to reaction.

HEBM samples of greater than $\sim$93% density reveal that the reaction was not sustained past the sabot-anvil impact for any velocity tested. Figure 75 also shows that all low density (less than 93%TMD) compacts that were shot at an impact velocity above 220 m/s sustained reaction past complete deformation. Together, these trends point to a link between compact density and reaction initiation. Increased porosity causes localized heating due to void collapse which can lead to the initiation and perpetuation of the impact-initiated reaction, as observed in the mechanically pre-activated aluminum powder compacts.

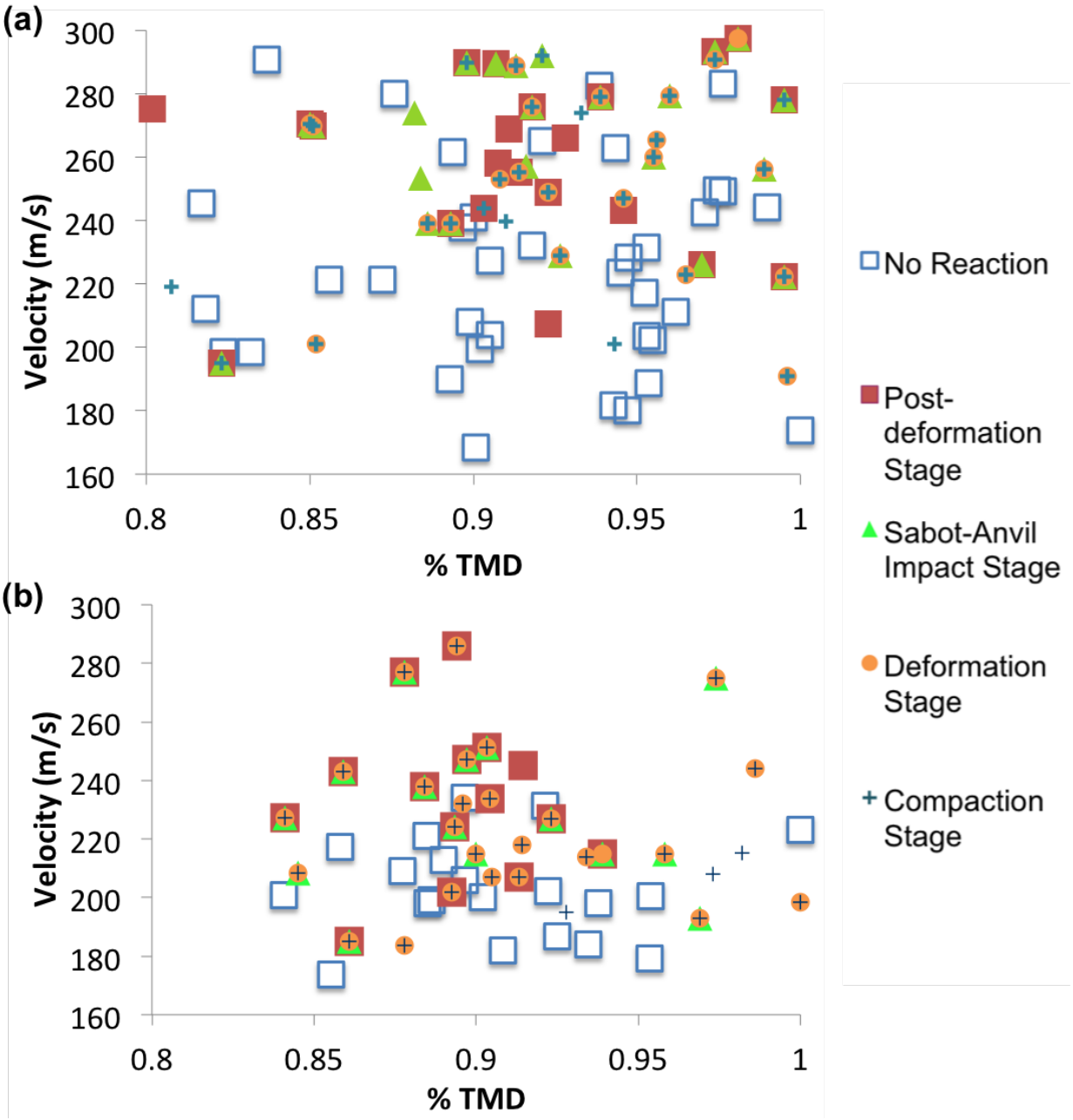

Figure 73: Light emission timing of H-series Valimet (a) and mechanically pre-activated powders (b).

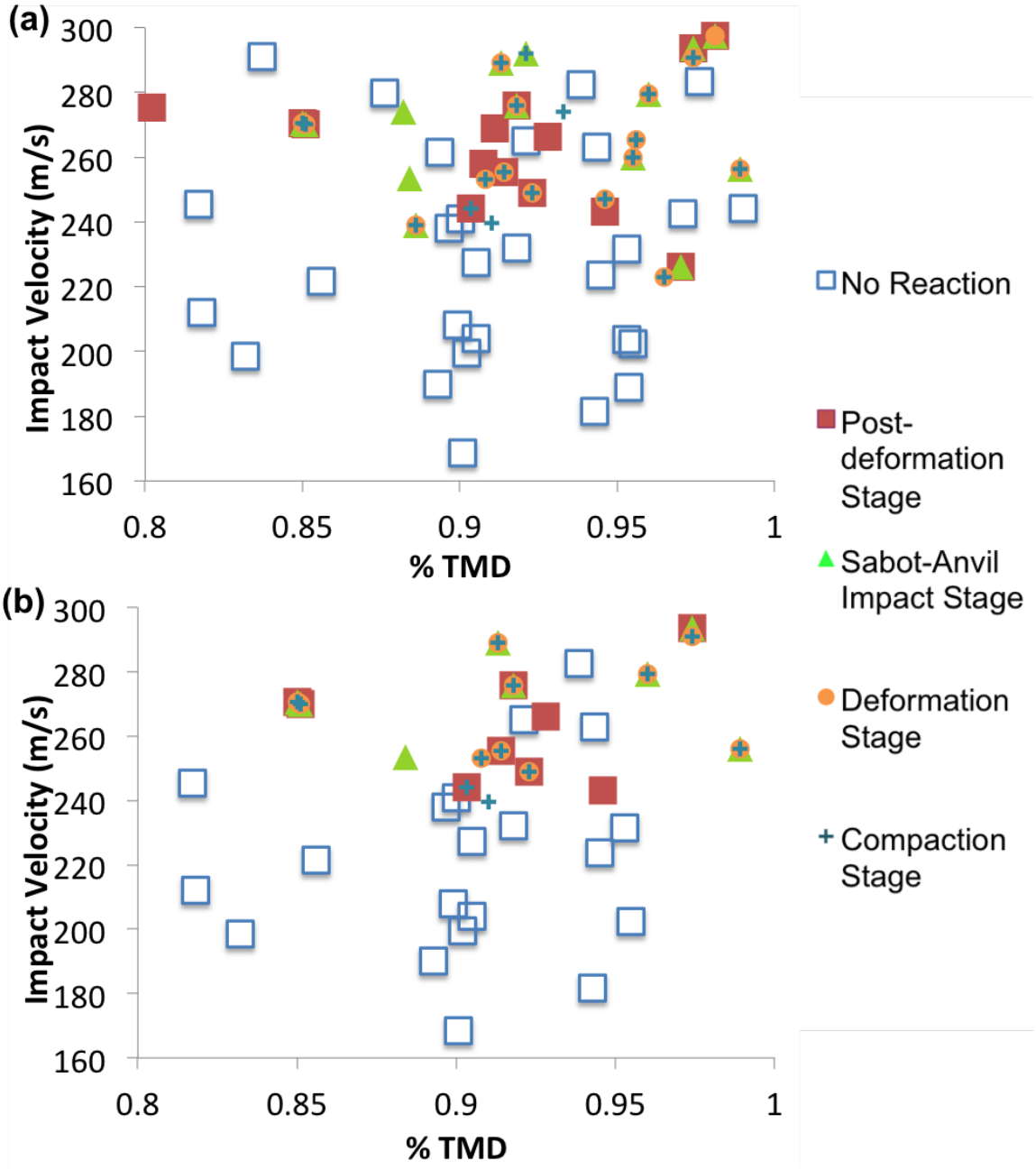

Figure 74: Light emission timing of fine H-series Valimet powders: H-2, H-15, and H-15 (a) and H-2 and H-5 only (b).

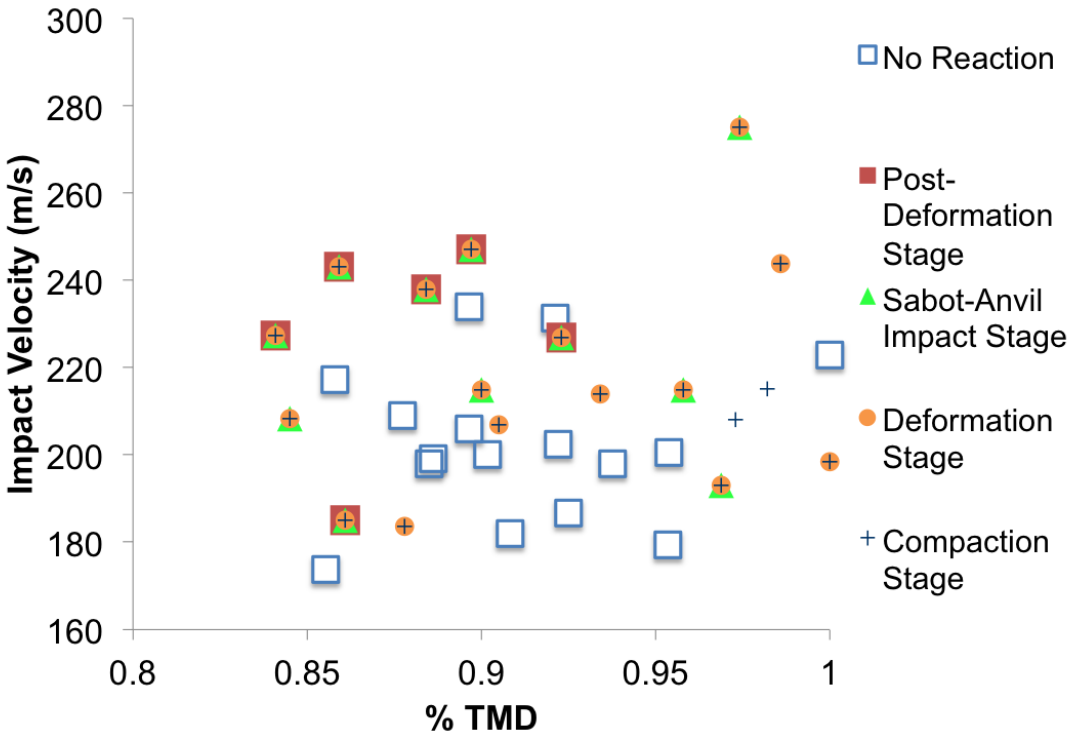

Figure 75: Light emission timing of HEBM powders.

All reactive HEBM samples initiated reaction during the compaction stage. This trend points to possible enhanced strain and heating in the HEBM samples as those compacts first impact the anvil. During the compaction stage, as the compact impacts the anvill, the particles closest to the anvil begin to rearrange, locally flow, and plastically deform around one another [43, 57, 140]. On the continuum level, the diameter of the compact in contact with the anvil begins to expand as kinetic energy continues to be applied to the compact and the particles plastically flow against the surface of the steel anvil. The increased reaction occurrence during crush-up observed in the HEBM samples could be attributed to the reaction of fresh nascent reactant surfaces within the HEBM aluminum or plastic deformation already experienced by the HEBM samples during HEBM processing as observed previously by Herbold *et. al* [11]. Additionally, the larger size of the HEBM particles could be causing the increased reactivity during crush-up in those samples. The other larger particles, both the H-60 and the platelet powder compacts typically exhibited

reaction initiation during the compaction stage as well.

In order to investigate the effects of size versus mechanical pre-activation by HEBM further, impact experiments were conducted on 3.5 μm diameter powder, Valimet H-2, that had been high-energy ball milled for 10 minutes and 30 minutes. Similar to H-60 HEBM powders, H-2 HEBM powders were prepared by loading 5 g of Valimet H-2 powder into an alumina vial along with a 12.6 mm diameter alumina sphere. The vial was prepared in a glove box purged with argon, sealed, and transferred to the SPEX mill, where the samples were ball milled for 10 minutes and 30 minutes. SEM micrographs of the H-2 30 minute HEBM powders compared side by side with the H-60 30 minute HEBM powders shown in Figure 76 (a) - (d), reveal that even after 30 minutes of ball milling, the H-2 particles typically remain 10 μm or less in diameter, as shown in Figure 76 (a). Figure 76 (b) provides evidence of cold welding of the H-2 HEBM particles, but, in comparison to H-60 particles of the same ball milling time, as shown in Figure 76 (c) and (d), the H-2 particles were much smaller in diameter and could be characterized by a much larger S_v.

Figure 77 shows the map with the reaction light timing of 10 and 30 minute H-2 HEBM powder compacts with respect to their impact velocity and compact density. The map reveals that light emission and, thus, impact-initiated reaction in H-2 HEBM powders occurs at impact velocities as low as 180 m/s. This reaction velocity is far below the H-2 compact reactivity threshold of 244 m/s, indicating that processing by HEBM ball milling enhances reactivity, regardless of the particle size. Additionally, the map shows that in all cases, reactions in the H-2 HEBM powder initiate during the compaction stage. The initiation of reaction upon initial impact of the H-2 HEBM powder compact against the anvil may be evidence of the fresh reactant surfaces or cracks in the alumina shell, resulting from HEBM processing, as being the primary driver of reaction initiation during the compaction stage in HEBM samples.

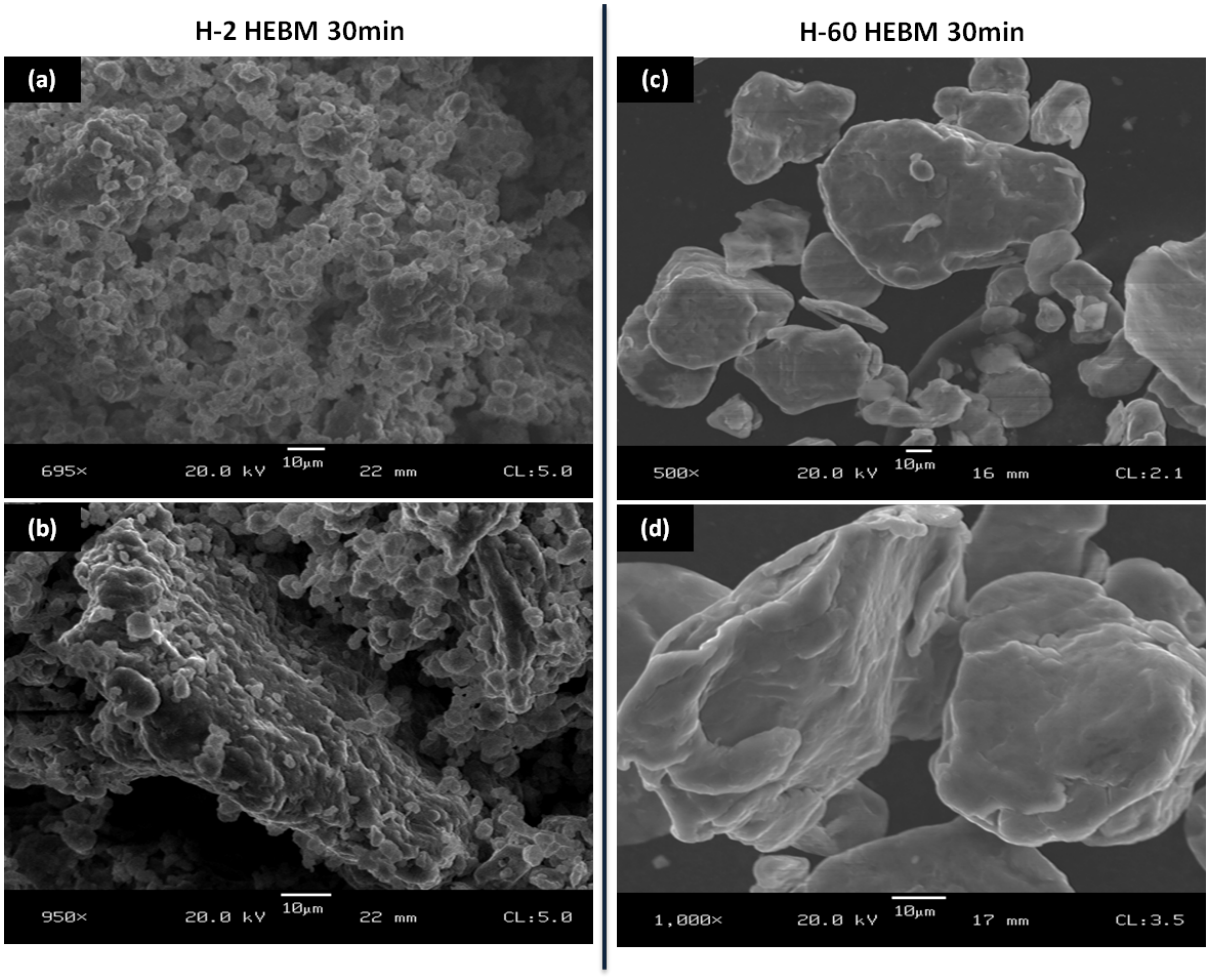

Figure 76: SEM images of H2 HEBM 30 minute powders (a) and H60 HEBM 30 minutes powders at comparable magnification levels.

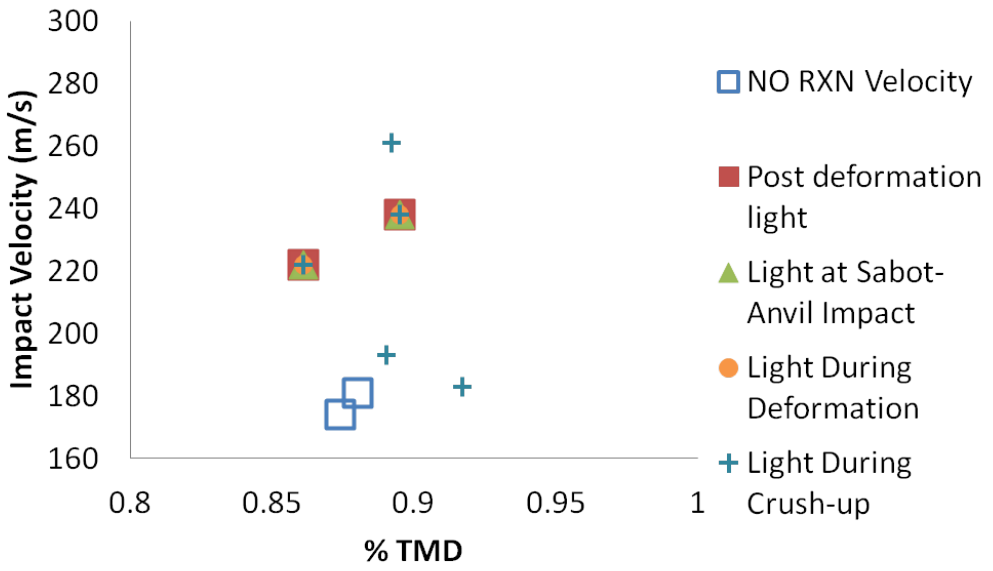

Figure 77: Light emission timing of H2 powders after undergoing processing by HEBM for 10 minutes and 30 minutes.

5.3.2 Microstructure-Based 2-D Computational Simulations

Particle-particle interactions and particle-level plastic deformation result in localized heating at the mesoscale during compaction and deformation of powder compacts. Understanding how these particle-level interactions are affected by changes in the mechanical properties and microstructure of the powder compacts is key to determining the processes responsible for combustion reaction initiation in aluminum powder compacts. These processes, occurring at the micro- and meso-scale, cannot be probed in real time under high-strain-rate impact loading conditions. Microstructure-based simulations are therefore, employed to help fill the gap and to investigate trends in localized strain and temperature behavior of the compacts as a function of the powder's mechanical properties and microstructure of the constituents.

Microstructure-based 2-D simulations can be used to examine how changing the compact microstructure and yield strength effects localized strain and heating. As particle geometry changes, the interfaces that are available to take on the stress being imparted to the

compact during impact change, which effects the localized strain, heating, and possibly reaction of the powder compact. Higher initial or evolving yield strength can result in greater resistance to plastic deformation, leading to lower levels of localized and continuum strain in the sample, but higher concentrations of defects in the particles as stress builds up within the sample. These phenomena were explored in depth in this work, through microstructure-based simulations.

The computational code, CTH [153], was used to investigate the particle-particle interactions during compaction and deformation of the aluminum powder compacts under uniaxial stress rod-on-anvil impact experiments. CTH is a multi-material, Eulerian, shock physics code that can be used to model particle-particle interactions in 2-D and 3-D. A two step Eulerian scheme is employed to handle the significant deformation that arises from uniaxial stress loading [153]. The first is a Lagrangian step that uses the mass, volume, momentum, and energy conservation equations to follow the material motion across each cell. Next, is a remesh step that deforms the cells back to the original state by moving mass, volume, momentum, and energy between the cells. This two step scheme requires that the time step be short enough to prevent the wave from crossing a cell in one time step. Additionally, the volume change is limited to ensure that excessive compression or expansion of a cell does not occur.

5.3.2.1 2-D Computational Set-Up

In order to get a true representation of the particle-particle interactions, actual 2-D microstructure images of the powder compacts were obtained and imported into CTH. First, several micrographs of sectioned and polished powder compacts were collected on an optical microscope and stitched together as shown in Figure 78 (a). A MATLAB code was then used to filter the image and convert it to a binary image. Once a binary form was created, the image was vectorized by the *image to diatom* (IDA) algorithm in MATLAB [130] and imported into CTH. Figure 78 (b) shows an illustration of the Al compact imported into the

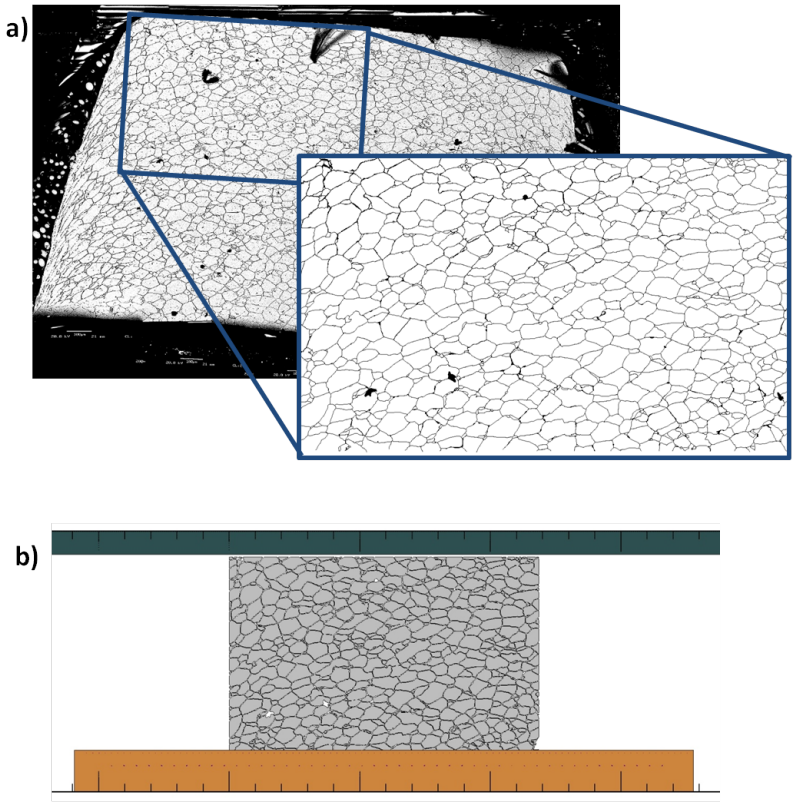

Figure 78: Creation of real 2D microstructures for computational simulations. (a) Image of the stitched together microstructure that was converted to binary. (b) Microstructure imported into CTH.

CTH code.

The mesh size was defined using adaptive mesh refinement (AMR), which changes the mesh size as a function of the interfaces within the simulation. This meshing method most thoroughly and efficiently captures the behavior at the particle-particle interfaces and the particle-void interfaces. Using AMR, the maximum resolution achieved was approximately 2 μm by 2 μm. Although mesh resolution studies indicated that the mesh was not completely optimized at this level, the strain and temperature profiles for this mesh were stable and consistent.

In CTH, several analytical equations of state are available to describe the relationship between the thermodynamic variables of pressure, density and energy. The Mie Gruniesan equation of state was used to model the response of the copper projectile and the steel anvil.

Material properties were obtained from the Sesame table (which is able to account for melting) to describe the response of the aluminum particles. The Johnson-Cook strength model was used to model the constitutive behavior of the copper rod and the steel anvil. Both the Johnson Cook and the Steinberg-Guinan-Lund models were investigated as possible constitutive models for determining the shock response of aluminum.

The fracture strength was estimated to be equivalent to the spall strength of all the materials [154]. An interface strength of 400 MPa was employed between the aluminum particle interfaces similar to Aydelotte's computational studies [32]. Between the copper anvil and the adhered particles, an interface strength, equal to the strength of epoxy (75 MPa) was used. Lastly, a sliding interface, that allowed for no friction was incorporated between the aluminum particles and the anvil. The impact velocity for all simulations was set to 200 m/s.

5.3.2.2 Comparison of computational results with experimental measurements of average dimensional strain

Both the Johnson-Cook and the Steinberg-Guinan-Lund strength model and their parameters were investigated to determine the optimal constitutive properties for the particles within the aluminum powder compact that best describe its behavior. The Johnson Cook model [155] is one of the most widely used constitutive models. The model employs fitting material constants to data from torsion tests and dynamic Hopkinson bar tensile tests, making it purely empirical. The central expression relates the von Mises flow stress, σ, to the strain, strain rate, and temperature in the form of the following equation,

$$\sigma = [A + B\epsilon^n][1 + Cln\dot{\epsilon}^*][1 - T^{*m}] \tag{41}$$

where ϵ is the plastic strain, $\dot{\epsilon}^* = \frac{\dot{\epsilon}}{\dot{\epsilon}_0}$ is the dimensionless plastic strain rate for $\dot{\epsilon}_0 = 1.0s^{-1}$, and *T** is the homologous temperature. *A*, *B*, *n*, *C*, and *m* are material constants determined from experiments. The terms in the first bracket gives the expression for stress as a function

of strain, with the dimensionless plastic strain rate set to '1' and the homologous temperature at '0'. The terms in the second and third brackets give the effect of strain rate and temperature, respectively. The constant, *A* is the yield stress, and can be easily changed according to the material properties; *B* and *n* represent the effects of strain hardening and can be determined experimentally through the torsion and tension tests; and *C* is the strain rate constant. In addition to its simplicity and ease of implementation into computer codes, the Johnson-Cook model includes the effects of strain-rate hardening, strain hardening, and thermal softening, allowing it to provide an accurate description of deformation for many material systems.

The Steinberg-Guinan-Lund model [156, 157] is a semi-empirical constitutive strength model that has been commonly employed for predicting the high strain rate deformation states for rate insensitive metals (FCC) [158]. The model assumes the following relationship between the shear modulus (*G*) and yield strength (*Y*),

$$\left(\frac{1}{Y_0}\frac{dY}{dP}\right)_0 \approx \left(\frac{1}{G_0}\frac{dG}{dP}\right)_0 \tag{42}$$

The yield strength is a function of temperature, pressure, and strain hardening, and is given by the expression,

$$Y = Y_0[1 + \beta(\epsilon^p + \epsilon_i)]\frac{G(P,T)}{G_0} \tag{43}$$

where β is a work hardening parameter and ϵ^p and ϵ_i are the equivalent and initial plastic strain. The subscript *0* refers to a reference state of *T=300K, P=0*. One of the primary features of the Steinberg-Guinan-Lund model is that it explicitly accounts for the pressure and temperature dependence of the shear modulus, *G(P,T)*, as well as the yield strength, *Y*. The shear modulus, *G(P,T)*, is expressed as,

$$G = G_0\left[1 + \frac{AP}{\eta^{1/3}} - B(T - T_0)\right] \tag{44}$$

where η is the compression, and *A* and *B* are material constants. Literature-based experimental values of the yield strength of several metals, over a wide range of pressures has been shown to correlate well with the model [156].

In the present work, measurements of the radial and longitudinal strain for each model were compared to the radial and longitudinal strain observed during rod-on-anvil impact experiments. Figure 79 (a) and (b) illustrate the values of d_{anvil}, d_{rod}, and h obtained from measurements that were gathered from high speed camera images. The d_{anvil} and d_{rod} are a measure of the diameter of the aluminum compact closest to the anvil-compact interface and closest to the rod-compact interface, respectively, at a particular point in time. The strain calculated from the experimentally measured value of the d_{anvil} (blue icon) and d_{rod} (red icon) over time are plotted in Figure 79 (c). The h value is the height of the powder compact at a particular point in time during the compaction and deformation process, and the longitudinal strain calculated from h over time is plotted in Figure 79 (d). As shown in Figure 79 (e), initially, the diameter of the compact at the anvil interface expands more rapidly than the compact diameter at the rod interface. After approximately 3 μs, the diameter at the anvil and at the rod begin to expand at similar rates. To capture the change in the compact diameter at the anvil interface with respect to the change in the compact diameter at the rod interface, the expression,

$$\frac{D_{rod} - D_{anvil}}{D_{initial}} \tag{45}$$

was used.

The optimal constitutive strength model for the aluminum particles was determined by measuring and comparing the change in the diameter and height of the powder compact in images generated by microstructure-based simulations of the rod-on-anvil impact experiment. Figure 80 (a) illustrates an example of powder compact diameter and height measurements taken on an aluminum microstructure whose strength is described by the Steinburg-Guinan-Lund (SGL) constitutive model. In a separate simulation, the Johnson-Cook constitutive strength model was used to describe the strength of the aluminum particles. The two models and the experimental measurements are compared in Figure 81.

The radial strain of the compact near the rod-compact interface, and the longitudinal strain of the compact correlate well between both simulations and the experiment. Yet,

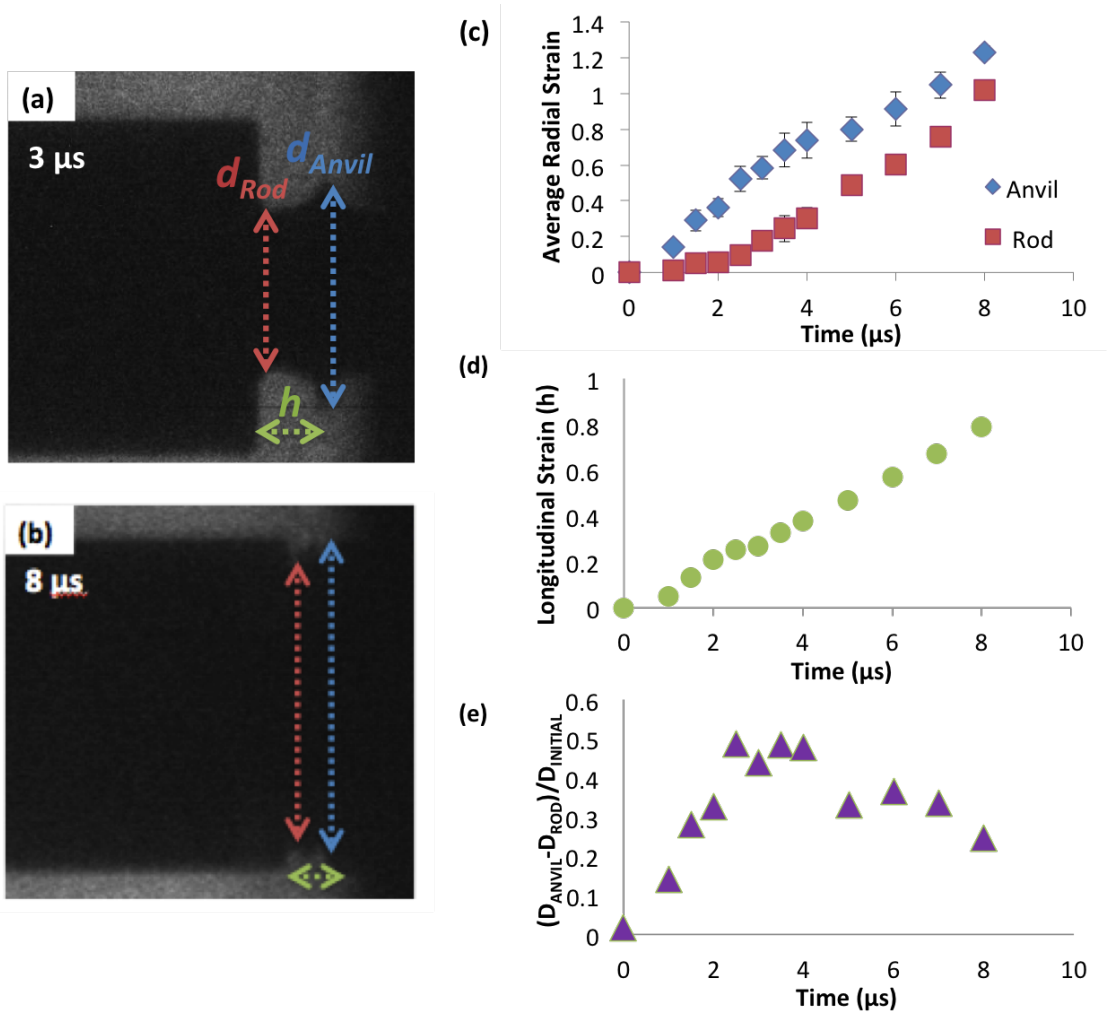

Figure 79: Experimental measurements of the dimensional strain in an 86.4% TMD H-60 sample impacting the anvil at a velocity of 202m/s. (a) and (b) d_{anvil}, d_{rod}, and h were measured from images captured on the high speed framing camera. (c) The dimensional strain at d_{anvil} a d_{rod} were calculated over time using experimental data. (d) The strain in h over time. (e) A measurement of the strain at the anvil with respect to the strain at the copper projectile and normalized by the initial diameter.

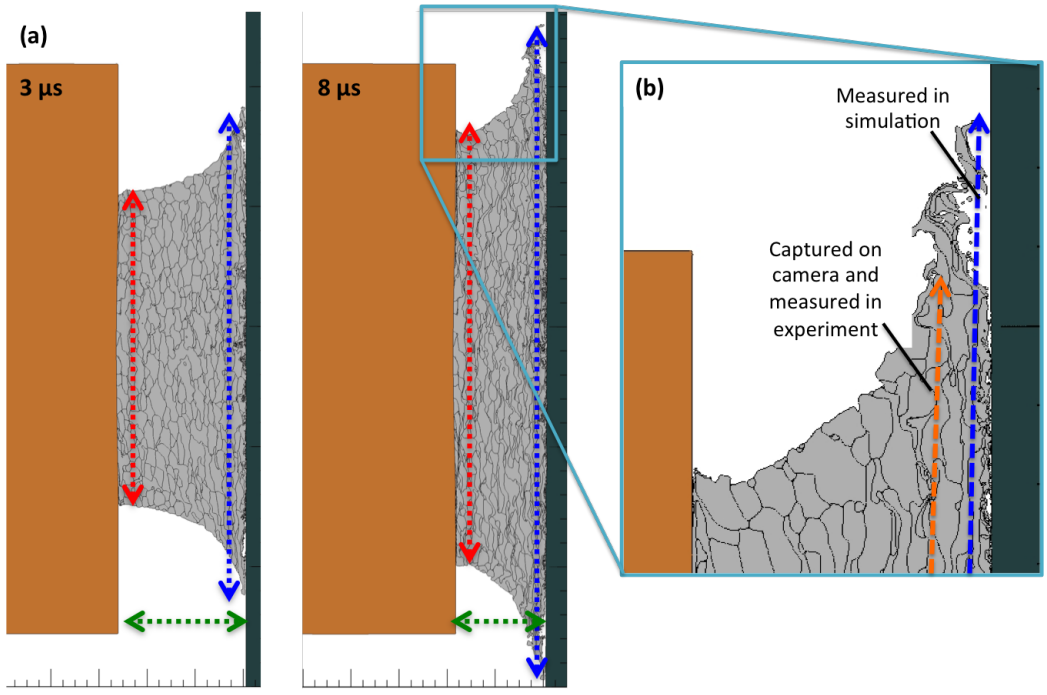

Figure 80: (a) An example of the diameter and height measurements on a microstructure-based simulation of an impact experiment using the Steinburg-Guinan-Lund constitutive strength model. (b) The magnified microstructure at 8 μs, indicating the possible differences between a diameter measurement made on a simulation and a diameter measurement made on an experiment.

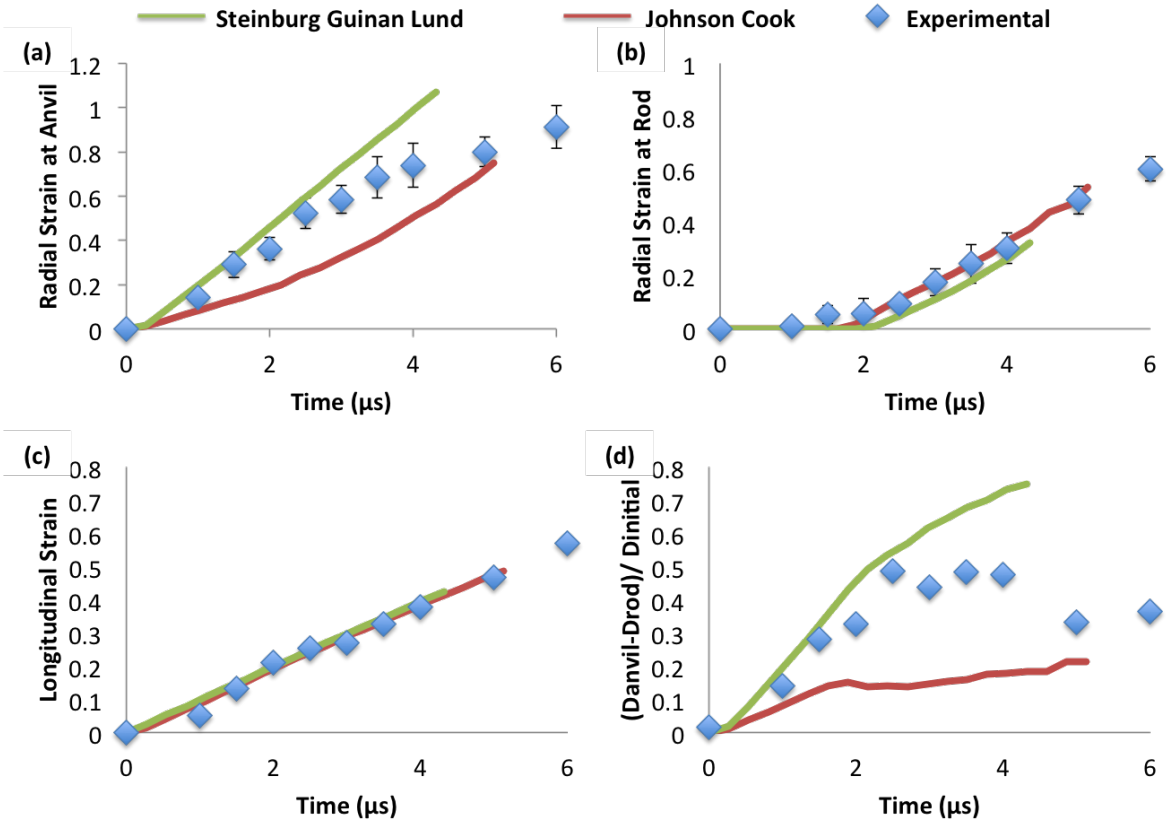

Figure 81: Comparison between experimental measurements of the dimensional strain in an 86.4% TMD H-60 sample impacting the anvil at a velocity of 202m/s and a simulation with the Johnson Cook and the Steinburg-Guinan-Lund model: (a) Strain in the powder compact at the anvil interface, (b) strain in the powder compact at the sabot interface, (c) longitudinal strain, and (d) the strain at the anvil with respect to the strain at the copper projectile, normalized by the initial diameter, were compared.

the behavior of the radial strain at the compact-anvil interface and the (D_{rod}-D_{anvil})/$D_{initial}$ do not correlate well between simulation and experiments. As shown in Figure 81 (a), the radial strain of the compact at the anvil interface for the simulation described by the Johnson-Cook model is initially much lower than the radial strain observed in the experiment and in the simulation employing the SGL model. As the impact process continues to 3 μs following initial impact, the sample becomes increasingly strained and the slope of the curve for the Johnson Cook simulation begins to increase. Thermal softening is accounted for in the empirically-based Johnson-Cook model, which leads to the enhanced strain in the compact at the anvil interface.

The radial strain obtained from simulations described by the SGL model matched the radial strain of the experiment closely during the first 3 μs of impact. After 3 μs, the powder compact strain in the experiment began to decrease, while the SGL simulation strain continued to linearly increase. This discrepancy may be due to the measurement technique. Measurement of the diameter of the compact based on images generated by the simulation is performed by identifying the number of pixels between the outer edges of the aluminum material closest to the anvil, as indicated by the blue lines in Figure 80 (b). Measurement of the diameter based on the experiments is performed in the same manner, but the high speed framing camera is not able to capture the compact diameter with the same level of detail as the simulation. Light may be reflected around particles that are not in contact with the anvil, or the very thin areas at the outer edges of the compact may be obscured by the anvil. It is likely that the portion of the compact that can be measured by the camera is similar to the diameter delineated by the orange line shown in Figure 80 (b). The compact diameter measured by the orange line is 27% smaller than the diameter measured by the blue line. This flaw in the diameter measurement technique in the experiment is evidenced by the calculated strain rates of the powder compacts at the anvil interface plotted in Figure 82. The plot shows a drop in the strain rate for the experimentally observed aluminum powder compact. This decrease in strain rate is not realistic and is most

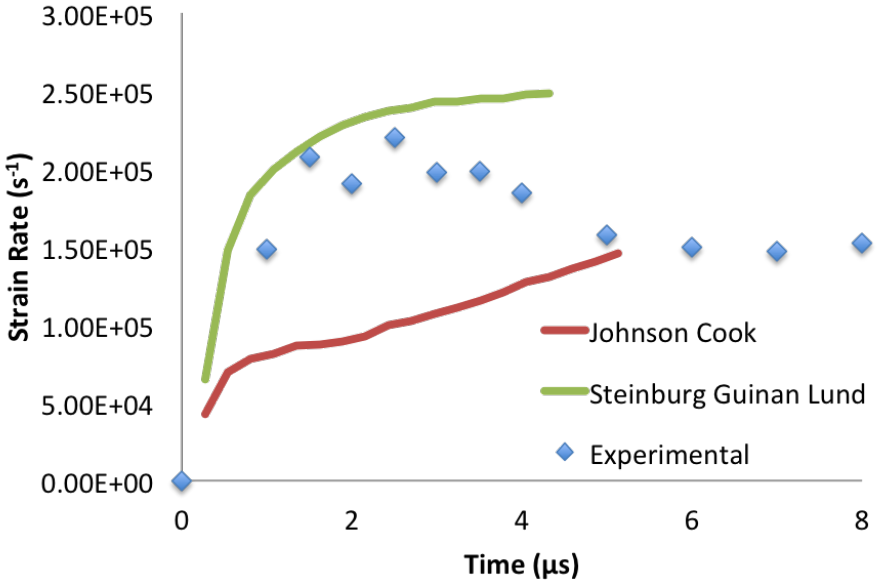

Figure 82: Comparison of the strain rate of the powder compact at the anvil interface.

likely an artifact of the measurement technique because aluminum, being an FCC metal, is not likely to exhibit much strain rate hardening in the range investigated. Whereas, the strain rate of the aluminum compact described by the SGL model in the simulation plateaus at 2.5E+5s^{-1}, 1.5 μs after initial impact, as would be expected of an FCC metal. Therefore, the Steinberg Guinean Lund constitutive model was considered to be representative of the experimental conditions and was used to describe the strength of the aluminum particles in all computational simulations.

5.3.2.3 Effect of Yield Strength

Two simulations, differing only in the strength definition, were carried out to investigate the effect of aluminum yield strength on the particle-level strain and temperature within the aluminum powder compact. The initial yield strength for aluminum in each simulation was set to mimic the experimentally observed extreme values in the particle yield strength given in Table 2 in Chapter 3, 10.8 MPa and 40.8 MPa, respectively.

Figure 83 compares the level of strain experienced by compacts composed of aluminum

particles of varying yield strengths at three points in time after initial impact, 1.0 μs, 2.5 μs, and 4.0 μs. The compact composed of the lower, 10.8 MPa, yield strength aluminum particles, exhibits much higher levels strain than the compact composed of higher, 40.8 MPa, aluminum particles. In both compact types, strain is initially concentrated to the portions of the compact where most deformation occurs, *i.e.,* at the interfaces of the aluminum powders and the impact face of the compact. As time continues and the compact continues to deform against the anvil, shear bands begin to form, leading to very high levels of strain throughout the aluminum compact composed of 10.8 MPa aluminum particles and moderate levels of strain in the aluminum compact composed of 40.8 MPa particles. It can be seen that the higher yield strength aluminum particles are better able to resist deformation, and therefore do not strain to the same degree as the lower yield strength aluminum particles throughout the entire impact process.

Contour plots of the simulated temperature differences between aluminum compacts composed of 10.8 MPa particles and 40.8MPa particles are illustrated in Figure 84. It can be seen that the higher yield strength compact exhibits much higher temperatures than the low yield strength compact. As the 40.8 MPa compact first impacts the anvil, heating takes place at the interfaces, and the temperature of the aluminum particles in contact with the anvil rises to 400K within the first 100 ns of impact. As the impact process continues, aluminum particles in contact with the anvil rise to at least 600K. In both compacts, the majority of the temperature rise takes place at the center of the compact where the least deformation occurs. Kinetic energy that is not dissipated into plastic deformation is converted to heat, or is stored as defects.

5.3.2.4 Effect of Microstructure

An SEM micrograph of a compact composed of 30 minute HEBM aluminum powders was converted to a binary image, vectorized, and then imported into CTH to investigate the influence of microstructure on strain localization and temperature rise. The HEBM

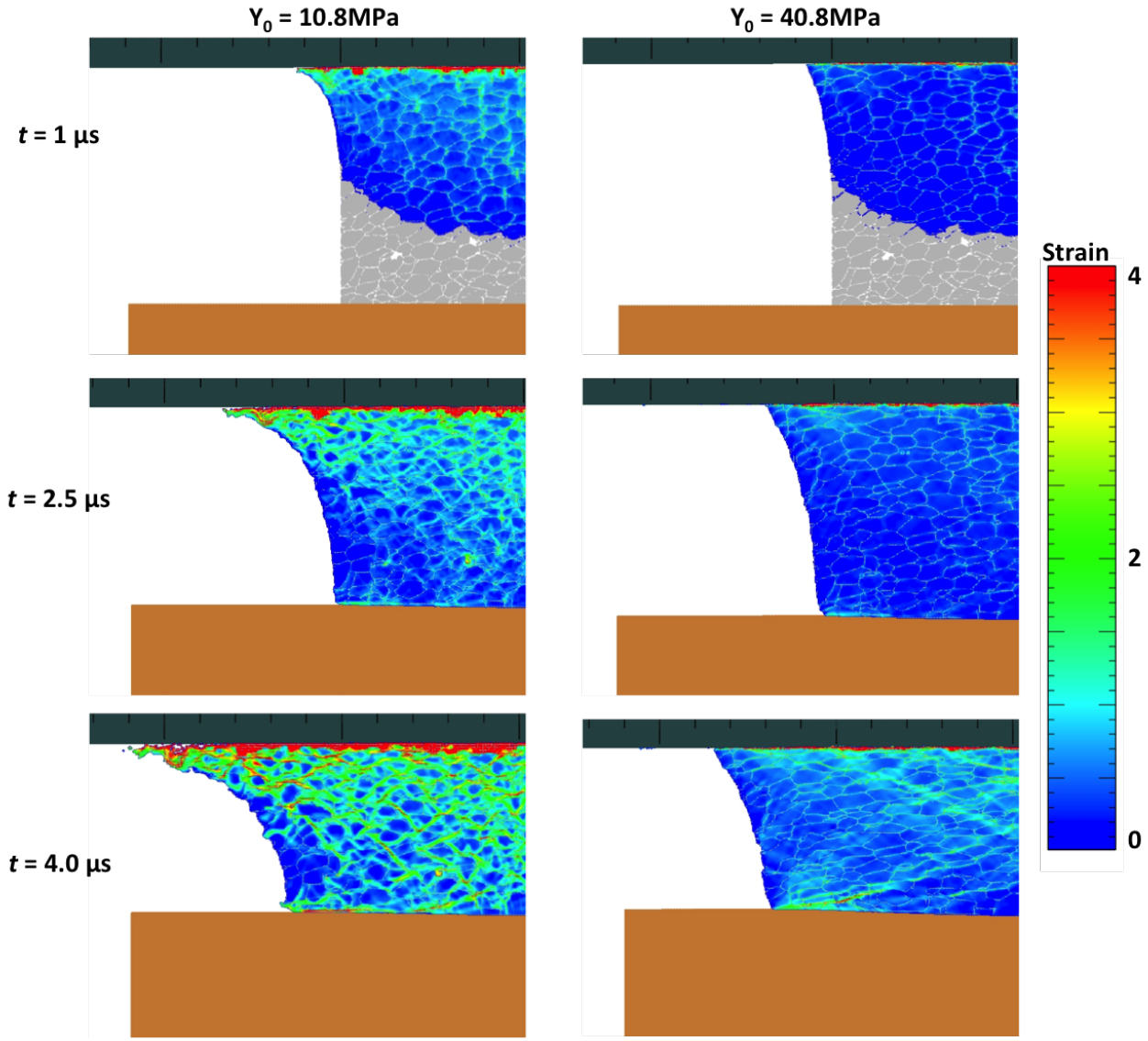

Figure 83: Contour plots of strain in H-60 powder compact

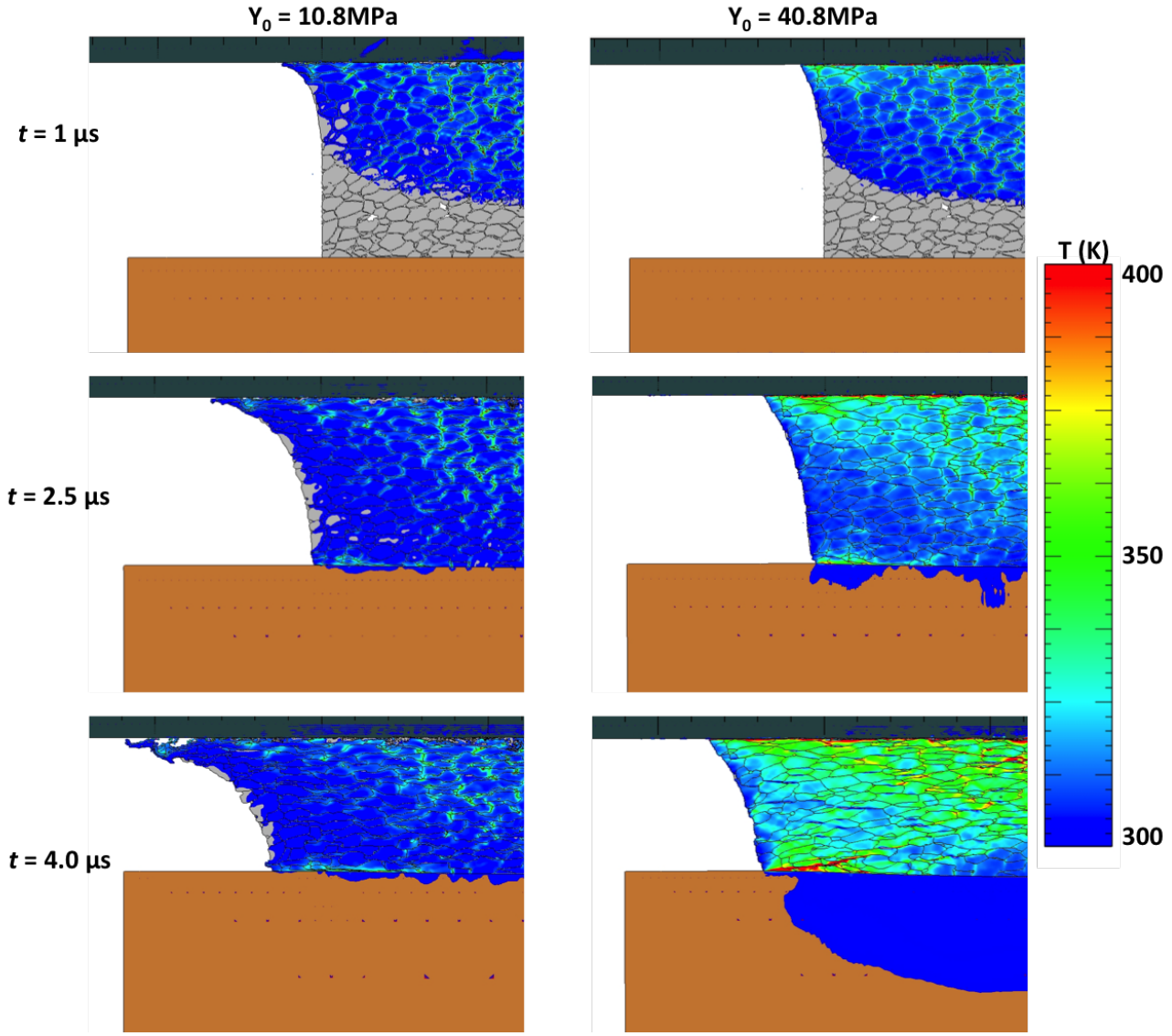

Figure 84: Contour plots of temperature in H-60 powder compacts

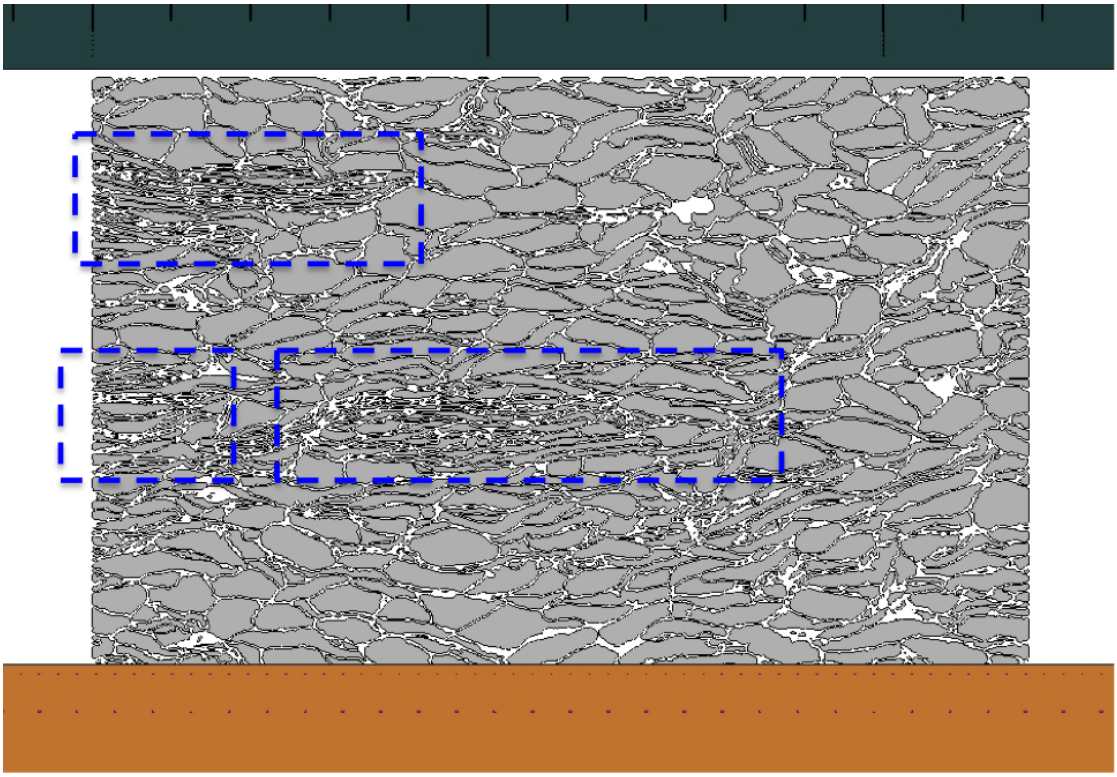

Figure 85: Actual microstructure used to simulate 30 minute HEBM powder compacts. Extremely deformed, platelet-like regions are demarcated in blue.

compact, pictured in Figure 85, contains both "slightly-deformed" and "severely-deformed" particles. The severely deformed particles, within the blue boxes, are smaller and have a flattened, platelet-type structure. During the impact process, these severely deformed particles serve to concentrate strain or enhance temperature rise within the powder compact.

Figure 86 shows a contour plot comparing the levels of strain within a powder compact of H-60 powder (also provided in Figure 83) with a powder compact of H-60 30 minute HEBM powder. The yield strengths of the aluminum particles within the compacts are not exactly the same but similar, 10.8 MPa and 15.7 MPa, respectively. Additionally, the H-60 and the 30 minute HEBM powder compacts have different densities, 93.7% TMD and 79.4% TMD, respectively. The images at t = 2.5 μs illustrate that the lower density, HEBM compact, requires much longer than the higher density H-60 compact to achieve full densification. Despite this difference in compaction time, both samples are fully compacted

by t = 4.0 μs. A comparison of the contour plots at 4.0 μs reveals that the highly deformed regions in the HEBM microstructure do result in more localized strain than that observed in the H-60 microstructure.

The strain levels observed in H-60 and HEBM 30 minute powder compacts, 4 μs after impact, are compared in Figure 87. The aluminum particles in both microstructures were given a yield strength 40.8 MPa. The contour plots reveal that both microstructures exhibit similar overall levels of strain. Yet, the strain is localized in the regions of the highly deformed particles in the the HEBM microstructure, as opposed to being concentrated as shear bands as illustrated in the case of the H-60 microstructure.

Figure 88 shows contour plot comparisons of the temperatures within H-60 and HEBM microstructures 4 μs after initial impact. Figure 88 (a) compares microstructures of compacts composed H-60 and 30 minute HEBM aluminum particles with lower yield strengths, 10.8 and 15.7 MPa, respectively. Both microstructures exhibit similar localized temperature increases of $\sim$60°C. Figure 88 (b) compares microstructures of compacts composed H-60 and 30 minute HEBM aluminum particles with higher yield strengths, 40.8 MPa. Both microstructures show a temperature rise of greater than 100°C at the impact face. The H-60 microstructure reveals temperature increases of $\sim$60°C throughout a large portion of the compact, and the HEBM microstructure remains at relatively lower temperatures throughout the powder compact.

5.3.2.5 Analysis of simulations with respect to light emission timing

Trends in light emission timing as a function of aluminum powder type and compact density were identified in Section 5.3.1. The primary observation regarding reaction initiation timing was that all compacts composed of HEBM aluminum powders immediately emit light due to reaction upon impacting the anvil, during the compaction stage. Microstructure-based simulations may be used to understand these trends in light emission timing by correlating the particle-level processes observed in simulations to the reaction initiation

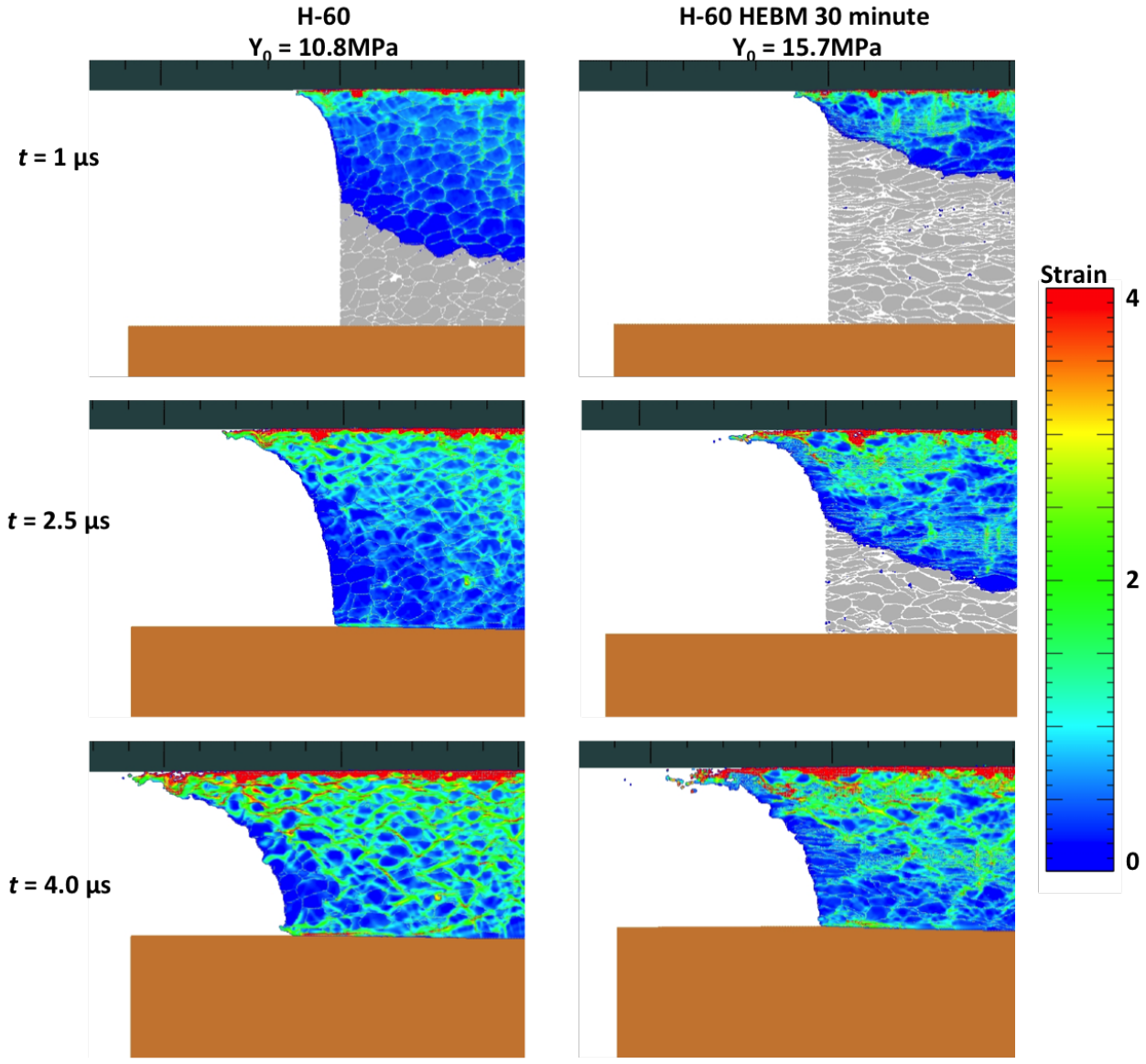

Figure 86: Images of strain in 93.7% TMD H-60 powder compact and a 79.4%TMD H-60 30 minute HEBM powder compact composed of aluminum particles of similar yield strengths.

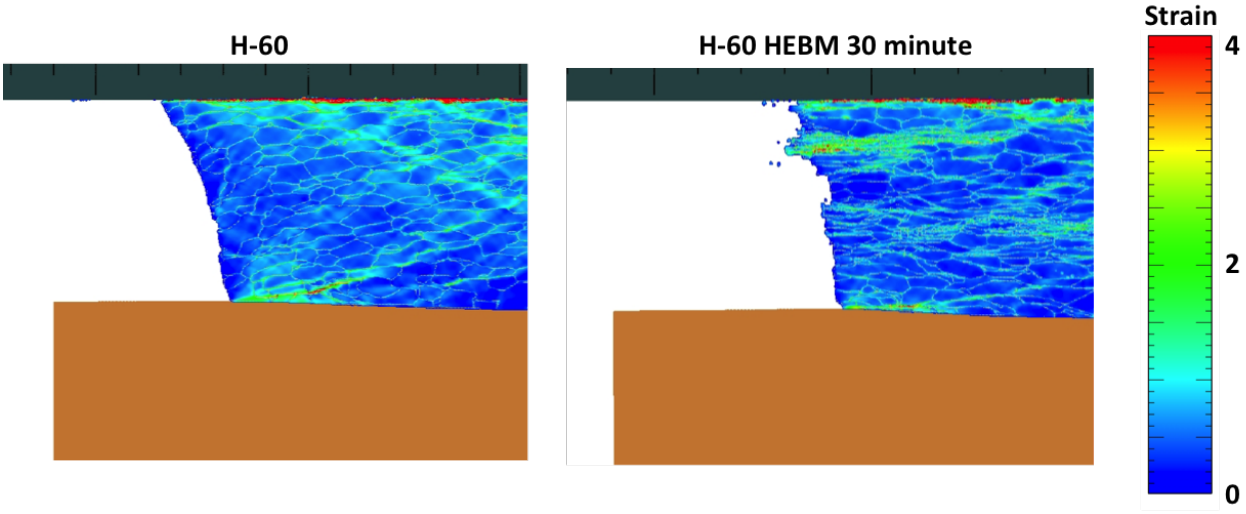

Figure 87: Comparison of the strain levels within an H-60 and a 30 minute HEBM compact with a yield strength of 40.8 MPa, 4 μs after impact.

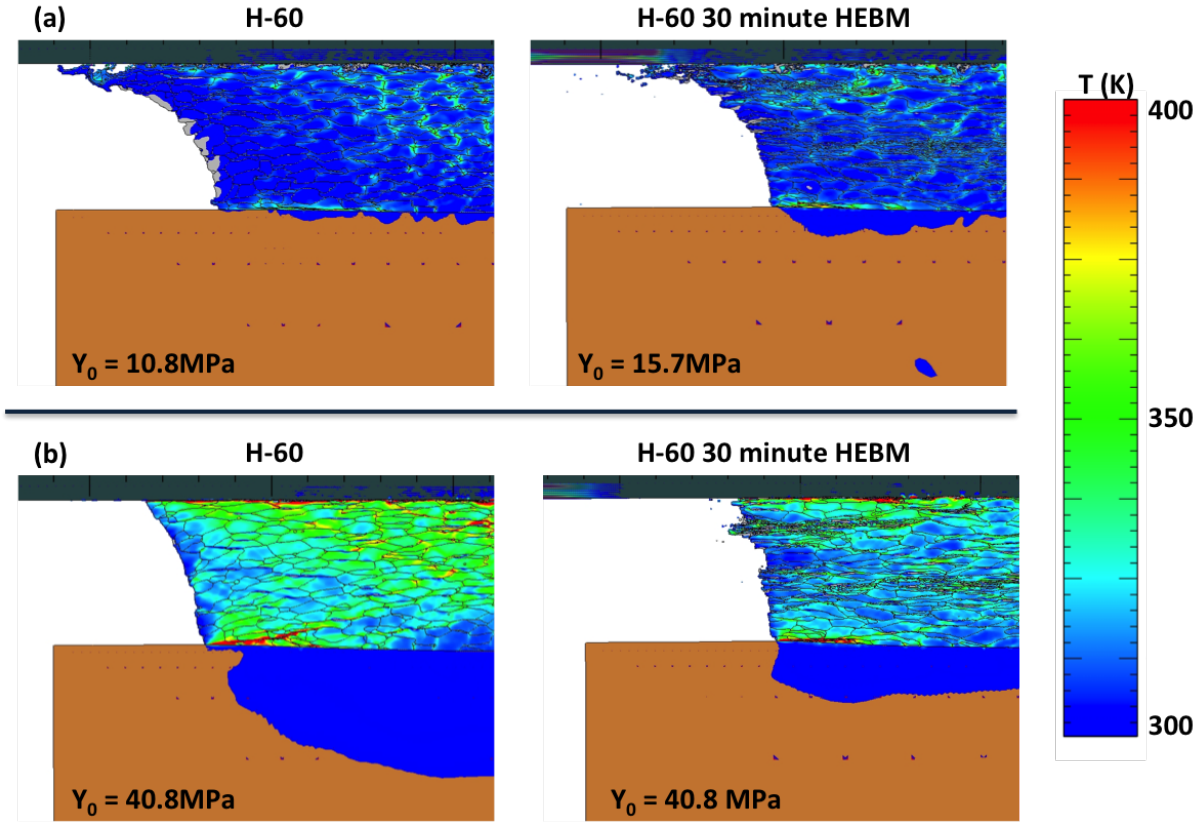

Figure 88: Comparison of the temperature rise within within an H-60 and a 30 minute HEBM compact with varying yield strengths, 4 μs after impact.

behavior observed in experiments.

High speed images of HEBM powder compacts obtained from impact experiments reveal consistent emission of light, and thus, provide evidence of a combustion reaction occurring upon initial impact against the steel anvil. Figure 89 shows magnified images of the temperatures observed in simulations at the anvil-compact interface 250 ns after initial impact. All samples, regardless of their microstructure or yield strength, reveal localized temperature increases at triple points in the microstructure. Yet, the maximum temperature at these triple points is typically only 80°C, which would not initiate a combustion reaction. At later times, 1 μs following initial impact, a few 20 μm diameter regions within the 30 minute HEBM microstructure exhibited a maximum temperature of 225°C, which is less the .5T_m for aluminum and may not be sufficient to initiate a combustion reaction in the aluminum powder compact. Additionally, high levels of strain are observed at the impact face during the compaction stage as shown in Figure 86, but these strain levels are similar in both microstructures and may not lead to the distinct light emission behavior observed in the HEBM powder compacts.

Microstructure-based simulations show that the light emission observed during the compaction stage in all HEBM powder compact impact experiments is most likely not influenced by the differences in the microstructure between the deformed HEBM powders and the spherical H-series Valimet powders. The occurrence of the light emission during the compaction stage of impact experiments conducted on all smaller, H-2, powders processed by HEBM strengthens this conclusion. Another possibility is that the HEBM process may store energy in the material in the form of defects, thereby, lowering activation barrier. However, the retained lattice elastic strain energy measured by the Williamson Hall line broadening analysis (in Chapter 3) was not found to be significant. Therefore, the enhanced reactivity during the compaction stage in HEBM powder impact experiments is most likely due to the deformation and cracking of the oxide layer and the creation of freshly exposed highly reactive surfaces during the ball milling process.

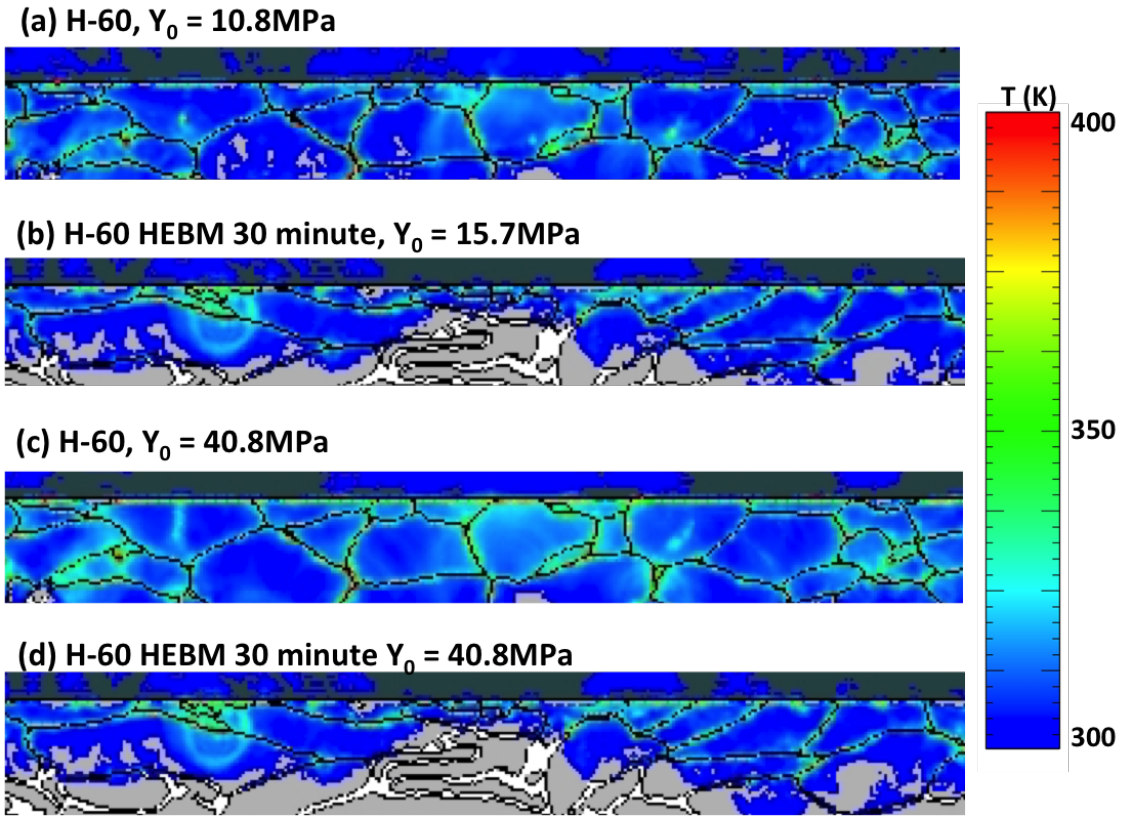

Figure 89: Magnified images generated by microstructure-based simulations of the anvil-compact interface, 250 ns after initial impact.

5.3.3 Information Revealed from Temperature Measurements

The temperature measurements presented in Section 4.3 reveal that temperature increase due to heating takes place upon impact. The maximum temperature measured in profile view, during the deformation stage, between 2 to 4 μs following impact, was only 220°C. Temperatures measured at the impact face of the sample reach 425°C during the initial compaction stage. Theoretical calculations and computational simulations can be used to better understand the processes that lead to the experimentally observed temperature rise.

5.3.3.1 Comparison of measured temperature with calculated heat of deformation

Experimental temperature measurements captured in profile view following the impact event, such as those discussed in Section 4.3.2, reveal information about the bulk temperature of the aluminum compact during impact. During the first several microseconds of the impact process, extreme plastic deformation occurs at a strain rate of $\sim$1.78E+5s^{-1}. At these high strain rates, there is not enough time available for thermal diffusion to occur, and plastic deformation can be assumed to be an adiabatic process [36]. Under this assumption, a fraction, η, of the work of deformation, *W*, is converted to heat, *Q*, and can be expressed as [159],

$$\eta \Delta \mathrm{W} = \Delta \mathrm{Q} \tag{46}$$

$$\eta \int_0^{\epsilon} \sigma \mathrm{d}\epsilon = \rho \mathrm{C}_V \Delta \mathrm{T} \tag{47}$$

$$\Delta \mathrm{T}(\epsilon) = \frac{\eta}{\rho \mathrm{C}_V} \int_0^{\epsilon} \sigma \mathrm{d}\epsilon \tag{48}$$

Typically for metals, the work rate to heat rate conversion fraction (η) is assumed to be 0.9 [42], leaving 10% of the work of deformation to be stored in the material as defects. To obtain the theoretical temperature rise due to deformation in aluminum, σ was substituted for the Johnson-Cook constitutive equation. A plot of the calculated temperature versus strain relationship is shown in Figure 90, for different Johnson-Cook parameters. As yield strength of aluminum increases, the temperature increases at a faster rate because more

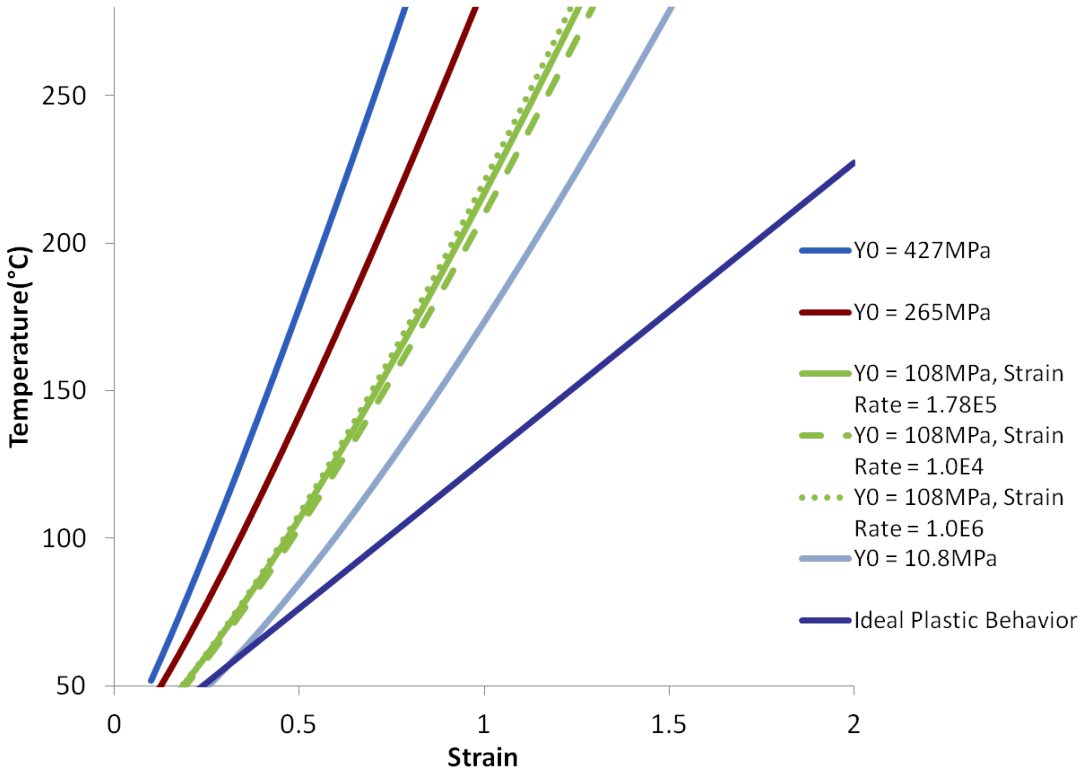

Figure 90: Theoretical increase in temperature as a function of strain.

work is being put in into the system (in the form of kinetic energy) to obtain similar amounts of strain in higher yield strength samples. Additionally, an order of magnitude change in the strain rate does not have a noticeable effect on the the heat generated during deformation.

Figure 91 shows the experimentally measured values of temperature rise overlaid on the theoretical temperature rise due to plastic deformation. The experimentally observed temperature rise at 50% strain was typically between 140 and 200°C. These temperature values are predicted for aluminum with a yield strength ranging from 108 and 427 MPa. As strain in the samples reaches 100%, *e.g.,* for aluminum displaying ideal plastic behavior, temperatures remain between 140 and 240°C. In Section 3.3, particle level yield strengths were measured to be between 10 MPa and 40 MPa, and the effective yield stress of the entire compact was between 724 and 1044 MPa. Experimentally measured temperatures fall within these ranges, but do not follow any obvious pattern based on particle size or level

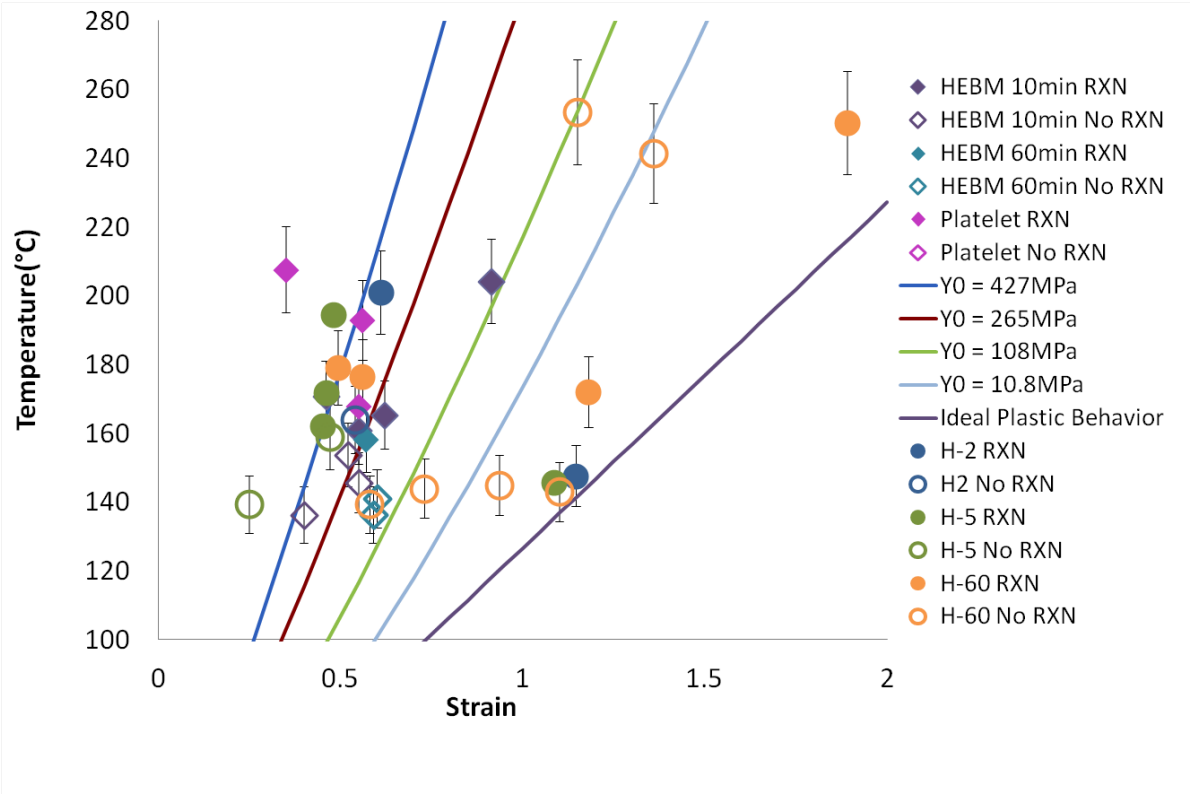

Figure 91: Experimentally measured temperature values compared with the theoretical calculations.

of mechanical pre-activation. In general, the predicted temperatures are below temperatures measured with the IR camera. This discrepancy could be due to heating at the particle level, as particle interfaces impact one another, or due to friction between the aluminum pellet and steel anvil as the pellet deforms against the anvil.

5.3.3.2 Comparison of measured temperature with 2-D simulations

Experimentally observed temperature rise was compared with that obtained from 2-D microstructure based CTH simulations to investigate the effects of strain and localized heating. All CTH simulations were conducted at an impact velocity of 200 m/s. Experimentally observed temperatures for experiments conducted at 200 m/s ranged from 130 and 170°C as shown in Figure 62 in Chapter 4. Figure 92 illustrates images generated by H-60 microstructure-based simulations during the deformation stage, 5 μs after initial impact,

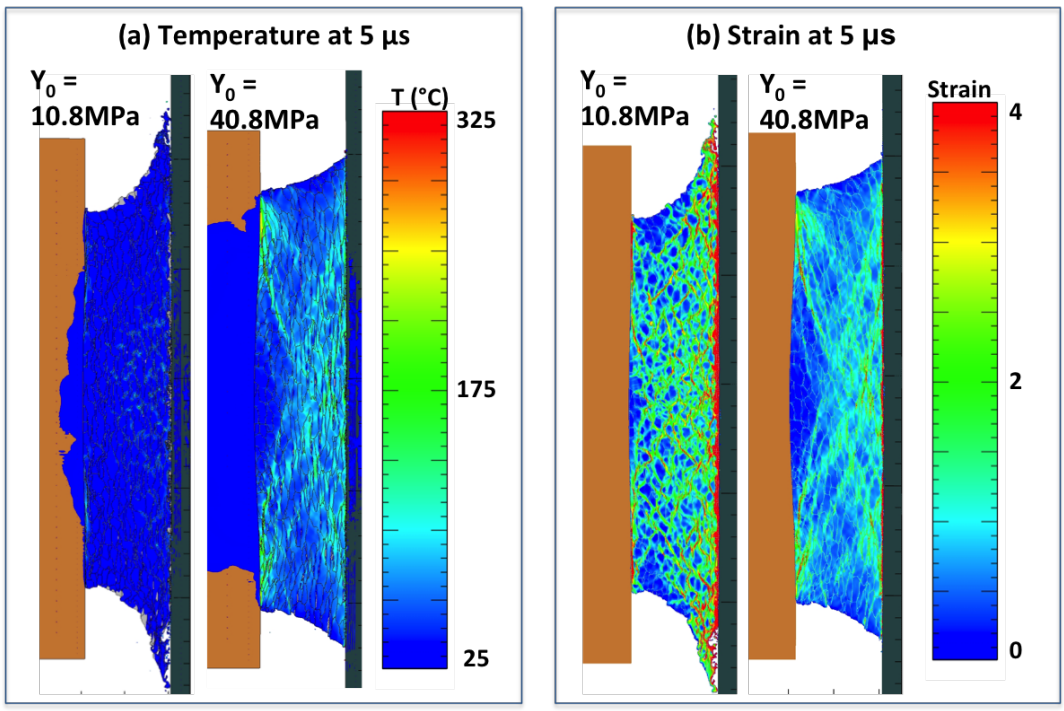

Figure 92: (a) Temperature and (b) strain contour plots of microstructure-based simulations of H-60 aluminum powder compacts, 5 μs after initial impact.

similar to the timing that the experimental temperature measurements were captured.

The H-60 compact composed of aluminum particles with a 10.8 MPa yield strength only reaches a maximum temperatures of $\sim$75°C as shown in Figure 92 (a). The experimentally observed temperature under a similar condition was 140°C. The other compact shown in Figure 92 (a) is composed of 40.8 MPa yield strength aluminum particles and is representative of the yield strength of highly strained platelets. The simulation predicts a maximum temperature of 175°C and an average temperature of $\sim$100°C. Experimentally observed temperatures for compacts composed of highly strained aluminum platelets ranged from 165°C to 190°C. The 2-D simulations predict temperature that are closer to the experimentally observed temperatures than the heat of deformation calculations, but again, the theoretical calculation underpredict the experimentally measured temperatures. The discrepancy may be due to the limitations of 2-D simulation. The magnitude of the temperature rise occurring in experiments, in three dimensions, as a result of extreme plastic

deformation and friction against the anvil, may not be completely captured in two dimensional simulations. Experimentally observed temperature rise typically only takes place at the impact face of the powder compact and takes the form of a vertical line at the anvil interface. Temperature rise in the simulation is observed throughout the entire compact. The contour plots of strain generated by the H-60 microstructure simulations and pictured in Figure 92 (b) more closely mimic the spatial character of the experimentally observed temperature rise. Powder compacts with 10.8 MPa yield strength aluminum particles reveal extremely strained regions at the interface of the anvil and at the outer most-deformed edges of the compact. This suggests that temperature rise due to strain and frictional heating is not appropriately accounted for in the simulation.

5.3.3.3 Comparison of impact face temperature with 3-D simulations

Spatial information about the temperature rise at the impact face of the powder compact against the sapphire anvil set-up summarized in Chapter 4.3.3 was captured using an IR camera. Three dimensional, continuum-level simulations of an aluminum powder compact impacting an anvil at 200 m/s were also conducted using CTH to investigate temperature rise at the impact face. The Mie-Gruniesen equation of state and the p-alpha model were used to describe the aluminum powder compact; all other parameters were identical to the 2-D simulations. Realistic temperatures could not be calculated using the simulation. Therefore, the experimentally observed temperature profiles are compared to the strain fields observed within the 3-D microstructure-based simulation.

The left column of Figure 93 shows the impact face images captured by the IR camera during the (a) compaction, (b) deformation, and (c) the sabot-anvil impact stages of the impact of H-60 powder compact against the sapphire anvil at 210 m/s. The right column of Figure 93 shows images generated by the 3-D simulation of the strain field at the impact face. During the compaction stage, experimentally captured heating is localized in nature, with regions of varying temperatures along the diameter of the powder compact, which

reaches a maximum of 404°C. Temperatures of this magnitude were not observed in 2-D microstructure-based simulations, and the strain field at the interface does not indicate that any localized straining occurs during this stage. During the deformation stage, heating up to 206°C is observed at the outer edges of the compact, where the most deformation occurs. The strain field captured by the 3-D simulation closely matches the spatial character of the experimentally observed heating. During the sabot-anvil impact stage, the temperature rise extends beyond the diameter of the initial compact ($\sim$2.5 times) and reaches a maximum temperature of 409°C; yet, the center of the aluminum compact remains much colder than the rest of the sample. The strain field at the impact face shows a highly strained region that is $\sim$2.5 times the diameter of the original powder compact, surrounding a lower strain region that is $\sim$0.5 of the diameter of the original powder compact.

Experimentally observed temperature rise and computationally generated strain fields at the impact face indicate that high strain levels are closely tied to high temperature regions during the deformation and sabot-anvil impact stages. Yet, the temperature profiles and strain fields do not correlate well during the compaction stage. This discrepancy may be attributed to the use of a continuum model that does not take into account particle level interactions.

5.4 Summary of Property and Process Effects on Impact Initiated Combustion of Aluminum

Logistic regression analysis, microstructure-based simulations, and temperature measurements were used to understand the effects of aluminum powder properties on the process of initiating reaction during impact of aluminum powder compacts against a steel anvil. Reaction occurrence was analyzed with respect to powder characteristics using a logistic regression analysis, which indicated that the surface area per unit volume ratio, S_v, and the compaction energy are most closely tied to promoting the occurrence of reaction.

It is observed that as S_v is decreased, the reaction threshold velocity decreases; this

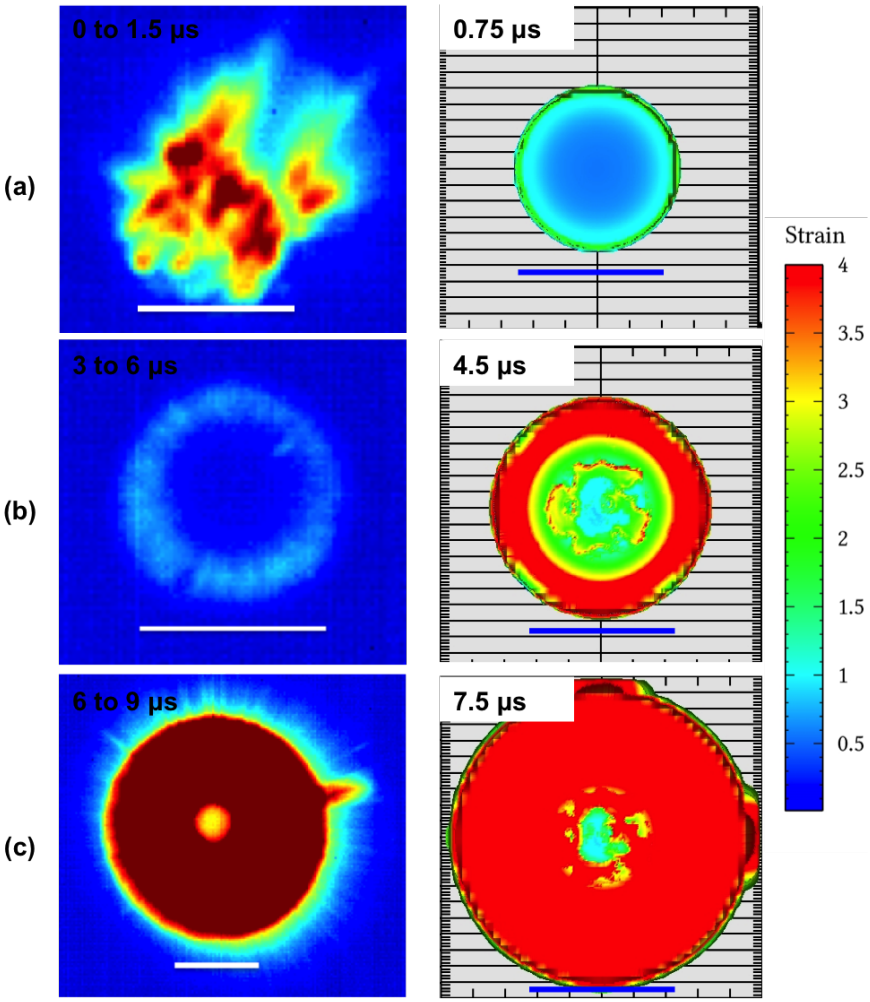

Figure 93: Images of temperature rise captured at the impact face through the sapphire anvil and simulations of strain at the impact face of the powder compact. The first three stages of the impact process, compaction (a), deformation (b), and the sabot-anvil impact (c) are represented.

trend indicates that reaction initiation is a result of localized stresses and strains that build-up at the limited interfaces available for reaction in the lower S_v powder compacts, similar to Gourdin's [83] energy deposition model of enhanced energy deposition and heating at the interfaces of lower surface area particles. Localized heating at the particle interfaces was observed experimentally through temperature measurements at the impact face of the anvil during the compaction stage of the impact process. Spatial images of temperature reveal regions differing in temperature by 100°C adjacent to one another. Additionally, microstructure-based simulations exhibit enhanced strain and heating at the interfaces, consistent with the energy deposition model.

As the compaction energy required to reach full density decreases, the reaction threshold velocity decreases. This trend reveals that not only do localized strain and heating cause reaction initiation, but overall energy input and consumption also play a role in reaction initiation. The more kinetic energy that is required for the compaction of particles, such as the H-2 and H-5 aluminum particles, leads to lower energy availability for reaction, and, thus, higher energies are required to drive reaction initiation.

Powder compacts composed of mechanically pre-activated aluminum particles did not show any relationship between the level of mechanical pre-activation (or yield strength) and the reaction threshold velocity according to the logistic regression analysis. Yet, light emission timing, microstructure-based simulations, and rod-on-anvil impact experiments of H-2 HEBM compacts were used to explain the changes in the reaction threshold velocity as a function of ball milling time (as described in Chapter 4). Light emission timing reveals that all HEBM samples initiate reaction during compaction, the first stage of impact. Microstructure-based simulations (and IR camera images) indicate that initial temperature rise is not dependent on microstructure or strength. Therefore, the enhanced reactivity of HEBM 30 minute powder compacts may be due to a phenomena that cannot be captured by the microstructure-based simulations. During ball milling, nascent reactive surfaces that can serve as reaction initiation center are exposed[11]. High S_v H-2 powder compacts that

were processed by HEBM also exhibitted enhanced reactivity, which points to the availability of nascent surfaces for reaction as the likely cause of the lower reaction threshold velocities in HEBM particles.

Chapter VI

QUANTUM DOTS AS MESO-SCALE SHOCK SENSORS

This chapter will focus on the development of a new method for monitoring the shock response of materials at the mesoscale. Up to this point, our understanding of the processes contributing to aluminum combustion has been based on correlating experimentally observed light emission using high speed camera with computational simulations, analysis of aluminum powder characteristics, and *in situ* temperature measurements. The simulations and experimental observations suggest that initiation of combustion of aluminum under impact conditions results from localized, mesoscale deformation and heating. This conclusion can be confirmed and more information can be obtained through the use of sensors capable of observing the localized, mesoscale processes directly during impact experiments.

6.1 Approach

Quantum dots hold much promise as a potential mesoscale shock diagnostic, because of their small size, typically tens of nanometers, and their rapid response time, limited only by their picosecond optical transition time. Additionally, the surface of quantum dots can be chemically modified or encapsulated in another material, allowing them to be incorporated easily to the system of interest.

CdTe semiconductor quantum dots (QDs) are being investigated as potential *in situ* meso-scale pressure sensors since their band gap is just a few nanometers wide. As the size of the semiconductor decreases, approaching the band gap distance, the semiconductor quantum exhibits a quantized behavior. Decreasing the quantum dot size decreases the number of energy levels in the material but increases the band gap width between those energy levels. Therefore, a smaller diameter quantum dot exhibits an increased band gap energy, resulting in a blue shift in the quantum dot's fluorescence spectra. The net effect of

this property is that QD's have a very narrow emission wavelength that is strongly dependent on size. Subjecting the QD to a shock wave can directly affect its lattice parameter, size, and shape. Compression of the QD should result in an upward, or blue, shift in energy, while elongation of the QD should result in a downward, or red, shift in energy. Capturing the quantum dot's spectra in real time during shock compression, using a spectrograph connected to a streak camera, can allow for monitoring of the energy shift as a function of pressure over nanosecond time scales. The schematic in Figure 94 illustrates an examples of a set-up in which a QD-filled polymer film can be used in contact with a heterogeneous (granular) material to monitor the spatial variations in shock pressures transmitted from the granular material. Before QDs can be used as mesoscale sensors with heterogeneous materials, it was necessary to determine the direct shock response of the QD-containing sensor materials. In the following, the method of fabrication of the QD-PVA nano composite sensor and its shock compression response is described

6.2 Preparation of Quantum Dot-PVA Nanocomposite Sensor

CdTe quantum dots were dispersed in polyvinyl alcohol (PVA) to fabricate nano composite films for use as shock-compression sensors. The PVA films provide a stable and repeatable media for testing of the quantum dot response. Additionally, PVA is soluble in water, the same solvent used to store and prepare the CdTe quantum dots.

The quantum dots were synthesized using Zhang *et.al*'s hydrothermal method [160]. Solutions of NaHTe and N_2-saturated $Cd(ClO_4)_2$ were heated in the presence of 3-mercaptopropionic acid (MPA) or 2-mercaptethylamine (MEA) in water to boiling temperature. The solution was refluxed for varying times to yield a controlled dot size [160, 161], which effected the absorption and emission wavelengths. Figure 95 illustrates the range of emission wavelengths, from 520nm to 680nm that can be prepared by changing the quantum dot size. The resulting quantum dots were suspended in an aqueous solution, shielded from light, and stored until they could be incorporated into a PVA film.

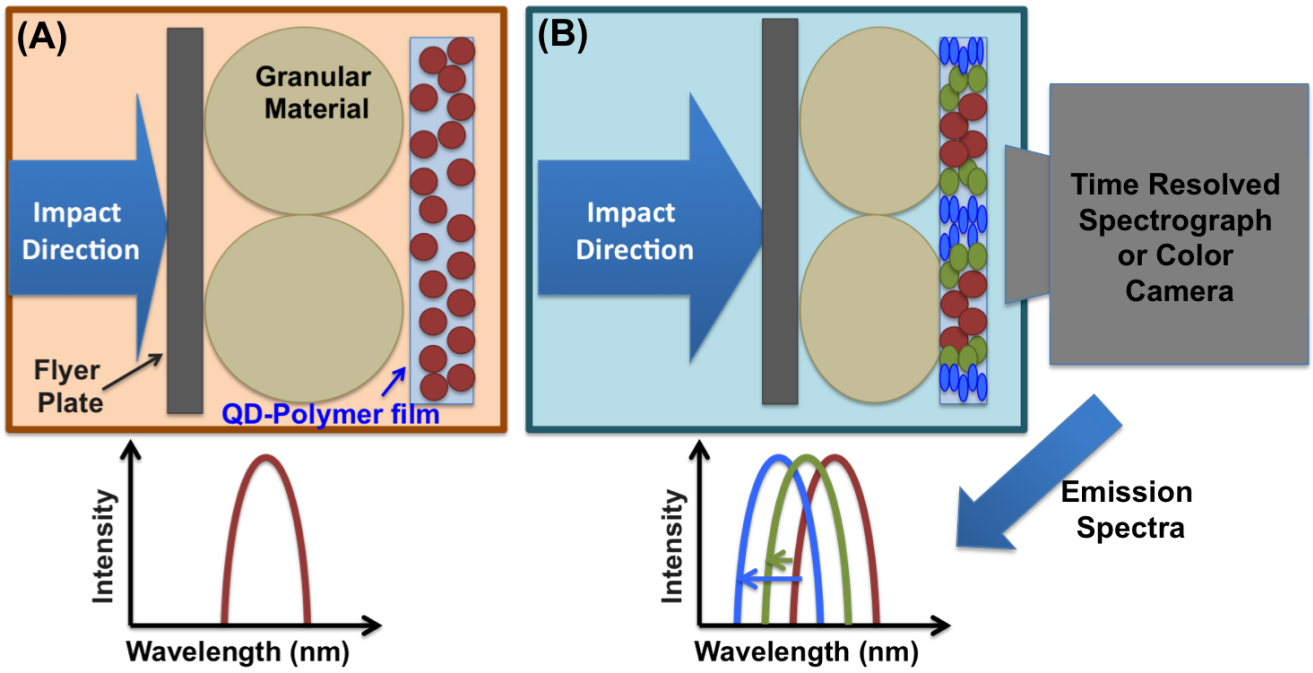

Figure 94: Schematic of setup to measure pressure changes with quantum dot films. (A) The experimental configuration prior to shock impact. (B) The experimental configuration during shock impact, indicating changes in emission spectra as a function of pressure on the quantum dot.

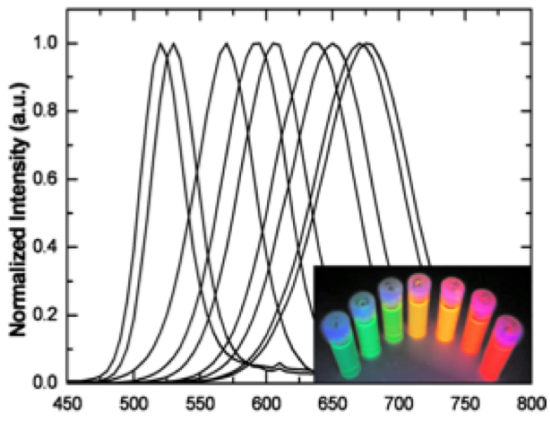

Figure 95: Steady state emission spectra of quantum dots of various sizes (from [161])

The PVA-quantum dot nanocomposite films were prepared by drop-coating a solution of quantum dots dispersed in PVA onto a glass slide. First, a 10% by mass stock solution of PVA was prepared by combining Airvol 523 PVA (1.0 g) with distilled water (10mL) and stirring at 80°C for two hours. This 10% solution was diluted to 5% and 2.5% by mass as needed. Next, the PVA-quantum dot mixture was prepared by dispersed quantum dots in the PVA solution and in a 1:1 by volume ratio (unless otherwise noted). The mixture was vortexed for one minute and degassed. Lastly, the PVA-quantum dot solution (800μL) was drop-coated onto a glass slide (1"x1", Delta Technologies) that had been thoroughly cleaned by soaking in a 1:1 by volume mixture of methanol and hydrochloric acid for 30 minutes, sonicating in distilled water two times, and storing in distilled water. Glass slides were thoroughly dried with house air and weighed prior to drop-coating. Several drying times and temperatures were tested. Once fully cured, the glass slide was weighed again to obtain the approximate mass of the film.

Once the basic PVA-quantum dot preparation method was determined, the procedure was optimized to achieve an absorption of greater than 0.2 at 520 nm and a film thickness of approximately 15 μm. The absorption spectra for each film was captured using a Cary 5000 UV-Vis-NIR spectrophotometer. The film mass was used to approximate the film thickness. A film mass of 12 mg was assumed to correlate to an ideal film thickness of approximately 15 μm. The properties of the PVA-quantum dot films were optimized by varying the quantum charge, the film curing temperature, and the PVA concentration.

6.2.1 Optimization of quantum dot charge

The quantum dot charge helps to control the dispersion and mixing of the quantum dots within the PVA matrix. The PVA polymer is composed of repeating vinyl alcohol groups, resulting in a repeating chemical structure of CH_2CHOH. The presence of hydroxyl groups give the PVA polymer a slightly negative charge. Initially, CdTe quantum dots were prepared in the presence of the ionic solvent mercaptopropionic acid, yielding quantum dots

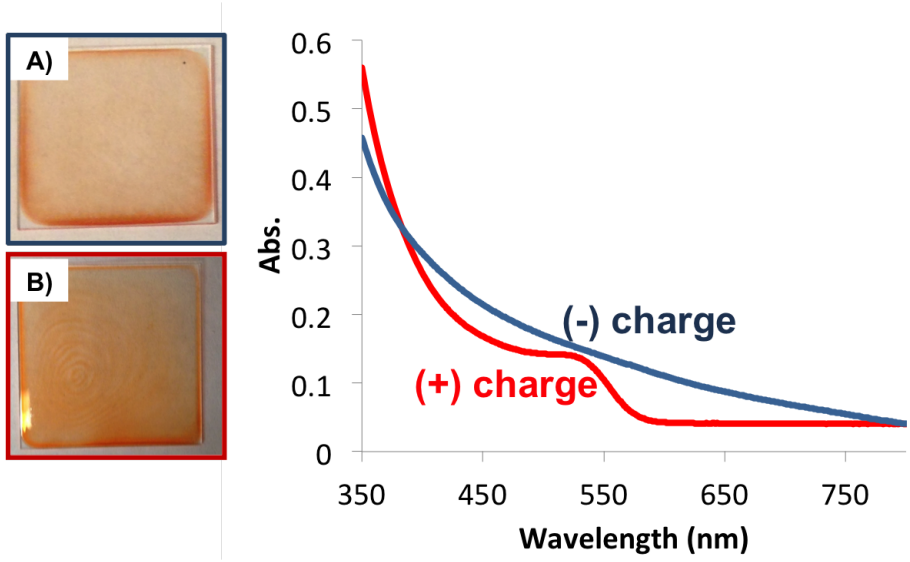

Figure 96: Absorbance spectra of PVA (a) negatively and (b) positivelycharged quantum dots.

with a negative charge. Once dried the negatively charged quantum dot-based PVA film resulted in a film with particles aggregated around the edges of the film as shown in Figure96 (A). Additionally, the absorption spectra showed no abrupt absorption increase, just a linear increase in absorption as the wavelength decreased, indicative of aggregation.

In order to decrease the likelihood of aggregation, CdTe quantum dots were prepared in the presence of 2-mercaptethylamine (MEA), to conjugate the outer shell with a positively charged surface. PVA-quantum dot films composed of positively-charged quantum dots resulted in a visibly more uniform film as shown in Figure 96 (B). Additionally, the absorption spectra for the positively charged quantum dot-PVA film began at an intensity of almost zero and exhibited an abrupt increase in absorption at approximately 530nm. The absorption increase is due to the first exciton absorption peak associated with the band gap energy of the quantum dot. The presence of this peak indicates that the quantum dots were well dispersed within the film.

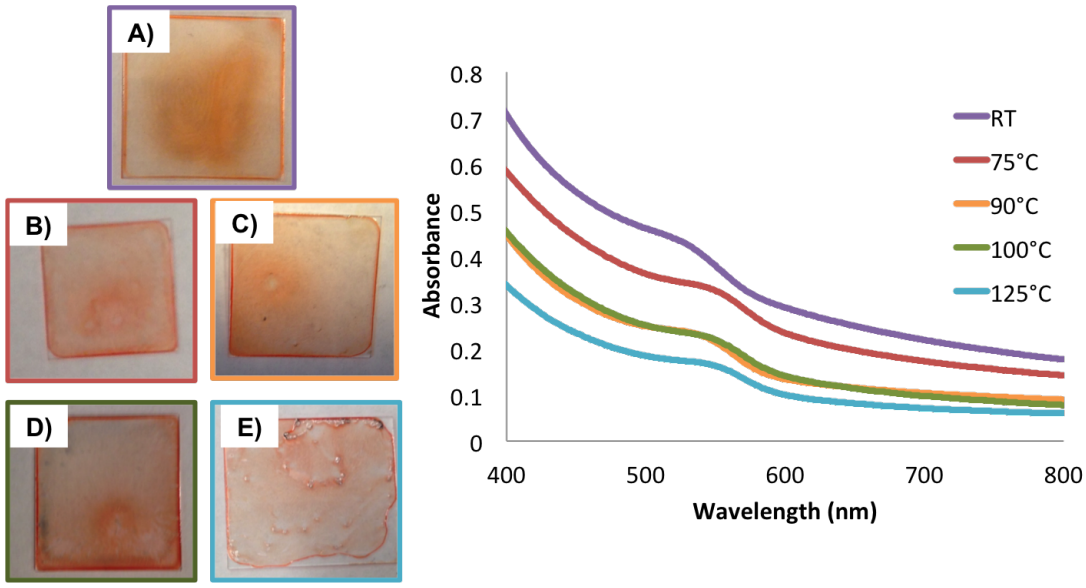

Figure 97: Images and absorption spectra of PVA-quantum dot nanocomposites prepared at temperatures of 25°(A), 75° (B), 90° (C), 100° (D), and 125° (E).

6.2.2 Optimization of curing temperature

The curing temperature was increased to accelerate the kinetics of quantum dot aggregation and film quality. A higher curing temperature accelerates the curing process and decreases the likelihood of quantum dot aggregation. PVA-quantum dot films were prepared by mixing the quantum dot solution and a 1.25% by mass PVA solution in 1:1 by volume ratio. Once deposited on the glass slide, films were cured at room temperature, 75°C, 90°C, 100°C, and 125°C respectively.

Films that were cured at various temperatures were imaged, and absorption measurements were collected. Figure 97 provides images of the films cured at each temperature and their absorption spectra. The absorption tends to decrease as curing temperature is increased. Additionally, film quality decreases as curing temperature increases. The heating caused bubbles to become trapped in the film, decreasing the uniformity of the film.

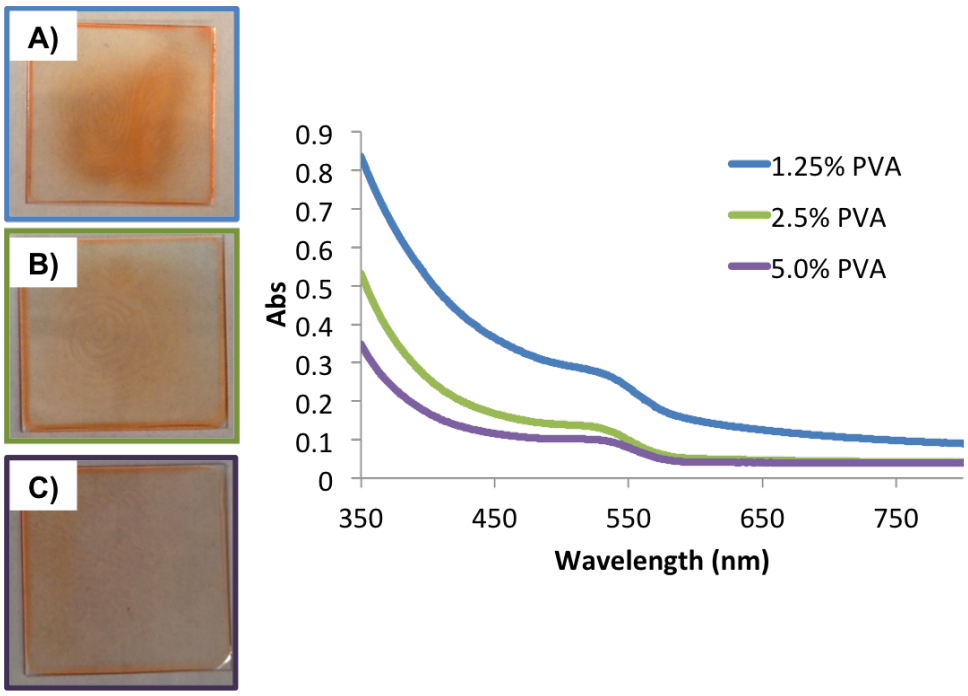

Figure 98: Images and absorption spectra of PVA-quantum dot nanocomposites prepared with various PVA concentrations of (A) 1.25%, (B) 2.5%, and (C) 5.0%.

6.2.3 Optimization of PVA concentration

The PVA concentration has an effect on the structure and thickness of the final film. As the PVA concentration is increased, the film thickness and mass are increased. Final PVA concentrations of 1.25%, 2.5%, and 5.0% were investigated to identify the concentration needed to achieve a 15 μm thick film. The film with a final PVA concentration of 2.5% has a mass of 12.7 mg, which correlated most closely with a film of 15 μm. Additionally, absorption spectra were collected to confirm the performance of the PVA-quantum dot films. Figure 98 shows that the 2.5% PVA film also had the best absorbance values.

6.2.4 Summary

Quantum dot charge, curing temperature, and PVA concentration were investigated to identify the best procedure for making a uniform PVA-quantum dot film with a high absorbance and a thickness of 15μm. Based on the results of these studies, the optimal PVA-quantum

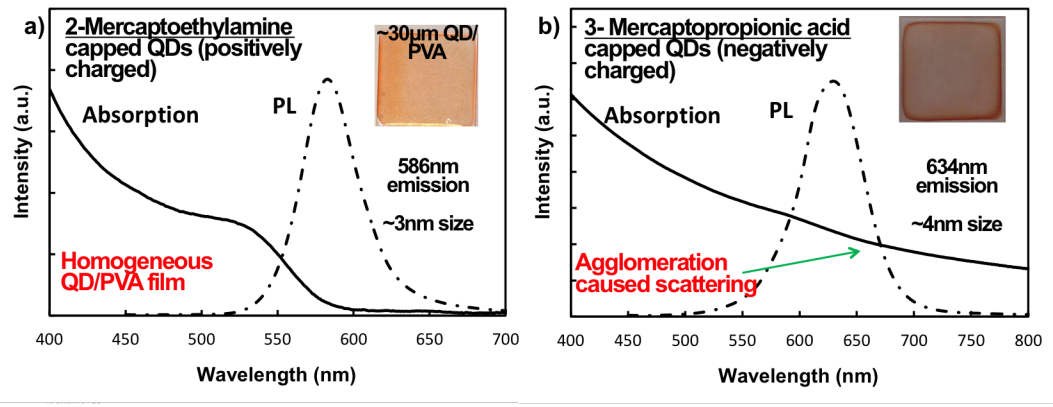

Figure 99: The absorption and emission spectra of the optimized PVA-quantum dot nanocomposites prepared with (a) positively charged quantum dots and (b) negatively charged quantum dots. From Zhitao Kang, unpublished results, [163].

dot films are prepared by combining positively charged quantum dots with PVA to a final PVA concentration of 2.5% and curing overnight at room temperature. The positively charged quantum dots could not be concentrated by centrifugation and re-dispersion in a smaller volume of water. Therefore, films of increased quantum dot concentration were prepared by combining a 10% by volume PVA solution and the quantum dot solution in 1:3 by volume ratio to achieve a final PVA concentration of 2.5%. The luminescence properties of the optimized positively and negatively charged PVA-quantum dot films are shown in Figure 99. It can be seen that the photoluminescence (PL) peaks have wavelengths characteristics of the QD size. The negatively charged QD's, however, show an absorption profile indicating increased scattering due to agglomeration. Positively charged QDs, however, do not show such effects of agglomeration.

6.3 Experimental Set-up

6.3.1 Laser Accelerated Flyer Impact Experiments

The PVA-quantum dot nano composite films were subjected to shock compression using a Continuum Powerlite Nd-YAG pump laser (3J). In contrast to gas gun experiments, laser driven shock compression experiments can be performed at a much smaller scale, allowing

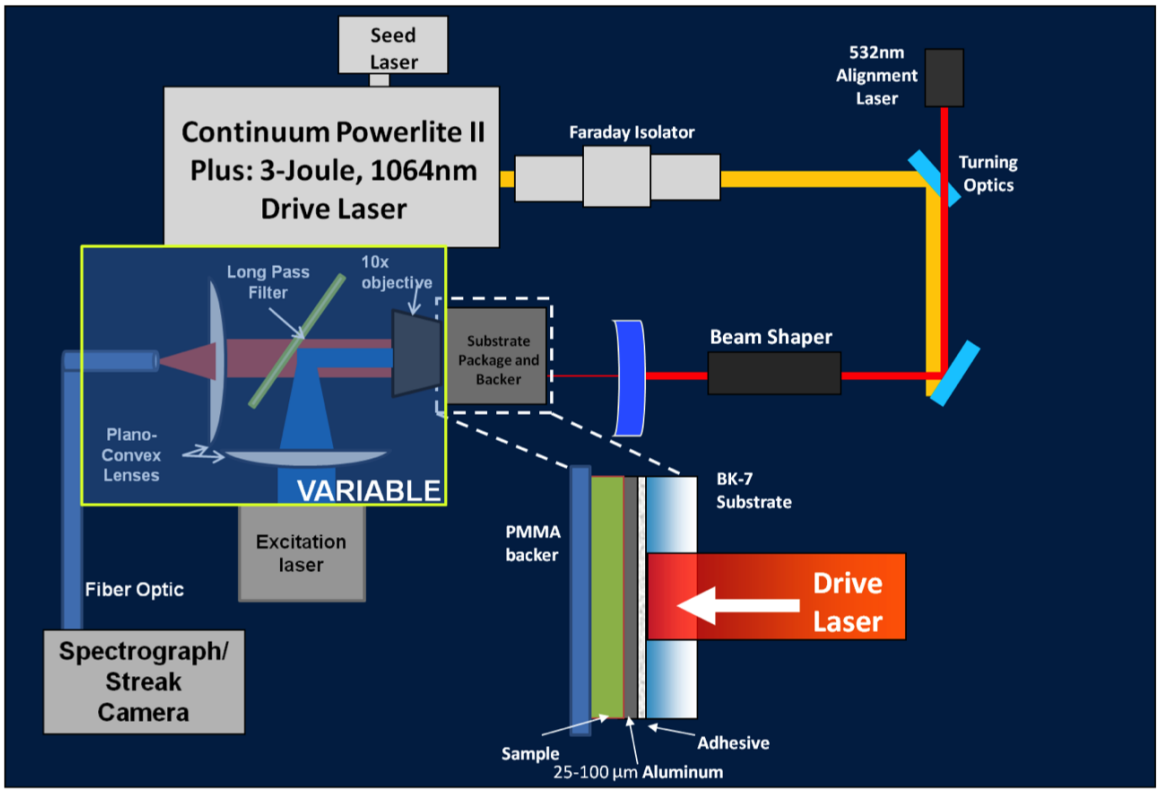

Figure 100: Schematic of the laser-accelerated flyer setup at Georgia Tech.

for the testing of much smaller samples, on the nanometer to micrometer scale. As a result, the laser-accelerated flyer setup provides much finer spatial control and shock-compression of the samples.

Figure 100 shows how energy from the laser is guided by the optics and focusing mirrors through a diffractive diffuse beam shaper, which provides top-hat output, onto the sample target. Once the laser beam interacts with the flyer assembly, a plasma is generated that builds up pressure through the flyer assembly, sending a high pressure wave into the PVA-quantum dot film. The flyer assembly was prepared by adhering a 3mm diameter x 25μm thick foil (aluminum or copper) onto a glass substrate with Eccobond epoxy and allowing the assembly to cure under a weight overnight.

Changes in band gap energy of the quantum dots during shock compression were monitored *in situ* by an Acton SP2556 spectrograph equipped with an Optronis SC-20 streak

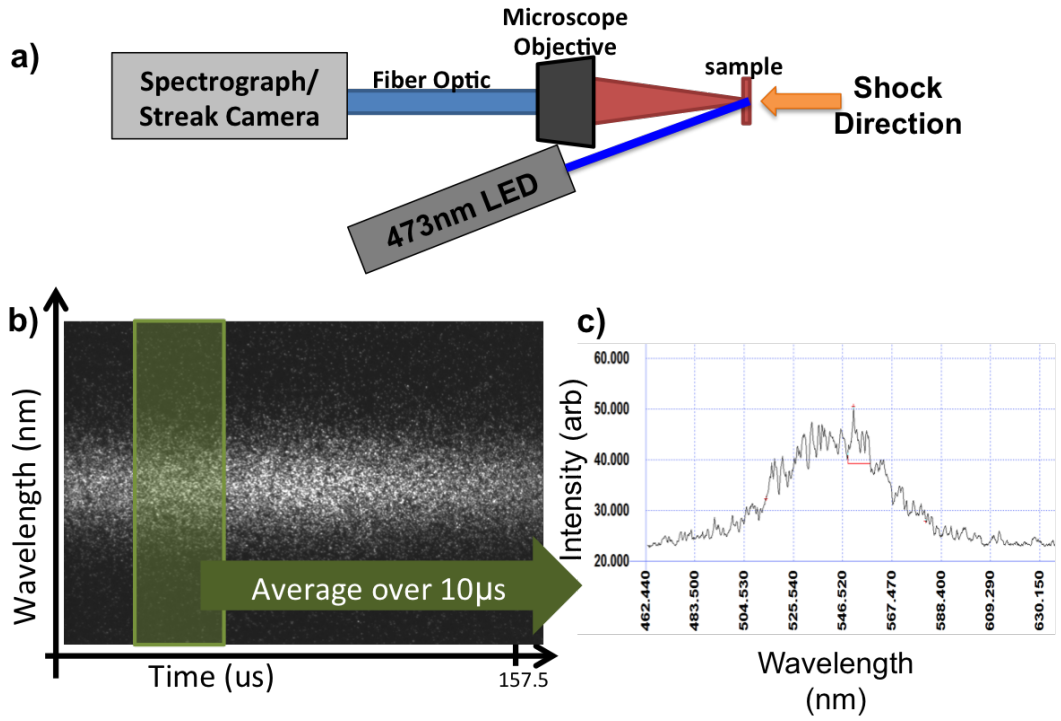

Figure 101: The setup and capture of dynamic emission spectra on the laser accelerated flyer setup. (a) A 473nm blue LED was used to excite the quantum dot sample and the emission light was directed into the spectrograph/streak camera via a microscope objective and fiber optic. (b) A typical dynamic spectra collected from the quantum dot sample. (c) The spectral signal was averaged over 10μs to obtain a spectral signal with a 2 to 1 signal to noise ratio.

camera. As shown in Figure 101A the PVA-quantum dot film was excited by directing a 473 nm blue LED at the back end of the film. Emission light from the quantum dots was collected by 20x microscope objective and directed into a 250μm fiber optic which was connected to the spectrograph. A typical dynamic spectra is shown in Figure 101B. In order to capture a spectra with a signal to noise ratio of 2 to 1, the signal was averaged over a time period of 10μs as shown in Figure 101C. Optimization of the collection optics did not lead to any significant improvements in the signal to noise ratio. A collection time of 10μs does not allow this experimental setup to probe the nanosecond time-scale response of the quantum dot to shock compression.

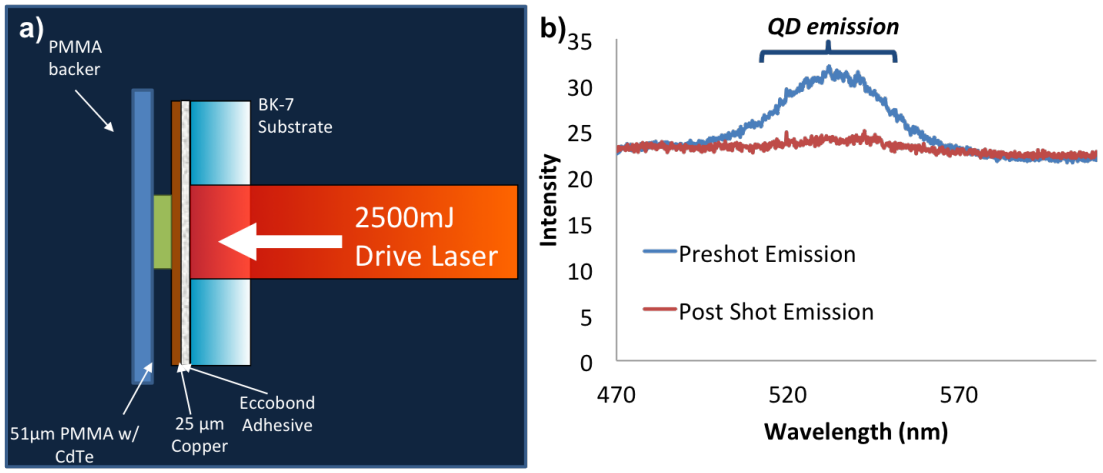

Figure 102: Pre- and post-mortem data: (a) The impact configuration of the quantum dot film. (b) Pre- and post-mortem emission spectra.

6.3.2 Pre- and Post-Mortem Results

In the absence of *in situ* monitoring, the quantum dot response to shock compression was investigated by collecting spectra before and after the shock compression event. A 51μm thick quantum dot-polymer nanocomposite was affixed to the sample holder as shown in Figure 102A and six spectra, varying slightly in spatial orientation, were collected and averaged to obtain the preshot emission spectra shown in Figure 102B. A shock wave was sent through the QD-polymer nano composite via a 2.5J laser pulse. Following shock compression, six static spectra were collected from the back end of the sample and averaged to obtain the post-shock emission spectra, which is shown in Figure 102B.

Prior to shock compression, a quantum dot emission peak was present at approximately 540nm; following shock compression, the quantum dot emission peak disappeared. Although this loss of emission intensity points to a change in the shape or size of the quantum dot due to shock compression, the intensity loss provides no information about the kinetics of the quantum dot response. Nanosecond time scale monitoring of the shock response is required to gather this information. A higher power excitation laser, improved collection optics, or a more sensitive streak camera are required to measure the quantum dot response

in situ.

6.3.3 Laser energy calculations

The laser excitation source was investigated to determine how significant of an effect any improvements in the excitation laser energy would be. In order to capture as much light as possible from the quantum dots, the laser energy required to excite (or pump) the quantum dots at their maximum rate was calculated. The maximum emission rate occurs when every quantum dot is emitting at its maximum rate, which is roughly one photon per emission lifetime. The laser energy that would provide the maximum signal was calculated using the saturation intensity equation,

$$I = \frac{h\nu}{\sigma\tau} \tag{49}$$

where *h* is Planck's constant, ν is the frequency in hertz, σ is the absorption cross-section, and τ is the fluorescence lifetime. In the absence of the emission data for CdTe quantum dots, the absorption cross-section and the fluorescence lifetime of CdTe were approximated using literature values obtained from Leatherdale [162] for CdSe quantum dots. Assuming an absorption cross-section of 5.5E-16cm^2 and a fluorescence lifetime of 1.5E-8s, the saturation intensity of a CdTe quantum dot would be 45.3kW/cm^2. From this number, the power needed to excite a 100μm diameter spot size is approximately 3.6W, which is beyond the capabilities of the laser available at Georgia Tech. Hence, a collaboration was initiated with the Dlott group at the University of Illinois Urban-Champaign (UIUC) to analyze the shock-compression response of the quantum dot-PVA nano composite film.

6.4 Shock Compression Response of Quantum Dot-PVA Films

The shock compression response of both positively and negatively charged quantum dot-PVA films were investigated using the laser-accelerated flyer impact system at UIUC illustrated in Figure 103a [116]. A Q-switched Nd:YAG laser (Quanta-Ray Pro-350) sends a pulse of up to 2.5J into a diffractive beam homogenizer (Silios) which converts the pulse

from a Gaussian to a top hat shape. The pulse is focused down to diameter of 700μ and directed into the flyer package consisting of 100μm thick aluminum foil adhered to a 6.35mm thick, 5 x 5 cm^2 glass substrate by a clear, low-viscosity, UV-curable acrylic adhesive (Dymax LIgh-Weld401). A spacer is used to control the flight distance of the flyer to the sample. Once the aluminum flyer is ejected from the glass slide by the laser pulse, it impacts the sample, composed of a 30μm QD-PVA film backed by a glass substrate. The entire flyer-sample package is held under vacuum to reduce the chance of impact flash which can drown out any emission signal. The QD sample is excited (or pumped) from the back using a Q-switched Nd:YLF excitation laser (Quantronix 527 DP) that delivers 1mJ, 250ns pulses long pulses, focused to a diameter of 50μm at 527nm to the sample. The emission light is captured using a 10x microscope objective and directed into a spectrograph-streak camera for analysis of the emission spectra *in situ*.

Flyer plate velocity is also captured on the back end of the sample package using Photonic Doppler Velocimetry (PDV). A dichroic beam splitter is used to direct a portion of light from the PDV into the sample and reflect that light back into the PDV to collect velocity data. An example trace from the PDV during a 4.3 GPa shock impact experiment is provided in Figure 103b . From the PDV response, the velocity over the course of the experiment can be monitored as shown in Figure 103c. The velocity of the flyer stabilizes as it moves toward the sample. Upon impacting the QD-PVA sample, an abrupt drop in the velocity is observed as the flyer continues to move into the sample at .89 km/s, corresponding to the particle velocity, the U_p. The U_p remains at .89 km/s for 15 ns, corresponding to a steady state shock pressure of 4.3 GPa propagating through the PVA. After 15 ns, the velocity decreases steadily to zero over the course of 20 ns.

The data captured by the spectrograph-streak camera during shock compression, including a contour plot of the fluorescence spectra over time, the intensity change over time, and the spectral shift over time for the positively charged QD-PVA films, are provided in

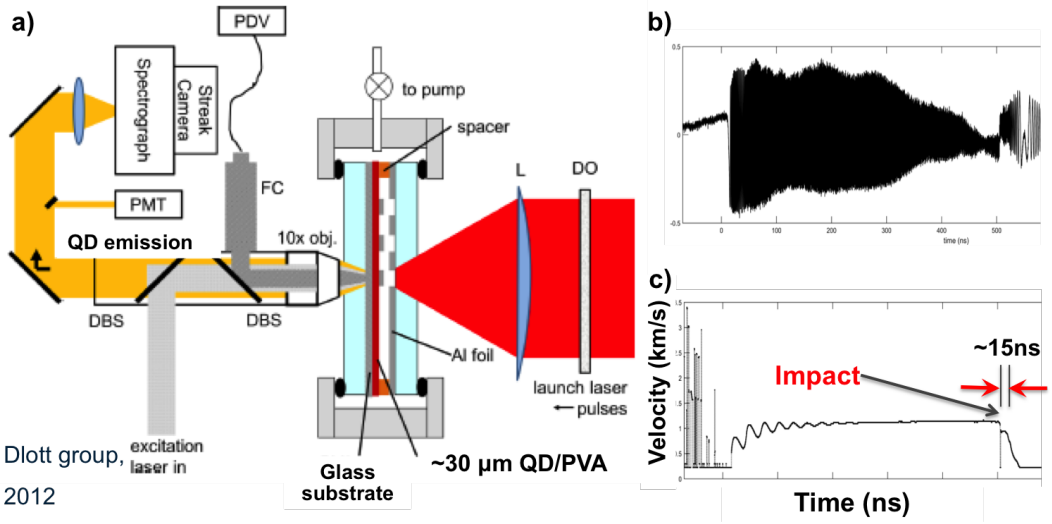

Figure 103: (a) Schematic of the laser set-up at UIUC used to analyze the QD-PVA films. (b) Velocity trace. (c) Example of the PDV response. (From [163])

Figure 104a-i. The contour plots provided in Figure 104a, d, and g show the spectra collected over time during shock compression at 1.7 GPa, 4.1 GPa, and 7.1 GPa, respectively. Initially, the quantum dots are under static conditions and emit at approximately 580 nm. Upon impact, as the shock wave moves through the sample, the fluorescence intensity drops and a blue shift occurs, due to the increase in pressure and/or the rise in temperature.

Figure 104 (a) - (c) demonstrates the spectroscopic response of quantum dots to shock compression at 1.7 GPa. Figure 104 (b) shows the drop in intensity to 40% of the initial intensity until 50 ns following impact. After 50 ns, the intensity begins to gradually increase to 80% of the initial emission intensity. Additionally, as depicted in Figure 104 (c), a 5 nm blueshift is observed in the emission peak during shock impact. After 50 ns, the blue shift steadily decreases almost to the original emission peak center.

Figure 104 (d) - (f) presents the spectroscopy data captured during shock compression of the quantum dots at 4.1 GPa. Similar to the response at 1.7 GPa pressure an initial intensity drop and a blueshift is observed. After 75 ns, the emission intensity drops to 20% of its initial emission intensity as shown in Figure 104 (e), before gradually increasing to 50% of the initial emission intensity of the quantum dot. A blueshift of a maximum of

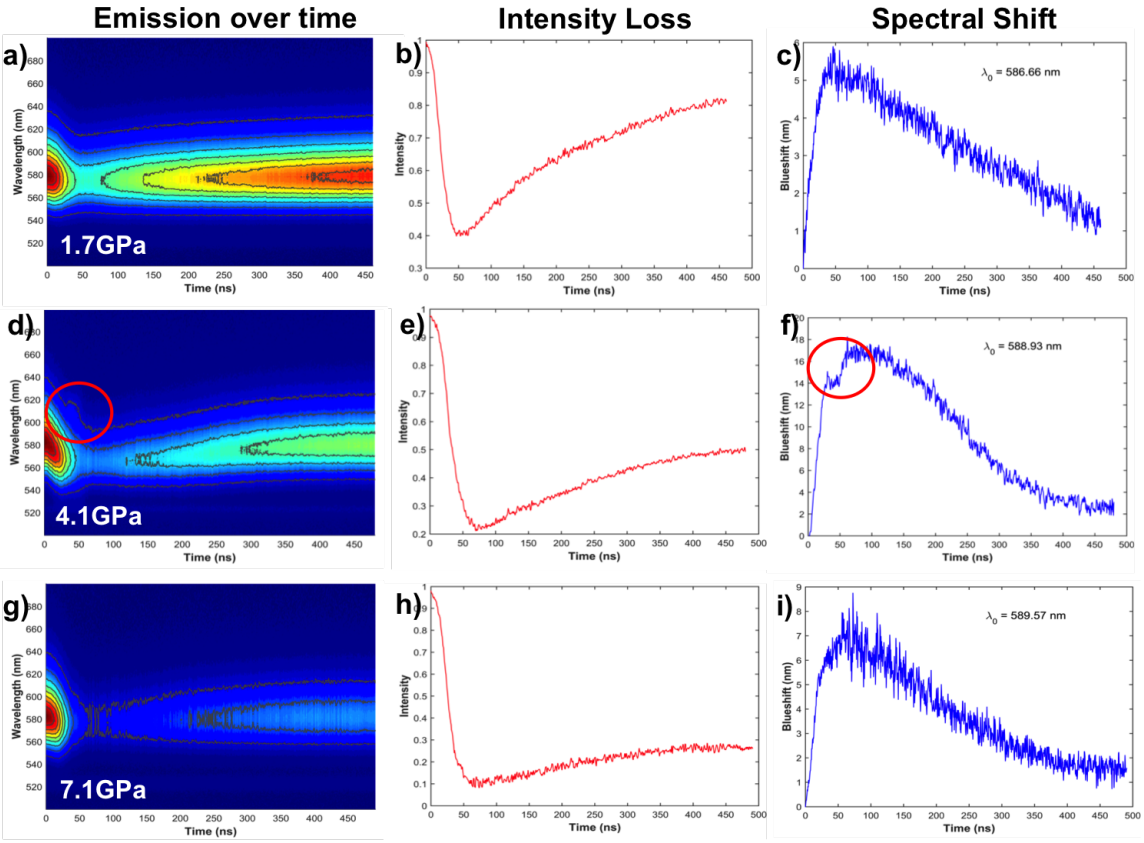

Figure 104: Examples of *in situ* data obtained from the shock impact of positively charged quantum dot-PVA films at pressures of (a-c) 1.7GPa, (d-f) 4.1GPa, and (g-i) 7.1GPa. The first column provides the fluorescence spectra as a function of time (a, d, and g). The second column provides the change in intensity over time (b, e, and h), and the last column provides the blueshift over time (c, f, and i) (From [163]).

17 nm was observed 75 ns after shock impact; following which, the blueshift gradually diminished almost to the original peak center about 500 ns after impact. Another feature noted at this pressure was a secondary emission peak, demarcated by the red circle in Figures 104 (d) and f. The secondary emission peak was noted at pressures between 4 and 6 GPa, but not above or below these pressures.

Figure 104 (g) - (i) shows the spectroscopic response of quantum dots at a pressure of 7.1 GPa . At this higher pressure, the emission intensity drops further to10% of the initial emission intensity after 70 ns, as shown in Figure 104 (h). Following the drop, a gradual increase to only 25% of the initial intensity is observed. Figure 104 (i) displays a decrease in the maximum blueshift to 7 nm during shock compression.

6.4.1 Fluorescence intensity loss

Figure 105 (a) - (b) demonstrates the changes in fluorescence intensity as a function of shock pressure. As shock pressure increases from 1.7 GPa to 7.1 GPa, the fluorescence intensity decreases from a maximum of 40% of the initial intensity to 10% of the initial intensity between 50 to 70 ns following impact. Over time, the sample begins to relax, and the intensity gradually increases, as shown in Figure 105 (a), but never returns to its original state. The intensity loss as a function of pressure is plotted in Figure 105 (b), which shows that the intensity loss increases with increasing pressure. The monotonic increase in intensity loss with pressure with could potentially enable quantum dots to be used as a pressure indicator. The observed intensity loss may also be due to temperature rise or a phase change [163]. Bueno *et. al.* [164] showed that CdTe PMMA nanocomposites exhibit an 80% drop in emission intensity with a 25° increase in temperature.

6.4.2 Blueshift

In addition to fluorescence intensity loss, a blueshift was observed in the fluorescence emission upon shock compression at pressures ranging from 1.7 GPa to 7.1 GPa. Figure 106 (a)

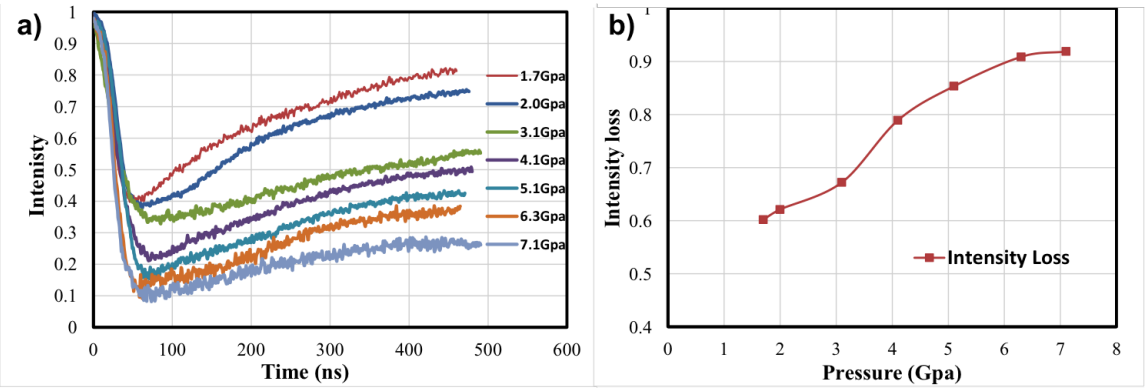

Figure 105: Summary of the change in intensity as a function of pressure. (a) The change in fluorescence intensity over time of each at each pressure tested. (b) The maximum intensity decrease as a function of pressure. (From [163])

and (b) shows that upon impact, a dramatic blue shift occurs, from a minimum of approximately 5 nm at a shock pressure of 1.7 GPa to a maximum of 17 nm at a shock pressure of 4.1 GPa. After the initial abrupt shift, the blueshift gradually decreases over time at varying rates, dependent on the magnitude of the shock pressure. The plot of the blue shift as a function of pressure provided in Figure 106 (b) shows that as pressure increases to approximately 4.0 GPa, the blue shift increases, but, at pressures of greater than 4.0 GPa, the blue shift decreases. This behavior does not follow the trends observed by Lin *et. al.* [165] who studied CdTe nanocrsytals under high quasistatic pressures and observed only a monotonic increase in the band gap energy with an increase in pressure.

6.4.3 Fluorescence peak width decrease

At certain pressures, the fluorescence peak width was observed to decrease. Figure 107 (a) shows the change in peak width at shock pressures ranging from 1.7 to 7.1 GPa as a function of time. At pressures of up to 2 GPa, there is very little change in the peak width. At pressures greater than 3.1 GPa, a decrease in the peak width is observed after impact. By 200 ns after impact, the peak width typically returns to its original width. In samples that were shock compressed at pressures between 4 and 6 GPa, an initial increase in peak width is observed due to the appearance of the secondary emission peak. Figure 107 (b)

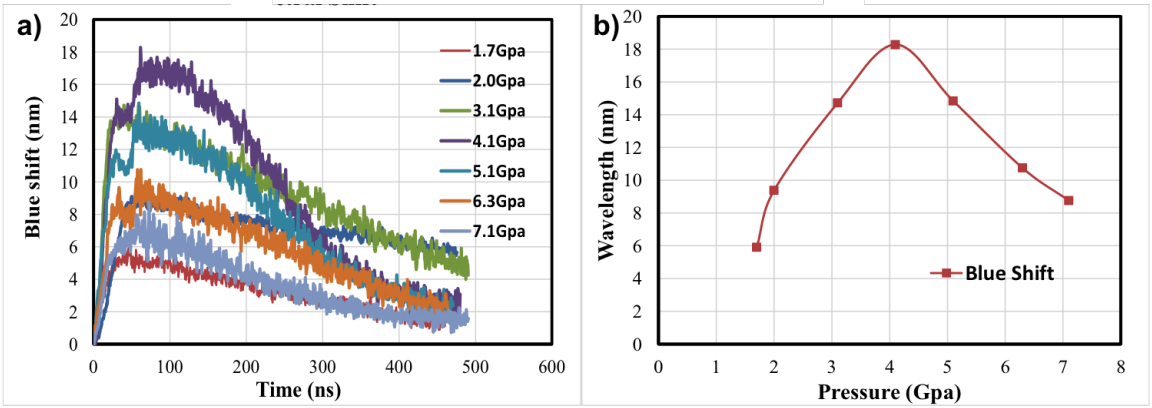

Figure 106: Summary of the change in blue shift as a function of pressure. (a) The change in blue shift over time of each at each pressure tested. (b) The in blue shift as a function of pressure. (From [163]).

illustrates that the maximum peak width reduction increases to a width reduction of 8 to 9 nm with pressure of up to 5 GPa. At pressures greater than 5 GPa, the peak width reduction stabilizes at remains at about 8 nm up to 7.1 GPa, the maximum pressure tested.

As described in Chapter 2 [117], quantum dot size controls the band gap energy and, hence, the fluorescence emission properties of the material. A solution of quantum dots of a single size would exhibit a very narrow emission peak, less than approximately 10 nm, that corresponds to the band gap energy. Therefore, a solution of quantum dots of a wide particle size distribution would exhibit a wide Gaussian-shaped emission peak, that corresponds to the average band gap energy of all of the particle sizes within the solution. Upon shock compression of a film containing quantum dots of a wide particle size distribution, both large and small particles are compressed to a smaller diameter. Yet, smaller particles are more difficult to compress than larger particles due to the contribution of a higher surface energy. Therefore, larger particles will experience a greater decrease in diameter than smaller particles, allowing the particle sizes to converge for a brief period as the shock wave passes through the film, corresponding to a decrease in the emission peak width. After the passage of the shock wave through the film, the particles recover and return to their original

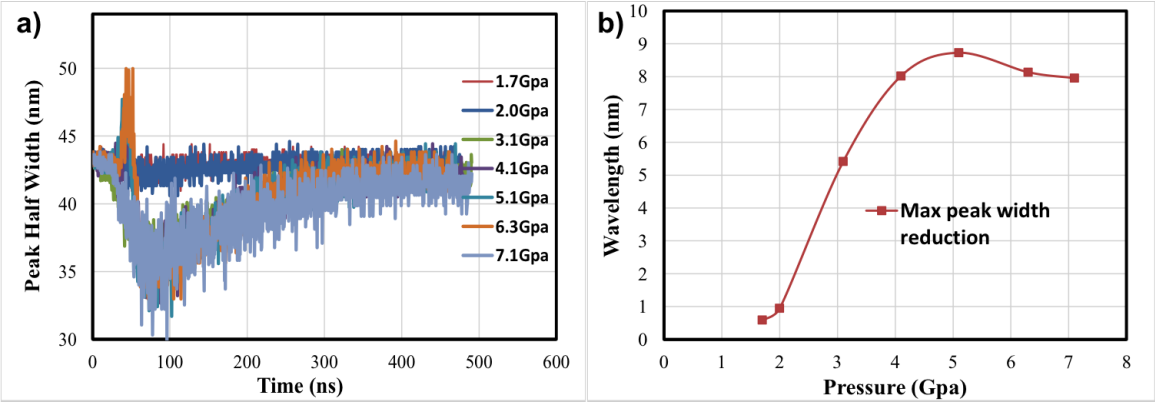

Figure 107: Summary of the QD FWHM change as a function of pressure. (a) The FWHM over time at each pressure tested. (b) The maximum peak width reduction as a function of pressure. (From [163])

diameter, and the emission peak width returns to its original value.

6.4.4 Presence of a secondary emission peak

At shock pressures ranging from 4.0 GPa to 6.0 GPa, a secondary emission peak becomes evident approximately 30 ns following impact. Figure 108 shows the emission spectra at times of 30, 35, 40, and 45 ns under a 5.1 GPa shock pressure. At 35 ns after impact, a shoulder begins to develop that is indicative of secondary emission peak centered at 605 nm, 35 nm away from the main emission peak centered at 570 nm. After 45 ns, the secondary emission peak disappears, and the spectra takes its original shape. Peak fitting of the emission profile at 45 ns was performed to confirm the presence of a secondary emission peak which resulted in two peaks, one at 570 and one at 606 nm. Additionally, peak fitting allows for the observation of a blue shift and peak width decrease in the secondary emission peak, similar to trends in the main emission peak response to dynamic pressure.

The presence of the secondary emission peak at dynamic pressures of 4 to 6 GPa can potentially be explained by a pressure induced phase transition [163]. As hydrostatic pressure increases to a range of 3.5 to 4.1 GPa, two successive phase transitions are observed in CdTe, first, a zinc-blende to a cinnabar phase transition, followed by a cinnabar to rock salt phase transition [166]. For bulk CdTe, the cinnabar to rock salt phase change has been

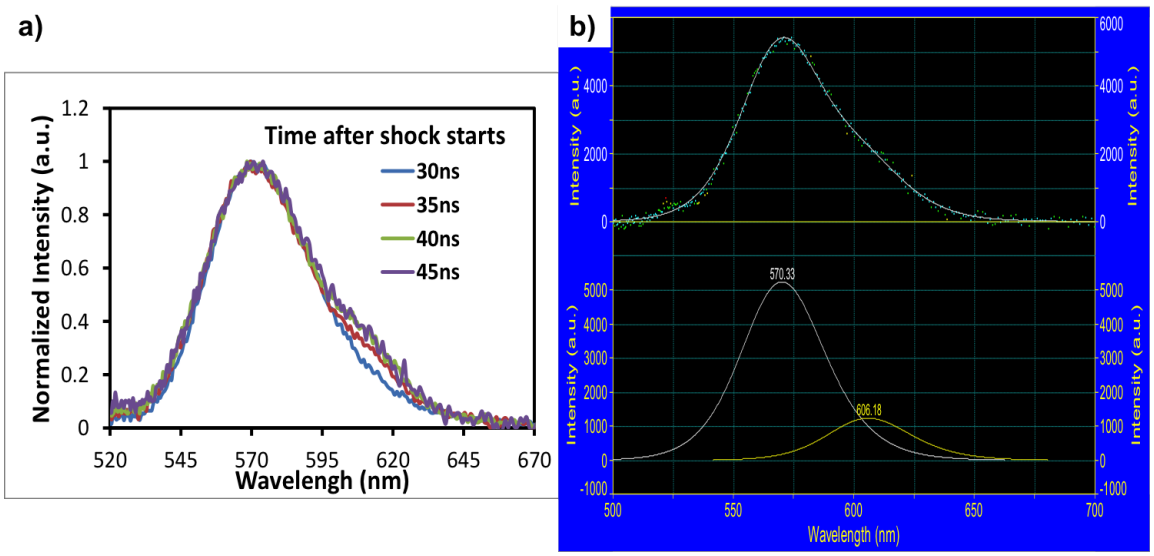

Figure 108: Summary of the secondary emission peak data. (a) The emission spectra of the positively charged quantum dot film during a 5.1 GPa shock compression event at 30, 35, 40, and 45 ns, exhibiting a secondary emission or overlapping peaks. (b) Double peak fit to the fluorescence spectrum 45 ns after shock initiation. (From [163])

observed at a hydrostatic pressure of 3.7GPa [167]. Yet, for CdTe nanoparticles in solution, Wu *et. al.* [168] observed an increase in the hydrostatic pressure, 5.7 GPa, required to induce the phase transition. The pressure increase is attributed to the increased influence of surface tension in the quantum dots, which aids in the material stability. Additionally, at the phase transition pressure of 5.7 GPa, Wu *et. al.* [168] observed a decrease in the band gap energy due to the direct-to-indirect bandgap transition that occurs with the cinnabar to rocksalt phase transition. In the CdTe quantum dot-PVA films, the band gap energy decreases or the redshift increases upon reaching the phase transition pressure, can result in the observed secondary emission peak.

Another possible explanation of the secondary emission peak is the occurrence of energy transfer between the nanoparticles under high pressure [163]. Lin *et. al* [165] reported double peak photoluminescence emission of CdTe nanocrystals at high pressures and attributed this observation to nonradiative energy transfer that can take place when the separation between the quantum dots is short and the energy of the small quantum dots

can be transferred to the larger quantum dots. The net effect is that the lower wavelength emission of the small quantum dots is quenched as the longer wavelength emission of the large quantum dots is enhanced [163], leading to the appearance of a redshifted secondary emission peak.

6.4.5 Shock response of negatively charged quantum dots

The MPA-capped, negatively charged quantum dot-PVA films were also investigated under shock compression, which responded differently than the positively charged quantum dots. Figure 109 illustrates the shock compression response of negatively charged QD-PVA films at pressures of 2.1 GPa (a-c) and 4.3 GPa (d-f). The negatively charged quantum dots experience a dramatic intensity loss and a redshift (negative blueshift) in the emission wavelength upon shock compression, as shown in Figure 109 (a) and (d), . At 2.1 GPa, the fluorescence intensity drops to 40% of its original value after 80 ns, similar to positively charged quantum dots as shown in Figure 109 (b). Figure 109 (c) reveals the negative blue shift or redshift of 7.5 nm that occurs $\tilde{3}0$ ns after impact. Following shock compression, the material equilibrates and the wavelength returns to its original position. Figure 109 (e) shows that QD-PVA films exposed to a shock pressure of 4.3 GPa exhibit an increased, 90%, intensity loss 30 ns after the shock that does not recover to its original value once the shock wave has passed through the material. A decreased maximum red shift of 5 nm is observed in samples shocked at 4.3 GPa as shown in Figure 109 (f). No secondary emission peaks were evident in the fluorescence spectra collected for negatively charged samples.

Figure 110 provides a summary of the data collected during shock compression of negatively charged quantum dot-PVA films at pressures from 1.3 to 6.5 GPa. Figure 110 (a) illustrates the intensity loss upon shock compression. The intensity loss increased monotonically, from 60% to almost 100%, as pressure increased. Compared to positively charged quantum dot films, the magnitude of the intensity loss is greater in negatively charged QD films at similar pressures. Additionally, at lower pressures, the time required to reach the

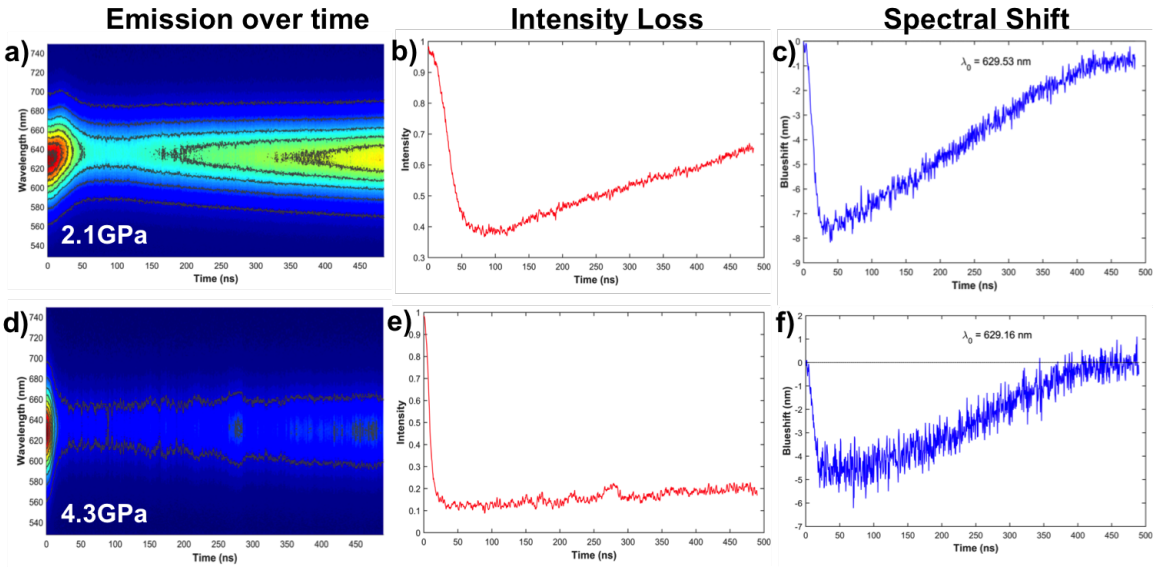

Figure 109: Examples of *in situ* data obtained from the shock impact of negatively charged quantum dot-PVA films at pressures of (a-c) 2.1GPa and (d-f) 4.3GPa. The first column provides the fluorescence spectra as a function of time (a, d). The second column provides the change in intensity over time (b, e), and the last column provides the blueshift over time (c, f). (From [163])

maximum intensity loss is longer than positively charged QD films (80 ns at 1.3 GPa), and as pressure increases, the negatively charged quantum dots experience intensity loss more quickly (20 ns at 6.5 GPa). Figure 110 (c) shows that, similar to the positively charged QD films, the peak half width decreases with increasing pressure. The maximum observed peak width reduction is 8 nm at 4.3 GPa. At higher pressures, above 4.3 GPa, the intensity loss is so large (greater than 90%) that the peak width decrease is artificially large due to background noise and the low fluorescence intensity.

The spectral shift observed during the shock compression of the negatively charged QD-PVA films is illustrated in Figure 110 (b) and (d). Instead of the blueshift observed in the positively charge quantum dots, a redshift is observed. The redshift increases with pressure to a maximum of 10 nm at 3.5 GPa. At pressures higher the 3.5 GPa, the red-shift drops to approximately 6 nm. The phenomena causing the redshift needs additional investigation. It is possible that the redshift results from energy transfer from the small

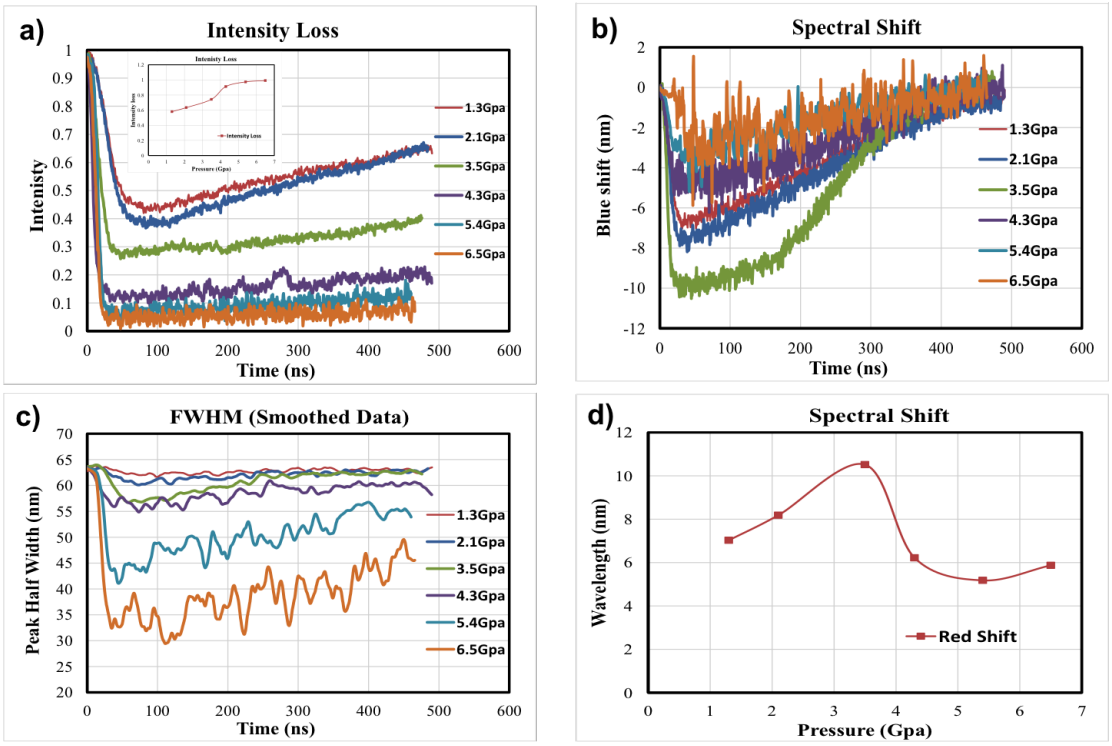

Figure 110: Summary of intensity loss, blueshift, and FWHM data for negatively charged quantum dots. (a) The intensity loss of the negatively charged quantum dot films during shock compression at pressures ranging from 1.3 to 6.5 GPa over time. (b) Blue shift of the negatively charged quantum dots over the duration of the shock compression. (c) The change in the FWHM over time. (d) The spectral shift of the negatively charged quantum dots as a function of pressure. (From [163])

quantum dots to the larger quantum dots formed due to aggregation [165]. The negatively charged QD-PVA films were much more aggregated than the positively charged QD-PVA films as evidenced by their absorbance spectra given in Figure 99. The aggregation makes the distance between the quantum dots shorter, allowing for enhanced energy transfer between the quantum dots. At lower pressures, the energy transfer process, which causes a redshift, may dominate and wash out any effects resulting from the compression of the QD and subsequent band gap increase or blueshift, leading to an apparent redshift. As the applied pressure increases to greater than 3.5 GPa, the blueshift may become more dominant and cause a decrease in the apparent redshift.

6.5 Application of Quantum Dots as Meso-scale Sensors

The spectroscopic shock compression results provided in the above Section indicate that quantum dots are quite sensitive to shock pressures. Positively charged quantum dot-PVA films exhibit a monotonic decrease in intensity with increase in applied pressure. The positively charged QD-PVA films also show an increase in blue shift, up to pressures of 4.0 GPa. Predictable changes in intensity and blue shift as a function of pressure can be calibrated and used as sensors to monitor shock pressure at the mesoscale.

Continued optimization, characterization, and development of the QD's is required to utilize these as sensors for meso-scale diagnostic. Figure 111 outlines the possible concept that can be used to investigate the application of QD's for mesoscale diagnostics. The QD-PVA configuration used in the preliminary experimentsis given in Figure 111 (a). In this configuration, a flyer plate impacts the QD-PVA film directly and the quantum dot response is monitored by a spectrograph/streak camera from the back end. The setup allows the shock compression response of the QD-PVA film to be investigated by itself, without the influence of other materials. The characterization can be performed at a single point, 50 μm in diameter, within the QD-PVA film or using two dimensional spatial imaging.

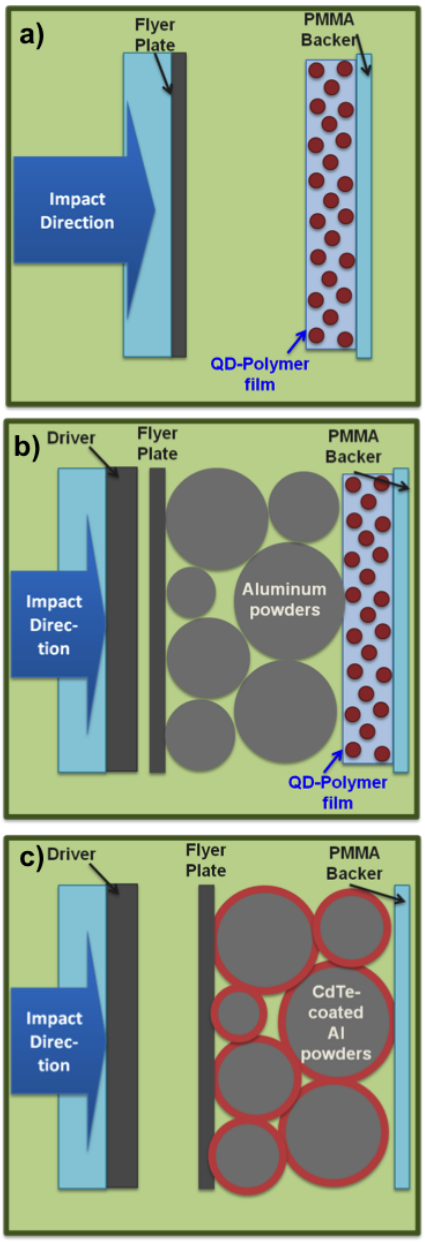

Figure 111: Series of concepts that can be used to test quantum dots as mesoscale diagnostic sensors (a) Stage 1: The quantum dots are incorporated into a polymer material and are shocked directly. (b) Stage 2: A granular material is placed in contact with the quantum dot film and shock compressed. (c) Aluminum particles are coated with quantum dots.

Figure 111 (b) illustrates a set-up in which the shock is transmitted through a heterogeneous (granular) medium (Al powder) before propagation through the QD-PVA film. The QD-PVA response can be monitored at a single point using a spectrograph/streak camera or photodiode to follow the blueshift and changes in intensity. Alternately, excitation of 1D line within the QD-PVA film, can allow for highly time-resolved tracking of changes in intensity across the line using a streak camera. Additionally, a black and white camera can be used to provide spatial information along a 2-D surface, corresponding to the changes in the aluminum powder as a function of pressure.

Figure 111 (c) shows a schematic of the configuration in which the granular material of interest is coated with quantum dots and PVA. The QD-coated granular material can be sandwiched between an aluminum driver and a PMMA backer. The impact of the aluminum flyer onto the aluminum driver can result in a shock wave propagating through the QD-coated granular material. The quantum dot response can be monitored from the back end using a spectrograph/streak camera, photodiode, or framing camera.

6.5.1 Further investigations of QD-PVA film

Experiments to date have provided a general understanding of the shock compression response of the QD-PVA film. The QD-PVA results can be further optimized by decreasing the particle size distribution of the quantum dots, which can result in both an increase in the signal to noise ratio of the emission peak and a decrease in the initial emission peak width. These improvements can make both the shock-induced intensity decrease and the blueshift more easily discernible, leading to more robust data analysis.

Investigation of QD-PVA films containing a smaller particle size distribution can also aid in the analysis of the secondary emission peak. The smaller particle size distribution can result in a decreased secondary emission peak, which can point to energy transfer from small quantum dots to larger quantum dots as being responsible for energy transfer. Should a smaller particle size distribution result in an increased secondary emission peak,

the outcome would point to the cinnabar to rocksalt phase transition as being responsible for the secondary emission peak. Additionally, the secondary emission peak can be investigated by preparing QD-PVA films containing a lower concentration of quantum dots. This would lead to decrease in the distance between quantum dots and a resulting decrease in the secondary emission peak, thus, pointing to energy transfer as the cause of the secondary emission peak,

The effects of temperature on quantum dot fluorescence emission are not well understood. Temperature rise during shock compression may play a role in the intensity decrease. If so, this effect needs to be decoupled from the effects of pressure to develop a reliable mesoscale sensor. Temperature effects on QD-PVA intensity may be investigated by heating the film and monitoring the emission response with the spectrograph/streak camera or a photodiode.

6.5.2 QD-PVA films as shock-compression sensors

Figure 111 (b) illustrates the set-up that can be used to investigate the shock compression response of QD-PVA backing a granular material. The spatial sensitivity of the QD-PVA sensor can be investigated by studying different material configurations. Figure 112 illustrates examples of three material configurations, (a) a plate of aluminum, (b) coarse aluminum particles, and (c) fine aluminum particles. Upon shock compression, through each of these, a different response in the QD-PVA would be expected. Shock propagating through solid aluminum plate, as shown in Figure 112 (a) will result in homogenous, uniaxial compression of the QD-PVA film, and cause a decreased intensity and a blue shift across the entirety of the film. On the other hand, shock compression of coarse and fine aluminum particles, as shown in Figure 112 (b) and (c), will result in higher pressure localization within the diameter of the aluminum particles, and lower pressure areas near the void spaces. QD's in contact with the aluminum particles will compress and exhibit intensity loss and blueshift first. As the void space is filled, the areas surrounding the diameter

of the particles will increase in pressure and exhibit intensity loss and blue shift at a later time. Hence, the coarse and fine particles should give differing spatial signatures upon compression, with high pressure, low intensity spots corresponding to the particle area.

In addition to point probes, various cameras and photodiodes can be used to analyze the quantum dot emissions to determine the maximum spatial sensitivity and time resolution. Spectroscopic data collected to this point reveal that either intensity or blueshift may be used to monitor pressure variations in shock compressed materials.

An intensity loss-based pressure measurement system is ideal because several types of cameras and photodiodes can be used to monitor the change in intensity at various spatial and time resolutions. As illustrated in Figure 112, a black and white high speed framing camera equipped with the appropriate magnifying lenses can be used to monitor intensity changes in two dimensional space over time. The only drawback would be the limited time resolution; even the fastest cameras are only able to collect one frame every 25 ns and may not be able to detect light emission from quantum dots at these speeds. One dimensional data, in the form of a line across the sample may also be collected through the use of a streak camera. In a manner similar to the line VISAR discussed in Section 2.4.1.1, the excitation laser can be shaped in the form of a line and focused onto the sample to excite the quantum dots. The changes in intensity across the line during the shock compression time-scale can then be monitored by a streak camera. Changes in intensity can also be collected from a single point on the sample using a photodiode, which is inexpensive and has a high time resolution.

In lieu of an intensity loss-based analysis, the blueshift may also be analyzed to track the changes in pressure of the sample. Color cameras are not able to detect wavelength shifts of less than 10 nm, therefore analysis of the blueshift may be limited to collection of data at a single, 50 μm diameter, point on the sample. Analysis of coarse and fine particles using this method may provide information about the changes in the time duration and magnitude of the pressure increase as mesoscale features are incorporated into a sample.

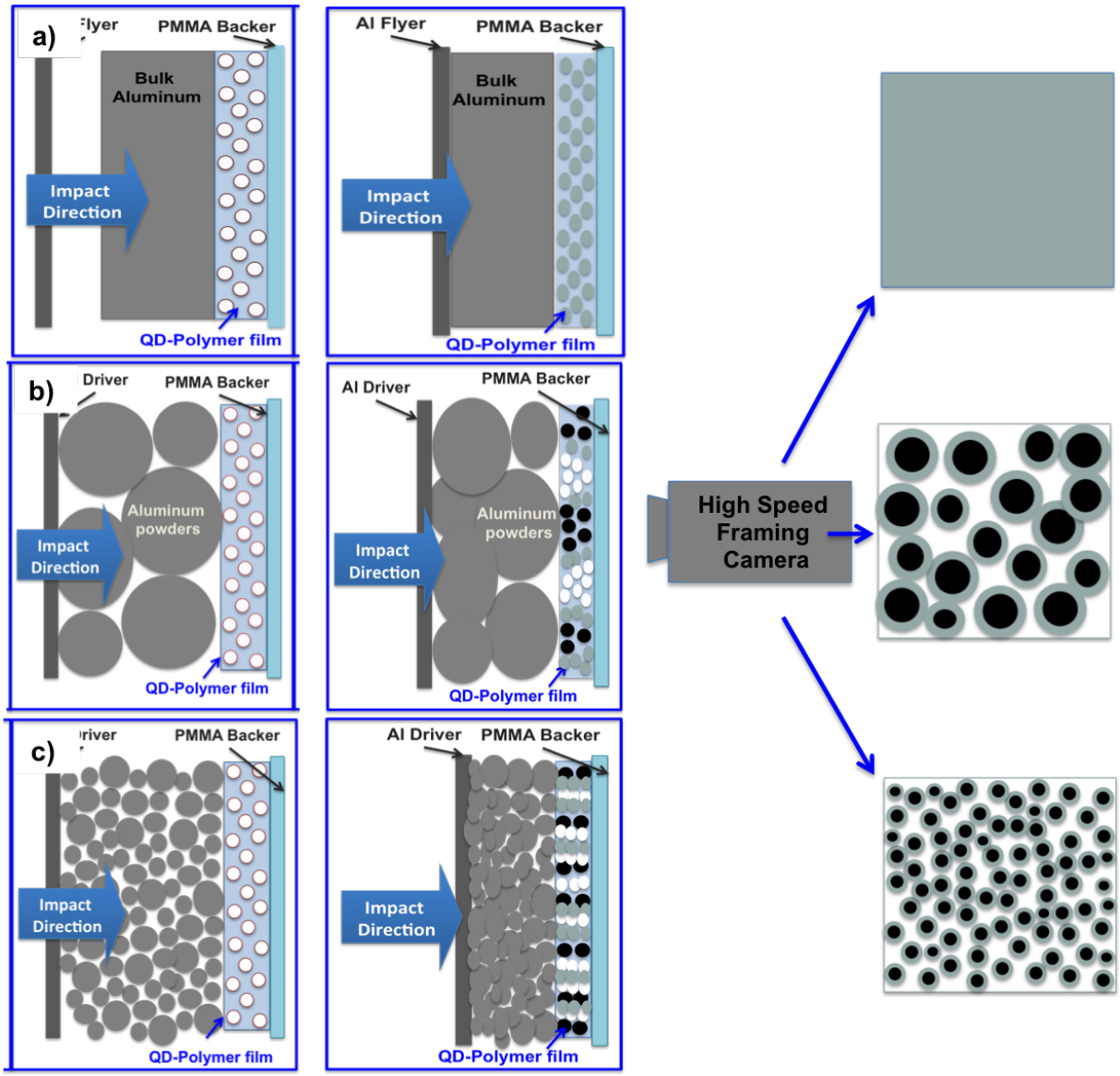

Figure 112: Experiments planned for stage two testing of quantum dot films. (a) Impact of bulk aluminum to establish a baseline. (b) Impact of large aluminum powders. (c) Impact of small aluminum powders.

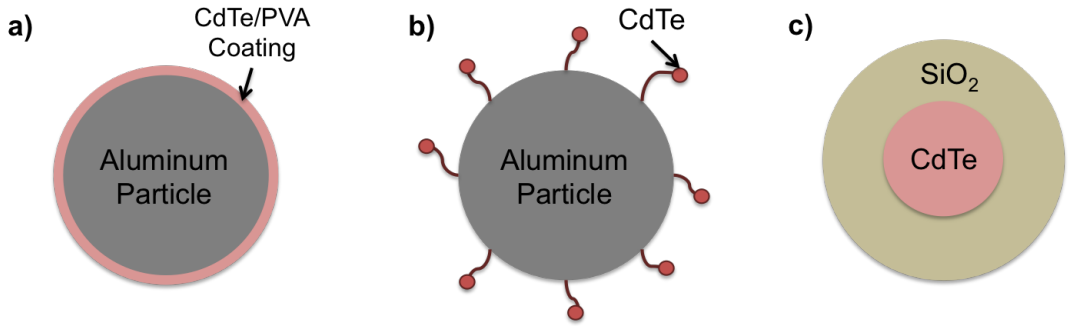

Figure 113: Approaches to coating granular materials with quantum dots: (a) Application of a CdTe/PVA thin film coating onto aluminum particles. (b) Surface chemistry approach to attaching CdTe to aluminum powders. (c) Encapsulation of CdTe into a SiO2 shell.

6.5.3 Shock compression of quantum dots incorporated in granular materials

Figure 113 illustrates the possible methods that can be used to incorporate the quantum dot directly onto the granular material of interest, including (a) coating the particles with a QD-PVA film, (b) using surface chemistry to chemically attach the quantum dots to the surface of the material, and (c) encapsulating the quantum dots in SiO_2. A QD-PVA particle coating may be prepared by following the technique reported by Rahimi *et. al.* [169], who combined PVA with the quantum dots to be coated and ultra-sonicated the mixture for 15 minutes, followed by a drying at 100°C for four hours. The surface chemistry approach can be taken by building on the work of Fogliazza *et. al.* [170] and functionalizing the quantum dots with an alkyl halide or bromide and chemically grafting the quantum dots on to the aluminum particle.

Alternatively, the quantum dots can be encapsulated in an SiO_2 shell. Methods for encapsulating quantum dots within a silica gel include the Stober process [171] and the reverse micro emulsion method [172]. The Stober process also allows for wavelength and intensity encoding so that silica encapsulated QD's of a specific intensity and wavelength can be prepared. Christensen *et. al.* [173] studied the shock compression response of rhodamine 6G encapsulated in silica microspheres and observed higher initial intensities, a

faster intensity response to shock compression and a faster spectral shift with the encapsulated dye as opposed to a free dye.

Monitoring of these systems would be similar to the previous case, using either the intensity drop or the spectral shift as indicators of pressure change. The added benefit of this configuration is that quantum dots of varying emission wavelengths can be coated preferentially onto particles of a particular size to more easily monitor the behavior of a certain type of particle. For instance, fine aluminum particles can be labelled with one wavelength, while coarse aluminum particles can be labelled with a different quantum dot wavelength. Hence, quantum dots of different wavelength can be dispersed in the void space or the matrix. Analysis of this type of system can be performed with a spectrograph/streak camera. A 50 μm diameter spot can be focused to include an area containing all three wavelengths of quantum dots, and the time duration of the response of the different materials can be monitored at once by following the three separate emission wavelengths in the spectrograph.

6.6 Summary of QD-Based Meso-scale Sensors

Quantum dot (QD)-PVA nanocomposite films were prepared and shock compressed at pressures ranging from 1.7 to 7.1 GPa via the laser-accelerated flyer setup at UIUC to assess the performance of quantum dots as a meso-scale shock sensor. The following contributions and observations were made:

- QD-PVA nano composite films were composed of positively- and negatively-charged quantum dots. The nanocomposite films containing negatively charged quantum dots exhibited increased aggregation as evidenced by their absorbance spectra. However nanocomposite films containing positively charged quantum dots do not show such agglomeration.

- Shock compression of the positively charged QD-PVA nanocomposite films showed increasing intensity loss and an increase in the maximum peak width reduction with

increasing pressures. Additionally, a blue shift linearly increases with pressure up to 4.1 GPa, and then decreases. Lastly, at pressures ranging from 4 to 6 GPa, a secondary emission peak is observed.

- Shock compression of the negatively charged QD-PVA nanocomposite results in an increasing intensity loss with increasing pressure. Instead of a blue shift, the negatively charged QD's display a red shift that linearly increases with pressure up to 3.5 GPA and then drops to an average of 6 nm at higher pressures.

- Based on the trends in intensity change, maximum peak width, and blue shift observed in the QD-PVA nanocomposite film, the shock compression granular materials may be monitored using quantum dots as mesoscale diagnostic sensors.

Chapter VII

CONCLUDING REMARKS AND FUTURE WORK

7.1 Summary and Conclusions

The goal of the work conducted in this study was to investigate the properties and processes that effect the initiation of the combustion of aluminum powders of various types under uniaxial stress rod-on-anvil impact conditions. Spherical aluminum powder of a range of sizes, between 3.5 μm to 67 μm in diameter, and powders that had been mechanically pre-activated by high energy ball milling (HEBM) or high strain machining were studied. The impact-initiated combustion of aluminum was analyzed using a combination of in depth characterization of the starting powders, high speed imaging, *in situ* temperature measurements, and microstructure-based computational simulations. The analysis of the starting aluminum powders included characterization based on their microstructure, particle size distribution, yield strength, and compaction behavior. Investigation of the relationship between the initial material properties and the reaction behavior using logistic regression analysis, combined with the correlation of light emission timing and temperature measurements to numerical simulations, provided an understanding of the dominant processes influencing impact-initiated reaction.

7.1.1 Various Al powder characteristics

The compacted powders were subjected to uniaxial stress loading in the rod-on-anvil impact configuration using a 7.62 mm gas gun. A reaction threshold velocity for each powder compact was determined based on the lowest velocity at which light emission as evidence of reaction initiation was observed. The kinetic energy (KE) corresponding to the reaction threshold velocity for each powder type was calculated and compared to the aluminum

powder properties as shown in Figure 114. Figure 114 (a) shows that for H-series aluminum, as S_v decreases, the KE threshold for reaction generally decreases, but for HEBM powder compacts, as S_v increases, the KE threshold for reaction does not increase but varies. Figure 114 (b) shows a similar trend for the relationship between yield strength and the KE threshold for RXN. As yield strength decreases in the H-series aluminum, the KE threshold generally decreases, and as the yield strength of the HEBM powders increases, the KE threshold for reaction varies. Figure 114 (c) displays the fluctuations in the effective yield stress of the powder compacts against the changes in the KE threshold for reaction. Last, Figure 114 (d) shows the similarity between the variations in the compaction energy and the KE threshold for reaction as the particle type changes. As the H-series particle diameter initially increases, both the KE threshold for reaction and the compaction energy increase. As the H-series particle diameter continues to increase, both the KE threshold for reaction and the compaction energy decrease. Upon HEBM of H-60 for 10 minutes, both the KE threshold for reaction and the compaction energy increase. Upon HEBM of H-60 for 30 minutes, both the KE threshold for reaction and the compaction energy decrease. Following 60 minutes of ball milling, both the KE threshold for reaction and the compaction energy increase.

7.1.2 Process and property effects on reactivity.

Logistic regression analysis revealed that the surface area per unit volume, S_v, shown in Figure 114 (a), and the compaction energy, shown in Figure 114 (d), were most closely related to the occurrence of reaction. Results of the impact-initiated reactivity experiments show that as the S_v decreases, the threshold velocity for reaction initiation decreases. Thus, a higher kinetic energy is required to initiate reaction in the smallest, H-2, particles. The differences in the reaction threshold are likely due to the discrepancy between the energy being deposited at the surfaces of the particles. Input of the same amount of kinetic energy into each system results in higher energy deposition at the few surfaces available in the

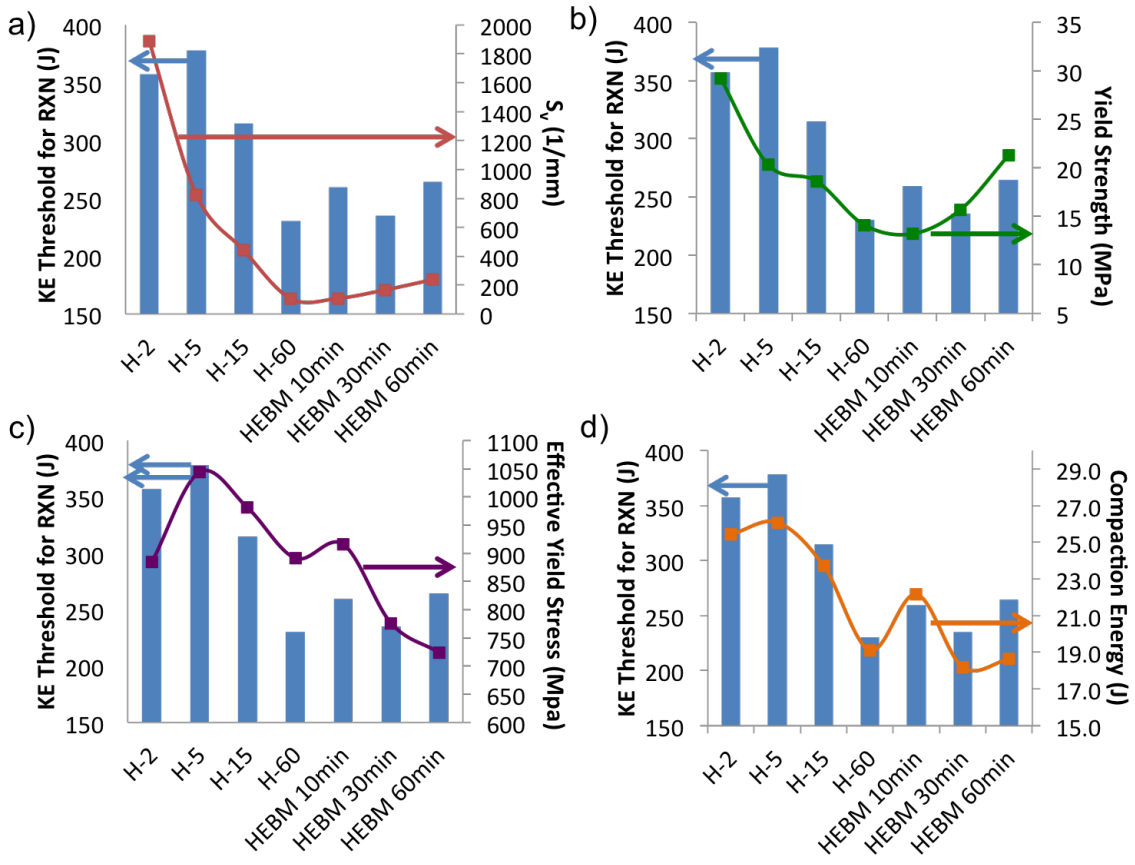

Figure 114: Summary of the effects of the powder properties on the kinetic energy threshold for reaction of each powder type. The surface are per unit volume (a), the yield strength of the particles (b), the effective yield strength of the compact (c), and the compaction energy (d) overlaid on a bar graph of the kinetic energy threshold for reaction.

compacts composed of larger particles, and, conversely, lower energy deposition at the many surfaces of the smaller particles.

The compaction energy and reactivity relationship follows a similar trend as the S_v-reactivity relationship. As the energy necessary for compaction decreases, the reaction threshold velocity decreases. A lower energy requirement for compaction leaves more energy available for reaction.

The impact-initiated reactivity experiments also reveal that aluminum powders processed by HEBM for 30 minutes or less are more sensitive to impact than those that are not mechanically pre-activated. Even high S_v aluminum particles that have been ball milled exhibit enhanced reactivity. This trend implies that processing by HEBM "activates" the aluminum powders by cracking the aluminum oxide layer and exposing fresh reactive surfaces. Aluminum powder processed by HEBM for 60 minutes show decreased reactivity, because of work hardening to such a degree that additional energy is required for compaction and deformation process.

In situ temperature measurements indicate that aluminum powder compacts do not reach melting temperatures during impact under the conditions investigated. During deformation, a bulk temperature rise to only 220°C was typically measured. Theoretical calculations and microstructure-based simulations predicted even lower temperatures than were observed experimentally. This conclusion points to a mechanochemical combustion mechanism that is driven by localized plastic deformation as opposed to a thermally initiated reaction.

7.1.3 QD's as meso-scale sensors: shock response and possibilities

Results of impact-initiated reactions, temperature measurements, and microstructure based simulations reveal that reaction initiation may result from both localized processes at the particle interface and by energy availability. The degree to which each of these processes play a role in the reaction initiation process needs to be studied more thoroughly using

mesoscale diagnostic sensors. Quantum dot-based mesoscale sensors were developed to probe very small spatial areas, several microns in diameter, at nanosecond time resolutions. These quantum dot based sensors can be well-suited to interrogate the local pressure and temperature states of aluminum powder compacts during impact-initiated reaction.

A quantum dot (QD)-PVA nanocomposite film was prepared to study shock compression response. The CdTe quantum dots embedded in PVA films were tested using the laser-driven flyer plate setup at the University of Illinois Urbana-Champaign. A decrease in emission intensity and blueshift with increasing applied pressures was observed. These results illustrate promise for utilization of QD's as sensors to monitor the pressure of granular materials and capture the effects of heterogeneities.

7.2 Significant Contributions

The following significant contributions have been made in this work:

- The threshold velocity for reaction of aluminum powder compacts of varying particle diameters and of varying levels of mechanical pre-activation was determined. Logistic regression analysis of the relationship between the occurrence of reaction and the aluminum powder compact properties indicated that the powder surface area per unit volume ratio and the powder compaction energy were most closely related to the reaction threshold of the aluminum powder compact.

- *In situ* temperature rise of the aluminum powder compact at the impact face was observed via the IR camera and sapphire anvil set-up. Images of the temperature rise during the compaction stage indicate that localized processes influence heating and reaction initiation. Images of temperature rise during the deformation and sabot-anvil impact stages display the effect of enhanced plastic strain on heating and reaction initiation.

- Processing of aluminum by HEBM was observed to enhance the reactivity of the

aluminum particles by exposing fresh, reactive surfaces. The light emission timing of HEBM samples shows that these nascent surfaces react immediately upon impact in the H-60 and H-2 HEBM particles. Additionally, 2D microstructure-based simulations (that cannot capture chemical reactions) indicate that both the H-60 and H-60 30 minute HEBM microstructure behave similarly with respect to temperature rise and enhanced strain.

- Quantum dot (QD)-PVA nanocomposite films were prepared to monitor the shock compression response of granular materials. Upon shock compression via a laser-accelerated flyer set-up at pressures ranging from 1.7 to 7.1 GPa, the quantum dots exhibit variations in blue shift and emission intensity that may be calibrated to the pressure increase allowing them to be utilized as a meso-scale sensor.

7.3 Future Work

The work performed in this study focuses on understanding the effects of properties of aluminum powders on the processes leading to the initiation of combustion reaction under impact conditions. Although several trends and possible processes have been identified, the research leaves open the question of the influence of localized strain on impact-initiated combustion.

The influence of mechanochemical processes can be explored further by creating powder mixtures composed of aluminum and a hard constituent, such as tungsten or even highly strained aluminum platelets. The addition of a hard constituent to the aluminum powder compact would clearly illustrate the effect of enhanced plastic strain localization at the particle level and its effects on reaction initiation during compaction and deformation. Comparison of reaction behavior between these systems would help to identify the role of mechanochemical processes on reaction initiation.

An important long-term goal of impact-initiated combustion of aluminum is to better understand impact-initiated reactions in intermetallic-forming energetic materials. This

study showed that larger aluminum particles and particles mechanically pre-activated by HEBM are more sensitive to reaction. The different aluminum powder types can be mixed with another constituent, such as Ta, Ni, or W, to understand if changing the aluminum powder effects the intermetallic forming reaction in the same way the the aluminum powder properties effect the combustion reaction. For instance, are Ni+Al powder mixtures made with of HEBM aluminum more likely to react than powder mixtures made with spherical aluminum that has not been mechanically pre-activated? Hence, energetic materials can be specifically designed for performance specific application based on the desired threshold for reaction initiation.

Further, this work has shown that aluminum-containing structural energetic materials (SEM) may be designed to a desired kinetic energy threshold for reaction. Applications requiring a more sensitive SEM, needed to react at lower impact velocities, may incorporate an aluminum that has been processed by HEBM into the design. Whereas, applications requiring a more inert SEM that can withstand higher impact velocities without being detonated, may utilize smaller, 2 μm, spherical particles in the design. Additional studies would be useful to determine to what extent the aluminum particle properties can control the reaction initiation behavior and how predictable the reaction initiation may be in specific scenarios.

The use of quantum dots as sensors dispersed in aluminum powder compacts, should be investigated further. It is well documented that granular systems exhibit a highly heterogeneous response to shock compression. Direct measurement of the difference between temperature and pressure rise in a compact composed of small, H-2, aluminum particle and a compact composed of large, H-60, aluminum particles would clarify the energy deposition mechanism for reaction initiation.

REFERENCES

[1] BROOKS, K. P. and BECKSTEAD, M. W., "Dynamics of aluminum combustion," *Journal of Propulsion and Power*, vol. 11, no. 4, pp. 769–780, 1995.

[2] NATIONS, U., "Afghanistan annual report 2014: Protection of civilians in armed conflict," tech. rep., United Nations Assistance Mission in Afghanistan, February 2015.

[3] BOER, R., SCHUURMAN, B., and STRUYK, M., "Protecting civilians from explosive violence: Defining the humanitarian problem," tech. rep., IKV Pax Christi, 2011.

[4] AYDELOTTE, B., *Fragmentation and Reaction of Structural Energetic Materials*. PhD thesis, Georgia Institute of Technology, 2013.

[5] ZHANG, X. F., SHI, A. S., QIAO, L., ZHANG, J., ZHANG, Y. G., and GUAN, Z. W., "Experimental study on impact-initiated characters of multifunctional energetic structural materials," *Journal of Applied Physics*, vol. 113, no. 083508, 2013.

[6] THADHANI, N. N., GRAHAM, R. A., ROYAL, T., DUNBAR, E., ANDERSON, M. U., and HOLMAN, G. T., "Shock-induced chemical reactions in titanium-silicon powder mixtures of different morphologies: Time-resolved pressure measurements and materials analysis," *Journal of Applied Physics*, vol. 82, no. 3, pp. 1113–1127, 1997.

[7] AYDELOTTE, B. B. and THADHANI, N. N., "Mechanistic aspects of impact initiated reactions in explosively consolidates metal + aluminum powder mixtures," *Materials Science and Engineering A*, vol. 570, pp. 164–171, 2013.

[8] EAKINS, D. and THADHANI, N. N., "Shock-induced reaction in flake nickel + spherical aluminum powder mixture," *Journal of Applied Physics*, vol. 100, no. 113521, 2006.

[9] CHENG, J., HNG, H., LEE, Y., DU, S., and THADHANI, N., "Kinetic study of thermal- and impact-initiated reactions in al-fe2o3 nanothermite," *Combustion and Flame*, vol. 157, pp. 2241–2249, 2010.

[10] TUCKER, M. D., "Characterization of impact initiation of aluminum-based intermetallic-forming reactive materials," Master's thesis, Georgia Institute of Technology, December 2011.

[11] HERBOLD, E. B., THADHANI, N. N., and JORDAN, J. L., "Observation of minimum reaction initiation threshold in ball-milled ni+al under high-rate mechanical loading," *Journal of Applied Physics*, vol. 109, no. 066108, 2011.

[12] PANGILINAN, G. I. and RUSSELL, T. P., "Role of al-o2 chemistry in the laser-induced vaporization of al films in air," *Journal of Chemical Physics*, vol. 111, no. 2, pp. 445–448, 1999.

[13] GLASSMAN, I., *Metal Combustion Processes*, pp. 938–959. New York: Defense Technical Information Center, 1959.

[14] BRZUSTOWSKI, T. A. and GLASSMAN, I., *Vapor Phase Diffusion Flames in the Combustion of Magnesium and Aluminum*, vol. 15 of *Progress in Astronautics and Aeronautics*, pp. 75–158. New York: Academic Press, 1964.

[15] FRIEDMAN, R. and MACEK, A., "Ignition and combustion of aluminium particles in hot ambient gases," *Combustion and Flame*, vol. 6, pp. 9–19, 1962.

[16] LAW, C. K. and WILLIAMS, F. A., "On a class of models for droplet combustion," in *American Institute of Aeronautics and Astronautics*, 1974.

[17] KHAIKIN, B. I., BLOSHENKO, V. N., and MERZHANOV, A. G., "On the igntion of metal particles," *Combustion, Explosion, and Shock Waves*, vol. 4, pp. 412–422, 1970.

[18] GREMYACHKIN, V. M., "Theory of ignition of metallic particles," *Combustion, Explosion, and Flame*, vol. 19, no. 3, pp. 9–14, 1983.

[19] DESJARDIN, P. E., FELSKE, J. D., and CARRARA, M. D., "Mechanistic model for aluminum particle ignition and combustion in air," *Journal of Propulsion and Power*, vol. 21, no. 3, pp. 478–485, 2005.

[20] BREITER, A. L., MAL'TSEV, V. M., and POPOV, E. I., "Models of metal ignition," *Fizika Goreniya i Vzryva*, vol. 13, no. 4, pp. 558–570, 1977.

[21] MERZHANOV, A. G., GRIGORJEV, Y. M., and GAL'CHENKO, Y. A., "Aluminium ignition," *Combustion and Flame*, vol. 29, pp. 1–14, 1977.

[22] ERMAKOV, V. A., RAZDOBREEV, A. A., SKORIK, A. I., POZDEEV, V. V., and SMOLYAKOV, S. S., "Termpature of aluminum particles at the time of ignition and combustion," *Combustion, Explosion, and Shock Waves*, vol. 18, no. 2, pp. 141–143, 1982.

[23] LOKENBAKH, A. K., ZAPORINA, N. A., KNIPELE, A. Z., STROD, V. V., and LEPIN, L. K., "Effects of heating conditions on the agglomeration of aluminum powder in air," *Fizika Goreniya i Vzryva*, vol. 21, no. 1, pp. 73–82, 1985.

[24] ROZENBRAND, V. I. and VAGANOVA, N. I., "A strength model of heterogeneous ignition of metal particles," *Combustion and Flame*, vol. 88, pp. 113–118, 1992.

[25] HUANG, Y., RISHA, G. A., YANG, V., and YETTER, R. A., "Effect of particle size on combustion of aluminum particle dust in air," *Combustion and Flame*, vol. 156, pp. 5–13, 2009.

[26] TRUNOV, M. A., SCHOENITZ, M., ZHU, X., and DREIZIN, E. L., "Effect of polymorphic phase transformations in al2o3 film on oxidation kinetics of aluminum powders," *Combustion and Flame*, vol. 140, pp. 310–318, 2005.

[27] LEVITAS, V. L., ASAY, B. W., SON, S. F., and PANTOYA, M., "Melt dispersion mechanism for fast reaction of nanothermites," *Applied Physics Letters*, vol. 89, p. 071909, 2006.

[28] RAI, A., LEE, D., PARK, K., and ZACHARIAH, M. R., "The importance of phase change of aluminum in oxidation of aluminum nanoparticles," *Journal of Physical Chemistry B*, vol. 108, pp. 14793–14795, 2004.

[29] BOIKO, V. M., LOTOV, V. V., and PAPYRIN, A. N., "Ignition of gas suspensions of metallic powders in reflected shock waves," *Combustion, Explosion, and Shock Waves*, vol. 25, no. 2, pp. 67–74, 1989.

[30] ZHANG, F., MURRAY, S. B., and GERRARD, K. B., "Aluminum particles-air detonation at elevated pressures," *Shock Waves*, vol. 15, pp. 313–324, 2006.

[31] YOSHINAKA, A., ZHANG, F., and WILSON, W., "Effect of shock compression on aluminum particles in condensed media," in *Shock Compression of Condensed Matter* (ELERT, M., FURNISH, M. D., CHAU, R., HOLMES, N., and NGUYEN, J., eds.), pp. 1057–1060, American Institute of Physics, 2007.

[32] SCHLOFFEL, G., EICHHORN, A., ALBERS, H., MUNDT, C., SEILER, F., and ZHANG, F., "The effect of a shock wave on the ignition behavior of aluminum particles in a shock tube," *Combustion and Flame*, vol. 157, pp. 446–454, 2010.

[33] GILL, R. J., BADIOLA, C., and DREIZEN, E. L., "Combustion times and emission profiles of micron-sized aluminum particles burning in different environments," *Combustion and Flame*, vol. 157, pp. 2015–2023, 2010.

[34] BADIOLA, C., GILL, R. J., and DREIZIN, E. L., "Combustion characteristics of micron sized aluminum particles in oxygenated environments," *Combustion and Flame*, 2011.

[35] BAZYN, T., KRIER, H., and GLUMAC, N., "Evidence for the transition from the diffustion-limit in aluminum particle combustion," *Proceedings of the Combustion Institute*, vol. 31, pp. 2021–2028, 2007.

[36] MEYERS, M. A., *Dynamic Behavior of Materials*. New York: John Wiley and Sons, Inc, 1994.

[37] MEYERS, M. A., BENSON, D., and OLEVSKY, E. A., "Shock consolidation: Microstructurally-based analysis and computational modeling," *Acta Materialia*, vol. 47, no. 7, pp. 2089–2108, 1999.

[38] HELLE, A. S., EASTERLING, K. E., and ASHBY, M. F., "Hot-isostatic pressing diagrams: New developments," *Acta Metallurgica*, vol. 33, no. 12, pp. 2163–2174, 1985.

[39] BENSON, D. J., NESTERENKO, V. F., JONSDOTTIR, F., and MEYERS, M. A., "Quasistatic and dynamic regimes of granular material deformation under impulse loading," *J. Mech. Phys. Solids*, vol. 45, no. 11/12, pp. 1955–1999, 1997.

[40] KATOR, L. and NYULAS, P., "Method for determining the changes in energy stored by a metal during plastic deformation," *Strength of Materials*, no. 1, pp. 31–34, 1971.

[41] TAYLOR, G. I. and QUINNEY, H., "The latent energy remaining in a metal after cold working," *Proceedings of the Royal Society of London*, vol. 143, no. 849, pp. 307–326, 1934.

[42] MASON, J. J., ROSAKIS, A. J., and RAVICHANDRAN, G., "On the strain and strain rate dependence of the fraction of plastic work converted to heat: an experimental study using high speed infrared detectors and kolsky bar," *Mechanics of Materials*, vol. 17, pp. 135–145, 1994.

[43] EAKINS, D. E. and THADHANI, N. N., "Shock compression of reactive powder mixtures," *International Materials Reviews*, vol. 54, no. 4, pp. 181–213, 2009.

[44] RICE, M. H., MCQUEEN, R. G., and WALSH, J. M., "Compression of solids by strong shock waves," *Solid State Physics*, vol. 6, pp. 1–63, 1958.

[45] DAI, C. D., EAKINS, D. E., and THADHANI, N. N., "Dynamic densification behavior of nanoiron powders under shock compression," *Journal of Applied Physics*, vol. 103, no. 093503, 2008.

[46] HERMANN, W., "Constitutive equation for the dynamic compaction of ductile porous materials," *Journal of Applied Physics*, vol. 40, no. 6, pp. 2490–2499, 1968.

[47] CARROLL, M. M. and HOLT, A. C., "Static and dynamic pore-collapse relations for ductile porous materials," *Journal of Applied Physics*, vol. 43, no. 4, pp. 1626–1636, 1972.

[48] BUTCHER, B. M., CARROLL, M. M., and HOLT, A. C., "Shock-wave compaction of porous aluminum," *Journal of Applied Physics*, vol. 45, no. 9, pp. 3864–3875, 1974.

[49] BONNAN, S. and HERRELL, P.-L., "Experimental characterization of quasi static and shock wave behavrio of porous aluminum," *Journal of Applied Physics*, vol. 83, no. 11, pp. 5741–5749, 1998.

[50] THADHANI, N. N., "Shock-induced and shock-assisted solid-state chemical reactions in powder mixtures," *Journal of Applied Physics*, vol. 76, pp. 2129–2138, 1994.

[51] KOVALENKO, A. N., IVANOV, G. V., MEL'NIKOV, M. A., and USOV, V. F., "Physicochemical transformations in mixtures of lithium perchlorate with finely divided metals in shock compression," *Combustion, Explosion, and Shock Waves*, vol. 19, no. 4, pp. 116–119, 1983.

[52] BATSANOV, S. S., DORONIN, G. S., and KLOCHKOV, S. V., "Synthesis reactions behind shock fronts," *Combustion, Explosion, and Flame*, vol. 22, pp. 765–768, 1986.

[53] GRAHAM, R. A., ANDERSON, M. U., HORIE, Y., YOU, S.-K., and HOLMAN, G. T., "Pressure measurements in chemically reacting powder mixtures with the bauer piezoelectric polymer gauge," *Shock Waves*, vol. 3, pp. 79–82, 1993.

[54] THADHANI, N. N. and AIZAWA, T., *Shock-Induced Chemical Reactions in Porous Solids*. New York: Springer, 1997.

[55] BOSLOUGH, M. B., "A thermochemical model for shock-induced reactions (heat detonations) in solids," *Journal of Chemical Physics*, vol. 92, no. 3, pp. 1839–1848, 1990.

[56] THADHANI, N. N., WORK, S., GRAHAM, R. A., and HAMMETTER, W. F., "Shock-induced reaction synthesis (srs) of nickel aluminides," *Journal of Materials Research*, vol. 7, no. 5, 1992.

[57] THADHANI, N. N., "Shock-induced chemical reactions and synthesis of materials," *Progress in Materials Science*, vol. 37, pp. 117–226, 1993.

[58] JETTE, F.-X., HIGGINS, A. J., GOROSHIN, S., FROST, D. L., CHARRON-TOUSIGNANT, Y., RADULESCU, M. I., and LEE, J. J., "In-situ measurements of the onset of bulk exothermicity in shock initiation of reactive powder mixtures," *Journal of Applied Physics*, vol. 109, p. 084905, 2011.

[59] TAYLOR, G., "The use of flat-ended projectiles for determining dynamic yield stress. i. theoretical considerations," *Proceedings of the Royal Society of London*, vol. 194, no. 1038, pp. 289–299, 1948.

[60] AMES, R. G., "Energy release characteristics of impact-initiated energetic materials," in *MRS Proceedings* (GASH, A., N.N.THADHANI, WILSON, W., ARMSTRONG, R., and MUNIR, Z., eds.), vol. 896, Materials Research Society, 2006.

[61] DENSMORE, J. M., BISS, M. M., HOMANN, B. E., and MCNESBY, K. L., "Thermal imaging of nickel-aluminum and aluminum-polytetrafluoroethylene impact initiated combustion," *Journal of Applied Physics*, vol. 112, no. 084911, 2012.

[62] DU, S. W. and THADHANI, N. N., "Impact initiation of pressed al based intermetallic-forming powder mixture compacts," in *Shock Compression of Condensed Matter* (ELERT, M. L., BUTLER, W. T., FURNISH, M. D., ANDERSON, W. W., and PROUD, W. G., eds.), vol. 1195, AIP Publishing, 2009.

[63] HUNT, E. M., MALCOM, S., PANTOYA, M. L., and DAVIS, F., "Impact ignition of nano and micron composite energetic materials," *International Journal of Impact Engineering*, vol. 36, pp. 842–846, 2009.

[64] HUNT, E. M. and PANTOYA, M. L., "Impact sensitivity of intermetallic nanocomposites: A study on compositional and bulk density," *Intermetallics*, vol. 18, p. 1612, 2010.

[65] ASAY, B. W., HENSON, B. F., DICKSON, P. M., FUGARD, C. S., and FUNK, D. J., "Direct measurement of strain field evolution during dynamic deformation of an energetic material," Shock Compression of Condensed Matter, AIP Conference Proceedings, 1997.

[66] MASON, B. A., GROVEN, L. J., and SON, S. F., "The role of microstructure refinement on the impact ignition and combustion behavior of mechanically activated ni/al reactive composites," *Journal of Applied Physics*, vol. 114, no. 113501, 2013.

[67] MANUKYAN, K. V., MASON, B. A., GROVEN, L. J., LIN, Y., CHERUKARA, M., SON, S. F., STRACHAN, A., and MUKASYAN, A. S., "Tailored reactivity of ni+al nanocomposites: Microstructural correlations," *Journal of Physical Chemistry C*, vol. 116, pp. 21027–21038, 2012.

[68] REEVES, R. V., MUKASYAN, A. S., and SON, S. F., "Thermal and impact raction initiation in ni/al heterogeneous reactive systems," *Journal of Physical Chemistry C*, vol. 114, pp. 14772–14780, 2010.

[69] GOURDIN, W. H., "Microstructure and deformation in a dynamically compacted copper powder," *Materials Science and Engineering*, vol. 67, pp. 179–184, 1984.

[70] CHIU, P., WANG, S., VITALI, E., HERBOLD, E. B., BENSON, D. J., and NESTERENKO, V. F., "Particle size effect in granular composite aluminum/tungsten," Shock Compression of Condensed Matter, AIP Publishing, 2009.

[71] OLNEY, K. L., CHIU, P. H., LEE, C. W., NESTERENKO, V. F., and BENSON, D. J., "Role of material properties and mesostructure on dynamic deformation and shear instability in al-w composites," *Journal of Applied Physics*, vol. 110, no. 114908, 2011.

[72] WEI, C. T., VITALI, E., JIANG, F., DU, S. W., BENSON, D. J., VECCHIO, K. S., THADHANI, N. N., and MEYERS, M. A., "Quasi-static and dynamic response of explosively consolidated metal-aluminum powder mixtures," *Acta Materialia*, vol. 60, pp. 1418–1432, 2012.

[73] BEVER, M. B., HOLT, D. L., and TITCHENER, A. L., "The stored energy of cold work," *Progress in Materials Science*, pp. 5–177, 1972.

[74] REEVES, R. V., MUKASYAN, A. S., and SON, S., "Microstructural effects on ignition sensitivity in ni/al systems subjected to high strain rate impacts," Shock Compression of Condensed Matter, AIP Conference Proceedings, 2012.

[75] SHANKAR, M. R., CHANDRASEKAR, S., COMPTON, W. D., and KING, A. H., "Characteristics of aluminum 6061-t6 deformed to large plastic strains by machining," *Materials Science and Engineering A*, vol. 410-411, pp. 364–368, 2005.

[76] SHANKAR, M. R., CHANDRASEKAR, S., KING, A. H., and COMPTON, W., "Microstructure and stability of nanocrystalline aluminum 6061 created by large strain machining," *Acta Materialia*, vol. 53, pp. 4781–4793, 2005.

[77] HAMMETTER, W. F., GRAHAM, R. A., MOROSIN, B., and HORIE, Y., *Shock Waves in Condensed Matter*. Elsevier, 1988.

[78] DUNBAR, E., THADHANI, N. N., and GRAHAM, R. A., "High-pressure shock activation and mixing of nickel-aluminum powder mixtures," *Journal of Materials Science*, vol. 28, 1993.

[79] FISCHMEISTER, H. and ARTZ, E., "Densification of powders by particle deformation," *Powder Metallurgy*, vol. 26, pp. 82–88, 1983.

[80] FISCHMEISTER, H. F., ARTZ, E., and OLSSON, L., "Particle deformation and sliding during compaction of spherical powders: a study by quantitative metallography," *Powder Metallurgy*, no. 4, p. 179, 1978.

[81] MEYERS, M., SHANG, S., and HOKAMOTO, K., *Shock Waves in Material Science*. Springer-Verlag, 1993.

[82] BUTCHER, B. M. and KARNES, C. H., "Sc-rr-67-3040," tech. rep., Sandia Labs, 1968.

[83] GOURDIN, W. H., "Energy deposition and microstructural modification in dynamically consolidated metal powders," *Journal of Applied Physics*, vol. 55, p. 172, 1984.

[84] WILLIAMSON, R. L., "Parametric studies of dynamic powder consolidation using a particle level numerical model.," *Journal of Applied Physics*, vol. 68, p. 1287, 1990.

[85] WRIGHT, R. N., KORTH, G. E., and FLINN, J. E., "Particle bonding annealing response and mechanical properties of dynamically consolidated type 304 stainless steel powders," *Metallurgical Transactions A*, vol. 20, no. 11, pp. 2449–2457, 1989.

[86] BENSON, D. J., "An analysis by direct numerical simulation of the effects of particle morphology on the shock compaction of copper powder," *Modelling Simul. Mater. Sci. Eng. 2*, pp. 535–550, 1994.

[87] BENSON, D. J. and NELLIS, W. J., "Dynamic compaction of copper powder: Computation and experiment," *Applied Physics Letters*, vol. 65, no. 418, 1994.

[88] NIEH, T. G., LUO, P., NELLIS, W., LESUER, D., and BENSON, D., "Dynamic compaction of aluminum nanocrystals," *Acta Materialia*, vol. 44, no. 9, pp. 3781–3788, 1996.

[89] AUSTIN, R. A., MCDOWELL, D. L., and BENSON, D. J., "Numerical simulation of shock wave propagation in spatially-resolved particle systems," *Modelling Simul. Mater. Sci. Eng.*, vol. 14, pp. 537–561, 2006.

[90] BAER, M. R., "Computational modeling of heterogeneous reactive materials at the mesoscale," *AIP Conference Proceedings*, vol. 505, no. 27, 2000.

[91] BAER, M. R., "Modeling heterogeneous energetic materials at the mesoscale," *Thermochimica Acta*, vol. 384, pp. 351–367, 2002.

[92] EAKINS, D. and THADHANI, N. N., "Discrete particle simulation of shock wave propogation in a binary ni+al powder mixture," *Journal of Applied Physics*, vol. 101, no. 043508, 2007.

[93] BARKER, L. M. and HOLLENBACK, R. E., "Interferometer technique for measuring the dynamic mechanical properties of materials," *Review of Scientific Instruments*, vol. 36, no. 1617, 1965.

[94] BARKER, L. and HOLLEBACH, R. E., "Laser interferometer for measuring high velocities of any reflecting surface," *Journal of Applied Physics*, vol. 43, no. 4669, 1972.

[95] FORBES, J. W., *Shock Wave Compression of Condensed Matter*. Springer-Verlag, 2012.

[96] BAER, M. R., HALL, C. A., GUSTAVSEN, R. L., HOOKS, D. E., and SHEFFIELD, S. A., "Isentropic compression experiments for mesoscale studies of energetic composites," *AIP Conference Proceedings*, vol. 845, no. 1307, 2006.

[97] BORG, J. P., MAINES, W. R., and CHHABILDAS, L. C., "Equation of state and isentropic release of aluminum foam and polyvinyldine fluoride systems," *Jounral of Applied Physics*, vol. 115, no. 213515, 2014.

[98] TROTT, W. M., KNUDSON, M. D., CHHABILDAS, L. C., and ASAY, J. R., "Measurements of spatially resolved velocity variations in shock compressed heterogeneous materials using line-imaging velocity interferometer," Shock Compression of Condensed Matter, American Institute of Physics, 1999.

[99] TROTT, W. M., CASTANEDA, M. R. B. J. N., CHHABILDAS, L. C., and ASAY, J. R., "Investigation of the mesoscopic scale response of low-density pressings of granular sugar," *Journal of Applied Physics*, vol. 101, no. 024917, 2007.

[100] VOGLER, T. J., ALEXANDER, C. S., WISE, J. L., and MONTGOMERY, S. T., "Dynamic behavior of tungsten carbide and alumina filled epoxy composites," *Journal of Applied Physics*, vol. 107, 2010.

[101] FURNISH, M. D., TROTT, W. M., MASON, J., PODSEDNIK, J., REINHART, W. D., and HALL, C., "Assessing mesoscale material response via high resolution line-imaging visar," *AIP Conference Proceedings*, p. 1159, 2003.

[102] VOGLER, T. J., TROTT, W., REINHART, W. D., ALEXANDER, C. S., FURNISH, M. D., KNUDSON, M. D., and CHHABILDAS, L. C., "Using the line-visar to study multi dimensional and mesoscale impact phenomena," *International Journal of Impact Engineering*, vol. 35, p. 1844, 2008.

[103] YU, H., FEDOTOV, V., BACK, W., and YOH, J. J., "Towards controlled flyer acceleration by a laser driven mini flyer," *Applied Physics A.*, 2013.

[104] LEE, K.-C., TAIRA, T., KOO, G. M., LEE, J. Y., and YOH, J. J., "Ignition characteristics of laser-ablated aluminum at shock pressures up to 2gpa," *Journal of Applied Physics*, vol. 115, no. 013503, 2014.

[105] YU, H., KIM, J., and YOH, J. J., "A high velocity impact experiment of microscale ice particles using laser-driven system," *Journal of Applied Physics*, vol. 116, no. 173508, 2014.

[106] DENSMORE, J. M., HOMAN, B. E., BISS, M. M., and MCNESBY, K. L., "High-speed two-camera imaging pyrometer for mapping fireball temperatures," *Applied Optics*, vol. 50, no. 33, 2011.

[107] BOURNE, N. K., MILLETT, J. C. F., and III, G. T. G., "On the shock compression of polycrystalline metals," *Journal of Materials Science*, vol. 44, pp. 3319–3343, 2009.

[108] GRAHAM, R. A., NEILSON, F. W., and BENEDICK, W. B., "Piezoelectric current from shock loaded quartz-a submicrosecond stress gauge," *Journal of Applied Physics*, vol. 36, no. 1775, 1965.

[109] JORDAN, J. L., DATTELBAUM, D. M., SUTHERLAND, G., RICHARDS, D. W., SHEFFIELD, S. A., and DICK, R. D., "Shock eos of multi-phase epxoy-based composite(al-mno2-epoxy)," *Journal of Applied Physics*, vol. 107, no. 103528, 2010.

[110] SHEN, X. A. and GUPTA, Y. M., "Shock-induced fluorescence shift of rhodamine-6g in ethanol solution," *Journal of Applied Physics*, vol. 70, pp. 7549–7533, 1991.

[111] LEE, I. S., HILL, J. R., SUZUKI, H., DLOTT, D. D., BAER, B. J., and CHRONISTER, E. L., "Molecular dynamics observed 60ps behind a solid-state shock front," *Journal of Chemical Physics*, vol. 103, no. 19, p. 8313, 1995.

[112] BROWN, K., CONNOR, R., FU, Y., FUJIWARA, H., and DLOTT, D. D., "Microscopic states of shocked polymers," in *AIP Converence Proceedings*, vol. 1426, pp. 1593–1596, 2012.

[113] BROWN, K., FU, Y., SHAW, W. L., and DLOTT, D. D., "Time-resolved emission of dye probes in a shock compressed polymer," *Journal of Applied Physics*, vol. 112, no. 103508, 2012.

[114] BANISHEV, A. A., SHAW, W. L., and DLOTT, D. D., "Dynamics of polymer response to nanosecond shock compression," *Applied Physics Letters*, vol. 104, no. 101914, 2014.

[115] BANISHEV, A. A. and DLOTT, D. D., "Ultrafast pressure-sensitive paint for shock compression spectroscopy," *Journal of Applied Physics*, vol. 115, 2014.

[116] BROWN, K., SHAW, W. L., ZHENG, X., and DLOTT, D. D., "Simplified laser-driven flyer plates for shock compression science," *Review of Scientific Instruments*, vol. 83, no. 10, p. 103901, 2012.

[117] ALIVISATOS, A. P., "Semiconductor clusters, nanocrystals, and quantum dots," *Science*, vol. 271, pp. 933–937, 1996.

[118] BRUS, L. E., "Electron-electron and electron-hole interactions in small semiconductor crystallites: The size dependence of the lowest excited electronic state," *Journal of Chemical Physics*, vol. 80, no. 9, p. 4403, 1984.

[119] ALIVISATOS, A. P., HARRIS, T. D., BRUS, L. E., and JAYARAMAN, A., "Resonance raman scattering and optical absorption studies of cdse microsclusters at high pressure," *Journal of Chemical Physics*, vol. 89, no. 5979, 1988.

[120] ZHURAVLEV, K. K., PIETRYGA, J. M., SANDER, R. K., and SCHALLER, R. D., "Optical properties of pbse nanocrystal quantum dots under pressure," *Applied Physics Letters*, vol. 90, no. 043110, 2007.

[121] ZHAO, Z., ZENG, J., DING, Z., WANG, X., HOU, J., and ZHANG, Z., "High pressure photoluminescence of cdznse quantum dots: Alloying effect," *Journal of Applied Physics*, vol. 102, no. 053509, 2007.

[122] CHOI, C. L., KOSKI, K. J., SIVASANKAR, S., and ALIVISATOS, A. P., "Strain-dependent photoluminescenece behavior of cdse/cds nanocrystals with spherical, linear, and branched topologies," *Nano Letters*, vol. 9, no. 10, pp. 3544–3549, 2009.

[123] KAMISAKA, H., KILINA, S. V., YAMASHITA, K., and PREZHDO, O. V., "Ab initio study of temperature and pressure dependence of energy and phonon-induced dephasing of electronic excitations in cdse and pbse quantum dots," *Journal of Physical Chemistry C*, vol. 112, pp. 7800–7808, 2008.

[124] WITTENBERG, J. S., MERKLE, M. G., and ALIVISATOS, A. P., "Wurtzite to rocksalt phase transformation of cadmium selenide nanocrystals via laser-induced shock waves: Transition from single to multiple nucleation," *Physical Review Letters*, vol. 103, no. 125701, 2009.

[125] CHOI, C. L., KOSKI, K. J., OLSON, A. C. K., and ALIVISATOS, A. P., "Luminescent nanocrystal stress gauge," *Proceedings of the National Academy of Science*, vol. 107, no. 50, 2010.

[126] FORD, K. B., COLLINS, M. K., AJAMI, N. E., DOWDS, D., MESYEF, K., TROVILLION, J., AL-CHAAR, G., and MARSH, C. P., "Optical response to low applied pressure in a quantum dot nanocomposite," *Materials Letters*, vol. 106, pp. 301–303, 2013.

[127] VALIMET, "Chemical and physical characeristics of valimet spherical aluminum powder specifications."

[128] UNDERWOOD, E. E., *Particle-Size Distribution*. New York: McGraw-Hill, Inc., 1968.

[129] *Annual Book of ASTM Standards*, ch. Standard Test Method for Sieve Analysis of Metal Powders. No. B214-07, West Conshochocken, PA: ASTM International, 2011.

[130] SPECHT, P. E., *Shock Compression Response of Aluminum-Based Intermetallic-Forming Reactive Systems*. May, Georgia Institute of Technology, 2013.

[131] GOKHALE, A. and DRURY, W. J., "Efficient measurement of microstructural surface area using trisector," *Metallurgical and Materials Transactions A*, vol. 25A, pp. 919–929, 1994.

[132] ALLAN SCHRODER-PEDERSEN, JOHN KJOLLER, B. L., "A comparison of calculated geometric surface area and measured bet surface area for a metal powder," *Journal of Testing and Evaluation*, vol. 25, no. 4, pp. 365–369, 1997.

[133] TABOR, D., "The hardness of solids," *Review of Physics in Technology*, 1970.

[134] HALL, E. O., "Deformation and aging of mild steel: Iii discussion of results," in *Proceedings of Physical Society B*, vol. 64, p. 747, 1951.

[135] PETCH, N. J., "The cleavage strength of polycrystals," *The Journal of the Iron and Steel Institute*, vol. 173, pp. 25–27, 1953.

[136] HANSEN, N., "Boundary strengthening in undeformed and deformed polycrystals," *Materials Science and Engineering A*, vol. 409, pp. 39–45, 2005.

[137] WILLIAMSON, G. K. and SMALLMAN, R. E., "X-ray line broadening from filed aluminum and wolfram," *Acta Metallurgica*, vol. 1, no. 22, 1953.

[138] AYDELOTTE, B., TUCKER, M., KENNEDY, G., KELLY, S., and THADHANI, N., "A transparent anvil for experimental studies of reactive materials." in preparation, October 2012.

[139] CARNEY, J. R., MILLER, J. S., GUMP, J. C., and PANGILINAN, G. I., "Time-resolved optical measurements of the post detonation combustion of aluminized explosives," *Review of Scientific Instruments*, vol. 77, 2006.

[140] VOGLER, T. J., LEE, M. Y., and GRADY, D. E., "Static and dynamic compaction of ceramic powders," *International Journal of Solids and Structures*, vol. 44, pp. 636–658, 2007.

[141] BECKER, D. G. and HOLT, J. C., "Investigation of high-speed phenomena," tech. rep., National Aeronautics and Space Administration, 1972.

[142] EICHHORN, G., "Analysis of the hypervelocity impact process from impact measurements," *Planet, Space Science*, vol. 24, no. 771, 1976.

[143] SCHULTZ, P. H. and EBERHARDY, C. A., "Spectral probing of impact-generated vapor in laboratory experiments," *Icarus*, vol. 248, pp. 448–462, 2015.

[144] THORNHILL, T. F., REINHART, W., CHHABILDAS, L., BREILAND, W., ALEXANDER, C., and BROWN, J., "Characterization of prompt flash signatures using high-speed broadband diode detectors," *International Journal of Impact Engineering*, vol. 35, pp. 1827–1835, 2008.

[145] MILLER, G. H., "Jetting in oblique, assymetric impact," *Icarus*, vol. 134, pp. 163–175, 1998.

[146] FRIICHTENICHT, J. F. and SLATTERY, J. C., "Ionization associated with hypervelocity impact," Technical Note D-2091, National Aeronautics and Space Administration, 1963.

[147] SHEN, A. H., AHRENS, T. J., and O'KEEFE, J. D., "Shock wave induced vaporization of porous solids," *Journal of Applied Physics*, vol. 93, no. 5167, 2003.

[148] SCHULTZ, P. H. and ANDERSON, R. R., "Assymetry of the manson impact structure: Evidence for impact angle and direction," *Geological Society of America Special Papers*, vol. 302, pp. 397–417, 1996.

[149] KLEINBAUM, D. G. and KLEIN, M., *Logistic Regression: A Self-Learning Text*. Statistics for Biology and Health, Springer, 2010.

[150] HOSMER, D. W., LEMESHOW, S., and STURDIVANT, R. X., *Applied Logistic Regression*. Wiley Series in Probability and Statistics, John Wiley and Sons, Inc, 3rd ed., March 2013.

[151] *Using JMP6 Student Edition*. SAS Institute, 2006.

[152] LEVITAS, V. I., PANTOYA, M. L., CHAUHAN, G., and RIVERO, I., "Effect of the alumina shell on the melting temperature depression for aluminum nanoparticles," *Journal of Physical Chemistry C*, vol. 113, pp. 14088–14096, 2009.

[153] MCGLAUN, J. M. and THOMPSON, S. L., "Cth: A three-dimensional shock wave physics code," *International Journal of Impact Engineering*, vol. 10, pp. 351–360, 1990.

[154] ANTOUN, T., CURRAN, D., RAZORENOV, S., SEAMAN, L., KANEL, G., and UTKIN, A. V., *Spall Fracture*. Springer, 2003.

[155] JOHNSON, G. R. and COOK, W. H., "A constitutive model and data for metals subjected to large strains, high strain rates and high temperatures," Proceedings of the 7th International Symposium of Ballistics, 1983.

[156] STEINBERG, D. J., COCHRAN, S. G., and GUINAN, M. W., "A constitutive model for metals applicable at high strain rate," *Jounral of Applied Physics*, vol. 51, p. 1498, 1980.

[157] STEINBERG, D. J. and LUND, C. M., "A constitutive model for strain rates," *Journal of Applied Physics*, vol. 65, no. 4, 1989.

[158] EAKINS, D. E. and THADHANI, N. N., "Instrumented taylor anvil-on-rod impact tests for validating applicability of standard strength models to transient deformation states," *Journal of Applied Physics*, vol. 100, no. 073503, 2006.

[159] KAPOOR, R. and NEMAT-NASSER, S., "Determination of temperature rise during high strain rated deformation," *Mechanics of Materials*, vol. 27, pp. 1–12, 1998.

[160] ZHANG, H., WANG, L., XIONG, H., HU, L., YANG, B., and LI, W., "Hydrothermal synthesis for high-quality cdte nanocrystals," *Advanced Materials*, vol. 15, no. 20, pp. 1712–1715, 2003.

[161] KANG, Z., ZHANG, Y., MENKARA, H., WAGNER, B., SUMMERS, C., LAWRENCE, W., and NAGARKAR, V., "Cdte quantum dots and polymer nanocomposites for x-ray scintillation," *Applied Physics Letters*, vol. 98, no. 181914, 2011.

[162] LEATHERDALE, C. A., WOO, W.-K., MIKULEC, F. V., and BAWENDI, M. G., "On the absorption cross section of cdse nanocrystal quantum dots," *Journal of Physical Chemistry B*, vol. 106, no. 7619-7622, 2002.

[163] THADHANI, N., "Meso-scale time-resolved diagnostics employing photonic crystals for probing dynamic events in inert and reactive particulate materials," tech. rep., Georgia Institute of Technology, 2015.

[164] BUENO, A., SUAREZ, I., ABARGUES, R., SALES, S., and PASTOR, J. P. M., "Temperature sensor based on colloidal quantum dots-pmma nanocomposite waveguides," *IEEE Sensors Journal*, vol. 12, no. 10, 2012.

[165] LIN, Y.-C., CHOU, W.-C., SUSHA, A. S., KERSHAW, S. V., and ROGACH, A. L., "Photoluminescence and time-resolved carrier dynamics in thiol-capped cdte nanocrystals under high pressure," *Nanoscale*, vol. 5, 2013.

[166] GONZALEZ, J., PEREZ, F. V., MOYA, E., and CHERVIN, J. C., "Hydrostatic pressure dependence of the energy gaps of cdte in the zinc-blende and rocksalt phases," *Journal of Physcial Chemistry of Solids*, vol. 56, no. 3/4, pp. 335–340, 1995.

[167] MCMAHON, M. I., NELMES, R. J., WRIGHT, N. G., and ALLAN, D. R., "Phase transitions in cdte to 5 gpa," *Physical Review B*, vol. 48, no. 22, 1993.

[168] WU, F. W., ZAUG, J. M., YOUNG, C. E., and ZHANG, J. Z., "Pressure-induced phase transition in thiol-capped cdte nanoparticles," *Journal of Nanoscience and Nanotechnology*, 2006.

[169] RAHIMI, M., KAMELI, P., RANJBAR, M., and SALAMATI, H., "The effect of pva coating on structural, magnetic properties and spin dynamics of ni(.3)zn(.7)fe(2)o(4) ferrite nanoparticles," *Journal of Magnetism and Magnetic Materials*, vol. 347, pp. 139–145, 2013.

[170] FOGLIAZZA, M., SICARD, L., DECORSE, P., CHEVILLOT-BIRAUD, A., MANGENEY, C., and PINSON, J., "Powerful surface chemistry approach for the grafting of alkyl multilayers on aluminum nanoparticles," *Langmuir*, vol. 31, no. 22, pp. 6092–6098, 2015.

[171] YANG, Z., LI, L., MING, T., LI, G., WANG, J., and YU, J., "Direct encoding of silica submicrospheres with cadmium telluride nanocrystals," *Journal of Materials Chemistry*, vol. 19, 2009.

[172] JING, L., YANG, C., QIAO, R., NIU, M., DU, M., WANG, D., and GAO, M., "Highly fluorescent cdte@sio2 particles prepared via reverse microemulsion method," *Chemical Materials*, vol. 22, 2010.

[173] CHRISTENSEN, J. M., BANISHEV, A. A., and DLOTT, D. D., "Bright emissive core-shell spherical microparticles for shock compression spectroscopy," *Journal of Applied Physics*, vol. 116, no. 033513, 2014.